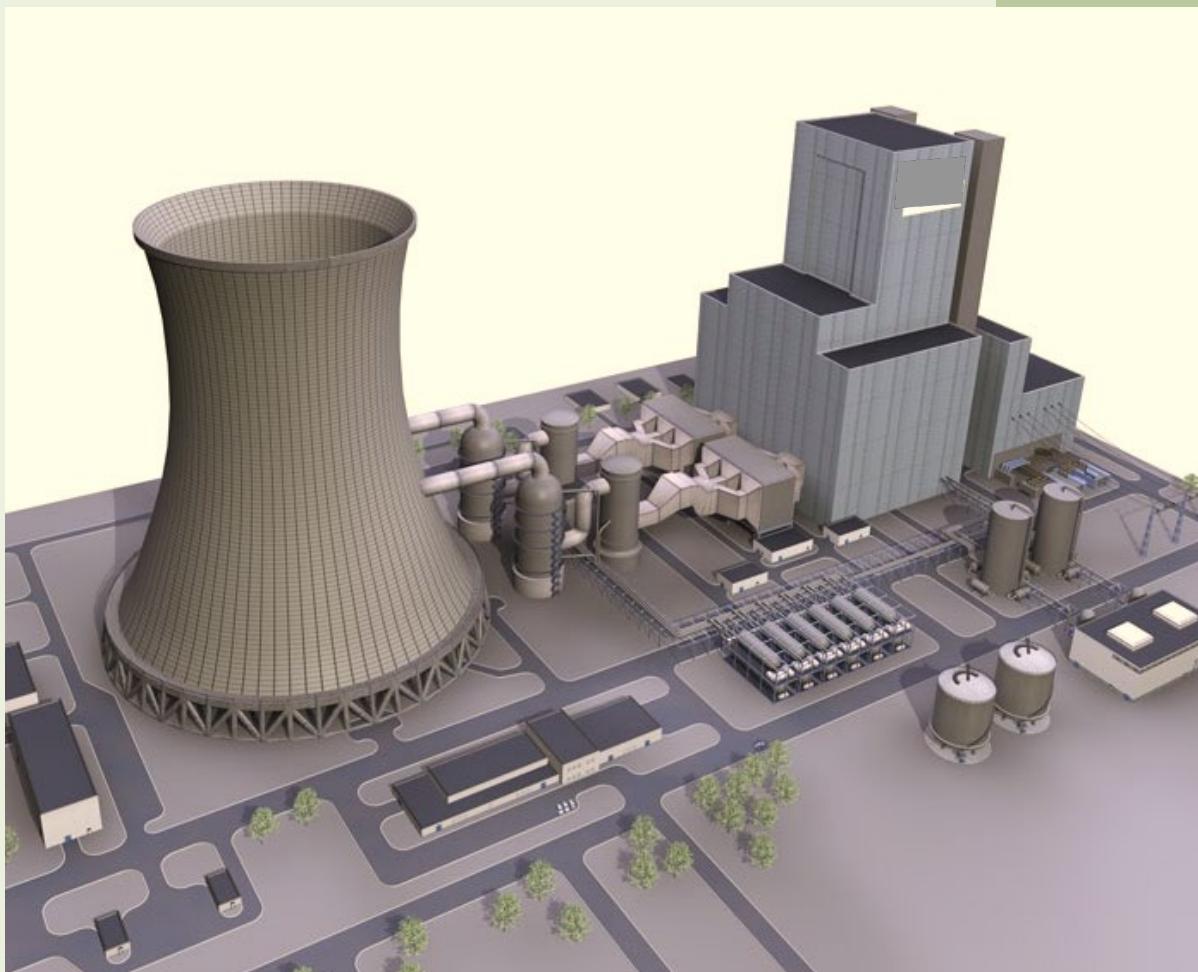**FINAL REPORT: Project: RDE-493-24**

Combining Thermochemical Energy Storage with Coal-Fired Power Generation:

A novel approach to managing variable loads without the need to cycle coal-fired generating units

28 February 2019 (Revised on 24 July 2019**)**

Authors:

Professor Behdad Moghtaderi
Dr Ahmad Seyfaee
Priority Research Centre for Frontier Energy Technologies & Utilisation;
Newcastle Institute for Energy & Resources;
The University of Newcastle
University Drive; Callaghan
NSW 2308; Australia

Report Type	Reporting Period		Report Number	Notes
	From	To		
Final Report	Oct. 2016	Oct. 2018	F-01-2019	

Project Information

Project Leader	**Prof Behdad Moghtaderi**
Chief Investigators	A/Prof Elham Doroodchi
	Prof Jianglong Yu
	Dr Ahmad Seyfaee
	Dr Cheng (Wallace) Zhou
Project Sponsors	NSW Department of Industry (100%)
Number of Project Phases	2
Current Lifecycle Phase	Project Completion
Total Project Budget	$422,029 (incl. GST)
Project Duration	22 months
Official Project Start Date **(Date of the execution of the agreement)**	15 December 2016
Actual Project Start Date	15 October 2016
Project End Date	14 October 2018

Note: Please find the SIGN OFF section at the end of the report.

Table of Contents

Chapter 1   1
Introduction

Chapter 2   6
State-of-the-Art in Energy Storage: Technology Status and Applications (Milestone 2)

Chapter 3   23

Proposed Thermochemical Concepts for Utility-Scale Energy Storage (Milestone 2)

Chapter 4   27

Research Methodologies (Milestones 3 and 4)

Chapter 5   59

Results and Discussion: Scoping study (Milestone 2)

Chapter 6   77

Results and Discussion: Techno-Economic Assessment and LCA Analysis (Milestone 3)

EXECUTIVE SUMMARY

This final report details the key findings and outcomes of the project "Combining Thermochemical Energy Storage With Coal-Fired Power Generation: A novel approach to managing variable loads without the need to cycle coal-fired generating units". The project, which was supported by generous funding from Coal Innovation NSW, was conducted over the period between 15 Oct 2016 and 15 Oct 2018 by a team of researchers from the University of Newcastle. The main objective of Stage 1 was to assess the feasibility of employing utility-scale thermochemical energy storage as a means of managing variable loads in coal-fired power plants. The vision was to help to develop a new technology concept for existing coal-fired power plants that, in addition to baseload production, enables such assets to control variable generation without necessarily exposing the generating units to cycling (note: cycling is detrimental to the operation and maintenance of coal-fired power plants which have traditionally been designed for baseload operation).

Two different classes of thermochemical processes were selected for the feasibility study in Stage 1. These were reversible chemical reactions based on: (i) the reduction/oxidation of metallic oxides, and (ii) the calcination/carbonation of calcium-rich particles. The former group, referred to as "Redox Energy Storage (RES)" here, centred around the reduction/oxidation of composite copper-rich particles (copper-rich particles on a silica substrate with an active metal concentration of about 60%). The latter group, hereafter referred to as "Calcium Looping (CaL)", focused on the calcination/carbonation of a naturally occurring mineral known as stone dust. The choice of these materials was based on the research team's experience in a number of previous chemical looping related projects.

The thermochemical energy storage unit was assumed to consist of two main components, namely: (i) the thermochemical block being either a RES or a CaL type system, and (ii) the power block being either an open cycle gas turbine (OCGT), or a secondary steam cycle (SSC).

Four different system configurations were considered in the Stage 1 feasibility studies, namely: RES+OCGT, CaL+OCGT, RES+SSC and CaL+SSC. Each configuration was thoroughly examined through a comprehensive series of process simulations (using ASPEN[+] software) as well as by detailed economic analyses comprised of levelised cost of electricity (LCOE), total cost of production (TCOP), net present value (NPV), internal rate of return (IRR) and simple payback period (SPP). Both sets of technical and economic studies were carried out using a scenario-based approach.

It was found that the CaL+SSC configuration was feasible from both a technical and economic point of view and that it successfully met all of the performance targets set out in the funding agreement. The RES+SSC and RES+OCGT systems were also found to be technically feasible but they were not economically viable unless a revenue stream was created by marketing their oxygen by-products. The use of OCGT as the power block for both the RES and CaL systems required the use of a secondary fuel (compressed natural gas (CNG) or liquefied natural gas [LNG]) which, apart from added cost and complexity, would result in additional greenhouse gas (GHG) emissions. For these reasons, it was recommended that both the CaL+SSC and RES+SSC systems to be selected as the most suitable configurations.

Stage 2 of the project (bench-scale studies) was initiated with a Reactivity/materials study, which included an extensive investigation into the reactivity of the chosen materials (copper-rich particles and calcium-rich particles). Different techniques were utilised to characterise the particles and to provide insights into their reaction kinetics. The effects of the three main

key parameters (size of bed inventory, temperature and gas flow rate) on the reactivities of the materials were investigated.

Since the reactions should have been reversible, the cycling stability of the particles was investigated in the reactivity/materials study milestone. Altogether, over 300 samples were analysed using thermal gravimetric analysis/differential scanning calorimetry (TGA/DSC), scanning electron microscopy (SEM) and X-ray diffraction (XRD) techniques. The TGA results of about 100 reactions were directly used to determine the reaction kinetics of both the CaO and copper-rich particles. In addition, the TGA results showed how the reactivity of the particles could be affected by cycling. The XRD and SEM results were used to relate the effects of the particle cycling to the changes in the structures of the particles.

The reactivity results from the reactivity/material study were incorporated in the design of the prototype units in order to assure the performance of the fluidised bed. Laboratory-scale, pilot-scale and large-scale prototypes developed (or modified) for the experiments. The scaleup factors based on the gas processing capacity for Laboratory-scale: Pilot-scale: Large-scale were 1:40:240. The main differences in the developed prototypes were their inventory size, maximum flow rate and their heating systems.

The laboratory-scale prototype investigated the reactivity of the particles on a small scale in both fluidised and fixed beds in a controlled laboratory environment.

The pilot-scale fluidised bed was used to demonstrate field trials and the flow rate, temperature and inventory of the fluid bed were chosen as the variables. The pilot-scale prototype was used in an open environment. The results showed that to make the reactor self-sustained, the bed inventory should be larger and the system should be insulated.

Therefore, a large-scale prototype was utilised to demonstrate that, at an industrial scale, it is feasible to produce power at a constant level for a long period.

The key findings of the first stage are summarised below:

- From a technical point of view, all four configurations of the energy storage unit were capable of storing electrical energy in a thermochemical form, and were therefore feasible.
- However, from an economic point of view, the RES+SSC and RES+OCGT configurations were found to be viable only when their oxygen by-product streams were assumed to generate revenue. Of the two configurations, the RES+OCGT was found to be the less attractive economically because of the need for a secondary fuel, either compressed natural gas (CNG) or liquefied natural gas (LNG).
- The CaL+OCGT system was found to not be economically viable, primarily because of the need for a secondary fuel (CNG or LNG) which, apart from the added cost and complexity, would result in additional GHG emissions.
- In contrast, the CaL+SSC configuration was found to be feasible from both a technical and economic point of view and it successfully met all of the performance targets set out in the funding agreement.

The key findings of the second stage are summarised below:

- The reactivity of the calcium-rich particles dropped after 5 cycles, however due to their lower energy requirements and low cost, they were more suitable than the copper-rich particles if the oxygen production is not important.

- The copper-rich particles demonstrated a stable reactivity after 5 cycles.

- The calcination and carbonation temperatures had an impact on the reactivities of the calcium-rich particles and low temperatures resulted in a high reactivity.

- The reaction mechanisms of the calcium-rich particles for high CO_2 concentrations was more complicated than for the copper-rich particles.

- Calcium-rich particles were used for the field trials. It was noticed that the temperature of the bed during the carbonation process remained constant and that the CO_2 concentration in the exhaust increased gradually over time. This showed that calcium-rich particles could be utilised to prevent the cycling of a power plant and decrease its maintenance and operational costs.

LAY SUMMARY

This project addresses the grand challenge of eliminating or at least mitigating the need for large-scale coal-fired power plants (e.g. primary power cycle) to decrease or increase their electricity output (e.g. cycling) to meet the electricity demand in the grid (variable load management). The cycling process has been known to be detrimental to the operational life of the components of the primary power cycles and increased the operation and maintenances. Hence, the outcome would be inefficient coal burning and the release of a larger amount of CO_2. Here, it is shown that a primary cycle can operate on a constant baseline (with power generation higher than the minimum demand and lower than the maximum demand) without cycling. The excess energy during the low demand period is utilised to energise solid particles (e.g. calcium-rich particles). Then, the energy gap during the peak period would be provided by the energised particles by releasing their stored energy via a smaller power generation unit (e.g. secondary power cycle). Moreover, since the type of the stored energy in particles is heat (thermal) and since chemical reactions are involved to energise/de-energise the particles, this technology is called thermochemical energy storage (TES).

With this approach, the coal-fired units of the primary power plant will provide the baseload and, hence, are not subjected to cycling, while the TES unit deals with the variable load and essentially functions as a peaking unit (secondary power plant).

The project consisted of two phases, namely Stage 1 and Stage 2. Stage 1 focused on a scoping study comparing the TES with other technological options for utility-scale energy storage. It was found in Stage 1 of the project that using calcium-rich particles ($CaO/CaCO_3$) as the energy carriers to generate electricity using a steam powerplant would be the most beneficial. In this configuration, the stored heat in the particles was used to produce steam which generated power by spinning turbine blades of the secondary power plant.

Stage 2 focused on bench-scale studies using a proof-of-concept prototype which was fabricated based on the outcomes and findings in Stage 1. Three different prototypes with different capacities were used in Stage 2. The laboratory-scale prototype was mainly used to investigate the reactivity of the particles. The results showed that the reactivity of copper-rich particles remained constant, while the reactivity of calcium-rich particles decreased over time. Therefore, a make-up stream for calcium-rich particles should be considered. The pilot-scale prototype was developed based on the results from the laboratory-scale prototype and an examination of the findings. The results showed that the best temperature to use calcium-rich particles was 600 °C. The large-scale prototype proved that using calcium-rich particles as the energy carrier in the TES can be utilised to produce energy and maintain the temperature constant, thus producing steam at constant temperature and providing enough energy to eliminate the detrimental effects of cycling of the primary unit.

LIST OF FIGURES

LIST OF TABLES

ACKNOWLEDGMENTS

ACRONYMS

2DS	≡	2 Degree (centigrade) Scenario
CAES	≡	Compressed Air Energy Storage
CaL	≡	Calcium Looping
CAPEX	≡	Capital Cost
CF	≡	Cash Flow
C_e	≡	Equipment cost
CLAS	≡	Chemical Looping Air Separation
CNG	≡	Compressed natural gas
FB	≡	Flow Battery
FCOP	≡	Full Cost of Production
FES	≡	Flywheel Energy Storage
GHG	≡	Greenhouse Gases
HAZOP	≡	Hazard and Operability
HFB	≡	Hybrid Flow Battery
IEA	≡	International Energy Agency
IRR	≡	Internal Rate of Return
ITM	≡	Ionic Transport Membrane
LCOE	≡	Levelised Cost of Electricity
LNG	≡	Liquefied Natural Gas
NaS	≡	Sodium Sulphur battery
NPV	≡	Net Present Value
O&M	≡	Operation and Maintenance
OCGT	≡	Open Cycle Gas Turbine
OPEX	≡	Operational Cost
P&ID	≡	Piping and Instrumentation Diagram
PCM	≡	Phase Change Material

PF	≡	Pulverised Fuel
PHES	≡	Pumped Heat Electrical Storage
PHS	≡	Pump Hydro Storage
PSA	≡	Pressure Swing Adsorption
R&D	≡	Research and Development
Redox	≡	Reduction Oxidation
RES	≡	Redox Energy Storage
RFB	≡	Redox Flow Battery
SC	≡	Supercapacitor
SCMS	≡	Super Conducting Magnetic Storage
SMGES	≡	Solid Mass Gravitational Energy Storage
SP	≡	Specific Power
SPP	≡	Simple Payback Period
SRC	≡	Steam Rankine Cycle
SSC	≡	Secondary Steam Cycle
SSRC	≡	Supercritical Steam Rankine Cycle
TCOP	≡	Total Cost of Production
TCWS	≡	Thermochemical Water Splitting
TES	≡	Thermal Energy Storage
TFCC	≡	Total Fixed Capital Cost
TWG	≡	Technical Working Group
UON	≡	University of Newcastle
UPS	≡	Uninterruptable Power Supply
VCOP	≡	Variable Cost of Production
VRFB	≡	Vanadium Redox Flow Battery
VSA	≡	Vacuum Swing Adsorption

Chapter 1

INTRODUCTION

1.1 MOTIVATION AND DRIVERS

The increasing penetration of intermittent energy sources (e.g., wind and solar) into electricity networks, coupled with changes in power consumption patterns due to demand-side management, electricity deregulation and smart grids, generally favours low cost power plants that have the ability to cycle on and off depending on their load variations [1-3]. Cycling here refers to the operation of generating units at different load levels in response to changes in the network load requirements. These include the on/off, load following and minimum load operations. To deal with the load variations in modern electricity networks, combined cycle gas turbine (CCGT) and open cycle gas turbine (OCGT) power plants are typically used, although these plants are generally very expensive to run.

Competition has also forced many coal-fired power plant operators and utilities to adopt the unit cycling of their assets, which are quite often aging hardware. This type of cycling would have onerous effects on conventional coal-fired power plants given that such systems have been principally designed for baseload operations with only a small number of start-ups and shut-downs per year. Cycling particularly damages the coal-fired units of the plant (often due to unavoidable thermal and pressure stresses), and increases their failure rates, thereby lowering their life expectancies compared to baseload operations. More importantly, the suboptimal operation of the coal-fired units during cycling will inevitably lead to efficiency losses and, hence, higher greenhouse gas (GHG) emissions [4].

While changes such as modifications to operational practices, proactive inspections and extensive training can reduce the extent of the damage and lower the costs of maintenance, the detrimental impacts of cycling cannot be fully eliminated using these approaches. The upgrading of a plant to a combined cycle configuration also does not completely resolve the issue since even modern combined cycle coal plants experience difficulties when cycling under variable loads [4].

Given the considerable work that has been undertaken in recent years to resolve the issues associated with unit cycling, any further work based on the relatively standard approaches might be difficult to justify. Clearly, there is a need for an entirely novel approach that is inherently simple and cost effective. The current project is concerned with the establishment and further development of just such an approach.

1.2 BRIEF PROJECT DESCRIPTION

This project addresses the grand challenge of variable load management with a vision to establish a new coal-fired power plant concept that, in addition to baseload production, can robustly and effectively control variable generation without necessarily exposing its coal-fired generation units to cycling. This vision is fulfilled by integrating a thermochemical energy storage (TES) unit with coal-fired generation. In this configuration, the TES unit, which can be a redox (reduction-oxidation) or non-redox type, stores the low cost thermal and/or electric energy generated by the coal-fired power plant during its off-peak period (up to 12 hours) and releases some of that energy back to the grid during its peak hours (up to 12 hours). With this approach, the coal-fired units of the power plant will provide the baseload production and, hence, are not subject to cycling, while the TES unit deals with the variable load and essentially functions as a peaking unit.

The project consists of two phases, namely Stage 1 and Stage 2. Stage 1 focused on a scoping study comparing TES with other technological options for utility-scale energy storage. Stage 2 focused on bench-scale studies using a proof-of-concept prototype which was fabricated based on the Stage 1 outcomes and findings.

1.3 EXPANDED PROJECT SCOPE

The original scope of the project outlined in the proposal was only limited to research and development activities on the redox type of TES concepts. However, the initial assessment indicated the potential in researching the Calcium looping (CaL) process in addition to redox energy storage (RES) under thermochemical energy storage concepts. Therefore, these two processes were studied for this project after consultation with Coal Innovation NSW (CINSW).

1.4 AIMS AND OBJECTIVES

The primary aims of this project are to determine the key underlying science and engineering issues that underpin the performance of the TES for utility-scale coal-fired power generation. In particular, the research focuses on:

Stage 1 (Scoping Study):
- Develop a range of process flowsheets to identify the most effective schemes for the integration of TES to either conventional or oxy-fuel type coal-fired power plants.
- Study the heat management in integrated TES coal-fired power generation.
- The bench-marking of selected TES process flowsheets against other competing technologies to address utility-scale variable load management (i.e., includes energy storage plus other technologies such as peaking gas turbines).
- Determine the operational envelope of integrated TES coal-fired power plants (especially a quantification of the energy losses and efficiencies in response to load variations) using dynamic process modelling.
- A techno-economic assessment.

Stage 2 (Experimental Studies):

- Understanding the chemistry and reactivity of mono- or bi-metallic synthetic/natural sorbents under prolonged redox (i.e., reduction/oxidation) or non-redox (e.g., carbonation-calcination) half-cycles of 12 hours or more.
- Understanding the operational limitations and robustness of the manifold switching reactor under conditions pertinent to TES.
- The design, construction and commissioning of a small-scale proof-of-concept prototype with a maximum flow rate of 200 m^3/h.
- Field trials and demonstrations of the 200 m^3/h prototype.

1.5 MILESTONES AND PROGRESS SUMMARY

Table 1.1: Milestone tasks and performance measures

Milestone ID and Title	Start Date	Scheduled Completion Date	Performance Measures
M1 – Completion of pre start-up administrative tasks	Sept 2016	15 Oct 2016	• Execution and exchange of the funding agreement, grant establishment, finalisation of safety and ethics clearance, staff recruitment
M2 – Desktop scoping study comparing TES with other technology options	15 Dec 2016	14 June 2017	• Quarterly reports Q4-2016, Q1-2017 and the Stage-Gate report • Establishment of claimed benefits and confirmation of performance criteria for Stage 2
M3 – Techno-economic Assessment	15 Jan 2017	14 Aug 2017	• Quarterly reports Q2-2017, Q3-2017 and the Stage-Gate report • Establishment of claimed benefits and confirmation of performance criteria for Stage 2
M4 – Reactivity/materials study	15 Sep 2017	14 Dec 2017	• Completion of 80 reaction and reaction pathways experiments • Completion of 40 SEM & XRD tests • Quarterly report Q1-2018 and annual report 1
M5 – Prototype development	15 Dec 2017	14 July 2018	• Design, fabrication, commissioning and delivery of the proposed 200 m^3/h prototype unit • Quarterly reports Q1-2018, Q2-2018
M6 – Field trials/demonstration	15 July 2018	30 Sep 2018	• Completion of 162 demonstration tests • Quarterly report Q3-2018
Final Report		Feb 2019	

Table 1.2: Progress Summary*

Milestone ID	Status	Planned Start Date	Planned End Date	Actual End Date	On Track	On Budget
M1	100% Completed	Sept 2016	15 October 2016	11 Jan 2017	✓	✓
M2	100% Completed	15 Dec 2016	14 June 2017	15 July 2017	✓	✓
M3	100% Completed	15 Jan 2017	14 Aug 2017	30 Sept 2017	✓	✓
M4	100% Completed	15 Sep 2017	14 Dec 2017	10 Jan 2017	✓	✓
M5	100% Completed	15 Dec 2017	14 July 2018	04 Aug 2018	✓	✓
M6	100% Completed	15 July 2018	30 Sep 2018	05 Oct 2018	✓	✓

Table 1.3: Key performance targets and the level of success

Performance Parameters				Level of Success
Category	Indicator	Measure	Target	
TES Process (Technical)	Variable Load Management	Cycling efficiency	85%	96% Achieved (Table 5.1)
		Load following	Better than gas-fired peaking plants	Achieved
	Energy Storage	Capacity	At least 0.8 MW/m^3	1.47 MW/m^3 (Table 5.2)
		Charging period	Flexible (minutes to hours)	10-30 min
		Self-discharge rate	~ 0.0	Achieved
TES Process (Economic)	Cost Effectiveness	Energy demand for O$_2$ production	1/3 of cryogenic based systems **(only for RES Version)**	Achieved
		CAPEX / OPEX	1/3 of battery systems	Achieved (Figs 6.2- to 6.4)
		LCoE	20%-40% lower than gas-fired plants	Achieved (Fig 6.1)
TES Process (Low Emission Features)	Pilot-Scale Demonstration	Energy storage	0.5 MW	Achieved
		O$_2$ production	2.5 tonne/day **(only for RES Version)**	The RES version was not tested at pilot-scale based on the findings from Stage-I of the project
	GHG reduction	At plant level	1.0 tonne/MWh of energy saved	Achieved (refer to Section 6.3 LCA analysis)
		If RES deployed across NSW	1.6 tonne/MWh of energy saved	Achieved (refer to Section 6.3 LCA analysis)
Project	Capacity	Track record		Achieved

		funding and/or in-kind support	Refer to Section 10 of the original submission	
	Support			
	Regulatory Compliance	Compliance with environmental and planning regulations		

1.6 STRUCTURE OF THIS REPORT

The present final report has been structured in a manner to demonstrate to an independent reviewer how the technical work undertaken in Stage 1 achieves the broad objectives of the project and how the proposed thermochemical energy storage concepts satisfy the relevant performance criteria. This is accomplished by providing sufficient details of the research activities undertaken in Stage 1, along with a detailed plan for the next phase of the project. It is against this backdrop that Chapter 1 has been dedicated to providing an overview of the project, its aims and objectives and key milestones, as well as the performance criteria/measures.

Given the importance of energy storage in the contexts of variable load management at the utility-scale (i.e., the focus of this project), Chapter 2 presents a state-of-the-art review of the proven, emerging and new energy storage technologies. The review is broad and not limited to just those technologies suitable for variable load management (typically achieved by employing a time-shifting strategy such as load levelling or peak shaving).

Chapter 3 provides a brief description of the thermochemical energy storage concepts proposed in this project, which include:

1. A redox type process based on the Chemical Looping Air Separation (CLAS) technology developed by the research team through a series of research and development projects between 2010 and 2015, including one funded by Coal Innovation NSW.

2. A calcium looping (CaL) cycle encompassing the calcination-carbonation of calcium carbonate-rich minerals such as limestone and/or stone dust.

Chapter 4 summarises the methodologies adopted in this study to achieve the aims and objectives of the project. The theoretical assumptions and experimental procedures are being discussed in detail in chapter 4.

Meanwhile, for the proposed energy storage concepts, Chapters 5 expresses the key findings of the scoping study, including their energy flows, responses to dynamic conditions and oxygen production. The techno-economic assessment and LCA analysis results are discussed in Chapter 6. In addition, the results reported in Chapter 7 include the experimental work of the project. The results of the three different levels of the conducted experiment are demonstrated and discussed in this chapter.

An overall conclusion is reported in Chapter 8, followed by the project recommendations in Chapter 9.

Chapter 2

The State-of-the-art in Energy Storage: Technology Status and Applications (Milestone 2)

2.1 BACKGROUND

2.1.1 Introduction

The growing demand for high quality and reliable electric power, and the recent advances in energy storage will likely result in energy storage becoming a much more important component of the electric power infrastructure [5-13]. Although the focus of this report is on the use of energy storage as a means of managing grid-scale variable loads, energy storage can also be employed in a number of other roles which benefit all of the major subsystems of a typical electric power grid, including: generation (i.e., supply), transmission, distribution and demand (end-users).

Because of the different operational requirements of these subsystems, a wide variety of storage technologies are being developed around the world which complement proven energy storage technologies, such as pump hydroelectric storage (PHS) and batteries. With such a variety of approaches, it is important to match the application with storage technology. However, this requires an in-depth understanding of the capabilities and limitations of both the proven and emerging energy storage technologies. The materials presented in this chapter can assist the reader in arriving at such an understanding.

With this in mind, the present chapter begins with an overview of electricity and its key features. Basically, electricity is an attractive form of energy for utilisation in domestic, commercial and industrial applications. Electricity can be generated in large quantities and transmitted over long distances for utilisation. It is a clean and easily controllable form of energy, but more importantly electricity is relatively cheap and has been a cheap product for over a century. Indeed, the rapid industrialisation of the developed countries was made possible after cheap electricity became widely available in the early 1920s. For this reason, one of the key parameters in assessing the standard of living of a given country is how much electricity is consumed in that country.

Unfortunately, unlike other forms of energy (e.g., mechanical, thermal, etc.), electrical energy cannot always be stored directly (e.g. electricity to electricity) and, hence, in a modern

distribution network, the supply of electricity must be continuously balanced against the demand (i.e., the load). This function has become more challenging in recent times owing to the sizable penetration of intermittent renewable energy sources (e.g., wind and solar) into the electricity networks leading to high levels of uncertainty in electricity supply. The constant act of balancing generation versus demand is very taxing on the grid's infrastructure and has significant operational and cost implications. For example, modern grids are generally designed based on the highest level of demand, despite the fact that the generating capacity required to satisfy this demand is only needed occasionally, and on each occasion only for short periods of time.

2.1.2 Factors Affecting the Selection of Storage Technologies

As far as the storage of electrical energy is concerned, electricity can be converted to a storable form of energy (e.g., chemical, mechanical or thermal) and then converted back to electricity on demand. Common examples include chemical energy (batteries), electrical potential energy (capacitors), gravitational potential energy (pumped hydroelectric), kinetic energy (flywheels and compressed air), magnetic fields (inductors), thermal (phase change materials) and thermochemical (reversible reactions such as redox).

The choice of one storage technology over another for any particular function within a modern electricity network depends on a number of factors, chiefly amongst them [13]:

1. Whether the end use application requires energy or power (*energy can be viewed as a volume while power is like a flow rate*).

2. Energy density (*amount of energy stored per unit weight and/or unit volume of the storage medium*).

3. Response time (*how quickly the storage device can discharge*).

4. Discharge duration (*length of the period that the storage device can discharge in a single charge-discharge cycle*).

5. Discharge frequency (*number of charge-discharge cycles per unit of time*).

6. Depth of discharge (*percentage of power discharged relative to full capacity; this is particularly important for storage devices like batteries which may quickly lose their storage capacity over time if they are deeply discharged*).

7. Efficiency (*describes the relationship between the input and output energy and can be defined in a number of different ways such as cycle efficiency, round trip efficiency, thermal efficiency, mechanical efficiency, etc.*).

Storage technologies such as the PHS and thermochemical redox based methods are well suited to applications such as load shifting, where a large volume of energy storage capacity is required. In contrast, a flywheel storage system is most suited to applications such as real-time voltage stabilisation, where a large responsive power capacity is required. Energy density is another important factor because, to a large extent, it underpins the physical dimensions of the storage device and thereby the capital cost. A storage device with a moderate energy efficiency but a large energy density might be more cost effective than a high efficiency storage device with a low energy density.

2.1.3 Key Objectives of Energy Storage in Electricity Networks

Energy storage deployment could be realised across the supply, transmission, distribution and demand (end-use) components of an electricity network, although the focus here is on the supply and transmission components. Utility-scale or bulk energy storage enables the generators to achieve a number of key objectives necessary in modern electricity networks for the supply and transmission of electricity, namely [13]:

1. Time-shift of energy delivery (*energy arbitrage over time enabling a generator to make use of price differences between off-peak and peak periods; time-shifting can be carried out in the form of either load-shifting or load levelling; in the time-shift role, the energy storage device can deal with variable loads*).

2. Integration of renewables generation (*balancing of intermittent renewable generation with load*).

3. Maintaining power quality and reliability (*alternating between absorbing and injecting power to keep the voltage and frequency within optimal ranges*).

4. Grid operational support (*also called ancillary services, is about promoting a coordinated operation of grid components and reducing efficiency losses*).

5. Transmission and distribution support (*providing utilities with a means of regulating power and reducing line congestion*).

6. Capacity credits (*deferring the need to upgrade existing generation or transmission infrastructure; this is of significant importance in Australia, and specifically NSW, where due to the age of the assets the current grid infrastructure is unlikely to meet future demands*).

2.1.4 Applications of Energy Storage in Electricity Networks

The effectiveness of a given energy storage technology, to a large extent, depends on the specific application for which the technology is used. Consequently, technologies that can be applied in several alternative applications may not necessarily feature the same performance characteristics in each application. Therefore, it is important to map the typical utility-scale applications against the operational requirements at such scales. This, in turn, will allow the feasibility of using a particular energy storage technology to be evaluated simply by comparing the technology's key performance characteristics against the operational requirements of the desired application.

Table 2.1 summarises the results of such a mapping and provides a list of the key utility-scale applications against performance measures such as discharge duration, response time, discharge depth, minimum cycle life and power, as well as energy efficiency and energy density. The definitions of the applications used in Table 2.1 are as below.

- **Load shifting** – storing energy during an off-peak period (period of low demand) for use during a peak period (period of high demand). Therefore, load shifting technologies are capable of operating for few hours.

- **Renewables time shifting** – matching the temporal pattern of the electrical load by storing energy from renewable sources of generation.

- **Renewables forecast hedging** – correcting the errors in forecasting the output of renewables generation.

- **Mitigating transmission curtailment** – decongestion of the transmission system so that more economic generation options can be used.

- **Power quality and reliability** – maintaining voltage and frequency within normal ranges of operation.

- **Spinning reserve** – compensating for unexpected outage generating units.

- **Regulation control** – maintaining a real-time balance between generation and load.

- **Fluctuation suppression** – smoothing out instantaneous (very short millisecond range) variations in voltage and current.

- **Grid voltage stability** – preventing voltage from falling below acceptable levels by providing reactive power support.

- **Frequency excursion suppression** – maintaining normal frequency when there is an imbalance between the load and generation.

- **Grid angular stability** – minimising power oscillations caused by the loss of generator synchronisation.

Table 2.1: Applications versus operational requirements [5-13]

Energy Storage Type	Energy Storage Application (Electricity Only)	Operational Requirements						Storage Objectives Met					
		Discharge Duration	Response Time	Discharge Depth	Min Cycle Life	Energy Storage Unit Power (MW)	Energy Efficiency and Energy Density	Time-Shifting	Integration of Renewables	Power Quality and Reliability	Grid Operational Support	Transmission & Distribution Support	Capacity Credits
Long Discharge - Frequent Use	Load shifting	3-10 Hours	10-20 min	Deep	< 5000	1 to 200	Important	×	×	×	×	×	×
	Renewables time-shifting	5-12 Hours	1 min	Deep	< 5000	2 to 200	Important	×	×	×	×	×	×
	Renewables forecast hedging	5-12 Hours	20 ms	Deep	< 5000	2 to 200	Important	×	×	×	×	×	×
	Mitigating transmission curtailment	5-12 Hours	1 min	Deep	< 5000	2 to 200	Important	×	×	×	×	×	×
Long Discharge - Infrequent Use	Renewables time-shifting	5-12 Hours	1 min	Deep	< 500	2 to 200	Not Important	×	×	×	×	×	
	Renewables forecast hedging	5-12 Hours	20 ms	Deep	< 500	2 to 200	Not Important	×	×	×	×	×	
	Mitigating transmission curtailment	5-12 Hours	1 min	Deep	< 500	2 to 200	Not Important	×	×	×	×	×	
	Power quality / reliability	4 Hours	20 ms	Deep	< 500	1 to 50	Not Important	×	×	×	×	×	
	Spinning reserve	Few Hours	Seconds	Deep	< 500	1 to 50	Not Important	×	×	×	×	×	
Short Discharge - Frequent Use	Regulation control	10 Seconds	20 ms	Shallow	> 10,000	2 to 50	Important	×	×	×	×	×	
	Fluctuation suppression	10 Seconds	20 ms	Shallow	> 10,000	2 to 50	Important	×	×	×	×	×	
	Grid voltage stability	1 Seconds	20 ms	Shallow	> 10,000	10 to 500	Important	×	×	×	×	×	
Short Discharge - Infrequent Use	Power quality / reliability	5 Seconds	20 ms	Shallow	< 500	1 to 50	Not Important		×	×	×		
	Frequency excursion suppression	15 min	20 ms	Shallow	< 500	10 to 500	Not Important		×	×	×		
	Grid frequency support	10-30 min	20 ms	shallow	< 500	2 to 200	Not Important		×	×	×		
	Grid angular stability	1 Second	20 ms	shallow	< 500	10 to 500	Not Important		×	×	×		

In Table 2.1, the long duration applications refer to the functions requiring sufficient storage capacity to accommodate one or more hours of discharges at full capacity. In contrast, the

short-duration applications refer to the functions requiring quick charging and discharging (typically a few seconds to several minutes). From a statistical point of view, the applications falling under the "infrequent use" category signify 20 events or less per year, whereas under the "frequent use" category the storage system is used on more than 20 occasions per year.

In addition to the utility-scale electrical applications, if the thermal and/or combined electrical-thermal applications are considered, the key performance characteristics can be summarised graphically in the form of the following plot (Figure 2.1).
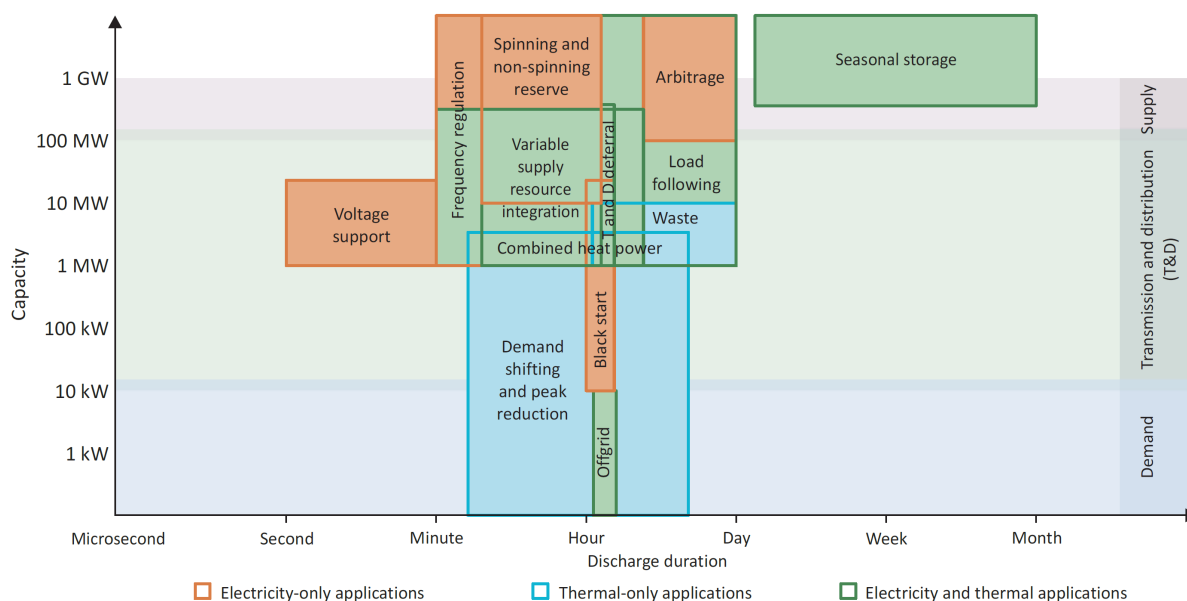
Figure 2.1: Power requirements versus discharge duration [12].

Both Table 2.1 and Figure 2.1 indicate that for load and time shifting applications (i.e., the demand shifting and peak reduction rectangle in Figure 2.1), which are the focus of the current study, the operational requirements are such that the energy storage unit is required to:

- discharge power for about 3-12 hours;
- maintain a response time in the order of minutes;
- depending on the application, have a storage capacity as high as 200 MW, and;
- operate for at least 5000 cycles before any major maintenance shutdown.

Chapters 5 and 7 demonstrate how the proposed thermochemical energy storage concepts meet the above performance measures, along with those listed in the project proposal.

2.2 TECHNOLOGIES

Figure 2.2 provides the classifications and examples of the energy storage technologies based on the form of stored energy, ranging from basic forms such as electrical, chemical, thermal and mechanical to combined forms such as electrochemical, thermochemical and thermomechanical. Electrical storage is the only method in which the electrical energy is stored in its original form without being converted into any other forms, with examples including supercapacitors (SC) and super conductive magnetic storage (SCMS). In the case of chemical energy storage, the electrical energy is used to form secondary energy carriers such as hydrogen and methanol. These chemical products are then used elsewhere after transportation. In thermal energy storage, the electricity is converted to heat for storage. This can happen through sensible energy storage (e.g., the use of cold/hot water) or alternatively by using the latent heat, which is the principle used phase change materials. In the case of mechanical energy storage, the electricity is converted into either potential energy (e.g., pumped hydro storage, PHS, compressed air energy storage (CAES), and solid mass gravitational energy storage (SMGES)) or kinetic energy (e.g., flywheel energy storage). In electrochemical storage, the electricity is stored or produced using chemical reactions. One of the main differences between chemical storage and electrochemical storage is that in electrochemical storage the stored electricity, in the form of chemical potential, is used on demand without further transportation. In thermochemical energy storage, reversible chemical reactions together with heat storage (which can be either sensible of latent) are employed. Examples of this type of energy storage include calcium looping and redox type energy storage systems. Lastly, in the thermomechanical energy systems, the electricity is used to pump heat, very much like the way water is pumped in PHS.

Brief descriptions of the various energy storage technology options and their working principles are provided in the following sections, along with an examination of their current statuses and potential future deployments in utility-scale energy storage [15-41].
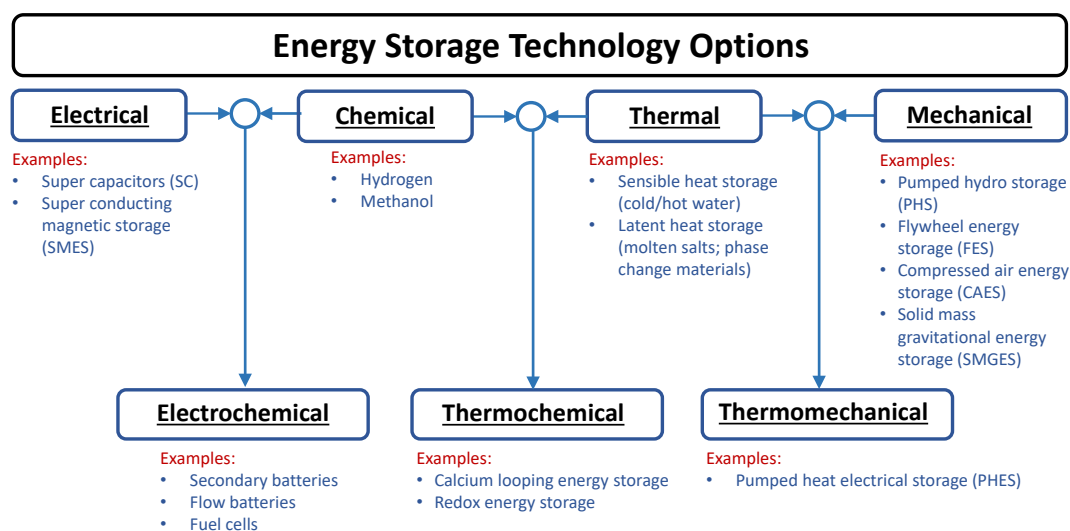
Figure 2.2: Energy storage technology options categorised based on the form of stored energy.

2.2.1 Electrical Energy Storage

Electrical energy can be stored directly without alteration in its form in supercapacitors (SCs) and superconducting magnetic energy storage devices (SMES). The former stores the electricity in an electrostatic field while the latter stores the electricity in a magnetic field.

2.2.1a Capacitors and Supercapacitors (SC)

Capacitors are devices that are used to store electrostatic energy. They are composed of at least two oppositely charged conductors (electrodes) usually separated by a polarizable electric dielectric insulator such as ceramic or glass (see Figure 2.3). Empty capacitors start to charge and store energy upon their connection to an electric power source [15-16]. A supercapacitor (or double-layer capacitor) is essentially the same as a capacitor and stores the energy electrostatically. However, due to its novel technology, it can store much more energy than the conventional capacitors. The electrodes in a conventional capacitor are substituted with porous electrodes in supercapacitors. Moreover, in a supercapacitor an electrolyte (instead of a dielectric material) and an ion permeable membrane (as separator or insulator) are used to keep the oppositely charged electrodes separated (see Figure 2.3(b)). These modifications have provided the feasibility of maximising the surface area and minimising the electrodes separation. Hence, more ions can be adsorbed to the electrode's surfaces and the storage capacity increases drastically [17]. The main application of capacitors is in power quality when there is a need to regulate the voltage variations or fluctuations. Moreover, supercapacitors are used in uninterruptible power supply (UPS) to overcome relatively short duration electricity shortages. They have a high power density, and require only a short period for charging. A limited capacity, low energy density and high self-discharge rate are their main drawbacks [16, 18].
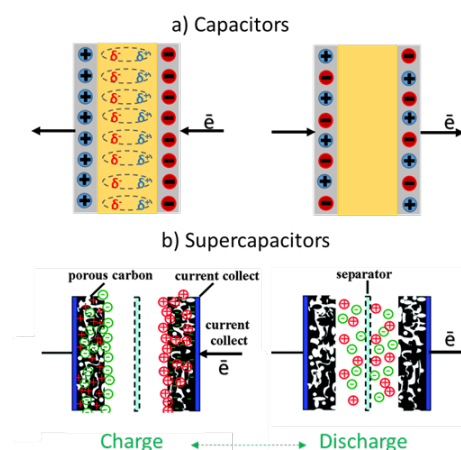
Figure 2.3: Operational principles of (a) capacitors and (b) supercapacitors.

2.2.1b Superconducting Magnetic Energy Storage (SMES)

Superconducting magnetic energy storage (SMES) combines the electrodynamic and super conductivity. The electrodynamic effect states that energy can be stored within the magnetic field of a coil by passing electrical current through it. The superconductivity effect occurs when the temperature of certain elements (mercury and lead), alloys (niobium-titanium,

germanium-niobium and niobium nitride) and ceramics (magnesium diboride) are kept below their superconducting critical temperature which eliminates their resistance to passing an electric current [19].

SMES consists of three main parts: a cryogenic system, a superconducting coil and magnet and a power-conditioning unit (see Figure 2.4). The cooling system lowers the temperature of the coil below the superconducting critical temperature to remove any electric resistance. The chilled superconductor coil stores the energy. The power conditioning unit insures that the input current into the coil is DC and then converts the leaving current to AC (see Figure 2.4). When a DC current passes through the coil, it energises the coil. Since the electrical resistance of the coil is reduced to zero, the passing current is not converted to heat, which means that SMES stores energy infinitely as an un-decayed current keeps on flowing through even after the applied voltage difference across the unit is zero [17, 19, 20]. The advantages of SMESs include their quick response time to load, their high round trip efficiency, which is similar to SCs (although, the power-conditioning unit in SMES usually wastes 2-3 % of the energy input), and their very high power density and unlimited cycle [18].
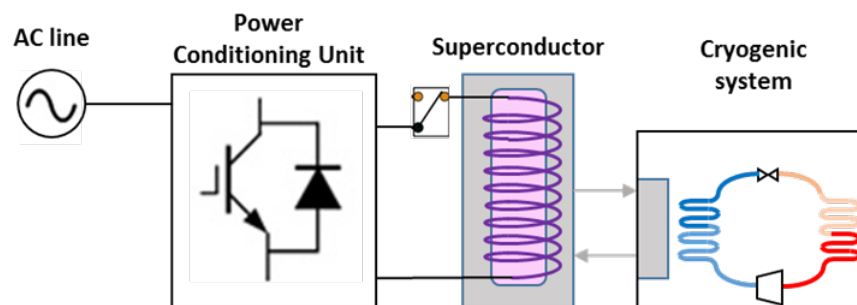
Figure 2.4: Schematic illustration of superconducting magnetic energy storage.

2.2.2 Chemical Energy Storage

The idea behind chemical energy storage is to produce chemicals such as hydrogen or methanol which can be used as energy carriers. In the case of hydrogen, water splitting is used (typically using electrolysis) to produce hydrogen. The hydrogen can then be stored and oxidised in the engine of a fuel cell to produce power when needed. Before storage, and depending on factors such as the location of power plants, accessibility and market, the hydrogen produced using the excess electricity can be subjected to additional processing steps to convert the hydrogen to higher grades energy carriers, such as methanol, ammonia or other chemicals. Although the round-trip efficiency of the chemical storage technique is usually lower than other large-scale technologies such as CAES or PHS, the stability of the chemical products provides a long-term storage capability [21].

2.2.3 Thermal Energy Storage

Thermal energy storage (TES) refers to the storage of electrical energy in the form of heat and, depending on the end-use, converting the heat to power or alternatively releasing it as heat. In TES, the energy is stored or released through a heat carrying medium in either homogeneous or heterogeneous forms. One main advantage of TES is that

there is a broad range of different materials, phases and operating temperatures with different volumetric or gravimetric energy/power densities available to store energy. The materials used for TES should have specifications such as a high thermal conductivity and heat capacity. They should also be chemically stable and have a low-density variation with temperature to minimise thermo-mechanical effects on their structure. Based on the nature of their interactions, TESs are categorised into methods based on sensible heat or latent heat exchange.

2.2.3a Sensible Heat Storage

The principle behind the sensible heat storage system is to make use of excess energy (e.g., electricity produced during an off-peak period) to raise and maintain the temperature of a heat exchange medium to a sufficiently high level. The heat content of the medium can then be extracted during high demand periods (e.g., peak hours) and converted either to power (if the temperature is high enough) or used directly for heating applications. For example, in residential settings the electricity can be used to heat up water during the off-peak period to store in a tank for further use, either as heat or power. In larger-scale applications, for example in seasonal heat storage, natural underground water can be extracted and brought to the surface, and after heating it can be injected into the ground at a different location nearby and stored there over any desired period of time for future use (typically a few months [22]).

Sensible heat storage can also be coupled with solar thermal power plants to produce power. In this system, there are two separate units, namely the storage unit and the power unit [23]. In the storage unit, the solar heat increases the sensible heat of a heating medium during the daylight period. After daylight, the stored heat in the heating medium is transferred to a working fluid (e.g., steam or organic fluids) using a heat exchanger. The heated working fluid, in turn, drives a power block (e.g., steam turbine plant or organic Rankine cycle plant) by converting its heat content to electricity. Molten salts are good candidates as heat absorbing mediums in solar thermal applications given that at atmospheric pressure their temperatures can be increased to levels as high as those required to drive conventional power cycles such as steam or organic Rankine cycles. Currently, the molten salts employed in solar thermal energy storage applications are predominately mixtures of sodium and potassium salts. However, new research is currently underway to find materials that are cheaper and easier to handle than molten sodium-potassium salt mixtures [23].

2.2.3b Latent Heat Storage

In this technique, the thermal energy is stored or released using a heat absorbing medium that undergoes a transformation of its physical state (e.g., solid to liquid). Since there is no sensible temperature change during the phase change, the heat storage is referred to as latent heat storage. Depending on the operation conditions, latent heat storage can store up to three times more energy when compared with sensible heat storage. The so-called phase change materials (PCMs) are particularly suited to latent heat storage applications as they remain unchanged during many freeze melt cycles and have a clear and fixed phase change temperature. PCMs can be either organic (e.g., paraffin) or inorganic (e.g., salt hydrates) in either single phase or eutectic forms. As noted earlier, the physical transformations of heat absorbing mediums are usually from solid to liquid or vice versa. However, there are heat

absorbing materials such as polyurethane polymers that store latent heat via a solid-solid phase transformation [24].

2.2.4 Mechanical Energy Storage

Electrical energy can be stored in a mechanical form by either harnessing the kinetic energy of a moving component (e.g., flywheels) or an energised fluid (compressed air, pumped hydro) or, alternatively, the potential energy stored in a solid mass. Common examples of mechanical energy storage are:

- Pumped Hydro Storage (PHS)
- Flywheel Energy Storage (FES)
- Compressed Air Energy Storage (CAES)
- Solid Mass Gravitational Energy Storage (SMGES)

2.2.4a Pumped Hydro Storage (PHS)

This method includes nearly 95% of the world's installed energy storage capacity. In a conventional PHS system (see Figure 2.5), two water reservoirs are used, one of which is located at a higher altitude than the other. Using a pump during the charging phase (off-peak period) the water is transferred from the lower reservoir to the higher one. During the peak period, the water flows back from the elevated reservoir to the lower reservoir due to gravity and passes through a turbine that is connected to an electricity generator (discharge). In the new generation of PHS systems, an adjustable speed reversible

Figure 2.5: Schematic representation of pumped hydro storage [25].

pump-turbine is used for charging and discharging purposes. The main advantages of the PHS systems include their large capacity, high round trip efficiency (around 70 to 85%), unlimited life cycle and low maintenance costs. Their main disadvantages are their large footprint and their geographical limitations [25-26].

2.2.4b Flywheel Energy Storage (FES)

A flywheel is a rotating disc or cylinder that is capable of storing rotational energy. Due to its moment of inertia, a flywheel resists any change in its rotational speed. As Figure 2.6 shows, apart from the rotating body/cylinder, a flywheel storage device also typically consists of a vacuum pump, bearings, generator/motor and the transmission apparatus. The bearings limit the motion of the rotating body/cylinder to only the desired direction and reduce the friction between the moving parts at the same time. The transmission device transfers the electricity into the rotational energy, and vice versa. The energy is restored by slowing down the rotational speed of the flywheel [27-28]. FESs have features such as an unlimited life cycle, low maintenance costs and a high power density. FESs are also constructed from

environmentally inert materials. The main disadvantages of FESs are their high levels of self-discharge due to air remaining in the chamber and the bearings resistance which lowers the current efficiency [27].
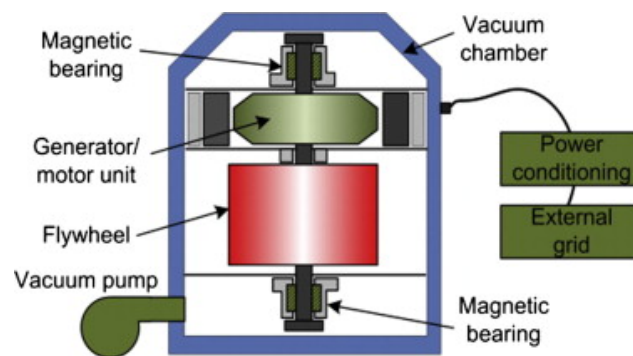
Figure 2.6: Schematic representation of flywheel energy storage [27].

2.2.4c Compressed Air Energy Storage (CAES)

Storing compressed air is a well-known technology which has been used since the early 19th century [29-30]. Electricity is used to drive compressors to store air in either underground structures, such as caverns, abandoned mines and aquifers, or in above ground facilities, such as storage tanks or pipes (see Figure 2.7). During periods of high demand, the compressed air is mixed with natural gas and is burned and expanded in an adapted gas turbine (see Figure 2.7). If the produced heat during the air compression is dissipated to the environment, the process is called an adiabatic process. In this process, the stored air should gain the lost thermal energy before expansion in the turbine, which lowers the round trip efficiency to less than 50%. In an underground form of CAES, the heat dissipation is minimal as the thermal energy of the air is transferred to the underground formation and stored there [30].
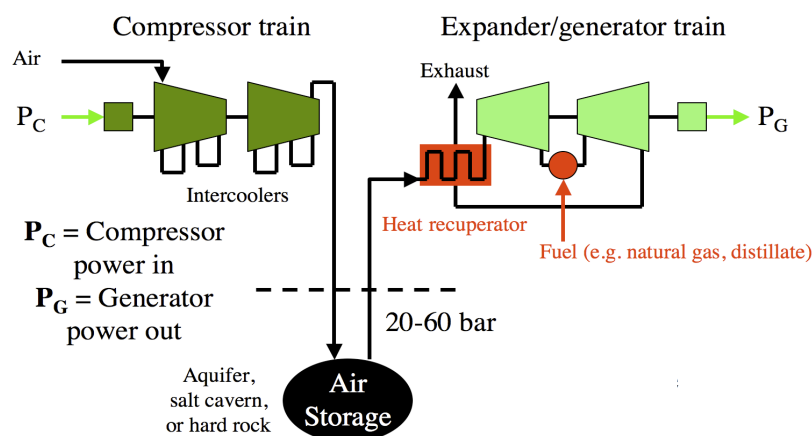
Figure 2.7: Schematic representation of compressed air energy storage [29].

2.2.4d Solid Mass Gravitational Energy Storage (SMGES)

Gravitational energy can be stored in solid masses whenever they are moved to a higher elevation. The amount of stored energy depends on the mass of the solid and its relative vertical displacement. Companies have recently been working on the idea of using gravity to store potential energy using solids during off-peak hours and releasing the energy during peaks hours [31]. This idea has been taken from the pumped hydro method. However, instead of water, solids are used as the energy carrier. This makes the method more advantageous than pumped hydro as it eliminates the need for large quantities of water and the difficulties associated with handling water, where the water flow is not easy to stop and instantly reverse [31-33]. A simplified schematic of SMGES is represented in Figure 2.8. During off-peak periods, the excess power is used to transport the solid masses to the upper yard. During high demand

A. Transmission Line
B. Sub-Station
C. Control / Maintenance Building
D. Redundant Winch Sets
E. Upper Storage Yard
F. Lower Storage Yard

Figure 2.8: Solid mass gravitational energy storage concept [33].

periods, the stored potential energy in the solid masses is released in the form electricity while descending from the upper storage yards towards the lower storage yards.

2.2.5 Electrochemical Energy Storage

Electrochemical devices store electrical energy in the form of chemical energy during charging and produce electricity via chemical reactions upon discharging. An electrochemical storage system usually consists of an array of spaced electrochemical cells (in series or parallel). All of the electrochemical cells are filled with electrolyte solutions. To charge the cells, they are connected to a DC source. The applied voltage to the electrodes initiates a set of chemical reactions which are reversed during the discharge period. The two main examples of electrochemical devices are [34-35]:

1. **Secondary (rechargeable) batteries**: in which the electrolyte or the ion-carrying medium is stagnant. The most widely known secondary batteries are lead acid (LA), nickel based batteries (nickel cadmium (NiCd) and metal hybrid batteries (NiMH)), lithium ion (Li-ion), metal air (Me-air), sodium sulphur (NaS) and sodium nickel chloride ($Na/NiCl_2$).

2. **Flow batteries:** in which the electrolyte is circulating. The two main types of flow batteries are the redox flow battery (RFB) and the hybrid flow battery (HFB).

2.2.5a Secondary Batteries

Secondary batteries, or rechargeable batteries, can be used many times, as opposed to primary or disposable batteries which can only be used once. In secondary batteries during charging, the material at the positive electrode (cathode) is oxidised and produces electrons. The electrons are consumed at the negative electrode and reduce the active materials of the

electrode. During discharging, the oxidation reaction occurs at the anode and the reduction reaction carries on at the cathode. The electrolyte in rechargeable batteries can either serve as a mere conductive medium for the internal charge flow through ions (Li-ion and Ni-Cd batteries) or participate in reduction-oxidation reactions (LA batteries) [36]. The life cycle of secondary batteries is less than SCs and SMES devices. Unlike SCs and SMESs, secondary batteries are also not designed to discharge completely or over a very short duration. Based on the current technology, secondary batteries are suitable for small- to medium-size grid-scale energy storage applications where rapid cycling is not an issue and environmental concerns are minimum [36]. The most important secondary batteries are:

- Lead acid (LA)

- Nickel based (NiCd and NiMH)

- Lithium ion batteries (Li-ion)

- Rechargeable metal air (Me-air)

- Sodium sulphur (NaS)

- Sodium nickel chloride (Na/NiCl$_2$)

2.2.5b Flow Batteries (FB)

Unlike secondary batteries that store the electrochemical energy within the electrodes, in flow batteries the energy is stored in the dissolved electroactive species in the electrolyte solutions. Moreover, a flow battery resembles an electrochemical cell in which the electrolytes, rather than being stored in separate electrode containing vessels, are kept in external tanks. In addition, there are two separate electrolyte circulation paths in a flow battery. A proton exchange membrane keeps the two flowing electrolyte solutions apart [16, 37-38]. In a flow battery, the power output depends on the size and design of the battery, while the energy output depends on the volume of the circulating electrolyte (or equivalently, the size of the external tanks). Flow batteries are capable of being recharged very quickly by substituting the working electrolyte with fresh one. In addition, flow batteries can deliver energy from several hours to days. There are two main types of flow batteries, redox flow batteries (RFB) and hybrid flow batteries (HFB), as discussed below [37-38].

2.2.5c Redox Flow Batteries (RFB)

In RFBs, two electrolytes are pumped to the opposite sides of a cell. Each electrolyte should contain at least two dissolved electroactive metallic ions, and their oxidation/reduction reactions generate the electricity. The flowing electrolytes at the positive and negative electrodes are called the "catholyte" and "anolyte", respectively. Throughout the discharge, fresh electrolytes are continuously supplied to both sides of the battery. It should be noted that during both charging and discharging, the electroactive materials remain dissolved in the electrolyte. Hence, no electrodeposition occurs, which drastically improves the life cycle of the battery. RFBs can be used in mobile applications, as ideally FBs are able to be recharged in a few minutes by replacing the discharged electrolyte with fresh electrolyte. The vanadium redox flow battery (VRFB) is the most developed redox flow battery. In VRFB, solutions of V^{2+}/V^{3+} and V^{4+}/V^{5+} in a dilute sulphuric acid solution act as the anolyte and catholyte, respectively. As shown in Figure 2.9, during the discharge phase in a VRFB, the anolyte oxidises and produces electrons, which powers the external circuit through their migration towards the catholyte. The electrons then react with the protons and VO_2^+ (or equivalently

V^{+5}) and reduce it to VO_2^+ (or equivalently V^{+4}) and water. In order to keep the charges balanced, the membrane should be permeable to the protons in order to complete the circuits by supplying the protons to the catholyte.
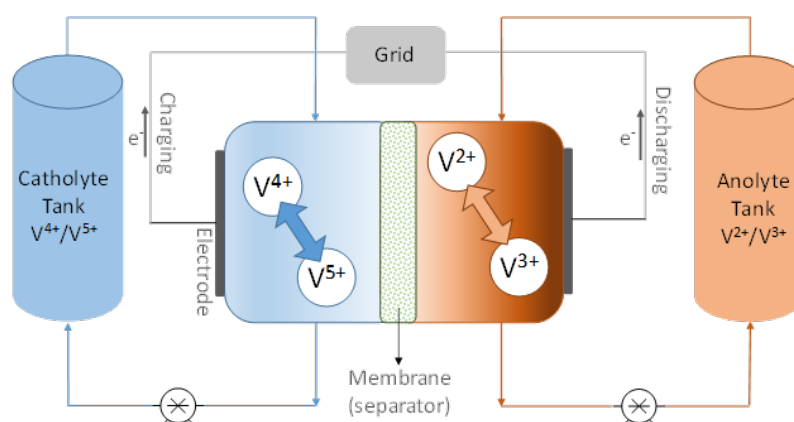
Figure 2.9: Schematic illustration of vanadium redox flow battery; the membrane is permeable to protons.

2.2.5d Hybrid Flow Batteries (HFB)

In HFBs, the externally stored electrolytes dissolve only one of the electroactive ions and the other electroactive material is deposited on the electrode's surface. Hence, a HFB is a combination of a conventional secondary battery and a redox flow battery. In addition, in the structure of a HFB a micro permeable proton membrane, usually made up of polyolefin material (with the general formula C_nH_{2n}) and two electrodes made up of carbon-plastic materials, is used [39]. The most developed examples of HFB batteries are the Zn-Ce and Zn-Br systems. The anolyte in the mentioned systems contains an acidic solution of Zn^{+2}. Zinc ion deposits on the negative electrode's surface during charging. During the discharge process, the zinc is oxidised and converted into Zn^{+2} and electrons. Zn^{+2} goes back into the solution and the produced electrons power the external circuit. The capacity of the batteries is directly related to the volume of the cell [39-40].

2.2.6 Thermochemical Energy Storage

In thermochemical energy storage, reversible chemical reactions are employed to generate a heat sink and a source. The heat sink is usually created by endothermic reactions which allow the excess electricity (e.g., during off-peak periods) to be consumed and stored in the form of chemical energy (i.e., breaking the molecular bonds of the reactants and producing new products). The heat source is created by the reverse reaction, which is exothermic. The heat generated through this process is then passed on to a working fluid that runs a power block, such as a gas turbine generator set, for the production of electrical power. Some examples of reversible reactions suitable for thermochemical energy storage are the:

- Hydration/dehydration of metal salt (temperatures between 40 – 300°C)

- Hydrogenation/dehydrogenation of metal hydrides (temperatures between 80 – 400°C)

- Hydration/dehydration of metal hydroxides (temperatures between 250 – 800°C)

- Calcination/carbonation of metal carbonates (temperatures between 100 – 950°C)
- Reduction/oxidation (redox) of metal oxides (temperatures between 600 – 1000°C)

Among the aforementioned processes, the last two options are the most suitable for coal-fired power plants because of their high side storage temperatures (e.g., 950°C for Calcination/Carbonation and 1000°C for Reduction/Oxidation). These are the processes which were considered by the University of Newcastle (UON) team for the current project and will be discussed in greater detail in the main body of this report.

2.2.7 Thermomechanical Energy Storage

In thermomechanical energy storage, the excess electricity generated during low demand periods is utilised to transfer heat from a low temperature reservoir to a high temperature reservoir, in a cycle. During discharge, the stored heat is used to drive a turbine and produce electricity. Since in this method the heat is stored separately in tanks using mechanical motors, this method of storage is called thermomechanical. Carbon dioxide, air and argon are normally used as the working fluids in thermomechanical cycles. In addition, by reversing the flow direction of the working fluid, the cycles reverse for discharging and charging, or vice versa. Pumped heat electrical storage (PHES) is the most favourable thermomechanical storage technique due to its high capacity and efficiency. Essentially, PHES consists of two tanks filled with gravel, a set of reciprocating compressors and expanders, and argon is the working fluid. The reason that argon is chosen is that it releases or stores more heat than air or carbon dioxide for the same pressure difference [41].

2.2.8 Current Status and Projected Demand and Cost

Up to 2013, 140 gigawatts (GW) of large-scale, grid-connected (sometimes referred to as utility-scale) electricity storage capacity had been installed worldwide [12]. Approximately 99% of the installed capacity up to 2013 consisted of PHS type systems (as shown in Figure 2.10), with the remaining 1% comprising other storage technologies, notably a mix of batteries (~0.52%), CAES (~0.45%) and flywheels (~0.03%).

However, the utility-scale energy storage scene is rapidly changing as many other storage technologies are emerging and are swiftly going through their development cycles. Figure 2.11 shows the capital cost versus maturity level of some of these emerging technologies as a function of their development cycle. The data presented in Figure 2.11 has been partly collected from several key references presented at the 2014 IEA Energy Storage Technology Roadmap Stakeholder Engagement Workshop held in France [12, 14, 42-43], and partly from the assessment of the chemical and thermochemical based systems conducted as part of this project by the UON team. As can be seen, after the recent pilot-scale trials conducted by UON researchers in partnership with Jord International Pty Ltd [44], the calcium looping (CaL) thermochemical energy storage technology has moved a step closer to its demonstration and deployment phase. However, the redox type thermochemical energy storage systems (e.g., those based on chemical looping air separation) are yet to be investigated at pilot-scales. These two options are discussed in greater detail in the following chapters.
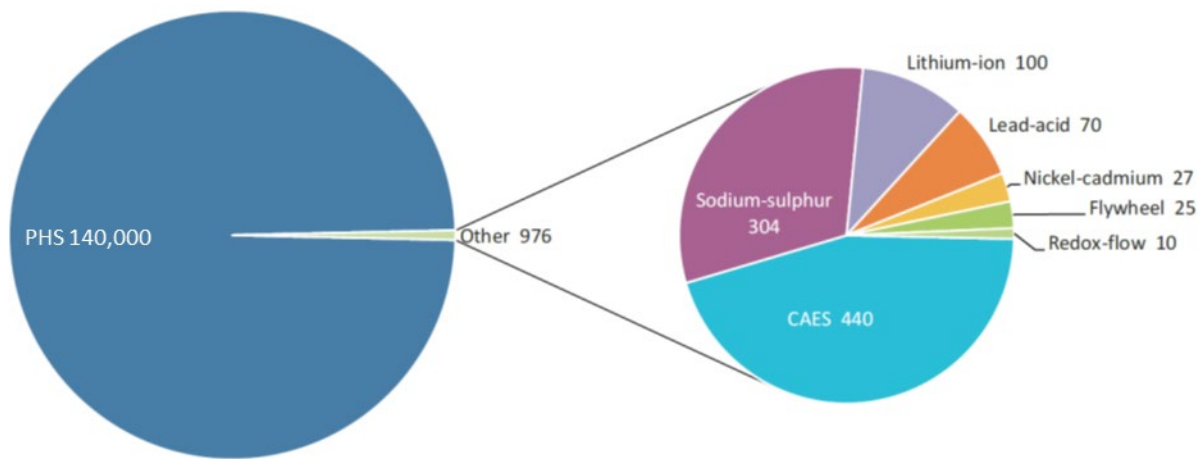
Figure 2.10: Global installed grid-connected electricity storage capacity (numbers shown in the above pie charts are all in MW) as of 2013-2014 [14].
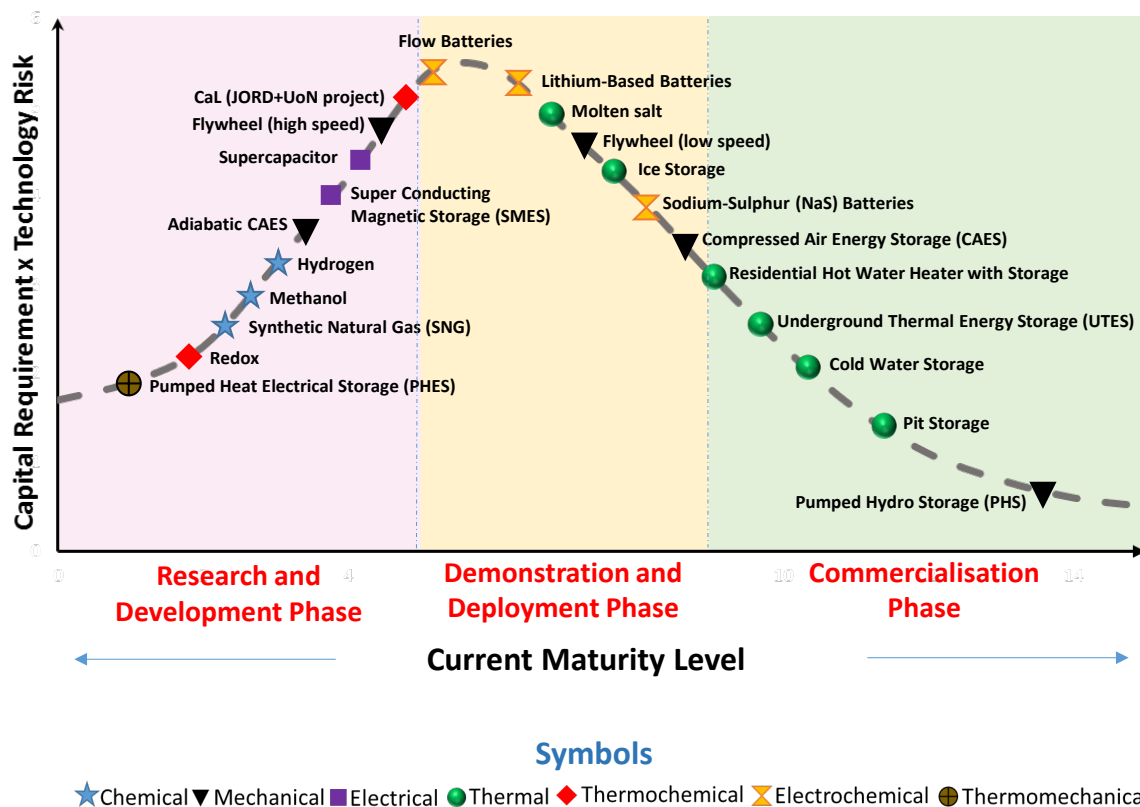
Figure 2.11: A plot of technical maturity versus the capital requirements and technical risks for emerging and matured energy storage technologies [data from 14, 42-43 and this study].

According to International Energy Agency (IEA) projections [14], to maintain the global temperature rise to below 2°C (the so-called 2 degree scenario, or 2DS) by facilitating a greater penetration of renewables, an estimated 365 GW of additional utility-scale energy storage capacity (currently 140 GW) will be needed worldwide by 2050. Of this figure, about 310 GW of storage capacity (~85% of total) is needed in the four major regions of China, India, Europe and North America alone. Much of the demand for the new storage capacity is

expected to be fulfilled by the following four categories of storage technologies which are most suited to utility-scale time-shifting and load-shifting applications:

1. Mechanical (particularly PHS and CAES)

2. Electrochemical (particularly flow batteries)

3. Chemical (particularly hydrogen storage)

4. Thermochemical (particularly calcination/carbonation, hydration/dehydration and redox type processes)

Considerable cost reductions in the above technology options must be achieved before they become competitive with the least expensive option currently available, i.e., open cycle gas-fired combustion turbines typically used as the peaking stations during peak demand periods.

As shown in Figure 2.12, the IEA projections suggest that for utility-scale energy storage the above cost reductions by 2050 should translate to a levelised cost of electricity (LCOE) of about 100 USD (the red dotted line in Figure 2.12 is equivalent to 124 AUD/MWh in 2017 Australian dollars [12]). This is a highly ambitious target considering the current high cost of the storage technologies (see Figure 2.12). In the case of the flow batteries shown in Figure 2.12, the LCOE would need to come down by a factor of at least ten to achieve the above target. Even for more established technologies, like PHS and CAES, improvements in the turbine technologies and significant reductions in the civil engineering costs are needed to meet the 124 AUD/MWh target by 2050.
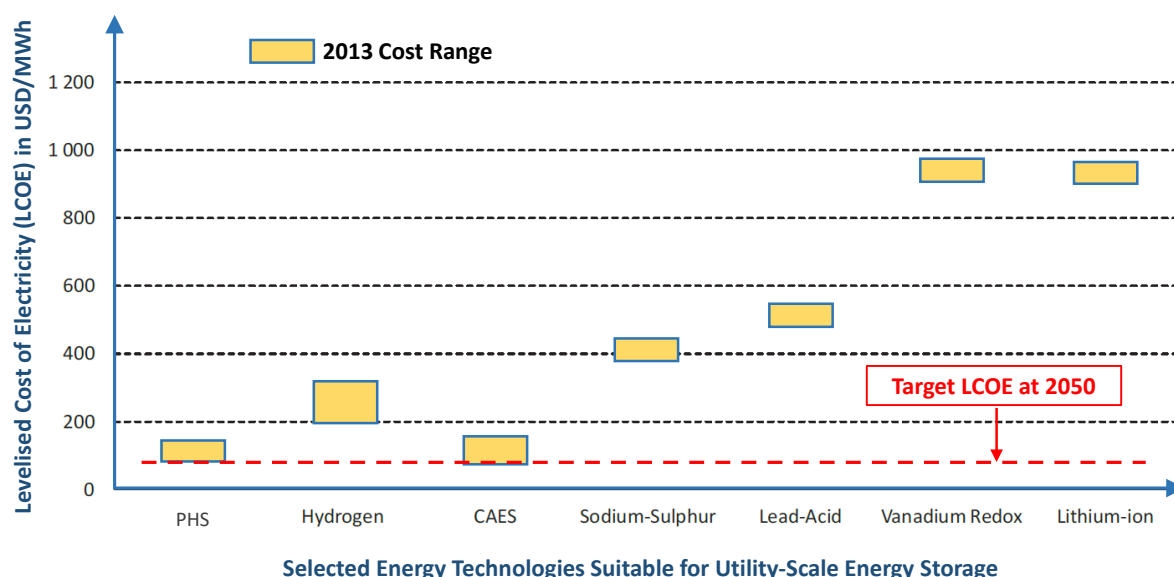
Figure 2.12: LCOE for selected energy storage technologies at 2013 and 2050 [12]. Please note that the LCOE for thermochemical energy storage options have not been included in this figure as they are presented in the following chapters.

Chapter 3

Proposed Thermochemical Concepts for Utility-Scale Energy Storage (Milestone 2)

3.1 INTRODUCTION

As noted earlier, thermochemical energy storage is principally based on reversible chemical reactions (i.e., two-way reactions). For a given set of reversible reactions, cheap excess energy is used to take the endothermic reaction to completion while heat is generated when the reaction is reversed (i.e., exothermic reaction). The heat, in turn, can be converted to electricity using a power block typically comprised of a gas turbine or a steam turbine plus a generator. Reversible reactions which can be employed for energy storage applications, as outlined above, can be broadly classified into the four groups listed earlier in Section 2.2.6. Of these, the calcination/carbonation and redox methods are more suited to coal-fired power plants due to their favourable operating conditions, particularly in terms of their ranges of operating temperatures. Accordingly, the project described in this report focused on the following processes, which are described in more detail in the subsequent sections:

1. A calcium carbonate–calcium oxide cycle referred to as CaL; based on a calcination/carbonation type reversible reaction.

2. A redox based cycle referred to as redox energy storage (RES); inspired by chemical looping air separation, although unlike chemical looping the process is carried out in a batch rather than a continuous mode.

3.2 REDOX ENERGY STORAGE (RES)

The working principles of the RES process are incredibly simple, relying on the cyclic reduction and oxidation (redox) of metal oxide species such as CuO, MnO or CoO. As Figure 3.1 shows, during an off-peak period, when low-cost excess electricity is available, the metal oxide particles undergo a reduction in a fluidised bed reactor. The necessary heat for this endothermic reaction is provided by the Joule heating of the reduction reactor using an electrical heating jacket. The use of Joule heating (electricity to heat) rather than the direct heating of the metal oxides is based on the following key points:

1. In the context of coal-fired power plants, direct heating translates to a reduced amount of heat input to the steam cycle which ultimately leads to the cycling of the steam turbines. This is precisely what the current project is trying to avoid by ensuring that the coal-fired boilers and steam turbines operate at baseload.

2. The conversion efficiency for Joule heating is quite high (98%) and therefore not much energy is wasted by exposing the metal oxide particles to Joule heating.

3. The direct use of electricity for the endothermic reduction of metal oxide particles makes the RES cycle more versatile as the electricity can originate not only from the coal-fired power stations but also from renewable power plants (wind farms, solar thermal plants, sola-PV plants and biomass) and other fossil-fuel based power systems such as natural gas fired power stations.

During the reduction process, the metal oxide particles are forced to relinquish their oxygen content in the same fluidised bed reactor, which now functions as a reduction reactor. The reduction is achieved by using a steady flow of steam to maintain the partial pressure of oxygen at levels which, according to Le Chatelier's principle, shifts the reduction reactor towards the production of oxygen (note: this is a relatively small scale oxygen production in which the hourly production rate of oxygen is in the range of 100 to 150 m^3 per MWh of the stored energy (see Section 5.3.2 for more details)). The resulting steam/O_2 mixture then runs through a heat exchanger (HEX-1 in Figure 3.1) and a condenser (Con in Figure 3.1) to remove the sensible heat from the mixture, and more importantly to separate the oxygen from the steam.

Meanwhile, the reduced metal particles are held in the reactor for the peak period operation. While during the hold up between the off-peak and peak period operations (if any) the particles can be maintained in fluidised state, the preference is not to do so in an attempt to minimise the heat losses resulting from the interaction of the fluidising agent and the solid particles.
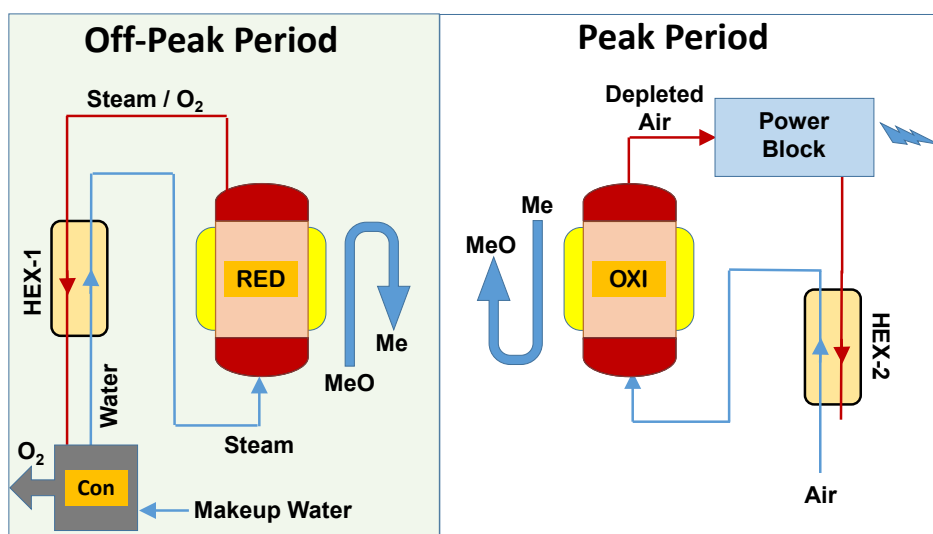
Figure 3.1: Schematic representation of the RES cycle.

During the peak period, when additional power is needed, the flow of steam into the reactor is stopped and instead a pre-heated air flow is introduced. The reduced metal particles heat up as they come into contact with the counter-current air flowing through the reactor. The metal particles then undergo a rapid and exothermic oxidation reaction as they continue their journey through the oxidation reactor. The regenerated metal oxide particles are then kept in the reactor for the next off-peak period cycle.

Meanwhile, the hot depleted air flow is taken from the outlet of the oxidation reactor and run through a power block (for instance an externally fired turbo-generator or a secondary steam cycle and generator) for the production of electricity. The exhaust gas from the power

block is then passed through a heat exchanger (HEX-2) and used to preheat the air entering the oxidation reactor.

3.3 "CaL" ENERGY STORAGE CYCLE

Very much like the RES cycle, the working principles of the CaL cycle are also very simple, relying on the cyclic calcination/carbonation of calcium carbonate rich minerals, for example stone dust. As Figure 3.2 shows, during off-peak periods, when low-cost excess electricity is available, the carbonate particles undergo calcination. The necessary heat for this endothermic reaction is provided by the Joule heating of the calcination reactor using an electrical heating jacket. The use of Joule heating is for the same reasons as outlined earlier in Section 3.2.

During calcination, the carbonate particles are forced to relinquish their CO_2 content. This is achieved at temperatures of greater than 800°C and by using a steady flow of flue gas (typically containing ~12%vol carbon dioxide) to maintain the partial pressure of the CO_2 at levels which, according to Le Chatelier's principle, shifts the reaction towards the production of more CO_2. The resulting CO_2 enriched flue gas is then vented out of the system.

Meanwhile, the calcined particles, which are now in the form of CaO, are kept in suspension (i.e., fluidisation state) until a peak period operation. During peak periods, when additional power is required, the calcium-rich particles undergo a rapid and exothermic reaction in the reactor (now operating as a carbonation reactor) by exposing them to the CO_2 content of the flue gas drawn from the coal-fired power plant. The hot CO_2 lean flue gas is then taken from the outlet of the carbonation reactor and is run through the power block for the production of electricity. The exhaust gas from the power block is then passed through a heat exchanger (HEX-2) and used to preheat the flue gas stream entering the carbonation reactor. The fully carbonated particles are kept in suspension in the reactor until the beginning of a new calcination cycle.
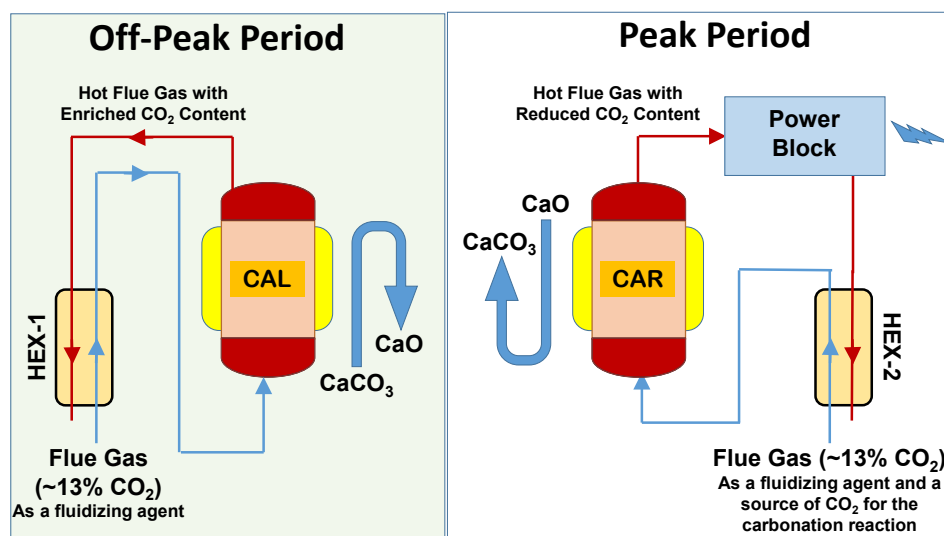
Figure 3.2: Schematic representation of the CaL cycle.

3.4 UNIQUE FEATURES OF THE RES AND CaL CYCLES

The RES and CaL cycles feature a number of unique and innovative characteristics which make these processes attractive for utility-scale bulk energy storage. The key features are:

- To ensure a high level of flexibility, the energy input for the RES and CaL cycles is in the form of electricity rather than heat. Therefore, these processes can be retrofitted to renewable and non-renewable power plants (one size fit all).

- The hardware for both the RES and CaL cycles is also very simple and consists of a single reactor and a series of peripheral units such as heat exchangers. The simplicity of the hardware and ease of operation lowers the capital costs (CAPEX) and operating costs (OPEX) to levels lower than those of conventional systems (see Chapters 5 and 6 for details).

- The RES and CaL cycles are highly efficient (see Chapter 5 for details) and have a zero self-discharge, fast response time (minutes), high energy rating (can operate 1-18$^+$ h), high power rating (kW to 500$^+$ MW) and high energy density (50-250 Wh/kg). The above features are typically much better than the performance characteristics of batteries and the PHS and CAES systems for utility-scale energy storage (see details in Chapter 5).

- If deployed in coal-fired power plants, the RES and CaL cycles would enable the power plant to serve as a load following/peaking plant without exposing its coal-fired generation units to cycling. In turn, this will minimise the periods of suboptimal operation, thereby improving efficiency and lowering GHG emissions by 15-30% v.

- The RES and CaL based energy systems are faster than gas and hydro plants and, therefore, in peaking and/or backup applications can cover the shortfall in generation within a short period of time (see details in Chapter 5). An EU study showed that a one hour difference between falls in demand and the wind power supply creates a need for about 5-7 GW of electricity in Germany [56]. Conventional gas-fired power plants can deliver the required electricity but they need 2 hours of ramping up. The RES can potentially meet the electricity demand during this 2-3 hour gap or CaL-based systems within 30 min to 1 hour (see details in Chapter 5).

- RES is a poly-generation process capable of producing heat, power and oxygen. The technology can be adapted and deployed to energy intensive industries (e.g., coal-fired oxyfuel power plants, IGCC plants, steelmaking, glassmaking, wastewater treatment, etc.) where, apart from energy storage, oxygen is required in the production processes. As shown in Chapters 5 and 6, the sale of oxygen makes a significant difference to the economic viability of the RES process.

Chapter 4

Research Methodologies

(Milestones 3 and 4)

4.1 INTRODUCTION

Two different sets of modelling and experimental studies were carried out in this study to determine the performance characteristics of the RES and CaL cycles from both the technical and economic points of view. The modelling studies included:

1. Thermodynamic chemical-equilibrium studies to determine the technical features of the RES and CaL cycles, particularly the efficiency, energy losses and response times to external disturbances (e.g., load variations/fluctuations). The calculations undertaken using this approach were predominately carried out using the commercially available process simulation package ASPEN⁺. The details of the thermodynamics approach, assumptions and methodology are provided in the following sections of this chapter.

2. Economic modelling studies, which included:

   • Levelised cost of electricity (LCOE) studies – to determine the combined impacts of the borrowing, capital investment, and operational and maintenance costs on the cost of the electricity produced when thermochemical energy storage technologies such as RES and CaL are retrofitted to a coal-fired power plant.

   • Net present value (NPV) studies – as an alternative to LCOE, to measure the potential profits made by RES and CaL over time by determining the current value of all future cash flows generated by them after accounting for the initial capital investment.

   • Internal rate of return (IRR) studies – as a complement to NPV, to measure the profitability of a given investment. The IRR is essentially a discount rate that makes the net present value (NPV) of all cash flows equal to zero.

   • Total cost of production (TCOP) studies – to determine the annual cost of producing the electricity by taking into account the total annual capital charge and the cash cost of the production.

   • Simple Payback Period (SPP) – to determine the length of time required to recover the costs of a given investment in utility-scale energy storage.

In addition to this economic modelling of RES and CaL, the techno-economic features of a conventional open cycle gas-fired peaking plant (OCGT) were also determined for benchmarking purposes using the abovementioned approaches. The characteristics (both technical and economic) of the RES, Cal and OCGT systems were then compared with other technology platforms suitable for utility-scale time and load shifting applications (e.g., PHES, CAES and batteries). The results of these comparisons are presented in Chapters 5 and 6.

The experimental studies included:

1. Reactivity and Material studies

In the reactivity and material studies, two types of particles were considered: calcium-rich particles for the CaL process and copper-rich particles for the RES process. Altogether, more than 300 samples were analysed using laser diffraction analysis (LDA), scanning electron microscopy (SEM), thermal gravimetric analysis/differential scanning calorimetry (TGA/DSC), X-ray diffraction (XRD) and energy dispersive X-ray spectroscopy (EDS) techniques. The samples were taken from more than 100 reactions and reaction pathways.

2. Laboratory-scale Experiments

Experiments conducted in laboratory-scale setups considered both the calcium-rich and copper-rich particles. These tests were carried out using both fixed and fluidised bed apparatus. In these experiments, a small number of particles (e.g., up to 16 grams) were treated with a small gas flow. The operating temperatures and CO_2 concentrations in the laboratory-scale tests covered a vast range of temperatures and concentrations of the inlet gas.

3. Pilot-scale Experiments

Pilot-Scale tests were focused on the scope of the project. Only calcium-rich particles were used in these tests. The inventory of the bed, gas flow rate, temperature and CO_2 concentration of the inlet gas during carbonation were the controlling parameters. Six preliminary experiments with low gas flow rates and inventories were performed prior to the primary demonstration tests.

4. Large-scale Experiments

The particle inventory in the large-scale experiments was more than 15 times that of the pilot-scale setup. These experiments aimed to show that, at a larger scale, the fluidised bed is self-sustained (e.g., no axillary heating is required to overcome the heat loss for a well-insulated industrial system) and that the temperature remains constant during the experiments.

4.2 THERMODYNAMIC MODELLING METHODOLOGY

4.2.1 Overview

The methodology employed to assess the techno-economic characteristics of the RES and CaL cycles was a scenario driven method. In the main scenario, a conventional pulverised fuel (PF) coal-fired power plant with a thermal efficiency of 34% and a net electrical power output of 660 MWe was considered as the base-case. The choice of this particular platform for the base-case was justified because PF type coal-fired plants constitute the bulk of the power assets in NSW. The main scenario was based on the assumption that the base-case plant had approximately 100 MWe of excess power during off-peak periods (8

h). The ultimate goal was to produce at least 35 MW of electricity (i.e., 35 MWe) for 8 hours during the peak period (8 h) from the excess power. The selection of the above figures (i.e., 100 MW$_e$ during charging and 35 MW$_e$ during discharging) was justified based on published data from Europe and North America which has indicated that due to the penetration of renewable energy sources, a 660 MW coal-fired power generation unit could provide up to 100 MW of spare capacity during off-peak periods. The output of such units may also have to be augmented by as much as 50 MW during peak periods using a secondary power unit (typically gas turbines). In this study, a 35 MW augmentation figure was considered, given that the penetration of renewable energy sources in Australia is currently not as high as in North America or Europe.

In addition to the base-case, five other case-studies were considered for thermodynamic calculations, as summarised in Table 4.1 below.

Table 4.1: List of case-studies

Case-Study Designation	Case-Study Short Name	Description	Type of Power Block		Secondary Fuel
			Primary	Secondary	
1	Base-Case	PF Coal-fired plant	SRC*	---	No
2	Standalone OCGT#	An open cycle gas-fired peaking plant	OCGT	---	No@
3	RES+OCGT	Base-Case plus a RES unit with an OCGT power block	SRC	OCGT	May need some to achieve the desired output
4	RES+SSC	Base-Case plus a RES unit with a SSRC power block	SRC	SSRC**	No
5	CaL+OCGT	Base-Case plus a CaL unit with an OCGT power block	SRC	OCGT	May need some to achieve the desired output
6	CaL+SSC	Base-Case plus a CaL unit with a SSRC power block	SRC	SSRC	No

SRC ≡ Steam Rankine Cycle

** SSRC ≡ Supercritical Steam Rankine Cycle

 # OCGT ≡ Open Cycle Gas Turbine

@ The primary fuel is either CNG or LNG

4.2.2 Theoretical Background

The ASPEN+ software was used in this study to carry out the required thermodynamic chemical-equilibrium calculations. There are several different approaches to solving this type of problem, and the approach adopted here was to minimise the Gibbs free energy of the heterogeneous system under consideration. For a given set of pressures

and temperatures, this was achieved by adjusting the species mole numbers so that the Gibbs function (G), defined by Eq (4.1), is minimised:

$$G = \sum_{i=1}^{I} n_i \left[\bar{g}_i^o(T) + \bar{R}T \ln X_i + \bar{R}T \ln\left(\frac{P}{P^0}\right) \right].$$

(4.1)

In Eq (4.1), $\bar{g}_i^0$ is the molar based Gibbs free energy of species i at the reference state, I is the total number of species in the heterogeneous mixture of metal oxide and gaseous species, n_i is the mole number of species i, P is the pressure, P^o is the pressure at the reference state, $\bar{R}$ is the universal gas constant, T is the temperature of the heterogeneous mixture, and X_i is the mole fraction of species i.

The minimisation of the Gibbs function is generally achieved by employing the Lagrangian multiplier method to ensure that the elemental conservation is met. A variant of this method, commonly known as the Element-Potential method, was used in the present chemical-equilibrium analysis. The calculations involved solving a total of $I+J$ equations for the I unknown species mole numbers (n_i) and J unknown element-potential multipliers (λ_j). These equations can be expressed using the following general equations, in which I and J are the total number of species and elements present in the heterogeneous mixture, respectively:

$$\sum_{j=1}^{J} a_{ji}\lambda_j = \left[\frac{\bar{g}_i^o(T)}{\bar{R}T} + \ln X_i + \ln\left(\frac{P}{P^0}\right) \right], \qquad i = 1,........,I.$$

(4.2)

$$\sum_{i=1}^{I} a_{ji}n_i = \tilde{n}_j, \qquad j = 1,........,J.$$

(4.3)

where a_{ji} is the number of j-element in species i, and $\tilde{n}_j$ is the element mole number of the j-element in the system (i.e., 6.023×10^{23} multiplied by the number of atoms of type j present in the system). The above approach allowed different types of species to be considered, including gas phase species, surface species, pure bulk species and bulk mixtures.

4.2.3 Base-Case

The base-case modelling essentially involved the simulation of a PF boiler and the primary steam Rankine cycle (SRC). The primary steam cycle was simulated using some of the data reported by Hanak et al. [57], which described a reheat-regen type Rankine cycle. As shown in Figure 4.1, the air passes through a blower followed by a preheater. The pre-heated air then burns the pulverised coal and produces hot gas and ash in the steam generator. The produced ash leaves the steam generator while the hot gas transfers its heat to the circulating water/steam by flowing over a complex array of coils with the circulating water/steam flowing inside. The heated water/steam takes the form of supercritical steam by absorbing the flue gas heat (live steam) and is transferred to the power unit.

The power block consists of three turbine units with different outlets and thermodynamic specifications, which are the: high-pressure (HP), intermediate-pressure (IP) and low-pressure (LP) turbines. The outgoing steam from the power block enters a condenser unit and takes the form of liquid water. The water, in turn, is introduced into a pump, passes through a set of feed water heaters, and enters the deaerator. The subcooled liquid leaving the deaerator passes through another set of feed water heaters and finally returns to the steam generator. It should be noted that a portion of the steam leaving the HP turbine (reheat steam) is directed back to the steam generator to gain heat and expands in the IP turbine.

To increase the thermal efficiency of the cycle further, an optimised portion of the steams exiting the turbines pass through feed waters to exchange their heat with the cold water flowing towards the steam generator. In Figure 4.1 below, the hot streams are shown in red and pink while the cooler streams are shown in green and blue as intermediate and cold temperatures, respectively.

The interactions between the base-case plant and the other unit operations, in particular the RES or CaL energy storage units, were made possible by considering the dedicated flow and energy streams transporting mass and energy from SRC to the storage unit. The key simulation parameters for the base-case primary SRC have been summarised in Table 4.2.

The coal-fired boiler was simulated using a combination of the "RYield" and "RGibbs" reactor options available in the ASPEN+ library of unit operations. The RYield reactor is a numerical tool which determines the decomposition of the coal feedstock into its constituents at a given ambient temperature, while the RGibbs reactor simulates the combustion of the coal with air adiabatically. The composition of the flue gas leaving the primary steam cycle used as an input to the energy storage simulations is reported in Table 4.3.
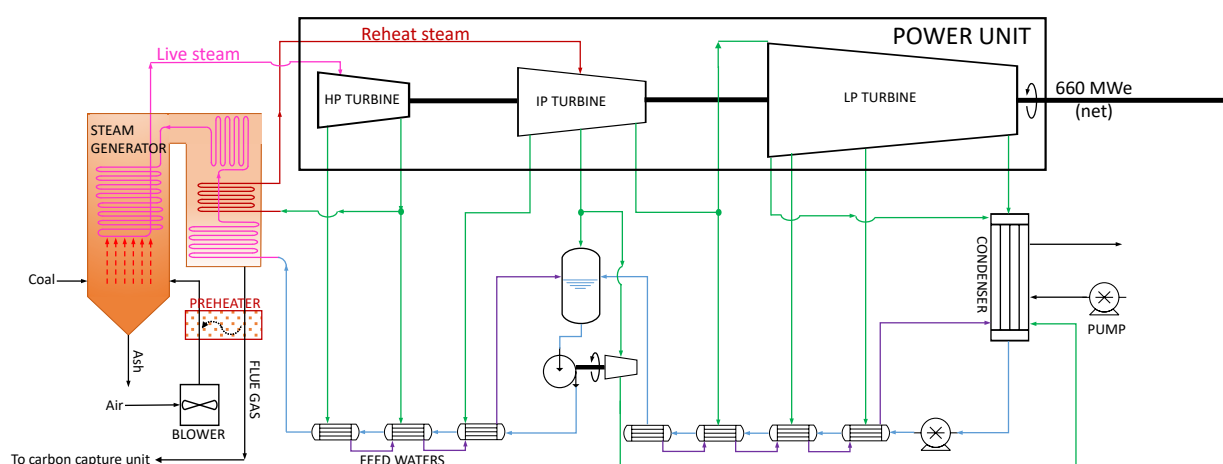
Figure 4.1: Schematic representation of the base-case PF coal-fired power plant.

Table 4.2: Key parameters and simulation results for the primary steam cycle

Key Parameters of the Primary Steam Cycle	Values
Isentropic efficiency of HP turbines (196 MW)	0.8
Isentropic efficiency of IP turbines (320 MW)	0.85
Isentropic efficiency of LP turbines (187 MW)	0.85
Isentropic efficiency of pumps	0.845
Electric generator efficiency	0.995
Thermal efficiency of the cycle	0.34
Leaving flue gas temperature (°C)	115
Live steam temperature (°C)	502
Live steam pressure (bar)	210
Regen steam temperature (°C)	530
Regen steam pressure (bar)	35
Air flow rate to boiler (kg/s)	800
Pulverised coal flow rate (kg/s)	62

Table 4.3: Composition of the flue gases leaving the primary steam cycle

Species	CO	CO_2	N_2	NO	O_2	H_2	SO_2	H_2O	Sum
Mole%	0.41	13.24	75.39	0.57	3.95	0.04	0.16	6.24	100

4.2.4 Standalone OCGT Case

An open cycle gas turbine (OCGT) capable of generating 35 MWe in a standalone mode was simulated as a representative of the gas-fired peaking plants. Figure 4.2 depicts a schematic flowsheet of an OCGT. In this configuration (see Figure 4.2), during off-peak periods the gas peaker remains out of service. However, during peak periods, the ambient air is compressed and fed to the combustion chamber to burn the natural gas feed. The flue gas leaving the combustion chamber is expanded in a turbine which, in turn, runs a generator for electrical power production. The hot flue gas exiting the turbine is introduced into a heat exchanger (LNG HX) to vaporise the liquefied natural gas (LNG) before entering the combustion chamber. In cases where compressed natural gas (CNG) is used as the secondary fuel, the LNG HX in Figure 4.2 pre-heats the CNG before feeding it to the combustion chamber. The basic simulation parameters of the standalone OCGT are presented in Table 4.4. Since the CNG is not stored on site and is supplied by a pipeline, no information on the storage pressure and temperature of the CNG is provided in Table 4.4. In addition, the flow rates of the CNG and LNG are equal as their chemical compositions are assumed to be identical.
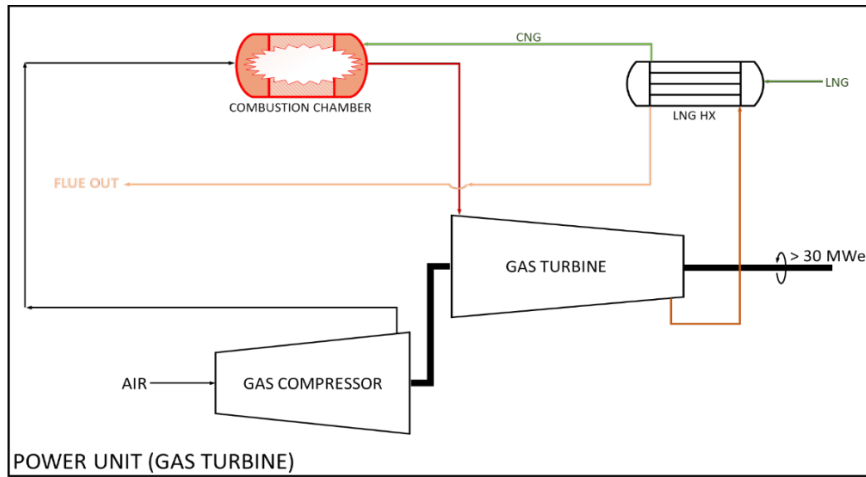
Figure 4.2: Schematic representation of the OCGT peaking plant considered in this study.

Table 4.4: Key parameters and simulation results for the standalone OCGT cycle

Key Parameters	ASPEN[+] model	Value/Spec
Isentropic efficiency of air compressor	Compressor	0.9
Turbine outlet pressure (bar)	Stream	1.05
Turbine outlet temperature (°C)	Stream	450
Isentropic efficiency of gas turbine	Turbine	0.9
Compressor outlet pressure (bar)	Turbine	8
Combustion chamber	Rgibbs	Adiabatic
LNG storage temperature (°C)	Stream	-165
LNG storage pressure (bar)	Stream	8.5
LNG and CNG flow rate (kg/s)	Stream	2.22
LNG heat exchanger (cold outlet temperature °C)	HeatX	300
Air flow rate (kg/s)	Stream	100

4.2.5 RES Based Cases (RES+OCGT and RES+SSC)

Figure 4.3 represents a schematic of the RES cycle during low demand or off-peak periods (the actual ASPEN[+] flowsheet is provided in Appendix A). This part of the cycle is identical in both the RES+OCGT and RES+SSC cases. During this period, the excess power (100 MWe) is used in the energy storage and oxygen separation units. Oxygen is produced via the reduction of CuO to Cu_2O (forward reaction in Eq 4.4 below) in the reactor under a steam environment. Adjusting the partial pressure of the steam allows the rate of the reduction to be controlled. In addition, the steam acts as a fluidising agent keeping the metal particles in suspension. The steam is also used to transport the oxygen produced in the reduction reactor to the oxygen separation unit. The steam is generated by pumping water to an evaporator before entering the reduction reactor. The hot O_2 rich gas leaving the reactor

provides the evaporator duty. The O_2 rich gas then enters the oxygen separation unit and, after passing through compression and cooling, is then expanded in a small turbine and produces pure oxygen. All of the mechanical work required for the oxygen separation process is taken from the available excess energy.

$$4CUO \leftrightarrow 2CU_2O + O_2 \qquad (4.4)$$

Figure 4.4 depicts a schematic representation of the RES cycle coupled with an OCGT type power block during a peak period, while Figure 4.5 shows the RES cycle interfaced with a secondary supercritical steam cycle (SSC). The actual ASPEN+ flowsheets corresponding to Figures 4.4 and 4.5 are provided in Appendix A. In the case of RES+OCGT, the oxidising air (see Figure 4.4) is blown into the reactor as a fluidising agent that oxidises the Cu_2O to CuO (reverse path in Eq 4.4). The hot gas (O_2 lean gas) resulting from the oxidation reaction is transported to the EXTERNAL HX in the "POWER UNIT (GAS TURBINE)" block (see Figure 4.4) to heat up the pre-heated compressed air leaving the PRE-HEAT HX, and it is then vented to the atmosphere. The heated up compressed air is then introduced into the combustion chamber where, if needed, a secondary fuel (CNG or LNG) is combusted to raise the temperature of the hot air to the desired values. The hot gas expands in the turbine and generates power. Before venting to the atmosphere, the flue gas leaving the turbine passes through two heat exchangers to evaporate the required LNG (LNG HX) and to pre-heat the compressed air (PRE-HEAT HX). In the cases where CNG is used as the secondary fuel, the LNG HX does not exist and the flue gas just heats up the compressed air. The blower duty is met by the power generated by the "POWER UNIT (GAS TURBINE)" block.
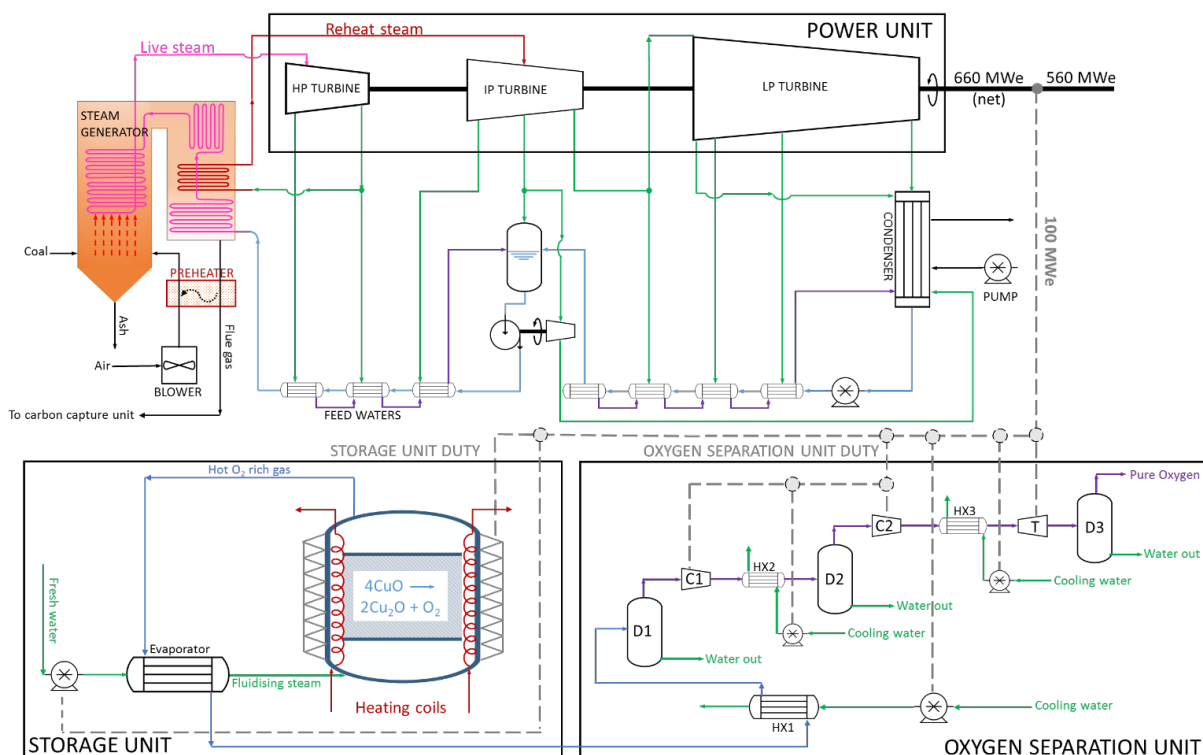
Figure 4.3: Schematic representation of the RES based process during an off-peak period.
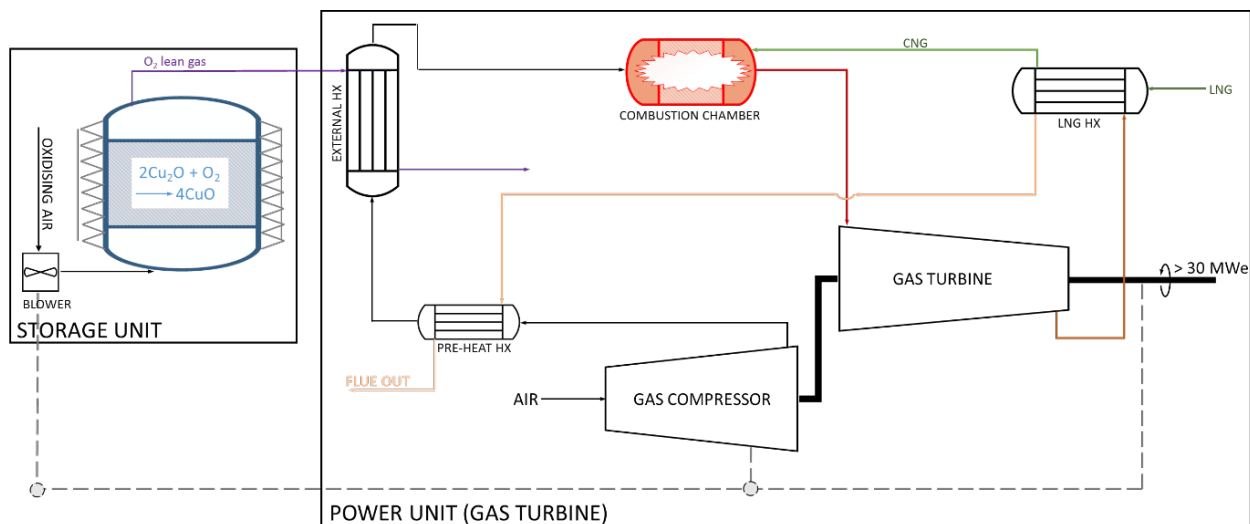
Figure 4.4: Schematic representation of the RES+OCGT cycle during a peak period.

For the RES+SSC energy storage option, the cycle during the low demand period is identical to that described earlier and depicted in Figure 4.3. The main difference between the RES+SSC option and the RES+OCGT option is in the power block.

As shown in Figure 4.5, in RES+SSC, the heat released from the oxidation reaction (the reversed path in Eq 4.4) heats up the highly pressurised water to temperatures beyond its critical temperature and produces supercritical steam (live steam in Figure 4.5). The steam is then expanded in a series of turbines for power generation. The steam leaving the low-pressure turbine (LP TURBINE) completely condenses into liquid water in the "CONDENSER." The liquid water reaches beyond its critical pressure by passing through two pumps, with an intermediate heat exchange step exchanging heat with the O_2 lean gas stream (HEAT EXCHANGER). The liquid water then enters the reactor, heats up, and completes the cycle.
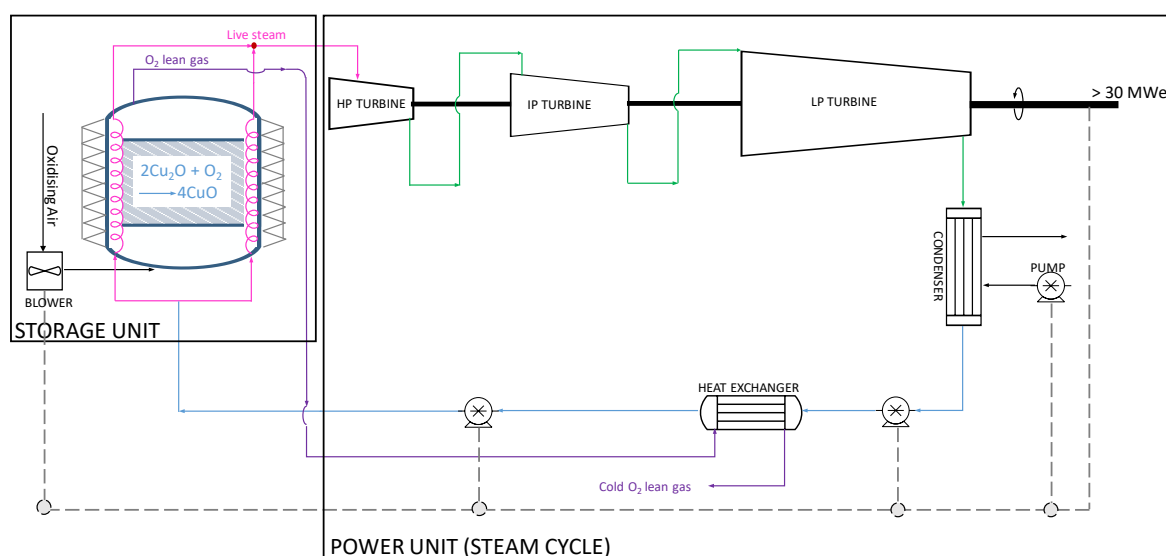
Figure 4.5: Schematic representation of the RES+SSC cycle during a peak period.

The assumptions and key simulation parameters for the RES based cycles are presented in Table 4.5:

Table 4.5: Assumptions and simulation parameters for the RES and integrated OCGT and SSC power blocks

	Key Parameters	ASPEN+ Model	Value/Spec
RES Component	Reducer reactor temperature (°C)	FORTRAN code	1100
	Isentropic efficiency of water pump	Pump	0.9
	Outlet pressure of pump (bar)	Compressor	1.4
	Percentage of the purged solid	Ssplit	0.01
	Total flow rate of water during off-peak (kg/s)	Stream	1.7
	Oxidiser reactor temperature (°C)	FORTRAN code	800
	Total flow rate of oxidising air during peak (kg/s)	Stream	105
	Isentropic efficiency compressors	Compressor	0.9
	Isentropic efficiency of the turbine	Turbine	0.9
	Flash drum (assuming 2:30 min residence time)	Flash2	Adiabatic
	Heat exchangers (cold outlet temperature (°C))	HeatX	35-50
Integrated OCGT	Isentropic efficiency of air compressor	Compressor	0.9
	Turbine outlet pressure (bar)	Compressor	1.05
	Isentropic efficiency of gas turbine	Turbine	0.9
	Compressor outlet pressure (bar)	Turbine	8
	Combustion chamber	Rgibbs	Adiabatic
	LNG storage temperature (°C)	Stream	-165
	LNG storage pressure (bar)	Stream	8.5
	LNG heat exchanger (cold outlet temp. (°C))	HeatX	300
	CNG storage temperature (°C)	N/A	N/A
	CNG storage pressure (bar)	N/A	N/A
	Secondary fuel (CNG or LNG) flow rate (kg/s)	Stream	1.065
	External heat exchanger (temp. approach (°C))	HeatX	5

	Compressed air pre-heater (temp. approach (°C))	HeatX	10
	Air flow rate (kg/s)	Stream	140
Integrated SSC	Isentropic efficiency of HP turbines (10 MW)	Turbine	0.92
	Isentropic efficiency of IP turbines (8 MW)	Turbine	0.94
	Isentropic efficiency of LP turbines (21 MW)	Turbine	0.88
	Isentropic efficiency of pumps	Pumps	0.85
	Live steam temperature (°C)	Stream	750
	Live steam pressure (bar)	Stream	242
	Live steam flow rate (kg/s)	Stream	22
	Heat exchangers in the boiler (outlet temp. (°C))	HeatX	360
	Re-heat heat exchanger (°C)	HeatX	53
	Condenser (Hot stream outlet temperature (°C))	HeatX	46

4.2.6 CaL Based Cases (CaL+OCGT and CaL+SSC)

The flowsheet for the off-peak CaL energy storage option is depicted in Figure 4.6 (the actual ASPEN⁺ flowsheet is provided in Appendix A). Similar to in the previous cases, the excess available power from the primary steam cycle is diverted to the "STORAGE UNIT" to meet the reactor duty. Unlike in the RES option, which uses the steam as both fluidising agent and carrier gas, in the CaL option a small fraction of the flue gas is used to fluidise the bed during the calcination (carried out via the forward path in Eq 4.5 below). The resulting CO_2 gas leaves the reactor and is sent to the carbon capture unit (the flue out [CO_2 rich] stream in Figure 4.6).

Another difference between the CaL and the RES energy storage options in the off-peak period is that in the former there is no need for an oxygen separation unit as no oxygen is produced, as shown in Eq 4.5:

$$CaCO_3 \leftrightarrow CaO + CO_2 \tag{4.5}$$

During peak periods, the activated particles (CaO) react with the introduced flue gas from the primary steam cycle, through the reverse path of Eq 4.5, and release heat. It should be noted that in this study an exothermic side reaction is considered, by which SO_2 permanently deactivates some of the quicklime (see Eq 4.6 below). This is a realistic assumption given that the flue gas from the primary steam cycle typically contains sulphur dioxide. The results, however, are quite environmentally favourable because the gases leaving the system would be lean in both CO_2 and SO_2.

$$CaO + SO_2 + \tfrac{1}{2}O_2 \rightarrow CaSO_4 \tag{4.6}$$
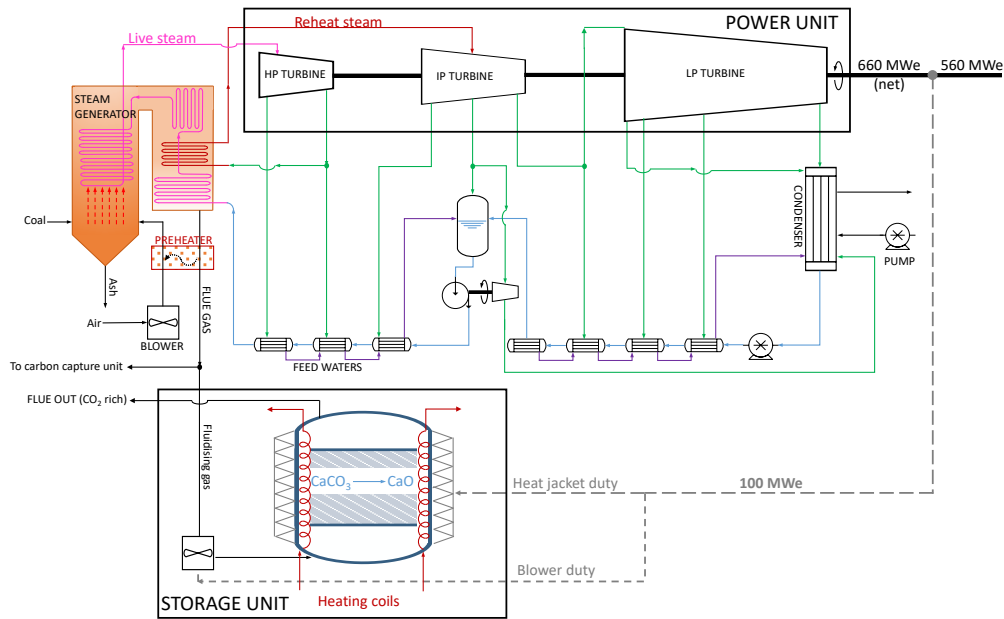
Figure 4.6: Schematic representation of the CaL cycle during an off-peak period.

In the case of the CaL+OCGT option, as shown in Figure 4.7 below, the CO_2 lean gas stream exchanges heat and preheats the compressed air using the "EXTERNAL HX" in the "POWER UNIT (GAS TURBINE)" before being vented to the atmosphere. Similar to the RES+OCGT cycle, the heated air then enters the combustion chamber and, if needed, is burnt along with natural gas to achieve higher temperatures before being expanded through the turbine. The energy content of the exhaust gas from the turbine is further used to vaporise the LNG (LNG HX) and preheat the compressed air (PRE-HEAT HX). However, in cases where CNG is used, the LNG HX is bypassed.
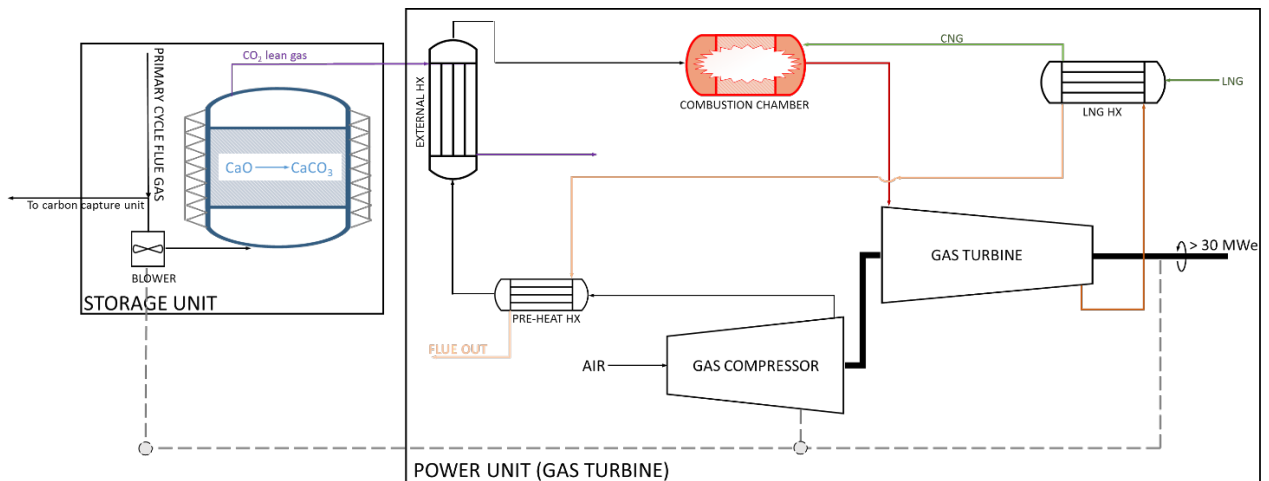
Figure 4.7: Schematic representation of the CaL+OCGT cycle during a peak period.

The CaL+SSC option is very similar to the CaL+OCGT option with the difference that the off-peak power block is comprised of the simple regen supercritical Rankine cycle described earlier for the RES+SSC option. This secondary steam cycle consists of its own high pressure, intermediate and low-pressure turbines (see Figure 4.8 below). Similar to the CaL+OCGT case,

the deactivation side reaction in Eq 4.6 is considered in the simulations associated with the CaL+SSC option.

The assumptions and key simulation parameters for the CaL cycle and its components during the off-peak and peak periods (i.e., those of the integrated OCGT and SSC power blocks) are presented in Table 4.6.
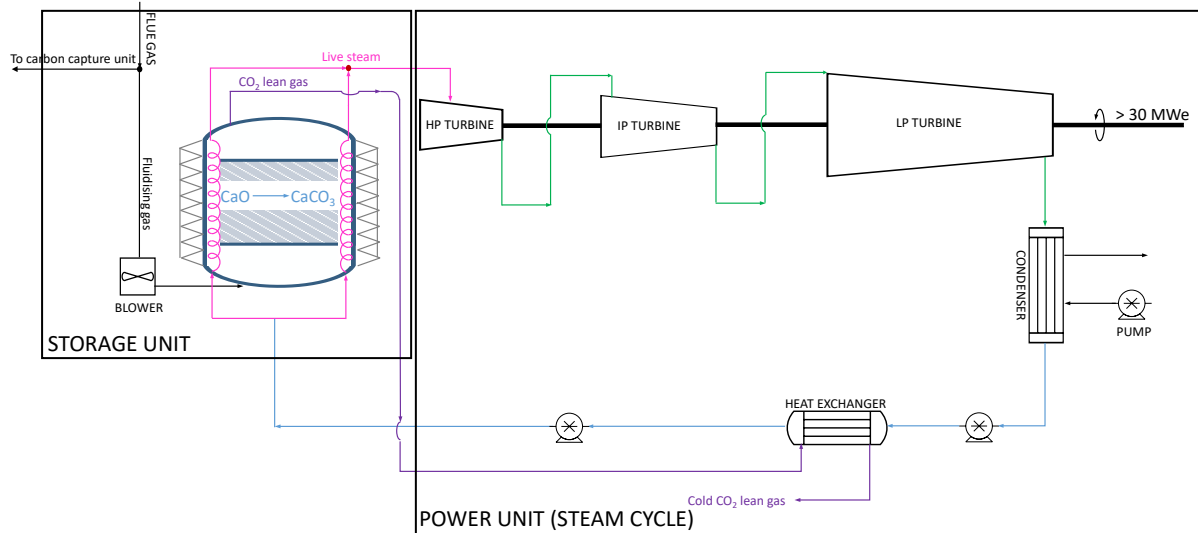
Figure 4.8: Schematic representation of the CaL+SSC cycle during a peak period.

Table 4.6: Assumptions and simulation parameters for the CaL and integrated OCGT and SSC power blocks

	Key Parameters	ASPEN+ Model	Value/Spec
CaL Component	Calciner temperature (°C)	Rgibbs	870
	Isentropic efficiency of Blower	Compressor	0.9
	Outlet pressure of Blower (bar)	Compressor	1.4
	Percentage of the purged solid	Ssplit	0.04
	Deactivated fraction of CaO	Sep2	0.05
	Total flow rate of flue gas during off-peak (kg/s)	Stream	2
	Carbonator temperature (°C)	Rgibbs	700
	Total flow rate of the flue gas to the carbonator (kg/s)	Stream	153
Integrated	Isentropic efficiency of air compressor	Compressor	0.9
	Turbine outlet pressure (bar)	Compressor	1.05
	Isentropic efficiency of gas turbine	Turbine	0.9
	Compressor outlet pressure (bar)	Turbine	8

	Combustion chamber	Rgibbs	Adiabatic
	LNG storage temperature (°C)	Stream	-165
	LNG storage pressure (bar)	Stream	8.5
	LNG heat exchanger (cold outlet temp. (°C))	HeatX	300
	CNG storage temperature (°C)	N/A	N/A
	CNG storage pressure (bar)	N/A	N/A
	Secondary fuel (CNG or LNG) flow rate (kg/s)	HeatX	1.23
	External heat exchanger (temperature approach (°C))	HeatX	300
	Compressed air pre-heater (temperature approach (°C))	HeatX	5
	Air flow rate (kg/s)	Stream	10
Integrated SSC	Isentropic efficiency of HP turbines	Turbine	0.92
	Isentropic efficiency of IP turbines	Turbine	0.94
	Isentropic efficiency of LP turbines	Turbine	0.88
	Isentropic efficiency of pumps	Pumps	0.85
	Live steam temperature (°C)	Stream	650
	Live steam pressure (bar)	Stream	242
	Live steam flow rate (kg/s)	Stream	28
	Heat exchangers in the boiler (hot outlet temp. (°C))	HeatX	110
	Re-heat heat exchanger (°C)	HeatX	62
	Condenser (Hot stream outlet temperature (°C))	HeatX	46

4.2.7 Optimisation of Process Flowsheets

In order to optimise each flowsheet, the output of the relevant power block was maximised by: (i) varying the operating temperatures of either the calcination/carbonation reactor in the CaL or the reduction/oxidation reactor in the RES process, and (ii) using the live steam temperature in the scenarios in which the supercritical steam was used as the working fluid of the power block. For cases where an OCGT was integrated to the flowsheet, the optimised flowsheet was considered to be that corresponding to the minimum flow rate of the secondary fuel (CNG or LNG) required to produce the maximum power, or at least the desired 35 MWe output. For all of the cases studied, the deactivation was accounted for by considering the purge stream and the bypass stream (5% of CaO and 1% of Cu_2O were bypassed from carbonation). Appendix B summarises some of the optimisation results.

4.3 ECONOMIC MODELLING METHODOLOGIES

4.3.1 LCOE Method

The cost of electricity generation was estimated for all of the selected technology options as well as the standalone OCGT peaking plant using the levelised cost of electricity (LCOE). The results were then compared with the LOCE figures reported in the literature for other energy storage technologies (detailed in Chapter 6). The LCOE was calculated using Eq 4.7:

$$\text{LCOE} \left(\frac{\text{A\$}}{\text{MWh}} \right) = \frac{TFCC \times ACCR(i,n) + FCOP}{P \times CFa \times 8766} + VOM + FC \times HR \tag{4.7}$$

where,

- $TFCC \equiv$ Total fixed capital cost (A\$)
- $ACCR \equiv$ Annual capital charge ratio (i=7%, n=25).
- $FCOP \equiv$ Fixed costs of operation calculated by summing the operating labour costs, maintenance, overheads, tax, and insurance (A\$)
- $P \equiv$ Plant's power output (MW)
- $CFa \equiv$ Plant's capacity factor (typically about 0.85)
- $VOM \equiv$ Variable operation and maintenance cost excluding the fuel cost
- $FC \equiv$ Fuel cost per unit of energy (A\$/MJ)
- $HR \equiv$ Heat rate

The total fixed capital cost ($TFCC$) was determined using Eq (4.8):

$$TFCC = ISBL + OSBL + D\&E + X \tag{4.8}$$

where,

- $ISBL \equiv$ Inside battery limits plant cost (ISBL is often defined as the "inner" cost of the plant, in that it is the costs associated with building the plant itself, including the purchase and shipping costs of equipment, land costs, infrastructure, piping, material needed for final plant operation and the construction of the plant as well as the fees associated with construction such as permits, insurance or equipment rental).

- $OSBL \equiv$ Outside battery limits plant cost (costs off-site to the actual plant, for instance fencing and security, utilities such as steam or electricity generators, sewers and waste treatment, firefighting and emergency equipment, offices and laboratories, and employee amenities). OSBL can be estimated from Eq (4.9):

$$OSBL = 0.3 \times ISBL \tag{4.9}$$

- $D\&E \equiv$ Design & engineering which can be estimated from Eq (4.10):

$$D\&E = 0.20 \times (ISBL + OSBL) \tag{4.10}$$

- $X \equiv$ Contingency calculated from Eq (4.11):

$$X = 0.20 \times (ISBL + OSBL) \tag{4.11}$$

The costs for the equipment used in retrofitting a given coal-fired power plant with units associated with energy storage (e.g., heat exchangers, blowers, pumps and oxygen production and storage equipment, etc.) was calculated individually based on the estimated unit size and physical dimensions. The unit sizes were estimated based on the specifications reported in the previously published works [58-61, 62]. In particular, the physical dimensions of the fluidised bed reactors and their cyclone were estimated first using the values reported in references [58-59, 62] and were then scaled using the reactors' surface area. The solid inventory per unit volume was kept equal to the ones reported in the literature [62-63].

As the costs of the open cycle gas turbine power blocks were reported in the literature [58-59, 64-65] as a whole, they were used directly in the cost estimations, although these cost figures had to be scaled based on the power output. The scaling was carried out based on the method proposed by references [58, 60], using $n = 0.7$ as the scaling exponent. The costs of the turbine trains in the secondary supercritical steam cycles (for RES+SSC and CaL+SSC) were estimated by applying the method reported in references [60-62].

The annual capital charge ratio (*ACCR*) in Eq 4.7 was calculated using the following equation:

$$ACCR\ (i,n) = \frac{i(1+i)^n}{(1+i)^n - 1} \tag{4.12}$$

In which *i* is the interest rate and *n* is the number of years.

The *FCOP* term in Eq 4.7 was determined using the following equation:

$$FCOP = \text{Operating labour costs} + \text{Supervision} + \text{Direct overhead} + \text{Maintenance} + \text{Plant overhead} + \text{Tax \& Insurance} + \text{Interest on Debt Financing} \tag{4.13}$$

Each term in Eq 4.13 was calculated for the main components of each technology option. For example, when considering the RES+SSC technology, the terms in Eq 4.13 were evaluated twice, once for the RES and once for the SSC power block. However, the sum of the *FCOP*s for the individual components was used in the LCOE calculations as the final value of the *FCOP*. Referring to Eq 4.13, the operating labour costs were calculated based on the information given in Table 4.7 and Eq 4.14 below.

Table 4.7: Assumed values for calculation of the operating labour costs

Technology	RES	CaL	SSC	OCGT
Operators per shift	2	2	1.5	2
Number of shift positions	3	2	3	3
Minimum wage	25 $/hr	25 $/hr	25 $/hr	25 $/hr
Working hrs	2482hr/yr	2482hr/yr	2482hr/yr	2482hr/yr

$$\text{Operating labour costs} = \text{Operators per shift} \times \text{Number of shift positions} \times \text{Minimum wage} \times \text{Working hrs} \tag{4.14}$$

Additional assumptions for the terms used in Eq 4.13 were:

- Supervision = 25% Operating labour costs
- Direct overhead = 45% (Operating labour costs + Supervision)
- Maintenance = 3% ISBL
- Plant overhead = 65% (Operating labour costs + Maintenance)
- Tax & Insurance = 2% TFCC
- Interest on Debt Financing = 6% Working Capital (WC)

The Working Capital (*WC*) was estimated using the following equation:

$$\text{WC} = 7 \text{ weeks Cash Cost Of Prod. (CCOP)} - 2 \text{ weeks of feed stock} + 0.01 \times \text{TFCC} \tag{4.15}$$

The cash cost of production (*CCOP*) was calculated by summing the *FCOP* and *VCOP* (variable cost of production). The feed stock to the storage unit was considered to be the secondary fuel (e.g., natural gas) if used. Given that the *FCOP* itself was an unknown, Eq 4.15 was solved iteratively to determine both the *CCOP* and *FCOP*. The *VCOP* was also calculated using the following equation:

$$\text{VCOP} = \text{ Annual fuel cost} + \text{consumables} + \text{utility cost} - \text{byproducts income} \tag{4.16}$$

Since the power ratio of the retrofitted power blocks to the primary steam cycle was ~5 %, it was assumed that the primary power plant could provide the extra utility requirements for the retrofitted power blocks. Therefore, the utility cost was considered to be zero in all cases. To avoid the calculation of a negative value for *VCOP*, the by-products income was set to zero for the RES cases and the income from the oxygen production was added to the main revenue stream.

Referring to Eq 4.7, the *VOM* is the variable operation and maintenance costs, excluding the fuel cost. The *VOM* was calculated by summing the cost of the consumables and utility minus the by-product revenues. Since the power ratio of the output of the retrofitted power units to the primary steam cycle was ~5 %, it was assumed that the primary power plant could provide the extra utility requirements for the retrofitted power units. Therefore, the utility cost was considered to be zero in all cases.

Referring to Eq 4.7, the *HR* was calculated using the following equation in which $\dot{m}$ (kg/s) is the fuel flow rate and ρ_E (MJ/kg) is the energy density of the fuel:

$$HR = \frac{\dot{m} \times \rho_E \times 3600}{P \times CFa} \tag{4.17}$$

4.3.2 NPV and IRR Methods

The net present value (NPV) provides an accurate view of all cash flows (*CF*) in an investment throughout its economic life *(t)* by considering an interest rate (*i_C* = cost of capital) and is used to decide whether a project is feasible or not. The NPV was calculated using the following equation:

$$NPV = \sum_{n=1}^{n=t} \frac{CF_n + S}{(1 + i_C)^n}$$

(4.18)

In Eq 4.18, "S" represents the net savings associated with the operation and maintenance of the primary steam cycle by avoiding the load cycling minus the costs associated with the cycling of the power units. The variable operation and maintenance cost per unit power of cycling was reported to be about $3/MWh (USD; 2012), while the fixed (capital) operation and maintenance cost per unit power of cycling was $5/MWh (USD; 2012) [66]. These values were summed and converted to $A (2017). With a cycling capacity of 100 MW, the total savings in the cost for the primary steam cycle was estimated as 21.9 MM$/yr, while the additional costs associated with the cycling of the OCGT or SSC power units was estimated as 2.5 MM$/yr. The net saving (S) was estimated as 19.4 MM$/yr.

"*CF*" was calculated using the methods reported in [58], but essentially it involved using the following equation:

$$CF_i = \text{Gr. Profit}_i - \text{Tax paid}_i - \text{CAPEX}_i$$

(4.19)

Where *i* is the year and, based on the year, takes a value of between 1 and 25 and the *Gr. Profit_i* is the gross profit received in year *i,* and is calculated using the following equation:

$$\text{Gr. Profit}_i = \text{Revenues}_i - CCOP_i$$

(4.20)

Where, the *CCOP* is the cash cost of operation in year *i*, and is calculated using Eq 4.21 below. The *%VCOP_i* and *%FCOP_i* are taken from the construction and operation schedule. In all of the considered cases, the construction schedule was one year and the rest of the 24 years were considered as the operation schedule. Hence, the *%FCOP* and *%VCOP* were equal to 0% for *i* = 1 and 100% for the rest of the period.

$$CCOP_i = VCOP_i \times \%VCOP_i - FCOP_i \times \%FCOP_i$$

(4.21)

The tax paid_i in Eq 4.19 is the tax paid in year *i,* and is calculated by using the following equation.

$$\text{Tax paid}_i = \text{Tax inc.}_{i-1} \times \text{Tax rate}$$

(4.22)

Since the tax is paid at the end of each year, the paid tax at year "i" is calculated by the multiplication of the taxable income of the plant (*Tax inc.$_{i-1}$*) in year "i-1" and the tax rate (~30%). Knowing that year 1 is mostly about the construction, no income could be associated with that year, which makes the *Tax paid$_i$* in Eq 4.22 zero for i = 1 and 2. The *Tax inc.$_i$* is calculated using the following equation:

$$\text{Tax inc.}_i = \text{Gr. Profit}_i - \text{Deprec}_i \qquad (4.23)$$

where *Deprec$_i$* is the depreciation amount at year i and is calculated using the straight-line method:

$$\text{Deprec.}_i = \frac{TFCC}{\text{Tax depreciation period}} \qquad (4.24)$$

The *CAPEX$_i$* in Eq 4.19 is the fixed capital costs that are spent at each year i of the project's life and the *TFCC* is the total of the fixed capital costs calculated using Eq 4.8. In all of the considered scenarios, the *CAPEX$_1$* was equal to the *TFCC*, while for the other years the $i{\neq}1$ was set to zero.

"i_c" in Eq. 4.18 was calculated using the following equation.

$$i_C = (DR \times i_d) + \big((1 - DR) \times i_e\big) \qquad (4.25)$$

where, *DR* is the debt ratio, i_d is the debt interest rate and i_e is the cost of equity.

As far as the IRR calculations are concerned, they can rely on the same set of formula as the NPV. To calculate the IRR in this study, the NPV was set to zero, up to the desired year (10th, 15th and 20th) and the *n* was calculated. The results are presented in Chapter 6.

4.3.3 TCOP Method

The total cost of production (TCOP) in this project was calculated using Eq 4.26, where the *CCOP* was determined by summing the *FCOP* and *VCOP* from Eqs 4.13 and 4.16, respectively. The variable *TACC* in Eq 4.26 below is the total annual capital charge and was calculated using Eq 4.27:

$$\mathbf{TCOP = TACC + CCOP} \qquad (4.26)$$

$$TACC = (TFCC + \text{Royalties}) \times ACCR(7\%, 25) + \text{Inventory Amortisation} \times ACCR(7\%, 3) \qquad (4.27)$$

In using Eq 4.27, the values of the *TFCC* and *ACCR* were determined from Eqs 4.8 and 4.12. In addition, it was assumed that the royalty and inventory amortisation were equal to 0.5% of revenues and 1% of TFCC, respectively.

4.3.4 SPP Method

The simple payback period was calculated by using Eq 4.28 below, where $\overline{CF}$ is the average cash flow and is calculated by averaging the cash flows of all years except year one. The other terms in Eq 4.28 (TFCC and WC) were determined from Eqs 4.8 and 4.15 described earlier:

$$SPP = \frac{TFCC + WC}{\overline{CF}} \qquad (4.28)$$

4.3.5 Additional Assumptions Used in Economic Models

Additional assumptions for the economic assessments were as follows:

- Cost of CNG and/or LNG = 9 A$/GJ [67]
- CNG and/or LNG energy density = 45 MJ/kg [67]
- Cost of calcium-rich particles = 150 A$/tonne
- Cost of copper-rich particles = 8000 A$/tonne
- Wholesale electricity price = 81.22 $/MWh [68]
- Tax rate = 30%
- Tax depreciation period = 25 yrs
- Tax depreciation method = Straight-line
- Cost of equity = 15%
- Cost of debt = 7%
- Debt ratio = 0.55
- Construction profile = Year 1 - 100%
- Carbon price = 23$ / 1 tonne CO_2

A sensitivity analysis on the cost of equity, cost of debt and the debt ratio are provided in Appendix C.

4.4 EXPERIMENTAL METHODOLOGIES

4.4.1 Overview

The effects of the key parameters on the reactivity of the particles were investigated in a stepwise approach. The results of each stage provided insights into the directions that were followed in its next stage. In the reactivity studies and laboratory-scale experiments, both the calcium-rich and copper-rich particles were examined. However, in the pilot-scale and large-scale experiments, only the calcium-rich particles were employed. The reason for excluding the copper-rich particles was their different energy requirements, which could lead to a different reactor design.

4.4.2 Reactivity and Material Study

4.4.2a Particle Preparation

The calcium-rich particles used in this project were purchased from Omya limestone (T-grade, purity > 99%) in the form of $CaCO_3$. These particles were used without any further modification. The average particle size was 300 μm.

However, the copper-rich particles were synthesised using a dry impregnation method. The high purity silica particles used as substrate and the copper (II) nitrate trihydrate used as the precursor were purchased from Sigma-Aldrich. The size distribution of the silica particles was between 70-200 μm. The silica particles were dried for 16 h at 110°C before the impregnation process. In the first step, the copper (II) nitrate trihydrate was dissolved in water and stirred at 80°C. The solution was then added to the dried silica powder, forming a paste, and dried for 12 h at 110°C. The paste was stirred multiple times during the initial hours of drying to avoid the formation of large lumps. In the final step, the powder was calcined at 600°C for 3 h. The synthesis steps were repeated multiple times (up to 6 times) to ensure that the coverage of the copper oxide (II) on the silica substrate was satisfactory. To enhance the physical strength, and to guarantee that all of the residual nitrates had been decomposed, the $CuO@SiO_2$ particles were sintered at 950°C for an additional 6h. The sintered product was sieved and the particles were categorised in four class sizes, namely: 53-57, 75-90, 90-125 and 125-150 μm.

4.4.2b Analytical Techniques

To characterise the particles and to investigate the effects of different parameters on their properties, different analytical techniques were employed. These techniques are described briefly in this section.

- Laser Diffraction Analysis (LDA)

In this technique, a laser beam is passed through a suspension of particles (4 g/L). Based on the scattered pattern of the laser from the particles, their size distribution is reported. This method was used to characterise the calcium-rich particles using a Malvern Mastersizer 3000 analyser.

- Scanning Electron Microscope (SEM)

Scanning electron microscope (SEM) utilises an electron beam with known energy to construct an image of the sample. Based on the type of electrons used, the focused electrons collide with the sample and eject secondary electrons (usually from the surface of the substrate) to an electron detector, which constructs the image. The samples being characterising with SEM should be covered with a conductive layer (usually platinum). The platinum sputtering stage is done as a separate step. In the sputtering process, a high voltage difference between an anode and a cathode accompanied by a magnetic field causes the bombardment of the substrate with a thin conductive layer (e.g., platinum layer) suitable for the SEM.

- Thermogravimetric Analysis/Differential Scanning Calorimetry (TGA/DSC)

Thermogravimetric analysis consists of four units, namely the: micro-balance chamber, heating control unit, gas control unit and data acquisition unit. Since any chemical reaction is accompanied by mass and energy generation or consumption, one can determine the reaction parameters and mechanisms by analysing the results. The heat generated or consumed during the chemical reaction is analysed using the DSC.

A TA Q50 TGA was employed in this project. In all of the experiments the particles (less than 50 mg) were placed in the sample holder in the micro-balance chamber. A known flow (100-300 ml/min) of a gas mixture (or pure) was also introduced to the TGA/DSC device. During each experiment, the TGA/DSC device was programmed to increase the temperature of the micro-balance chamber to a predefined value and maintain it over time, while the flow and concentration of the incoming gases were programmed to vary with time. The mass of the sample was recorded continuously. During the time that no reaction was happening, the mass of the sample remained constant.

To the contrary, the inception of any chemical reaction was marked with an increase or decrease in the mass of the sample due to the solid reacting with the flowing gas or releasing gas, respectively. At the end of any reaction, no changes in the solid mass were also recorded.

- X-Ray Diffraction (XRD)

In this technique, x-rays are used to study the crystalline structure of a solid powder. In XRD, the x-rays which are scattered from the different planes of the atoms in the solid sample are analysed and provide information about the different crystalline structures within the solids. This method is very reliable for investigating whether the cycling alters the structures of the solid powders, and hence affects their reactivity.

In all of the tests, the particles were ground to 10 µm and were then packed flat into the sample holder. The anode material was Cu Kα with 2θ in the range of ~5 to 90°. The received pattern from the sample was then compared with the reference pattern of the pure substance from the database and the structures in the examined sample were identified.

- Energy Dispersive X-Ray Spectroscopy (EDS)

A SEM device can be equipped with an EDS probe to identify the elemental composition of a sample. The emitted x-rays from the machine interact with the atoms of the sample and a signal is generated. This signal is analysed and the elemental composition of the sample is reported.

4.4.3 Prototype Development

4.4.3a Laboratory-scale Experiments

Laboratory-scale experiments were carried out in a fixed bed setup for the copper-rich particles and a fluidised bed reactor for the calcium-rich particles.

- Fixed bed reactor

Figures 4.9(a) and (b) present a schematic and photograph of the fixed bed reactor used in this study for the copper-rich particles. The copper-rich particles were placed in the reactor and fixed in their place using quartz wool. The reactor was placed horizontally in the centre of the furnace. During the reduction, nitrogen gas was used to carry away the produced oxygen. During the oxidation, the air was sent through the bed and its oxygen reacted with the particles. Mass flow rate controllers (MFC) were used to maintain the flow rate at the desired level. The reactor temperature was measured, controlled and recorded using a data acquisition system (DAS). The gas leaving from the reactor, after passing through a silica gel bed to capture its humidity, was sent to a gas analyser to measure its oxygen content. The computer interface was used to control the parameters and observe the results. In each experiment, about 5 g of particles were used. The furnace was set to increase the temperature at a rate equal to 10 °C/min. The experiment temperatures ranged from 800-950 °C. The gas flow rate was about 120 ml/min. At the end of each test, small amounts of solids were taken for further analysis using the SEM, TGA and XRD techniques.
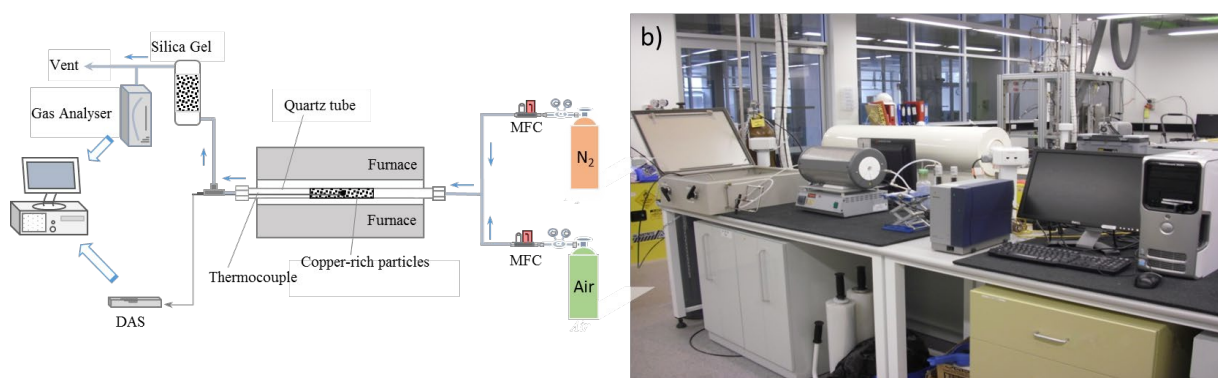
Figure 4.9: (a) Schematic illustration and (b) photograph of the fixed bed reactor used to analyse the reactivity of the copper-rich particles.

- Fluidised bed reactor

The laboratory-scale fluidised bed tests were carried out on calcium-rich particles with a wide range of gas flow rates (up to and including CO_2 concentrations). The raw sorbent used in the tests was an Omya limestone. The calcination of the limestone was performed in air and the carbonation was performed in 1 vol. % CO_2 in the air. The experiments were carried out in a stainless steel bubbling fluidised bed reactor (41 mm i.d.) operated at atmospheric pressure (see Figures 4.10(a)-(d)). The reactor consisted of three sections: (a) the pre-heater/pre-mixer of the fluidising gas (0.66 m high); (b) the fluidisation column (0.95 m high); and (c) the exit head placed on top of the reactor, which was connected with the exhaust line. The distributor plate was made of stainless steel with a 140 micron mesh size. The reactor temperature was

maintained during the experiment by using an electrically heated furnace placed around the pre-heater/pre-mixer and the fluidisation column. The temperature inside the fluidised bed was measured with a type Pt/Rh thermocouple. A fraction of the off-gas, after passing through a water trap, was continuously sent to a gas analyser to measure the CO_2 concentration. Before each experiment, the calibration gas (containing 1 vol. %CO_2 in air) was passed through the bed to calibrate the analyser.
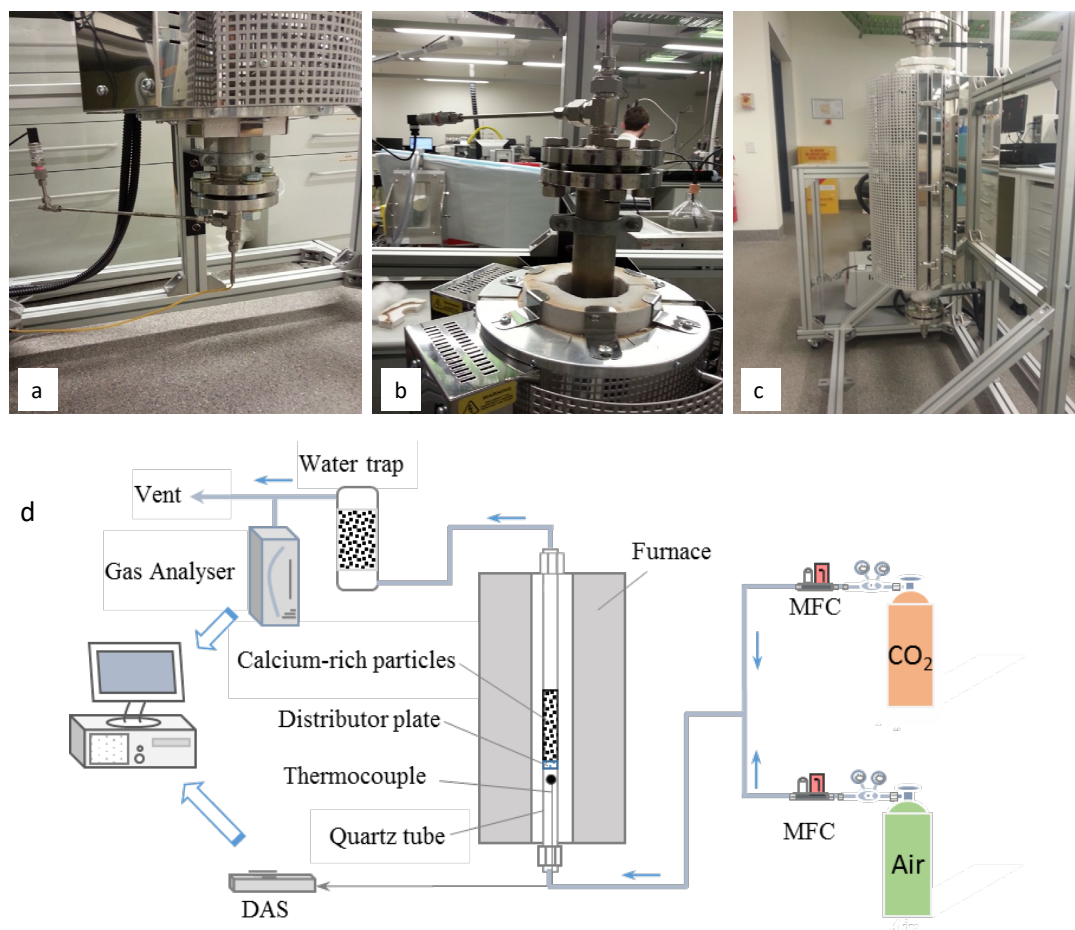
Figure 4.10: Laboratory-scale fluidised bed reactor: (a) fluidising gas input to the fluidised bed reactor, (b) gas leaving the fluidised bed reactor, (c) fluidised bed reactor and furnace, and (d) schematic of the laboratory-scale fluidised bed reactor setup.

Five calcination/carbonation cycles were carried out in all of the experiments using an initial amount of 100 g of fresh limestone. The fresh limestone was sieved to get particles with a size of 150-212 µm and were kept in an oven at 100°C prior to experimentation. The fluidising velocities were 0.023 m/s during the calcination and carbonation cycles. All of the flow rates were measured using calibrated rotameters operating at atmospheric pressure. Each test started with the heating of the reactor from the room temperature to the desired calcination temperature, with a rate equal to ~20 °C/min. The progress of the calcination reaction was monitored by measuring the CO_2 concentration at the exhaust. The calcination reaction was considered complete when the CO_2 measured in the exhaust returned to ambient concentrations.

The temperature of the bed was then set to the desired carbonation temperature (550°C) for 3 hours. When the new temperature was reached, the reactor was fed with gases consisting of 1, 5 and 10 vol. % CO_2 in the air. The progress of the carbonation was monitored by measuring the CO_2 concentrations at the exhaust. The carbonation reaction was considered complete when CO_2 was no longer captured. The above procedure was repeated for the subsequent cycles. The same duration of the first carbonation cycle was used for the successive carbonation cycles. A small sample was collected from the bed at the end of each calcination and carbonation cycle. These solid samples were investigated using scanning electron microscopy (SEM) for any changes in morphology after repeated cycling in comparison to the fresh limestone (initial bed material).

4.4.3b Pilot-scale Experiments

Figures 4.11(a) and (b) presents images of a new prototype developed for the CaL energy storage process. Similar to the fabricated laboratory-scale setup, the three main sections of the prototype are the gas feeding system, the fluid bed reactor and the controllers, including the data acquisition system (DAS) and the gas analysers. Based on the different gas compositions required in the process, the gas feeding system mixed air and CO_2. The concentration of the inlet gas was monitored with one of the gas analysers, and adjustments were made to the gas flow rates to get to the desired concentrations. In this unique design, the fluid bed reactor consisted of two concentric tubes. The internal tube had a metallic ball at its bottom which acted as the gas distributor. The bed inventory was placed on the top of the metallic ball. The fluid bed inlet gas lifted the metallic sphere and passed around it to form a homogenous fluid field in order to fluidise the particles. Two K-type sensors were used to measure the temperature at the top and bottom of the bed. The average bed temperature was controlled using a liquid pressurised gas (LPG) burner which surrounded the fluid bed, and was located in the annulus. According to Figure 4.11, the exhaust of the burner and the fluid bed were separated. The DAS collected the temperature, flow rate and concentration data for further analysis. A gas sampling tube was used to read the composition of the gas leaving the bed. Figure 4.11(b) shows a snapshot of the inside of the fluid bed during operation. The gas sampling tube was located above the fluidised particles. The temperature of the bed was monitored using two temperature sensors located at different bed heights. Due to the special material used in the construction of the fluid bed, it can withstand temperatures as high as 1200 °C. The fluid bed diameter and height (including exhaust) were 0.75 m and 3.5 m, respectively.

A T-grade limestone (97 wt% calcium carbonate) was used in these experiments. The particle size distribution (PSD) was measured using the Mastersizer 3000. The results of the PSD characterisations were used in the calculation of the fluid bed hydrodynamics and determined the fluid bed inventory and the total flow rate of the fluidising gas. Table 4.8 lists the initial six experiments that were designed to investigate the operation of the fluid bed. The temperatures for the carbonation and calcination were 650-700 °C and 850-900 °C, respectively. The CO_2 concentrations of the inlet gas varied from 5% to 20%. The number of cycles was equal to 2. Hence, each experiment included two consecutive calcination and carbonation cycles.
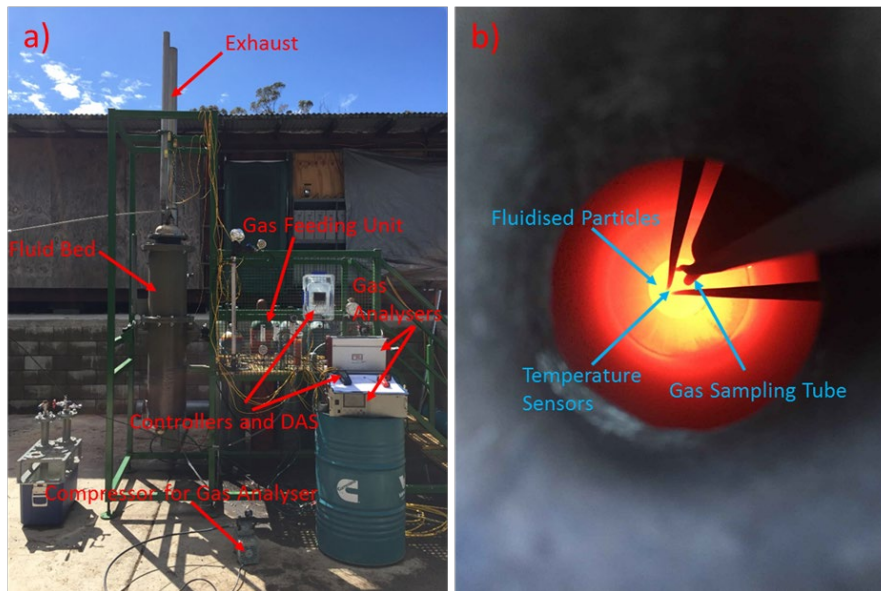
Figure 4.11: Photographs of: (a) Pilot-scale fluid bed and its components, (b) Inside the fluidised bed during the operation.

Table 4.8: List of the initial experiments carried out to investigate the operation of the pilot-scale fluidised bed

Experiment number	Calcination temperature (°C)	Carbonation temperature (°C)	Inlet gas composition (CO₂ %vol)	Total flow rate (m³/h)	Number of cycles
1	900	650	20	2	2
2	900	650	13	2	2
3	900	650	5	2	2
4	850	700	20	2	2
5	850	700	13	2	2
6	850	700	5	2	2

At the beginning of the initial experiments, the fluid bed was loaded with a known mass of particles. The inlet flow of the air was then increased from zero to about 2 m^3/h. In the next step the LPG burner was switched on, which marked the beginning of the calcination reaction. The fluid bed temperature was increased to 850 or 900 °C and was then kept constant throughout each calcination cycle. The ambient air was used during calcination. The calcination reaction continued to the extent that the CO_2 concentration at the exit was less than 1% for more than a few minutes. At the end of the calcination, the fluid bed temperature was allowed to cool down to 650 or 700 °C depending on the experimental conditions before the CO_2 was injected. The flow rate of the inlet gas mixture (air and CO_2) was adjusted to make sure that the inlet concentration of CO_2 was equal to the desired values (5, 13 and 20 %) while the total flow did not exceed 2 m^3/h. The duration of the carbonation process was two hours. The LPG burner was set to the minimum during the carbonation to keep the temperature constant. At the end of the first carbonation process, the second calcination started. The end of each preliminary test was at the end of the second carbonation. At the end of each experiment, the LPG burner was turned off and the mass of consumed fuel was measured.

The bed inventory was also removed from the fluid bed and its mass was measured. The differences in the particle masses contributed majorly to the elutriation of the particles or their adherence to the fluid bed's internal surface. The bed material for the initial experiments weighed approximately 3 kg.

After conducting the initial set of experiments and analysing the results, the pilot-scale fluidised bed was loaded for the primary tests (e.g., the field demonstration tests). The main differences between initial and primary tests were the bed inventories and gas flow rates. Moreover, the calcination reaction temperature for the primary tests was fixed (Table 4.8-9). The experimental procedure for the primary tests was very similar to that of the initial tests. After loading the bed and adjusting the air flow rate to 200 m³/h, the bed temperature was increased from the ambient temperature to 850 °C for the calcination. The rate of the temperature increase was about 20 °C/min. The calcination process lasted for 90 minutes. At the end of the calcination process, the bed temperature was allowed to drop to the desired carbonation temperature. The composition of the incoming gas (air and CO_2) and its flow rate were then adjusted according to the values reported in the experimental matrix (see Table 4.9 below). The carbonation process started when the bed temperature was sufficiently low and lasted for 240 minutes. At the end of each carbonation process, the gas flow rate was set to zero and the bed material was substituted with the fresh limestone for the next experiment. Table 4.9 below shows the complete experimental conditions used in the field demonstration tests. The sampling intervals were 1 minute for the calcination and 2 minutes the carbonation processes.

Table 4.9: List of primary experiments carried out to demonstrate the operation of the pilot-scale fluidised bed

Variables and Values	Runs	Cumulative number of experiments
Temperature: 600, 650, 700 °C	3	3
Bed Solid Inventory: 50, 100, 150 kg	3	9
Flow Rate: 100, 150, 200 m³/h	3	27
CO_2 Concentration of Incoming Gas: 5, 13, 20%	3	81
Repeated Experiments	2	162

4.4.3c Large-scale Experiments

Since the bed inventories in the laboratory-scale and pilot-scale experiments were small, they were not able to operate for a long period at a constant temperature during the carbonation, and auxiliary heat had to be provided. However, the large-scale reactor could overcome this problem and operated at a constant temperature for a long period. In the large-scale experiments, the gas flow rate was 1200 m³/h, and the bed inventory was 2300 kg. The calcination temperature was 750 °C and the carbonation temperature varied between 600 and 740 °C. The rate of the temperature increase for the calcination process was 5 °C/min. Figures 4.12(a) and (b) show the large-scale fluidised bed reactor.

As seen in Figure 4.12, a burner was used to provide the heat for the calcination and carbonation reactions if they were required. The combustion product of the natural gas with air leaving the burner was mixed with the incoming gas and entered the fluidised bed. The leaving gas then preheated the incoming air using a heat exchanger. To capture the entrained particles, the stream was further cooled down and sent to the baghouse filter. A series of experiments were conducted to investigate the heat produced during the carbonation process. The experiments were designed to show that the temperature of the fluid bed could be maintained at a specific temperature using only the heat released from the carbonation reaction. A single experiment investigating the increase in the bed temperature using heat from the carbonation reaction was also undertaken. The reactor was operated for 24 h for seven days per week during the experimental period. A summary of the experiments conducted is presented in Table 4.10 below.

Prior to each carbonation experiment, a calcination cycle was required to convert the bed from $CaCO_3$ to CaO. The calcination process was conducted at a maximum of 750°C, with the heat supplied from the combustion of the natural gas. The start-up period and initial calcination cycle required 3.5 days. The calcination time for the subsequent cycles was one to two days, depending on the experimental carbonation conditions.

At the commencement of each carbonation experiment, the natural gas burner and supplementary natural gas stream were turned off/closed, and the air flow rate was reduced to 1200 m^3/h. The fluid bed temperature was allowed to decrease to the desired experimental conditions before the introduction of the CO_2. The CO_2 flow rate was adjusted throughout the experiment to maintain the fluid bed temperature. For experiments 7, 8 and 9, the gas burner was restarted when the carbon dioxide was introduced to provide additional heat to the inlet air and to reduce the temperature difference between the inlet air and the fluidised bed. For experiment 10, the carbon dioxide flow rate was adjusted to maintain an increase in the bed temperature of approximately 5 °C/min.
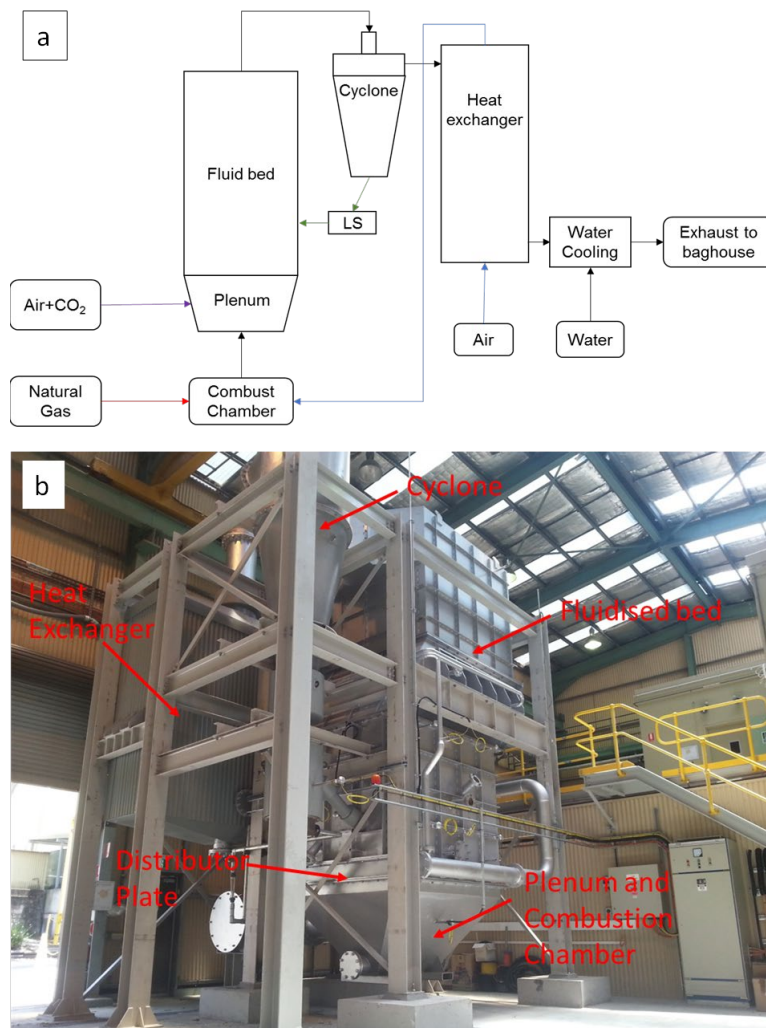
Figure 4.12: (a) Simplified process flow diagram of the large-scale fluidised bed and its components, (b) A photograph of the fluidised bed.

Table 4.10: The experimental matrix for the large-scale fluidised bed

Experiments	Carbonation Temperature	Burner	Air Flow rate (m³/h)
1	600	0	1200
2	700	0	1200
3	700	0	1200
4	700	0	1200
5	710	0	1200
6	710	0	1200
7	730	30	1200
8	730	30	1200
9	740	50	1200
10	Ramp to 710	0	1200

4.5 ERROR ANALYSIS OF THE EXPERIMENTAL DATA

All of the experimental works described in this chapter were repeated multiple times, except for the large-scale experiments. The R^2 was employed to investigate the integrity of the kinetic models (e.g., reaction mechanism) used to describe the experimental results. The standard deviation of the experimental results from the laboratory- and pilot-scale tests are shown as error bars in related figures in Chapter 7. However, in the case of TGA measurements each test comprises more than 10,000 data points. The error analysis revealed that the standard deviations of the results were very small (less than 0.5%). As such, the corresponding error bars are not shown in figures, as they are too small.

4.6 LIFE CYCLE ANALYSIS

4.6.1 Overview

Utility-scale energy storage in conjunction with coal-fired power generation is an emerging solution which if deployed along with renewable energy can resolve some of the issues caused recently by rapid penetration of renewable energy into the grid. However, more information is needed to determine the environmental impacts of large-scale energy storage. The objectives of this study were: (i) to conduct a life-cycle assessment and determine the environmental impacts of utility-scale energy storage versus switching to natural gas; and (ii) determine the cumulative impacts of using utility-scale energy storage versus natural gas over a 12-year period (2018 to 2030).

To meet the first objective, a life-cycle assessment (LCA) was conducted to quantify the environmental impacts of using a utility-scale CaL+SSC, a Li-ion battery and a hypothetical CNG power plant to deliver 1 MWh of electricity to the grid. The LCA analysis specifically assessed the environmental impacts of climate change (expressed in terms of greenhouse gas [GHG] emissions), terrestrial acidification, photochemical ozone formation, particulate matter formation, human toxicity, and freshwater eutrophication). These six environmental indicators are commonly used in LCA literature as they represent key impacts on the climate, air, water, ecosystems, and human health. The LCA analysis for each indicator was carried out using GaBi ThinkStep software.

To meet the second objective, the project team considered two scenarios, namely: (i) business as usual [BAU] where no utility-scale energy storage was considered and as such CNG was assumed to displace some of the coal in baseload power generation according to projections for the future energy mix of NSW, and (ii) utility-scale energy storage [USES] scenario where it was assumed that all the excess energy available from coal-fired power generation was stored in either a CaL+SSC based system or a Li-ion battery; displacing additional amounts of coal to that already projected for NSW by 2030.

4.6.2 Methodology

The International Organization for Standardization (ISO) specifies the definitions, principles, and framework for conducting LCA analysis in its standard 14040:2006 published in 2010. The LCA analysis conducted in this project complies with this standard. Essentially, any LCA analysis is about quantifying the environmental impact of a

given product as a function of product / service life, that is, from resource extraction to the end of product life. Two difference approaches can be undertaken to complete a LCA analysis, namely: attributional A-LCA or consequential C-LCA. The former is often adopted to determine the environmental impacts of a product at a given point in time whereas the latter provides the environmental impacts resulting from the changes in the product and/or in the system to which the product is attached to over a given period of time. For this reason, in the present study the A-LCA approach was employed to satisfy Objective-1 (Section 4.6.1) while Objective-2 was met using a C-LCA approach.

<u>A-LCA Methodology</u>: For a CaL+SSC based system the greatest environmental impact occurs during the extraction of the carbonate minerals and the construction phase of the facility, with little to no impact during the operational phase (i.e. use phase). In contrast, for CNG generated electricity, the majority of the environmental impacts occur during the operational phase where electricity is generated by the combustion of natural gas.

To capture this difference yet accurately compare the impacts of both systems based on a common reference, a functional unit was defined for all LCA analyses. This essentially involved defining a single unit of impact per amount of energy utilisation, that is, a functional unit capable of dispatching 1 MWh to the grid. The models used for both CaL+SSC and Li-ion battery in the LCA analysis were developed in-house using version 6 of the GaBi 6 software together with A-LCA inventories reported in the literature. An energy density of 1,111 kWh/tonne and a roundtrip efficiency of 36% (details in Section 5.1.3) were considered for the CaL+SSC in the model. For Li-ion battery typical values were considered for the energy density (130 kWh/tonne) and the roundtrip efficiency (~90%). Further, a 20-year lifetime with a single daily discharge was assumed for both the CaL+SSC and Li-ion battery models. This equates to 7,300 charge-discharge cycles over the lifetime of the unit. The inefficiencies in dispatching the power (e.g. depth of charge, parasitic losses, etc.) were determined either based on project findings in Stage 1 or the values reported in the literature. Accordingly, for the depth of charge a value of 95% was assumed for Cal+SSC while a figure of 80% was used for the Li-ion battery. The parasitic losses for both systems were assumed to be about 1%. The combination of roundtrip efficiency, depth of charge and parasitic losses allowed us to determine the size of the each functional unit (i.e. installed capacity) for the delivery of the desired 1 MWh to the grid. As an example:

$$\text{Inst. Cap. of CaL} + \text{SSC Functional Unit} = \frac{1 \text{ MWh}}{(0.36 \times 0.9 \times (1 - 0.1))} = 3.12 \text{ MW}$$

Which translates to:

$$\text{Required Quantity of Carbonate Material} = 3.12 \times \frac{\text{tonne}}{1.111 \text{ MWh}} \cong 2.81 \text{ tonne}$$

By the way of comparison, if a typical Li-ion battery was used, one would have:

$$\text{Inst. Cap. of Li} - \text{ion Functional Unit} = \frac{1 \text{ MWh}}{(0.9 \times 0.8 \times (1 - 0.1))} = 1.40 \text{ MW}$$

$$\text{Required Quantity of Li} - \text{ion Material} = 1.40 \times \frac{\text{tonne}}{0.13 \text{ MWh}} \cong 10.8 \text{ tonne}$$

As the above simple functional unit analysis shows, despite having a higher roundtrip efficiency a Li-ion battery requires 3.84 times more material than a calcium based energy storage system for dispatching the same 1 MWh to the grid. Thus Li-ion type energy storage systems will inevitably result in much greater environmental impacts.

C-LCA Methodology: As noted earlier, this methodology is adopted to satisfy the second objective of the LCA analysis by using BAU and USES scenarios. For these, particularly USES, the project team needed to determine how much energy storage would be implemented from 2018 to 2030. This required an understanding of NSW future electricity demand and generation mix between 2018 and 2030. To this end, the project team developed a projection model named "FUGEN" to determine the volume of excess energy available for storage during the 12-year period between 2018 and 2030. The necessary data for the above projection were obtained from CSIRO reports as well as several other reports commissioned by the Federal Government (e.g. Deloitte's reports).

Impact Assessment: The 6 selected environmental impact indicators were quantified as:

- Climate Change – Expressed in kg of carbon dioxide equivalent (kg CO_{2eq}), characterises the global warming potential of a given substance over a century.

- Terrestrial Acidification – Expressed in kg of sulfur dioxide (kg SO_{2eq}), characterises the potential of a substance to cause acid rain in a given ecosystem.

- Photochemical Ozone Formation – Expressed in kg of nitrogen oxide (NO_x) equivalent (kg NO_{xeq}), characterises photochemical oxidants in a given ecosystem.

- Particulate Matter Formation – Expressed in kg of 2.5-micrometer particulate matter equivalent (kg $PM_{2.5eq}$), characterises the potential of a substance to form fine particulate matter in the air.

- Human Toxicity – Expressed in kg of 1,4-dichlorobenzene-equivalent (kg 1,4-DBeq), characterises the potential of a substance to release carcinogenic toxicity into the atmosphere.

- Freshwater Eutrophication – Expressed in kg of phosphorous equivalent (kg Peq), characterises the potential of a substance to impact eutrophication in freshwater ecosystems.

Chapter 5

Results and Discussion:
Scoping Study
(Milestone 2)

5.1 ENERGY FLOWS

5.1.1 Energy Sources and Sinks (Sankey Diagrams) and Heat Management

In this section the energy sources and sinks associated with the proposed thermochemical energy storage processes (i.e., RES+OCGT, CaL+OCGT, RES+SSC and CaL+SSC) are discussed. The results are presented in the form of Sankey power diagrams (see Figures 5.1 and 5.2) so that the reader better understands the relationships among the key energy sources and sinks.

Sankey diagrams are a specific type of flow diagram which can be used to graphically summarise all of the energy or power transfers taking place in a given process. The graphical emphasis of the Sankey diagrams allows the flow quantities (e.g., energy or power) to be shown proportionally by the width of the lines (or arrows) used in drawing them. The thicker the line (or arrow), the greater the amount of energy or power involved.

In this study the flow quantity of choice is power (e.g., electrical, thermal and thermochemical) because by knowing the power and duration of the charging and discharging (i.e., the off-peak and peak periods) one can easily estimate the quantities of energy involved. This eliminates the need to redraw the Sankey diagrams every time a different charging and discharging timeframe is considered.

Figures 5.1(a) and (b) present the Sankey diagrams for the RES and CaL processes coupled with an open cycle type gas turbine (OCGT) power block, respectively, while Figures 5.2(a) and (b) show similar results when a supercritical secondary steam cycle (SSC) power block was employed. Note that the "Off-peak" and "Peak" signs in Figures 5.1 and 5.2 denote the charging and discharging periods, respectively. The reason that the values in the Sankey charts are reported in power rather than energy is that the reported values would remain constant even if the durations of the charging (off-peak) and discharging (peak) change. One then just needs to multiply the power by the charging/discharging duration times to get the relevant energy stored or released. These diagrams feature a number of very important and

quite interesting trends which are summarised below. Firstly, regardless of the thermochemical energy storage method, the power losses associated with the charging phase (i.e., the off-peak period) are always much lower than those during the discharging phase when the electrical power is generated. This feature highlights two important facts, namely: (i) as expected, the power losses due to the conversion of the electrical power to heat or Joule heating are insignificant, and (ii) much of the energy loss was due to the power block rather than the underlying thermochemical energy storage process.

The second interesting feature in the Sankey diagrams is that during the charging phase the power losses associated with the RES based processes are higher than those of their CaL based counterparts (compare, for example, Figures 5.1(a) and (b)). The primary reason for this difference is the parasitic losses associated with oxygen production (i.e., the reduction of the metal oxides and the separation of oxygen from the steam).

Another important feature of the Sankey diagrams presented in this section is that the two OCGT incorporated cycles (i.e., RES+OCGT and CaL+OCGT (see Figure 5.1)) could not achieve the desired 35 MWe electrical output unless a secondary fuel (CNG or LNG) was introduced into the overall cycle.
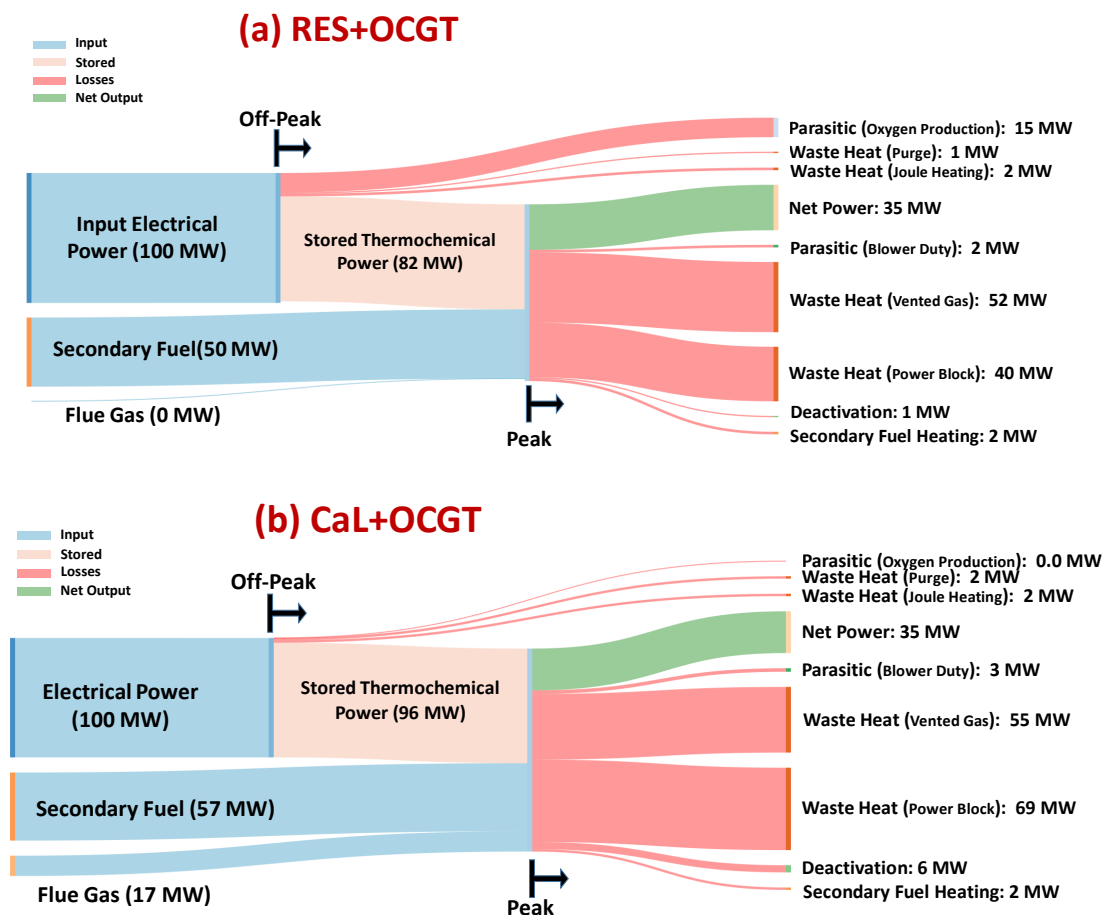
Figure 5.1: Sankey power diagrams for: (a) RES+OCGT and (b) CaL+OCGT cases.
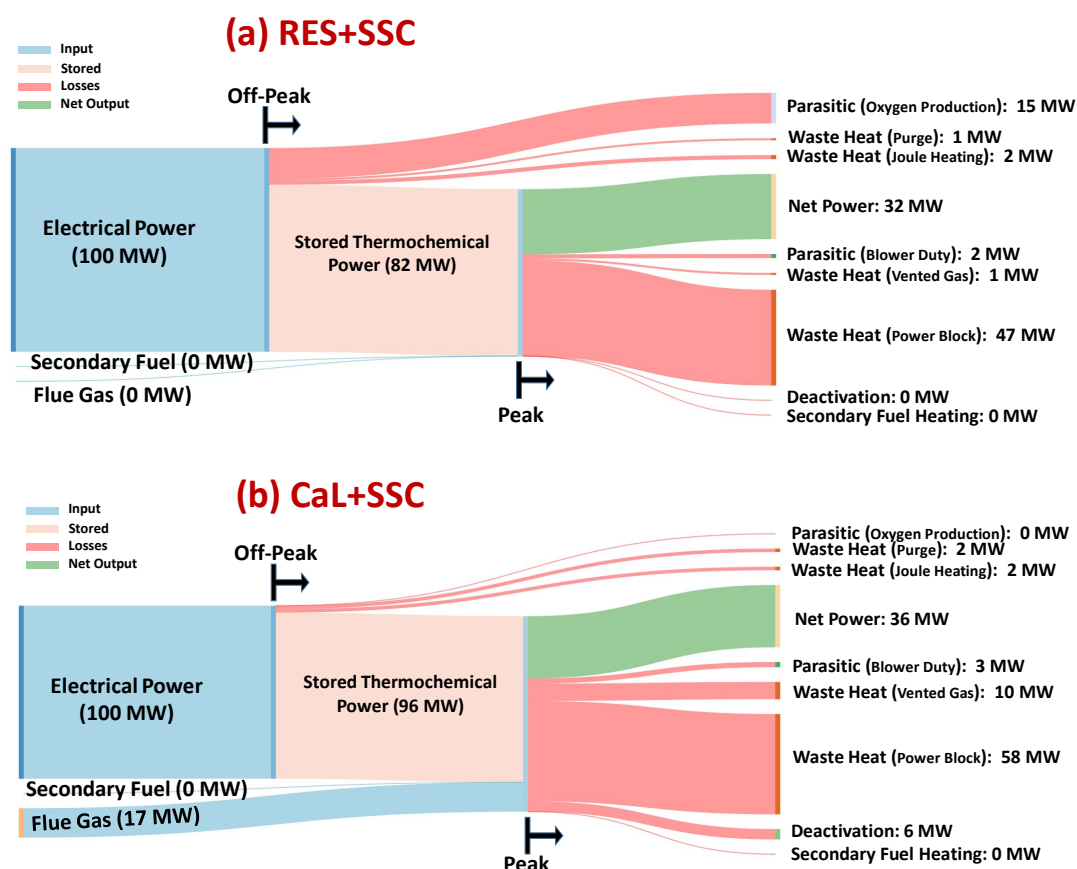
Figure 5.2: Sankey power diagram for: (a) RES+SSC and (b) CaL+SSC cases.

This can be assigned to two related contributing factors, namely:

1. The fact that in order to achieve the maximum thermal efficiency in the OCGT power block, the temperature of the inlet gas to the turbine unit must be raised to levels well above 1000 $^{\circ}$C (1037 $^{\circ}$C for RES and 1021 $^{\circ}$C for CaL). However, the temperature of the incoming gases to the power block from the thermochemical unit was much lower at 800°C in the case of RES and 700 $^{\circ}$C for the CaL. Offsetting this temperature gap obviously required additional energy input, which was supplied here by the secondary fuel (CNG or LNG). The artefact of the high temperatures in the OCGT turbine unit was the relatively high exhaust temperatures, and thereby greater power losses in the form of waste heat. For example, for the cases shown in Figure 5.1, the waste heat losses in the power blocks corresponding to the RES and CaL were 40 MW and 69 MW, respectively.

2. The heat losses associated with the pre-heating of the OCGT working fluid (i.e., air) using hot gases from the thermochemical unit. This heat exchange process, as shown in Appendix A, takes place in a dedicated heat exchanger (designated "External" in Figure B2 and "HEX2" in Figure B4). For the cases under investigation, the amount of waste heat from this process (designated as waste heat [vented gas] in the Sankey diagrams) was about 52 MW for the RES+OCGT case and 55 MW for the CaL+OCGT case. One option to avoid such heat losses is to directly use the hot gases from the thermochemical unit as the working fluid in the OCGT power block. The main issue with this approach is that the gases from the thermochemical unit may carry a considerable quantity of fine particulate matter which is detrimental to the operation

of the gas turbine unit. For this reason, an indirect approach has been adopted in the present study. Another option would be to add an Organic Rankine Cycle (ORC) waste heat recovery unit to the vented gas, although this option adds another layer of complexity, not to mention additional capital and operating costs. While the ORC option was not considered as a part of the first phase of the current project, it will be investigated further in the next phase.

Unlike in previous cases, when the RES and CaL are coupled with a supercritical steam cycle power block (see Figures 5.2(a) and (b)) they no longer need a secondary fuel input, although in the case of CaL a modest quantity of thermal energy was fed into the cycle by hot flue gases (used in both the calcination and carbonation steps). The primary reason for this phenomenon was that the operating temperature of the steam cycle was 700 $^{\circ}$C for RES and 650 $^{\circ}$C for CaL, and hence the steam can be adequately heated up to these levels using the incoming hot gases from the thermochemical unit, which was 800 $^{\circ}$C in the case of RES and 700 $^{\circ}$C for CaL.

5.1.2 Energy Efficiency

The energy efficiency can be defined in a number of alternative ways. However, for the benchmarking of the technologies under investigation here, the energy efficiency is defined in four different forms:

a. Cyclic efficiency of the energy storage unit:

$$\eta_{Cy} = \frac{\text{Output Energy from the Storage Unit (Discharging Period)}}{\text{Input Energy to the Storage Unit (Charging Period)}} \times 100 \tag{5.1}$$

For example, for the RES+OCGT case (see Figure 5.1(a)):

$$\eta_{Cy} = \frac{82 \ MW \times 8 \ hrs}{100 \ MW \times 8 \ hrs} \times 100 = 82\%$$

b. Thermal efficiency of the power block:

$$\eta_T = \frac{\text{Output Energy from the Power Block (Discharging Period)}}{\text{Input Energy to the Power Block (Discharging Period)}} \times 100 \tag{5.2}$$

For example, for the RES+OCGT case (see Figure 5.1(a)):

$$\eta_T = \frac{35 \ MW \times 8 \ hrs}{(82+50) \ MW \times 8 \ hrs} \times 100 \cong 27\%$$

c. Round trip electrical efficiency of the complete storage system expressed as:

$$\eta_{RT} = \frac{\text{Output Electrical Energy (Discharging Period)}}{\text{Input Electrical Energy (Charging Period)}} \times 100 \tag{5.3}$$

For example, for the RES+OCGT case (see Figure 5.1(a)):

$$\eta_{RT} = \frac{35 \ MW \times 8 \ hrs}{(100) \ MW \times 8 \ hrs} \times 100 \cong 35\%$$

d. Overall efficiency of the complete storage system expressed as:

$$\eta_{O} = \frac{\text{Output Electrical Energy (Discharging Period)}}{\text{Input Energy from all sources}} \times 100 \tag{5.4}$$

For example, for the RES+OCGT case (see Figure 5.1(a)):

$$\eta_{O} = \frac{35 \ MW \times 8 \ hrs}{(100+50) \ MW \times 8 \ hrs} \times 100 \cong 23\%$$

Table 5.1 summarises the results of the comparison between the thermochemical energy storage concepts under investigation in this study and other energy technology options which are suitable for time-shift and load-shift applications at the utility-scale. The first observation from the table was that among the thermochemical energy storage options studied, the CaL+SSC concept delivered the highest set of efficiencies. Furthermore, as can be seen from the table, in terms of the cycling efficiency, both the RES and CaL options outperformed the flow batteries, given that thermochemical energy storage processes inherently have no self-discharge. It should be highlighted that of the different definitions of efficiency, cycling efficiency has a special place for thermal and thermochemical storage systems because it underpins the conversion efficiency of the core technology. For example, in the case of RES, which is comprised of a chemical looping conversion unit plus a conventional off-the-shelf gas or steam turbine, the cycling efficiency summarises the performance characteristics of the chemical looping unit. The influence of the gas/steam turbine unit is measured using either the round trip or overall efficiency. That explains why, in the project proposal, the cycling efficiency rather than any other definitions of efficiency was singled out as a key performance measure.

Table 5.1: Energy efficiency comparisons for various technologies suitable for utility-scale time-shift and load-shift applications

Technology	Cycling Efficiency	Thermal Efficiency	Round Trip Efficiency	Overall Efficiency	References
CaL+OCGT	96%	21%	35%	22%	This study
RES+OCGT	85%	27%	35%	23%	This study
CaL+SSC	96%	32%	36%	36%	This study
RES+SSC	85%	39%	32%	32%	This study
Standalone-OCGT	-	35-40%	-	35-40%	This study
Flow Batteries	60-82%	-	60-80%	60-80%	[16-69-71]
PHS	87%	-	70-85%	70-80%	[71]
CAES	70-79%	-	42%	42%	[71]

In terms of their thermal efficiency, both the RES and CaL options registered lower figures than those of the Standalone-OCGT system. Likewise, the power block's round trip and the overall efficiencies for the batteries and standalone OCGT were greater than their thermochemical alternatives but CaL technologies delivered higher cycling efficiencies than the PHS and CAES systems.

In terms of the overall efficiency, the thermochemical processes are comparable to CAES systems. However, it should be highlighted that for a given energy storage technology the overall performance cannot be measured by efficiency alone, rather a combination of energy efficiency and energy density should be employed (discussed in detail in the next section).

5.1.3 Energy Density

Very much like energy efficiency, the energy density can be defined in a number of alternative ways. In this study, the gravimetric and volumetric energy densities were considered. The former is defined as:

$$\epsilon_g\left(\frac{kWh}{tonne}\right) = \frac{Quantity\ of\ Stored\ Energy\ (kWh)}{Weight\ of\ the\ Storage\ Medium\ (tonne)} \tag{5.5}$$

whereas the latter is expressed as:

$$\epsilon_v\left(\frac{kWh}{m^3}\right) = \frac{Quantity\ of\ Stored\ Energy\ (kWh)}{Volume\ of\ the\ Storage\ Medium\ (m^3)} \tag{5.6}$$

Given the results presented in the previous section of the thermochemical energy storage options, the CaL+SSC was selected for comparison against the non-thermochemical energy storage options, including batteries (in this case a Tesla Wall-2 flow battery), Standalone-

OCGT, PHS and CAES. A well-known thermal energy storage system (Nest Egg) was also included in the comparison, in spite of the fact that technically such a system can only be used for thermal to thermal conversion applications and not thermal to power. The key assumptions made in this benchmarking exercise were:

- The energy requirements for the Nest Egg thermal storage system were estimated based on the maximum module temperature of 450 °C.

- The energy output from the Standalone-OCGT system was subjected to some losses due to the thermodynamics of the system. Hence, its thermal efficiency (power output in the discharging mode) was estimated to be about 35-40 %.

- The mass of the storage medium for the secondary fuel was calculated based on the lower heating value of 45 MJ/kg.

The calculations were based on the power available during the charging phase. To convert the power (MW) to energy (MWh) over a one hour period, its value was multiplied by one. Furthermore, after calculating the required mass for each technology option using their densities, the required volume was calculated for each option. To get the gravimetric or volumetric energy density values for each option, its corresponding energy (i.e., MWh) was divided by its mass or volume, respectively. The results have been summarised in Table 5.2 below. The key findings were:

- While electrochemical systems like Tesla flow batteries have the highest round trip efficiencies, in terms of gravimetric and volumetric energy densities the proposed processes outperform other storage options considered here. For example, the gravimetric and volumetric energy densities of CaL are 8.5 (= 1111/130; see Table 5.2) and 12.3 (= 1424/116; see Table 5.2) times greater than those of Tesla batteries.

- The higher energy densities of CaL imply that for the same footprint or volume (roughly for the same capital cost) the energy output of a CaL+SSC system (i.e., 36 MWh per hour of operation in this study) would be actually greater than batteries (e.g., Tesla output for the same footprint = 90/12.3 = 7.3 MWh)

Similar conclusions have been reported about the high energy densities of calcium based thermochemical processes in the context of solar thermal energy storage [72]. Figure 5.3 below is an example where the volumetric energy density of various substances have been plotted against the exergetic efficiency (second law efficiency based on exergy or availability). As can be seen, despite having a lower exergetic efficiency, the calcium carbonate registers the highest energy density on this plot. The figure reported in this plot for calcium carbonate is slightly higher than what has been determined in this study (5,300 MJ/m^3 from Figure 5.3 versus 5,128 MJ/m^3 from Table 5.2) which suggests that the results reported here are conservative.

Table 5.2: Energy density comparisons

| Basic Parameters | Unit | STORAGE | | | | | | | | Reference FUEL (CNG) |
| | | Thermochemical | | Thermal | Electrochemical | | | Mechanical | | |
Technology Option		CaL+SSC	RES+SSC	Nest Egg Based on module weights	Tesla 1000 X Powerwall 2	VRFB [17,34]	NAS [17,34]	CAES [5,7]	PHS [5,7]	Standalone-OCGT
Input Power (charging phase)	MW	100	100	100	100	100	100	100	100	100
Output Power (discharging phase)	MW	36	32	20	90	90	90	30	40	35
Energy stored over 1 hour	MWh	96	82	100	100	100	100	100	100	100
Energy stored over 1 hour	MJ	345,600	295,200	360,000	360,000	360,000	360,000	360,000	360,000	360,000
Weight of storage medium	tonne	86	58	3,947	889	5,000	720	100,000	100,000	8
Bulk density as stored	kg/m3	1,282	1,227	1,556	1,034	1,134	850	1	1,000	456
Volume of storage material	m3	67	47	2,537	860	4,409	847	100,000,000	100,000	17.54
Energy Density Calcs per Unit Weight										
Gravimetric Energy density	kWh/ tonne	1,111	1,424	25	130	20	139	1	1.000	12,500
Gravimetric Energy density	MJ/kg	4.00	5.13	0.09	0.40	0.07	0.50	0.004	0.004	45.00
Recovered electricity density	kWh/ tonne	400	456	5	117	18	125	0.300	0.400	4,375
Ratio to reference fuel		9.1%	10.4%	0.1%	2.7%	0.4%	2.9%	0.007%	0.009%	100.0%
Energy Density Calcs per Unit Volume										
Volumetric Energy density	kWh/m3	1,424	1,747	39	116	23	118	0.0010	1.0	5,700
Volumetric Energy density	MJ/m3	5,128	6,288	142	419	82	425	0.0036	3.6	20,520
Recovered electricity density	kWh/m3	513	559	8	105	20	106	0.0003	0.40	1,995
Ratio to reference fuel		25.7%	28.0%	0.4%	5.2%	1.0%	5.3%	0.00002%	0.02%	100.0%
Storage Capacity Calcs										
Gravimetriv	MW/tonne	1.11	1.42	0.03	0.11	0.02	0.14	0.001	0.001	12.50
Volumetric	MW/m3	1.42	1.75	0.04	0.12	0.02	0.12	0.000001	0.001	5.70

1. Power for the Nest Egg system was estimated based on the maximum module temperature of 450 C

2. Power for the LNG system considers losses due to conversion to gas before the fuel is fed to a power generation unit

3. Mass of storage medium for LNG was calculated based on the lower heating value of 45 MJ/kg
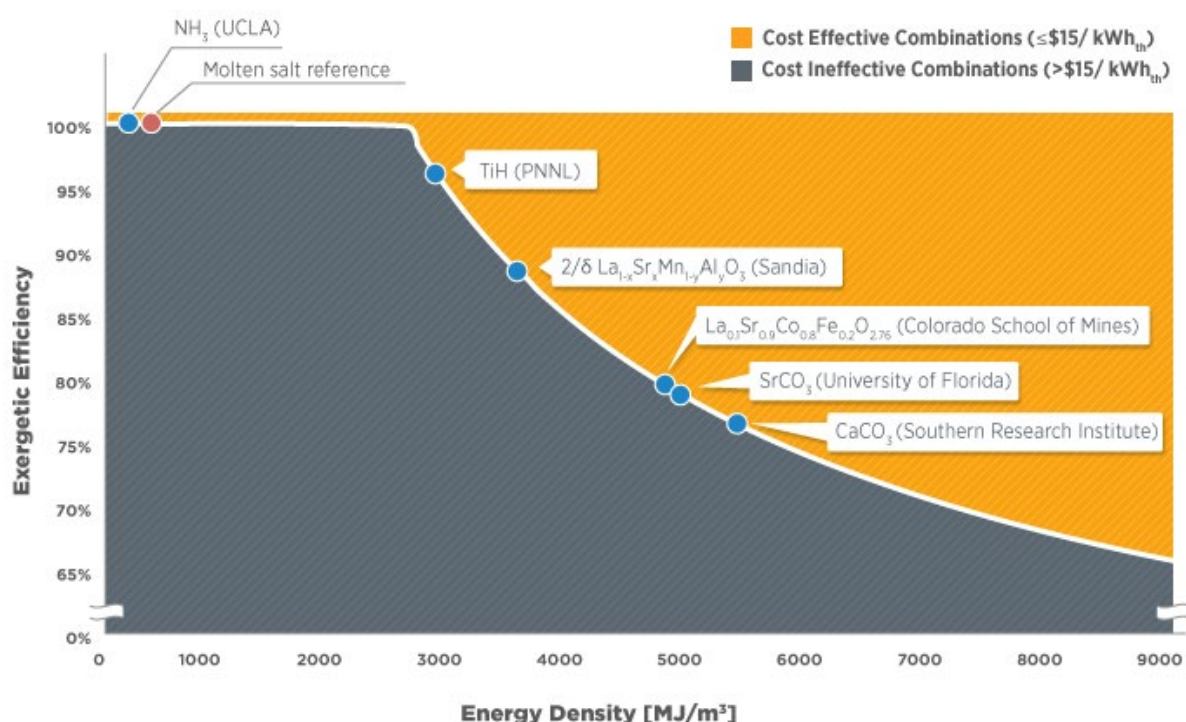
Figure 5.3: Volumetric energy density comparison for solar thermal energy storage [72].

5.2 DYNAMIC RESPONSE TO LOAD VARIATIONS

5.2.1 Overview

An in-depth knowledge of the dynamic responses is essential given that the proposed storage technologies are expected to deal with load variations. In this section the dynamic responses of the RES+SSC and CaL+SSC systems to load variations are examined. For this purpose, several scenarios were considered for both the off-peak and peak periods (details in Table 5.3). The calculations were carried out using the ASPEN$^+$ process simulation package. Although based on our previous experimental evidence, the response time for the variation was found to be ~1 min [44], the time step to study the system response to a disturbance or variable input was set to 15 min for the purpose of lowering the computational time without losing any accuracy (~1% over 8h period).

Table 5.3: Summary of scenarios considered in dynamic response analysis

Scenario	Technology Option	Operating Period	Variable Load Function
1a	CaL+SSC	Off-Peak	$100 \times \cos(2\pi \, / \, T \times t)$ (where T=32 hrs)
1b	CaL+SSC	Off-Peak	$100 - (6.6667 \times t)$
2a	RES+SSC	Off-Peak	$100 \times \cos(2\pi \, / \, T \times t)$ (where T=32 hrs)
2b	RES+SSC	Off-Peak	$100 - (6.6667 \times t)$
3a	CaL+SSC	Peak	$21 \times \left(1 + \sin\left(\frac{2\pi}{T} \times t\right)\right)(T = 8\,\text{hrs}), \quad 0 \leq t \leq 8\,\text{hrs}$
3b	CaL+SSC	Peak	$\begin{cases} 21 \times \left(1 + \sin\left(\frac{2\pi}{T} \times t\right)\right)(T = 8\,\text{hrs}) , 0 \leq t \leq 2\,\text{hrs} \\ 0 \hspace{3.5cm}, \, t > 2\,\text{hrs} \end{cases}$
4a	RES+SSC	Peak	$19 \times \left(1 + \sin\left(\frac{2\pi}{T} \times t\right)\right)(T = 8\,\text{hrs}), \quad 0 \leq t \leq 8\,\text{hrs}$
4b	RES+SSC	Peak	$\begin{cases} 19 \times \left(1 + \sin\left(\frac{2\pi}{T} \times t\right)\right)(T = 8\,\text{hrs}), \, 0 \leq t \leq 2\,\text{hrs} \\ 0 \hspace{3.5cm}, \, t > 2\,\text{hrs} \end{cases}$

5.2.2 Off-Peak Period Response to Variations in Input Power

So far all of the results provided cover cases in which the available power during the off-peak period was constant and equal to 100 Mwe. However, in reality the energy storage system can encounter power fluctuations which affect the level of storage that can be achieved. For the off-peak analysis, each technology option was subjected to two variable input powers as listed in Table 5.3. The first variable power input followed a "cosine" shape function, declining from 100 MW to 0 MW within 480 minutes. The second variable input followed a linear function, declining from 100 MW to 0 MW within 15 minutes.

It was found that both the RES and CaL systems could follow the variable input in a piecewise manner (resembling steps) with the length of each step being about 15 min which, as noted earlier, is the lag time required for a given particle to complete its reaction cycle. The results corresponding to CaL+SSC during the off-peak period are shown in Figures 5.4 and 5.5.
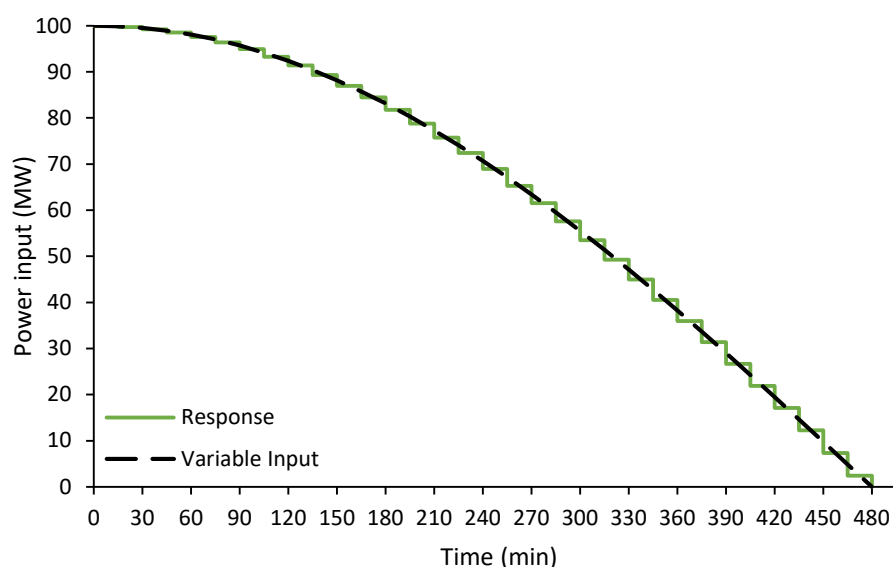
Figure 5.4: Dynamic response of CaL+SSC to the variable input power of Scenario 1a.
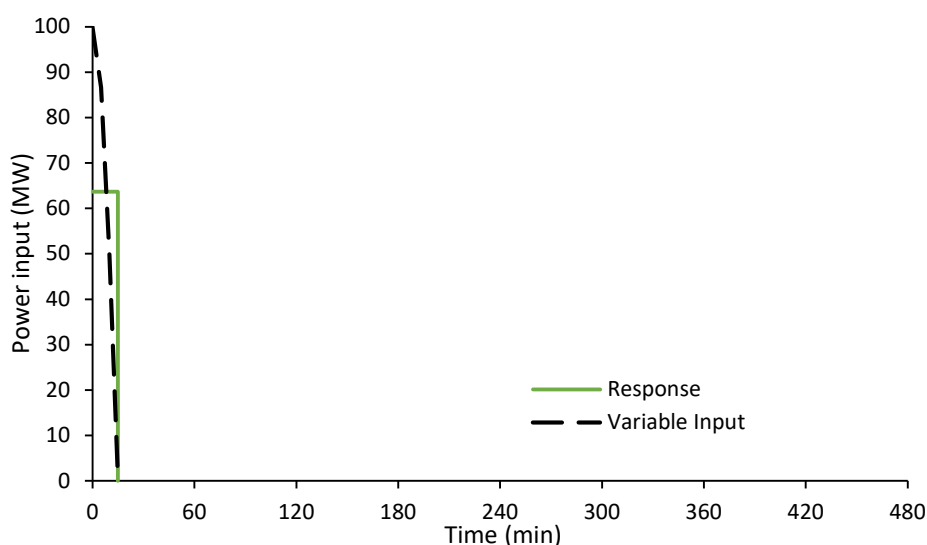
Figure 5.5: Dynamic response of CaL+SSC to the variable input power of Scenario 1b.

Figures 5.6 to 5.9 below also show the impacts of a declining variable input power on the storage capacity of the CaL system and its output capacity during peak periods. Figure 5.6 shows the cumulative calcined mass in the CaL system for Scenario 1a. It is evident that the maximum mass of the calcined particles at the end of the charging period was ~60% which implies that the system was not fully charged and, hence, a significant drop in the output should be expected during the discharging (peak) period. This can be clearly seen in Figure 5.7 where the average output power capacity drops to ~24Mwe, as opposed to the nominal figure of 36 MWh corresponding to the 100 Mwe constant input during the off-peak periods.

A very similar behaviour was exhibited in Scenario 1b where, as a result of the sharp drop in the input power over a 15 min period, only ~3% of the particle mass appears to be fully calcined by the end of the charging phase (see Figure 5.8). The corresponding decrease in the output power capacity is quite notable. As Figure 5.9 suggests, the average output power capacity for Scenario 1b corresponding to a variable input during the charging period is about 1Mwe, an almost 97% drop from the nominal figure of 36 MWh for the 100 Mwe constant input.
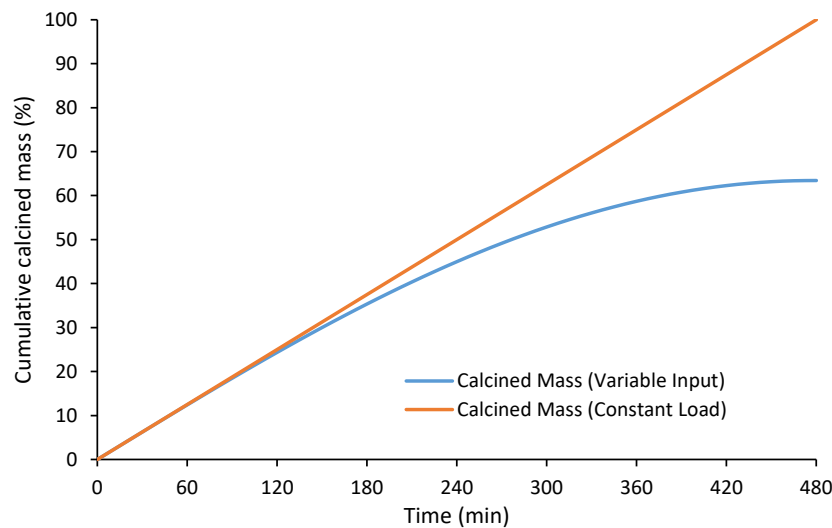
Figure 5.6: Impact of variable input power of Scenario 1a during the charging period on the mass of the calcined material for the CaL+SSC storage system during the same period.
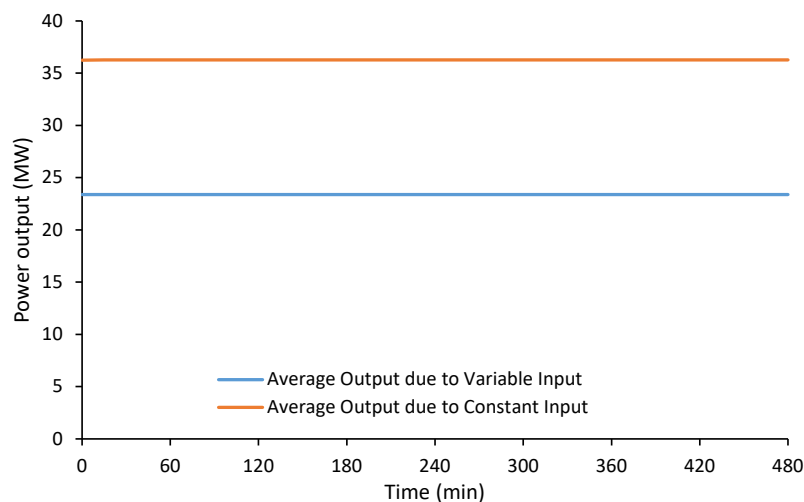
Figure 5.7: Impact of variable input power of Scenario 1a during the charging period on the average output power capacity of the CaL+SSC storage system during the discharging period.
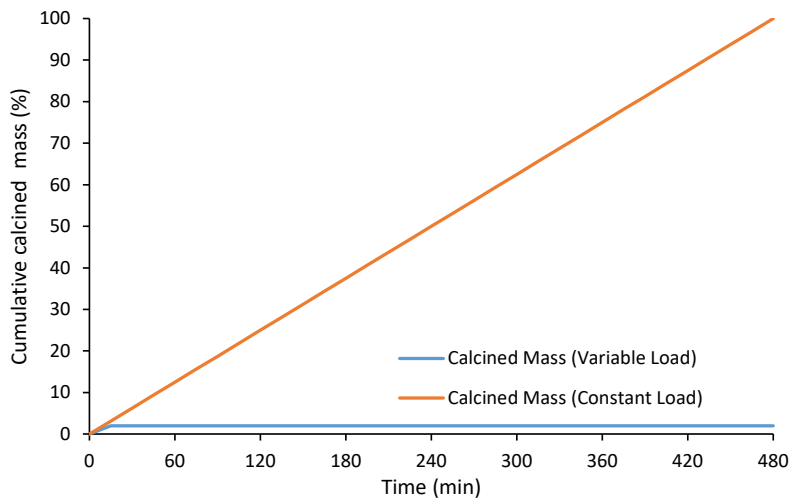
Figure 5.8: Impact of variable input power of Scenario 1b during the charging period on the mass of the calcined material for the CaL+SSC storage system during the same period.
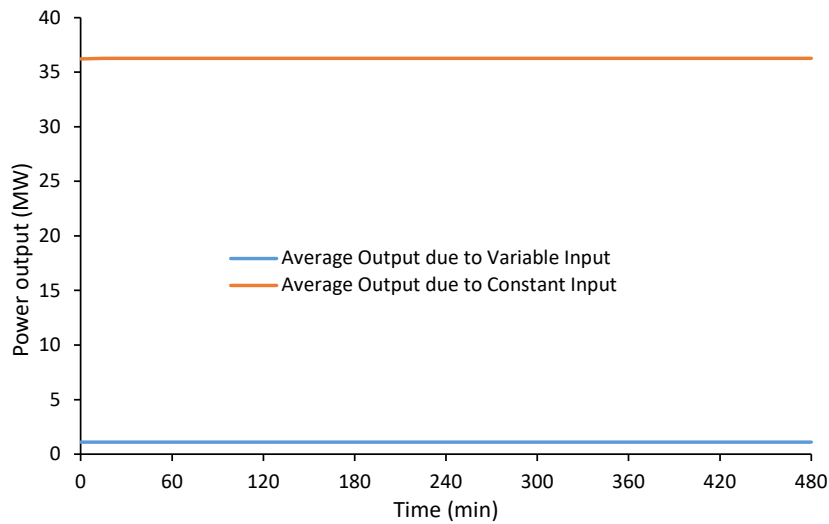
Figure 5.9: Impact of variable input power of Scenario 1b during the charging period on the average output power capacity of the CaL+SSC storage system during the discharging period.

Figures 5.10 to 5.13 below are analogues to Figures 5.6 to 5.9 and show the impacts of a declining variable input power on the storage capacity of the RES system and its output capacity during peak periods.

Figure 5.10, in particular, shows the average output power capacity corresponding to Scenario 2a, while Figure 5.11 illustrates that of Scenario 2b. As is evident for Scenario 2a (i.e., variable cosine shape input power), the average output power capacity of the RES+SSC system during the discharging phase was about 20 Mwe, which is roughly 4 Mwe lower than that of the CaL+SSC (Scenario 1a) reported earlier. The corresponding value for Scenario 2b (see Figure 5.11) was less than 1 Mwe.
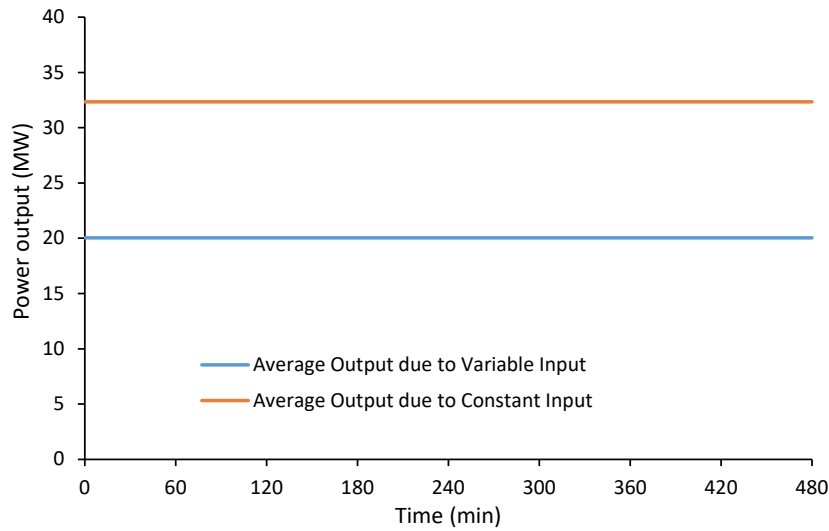
Figure 5.10: Impact of variable input power of Scenario 2a during the charging period on the average output power capacity of the RES+SSC storage system during the discharging period.
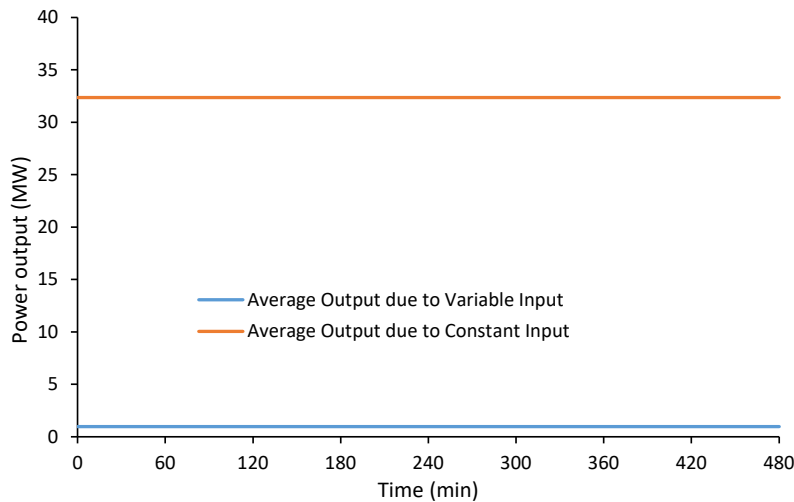
Figure 5.11: Impact of variable input power of Scenario 2b during the charging period on the average output power capacity of the RES+SSC storage system during the discharging period.

The amount of oxygen produced during the charging phase (off-peak period) was also affected by the variation of the input power. The cumulative values of the oxygen produced in Scenarios 2a and 2b are presented below in Figures 5.12 and 5.13, respectively. The amount of oxygen that can be potentially produced when a constant input power is applied was 180 kg/s for both scenarios. However, the cumulative amount of oxygen production due to a variable input was approximately 100 kg/s for Scenario 2a and less than 4 kg/s for Scenario 2b.
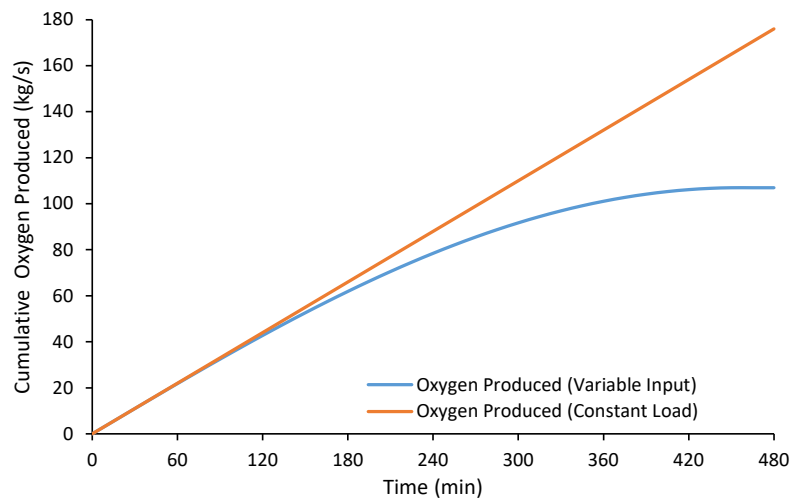
Figure 5.12: Impact of variable input power of Scenario 2a during the charging period on the oxygen production of the RES+SSC storage system during the charging period.
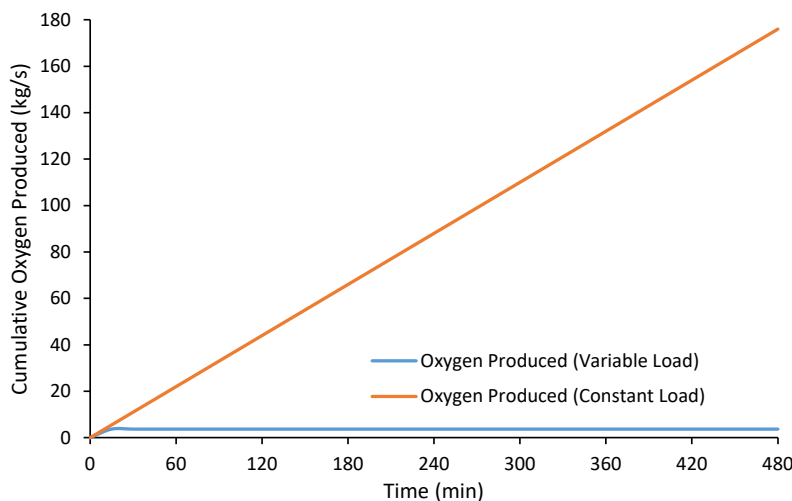
Figure 5.13: Impact of variable input power of Scenario 2b during the charging period on the oxygen production of the RES+SSC storage system during the charging period.

5.2.3 Peak Period Response to Load Variations

In the analysis associated with this section, the general assumption was that the storage system had been fully charged during the charging period (off-peak). Hence, for the CaL+SSC and RES+SSC systems under investigation, the available average output power capacities were 36 Mwe and 32 Mwe, respectively. However, as noted in Chapter 4 (Section 4.3.1), these power ratings were based on a plant capacity factor (CF_a) of 85% which implied that, if needed, the plant can ramp up to its 100% capacity to deliver the maximum power outputs of ~42 Mwe (CaL+SSC case) and ~38 Mwe (RES+SSC case). Two different "sine function" shape disturbances were considered in the analysis associated with the peak period responses (Scenarios 3a – 4b; Table 5.3). Process simulations were carried out to determine the impact of these disturbances on the output power capacity of the storage system.

The results have been summarised in Figures 5.14 and 5.15 below, where the responses of the CaL+SSC to the two disturbances are shown in Figures 5.14a and 5.14b while those of the

RES+SSC are presented in Figures 5.15(a) and (b). As can be seen, in all cases the energy storage unit can closely follow the variable load. Given the rate of chemical reactions involved, the responses were quite fast for both CaL and RES systems, and which allowed them to make the necessary corrections in time steps of no longer than 15 min. This is a major advantage over conventional gas-fired peaking plants, which typically need an hour or two to respond.
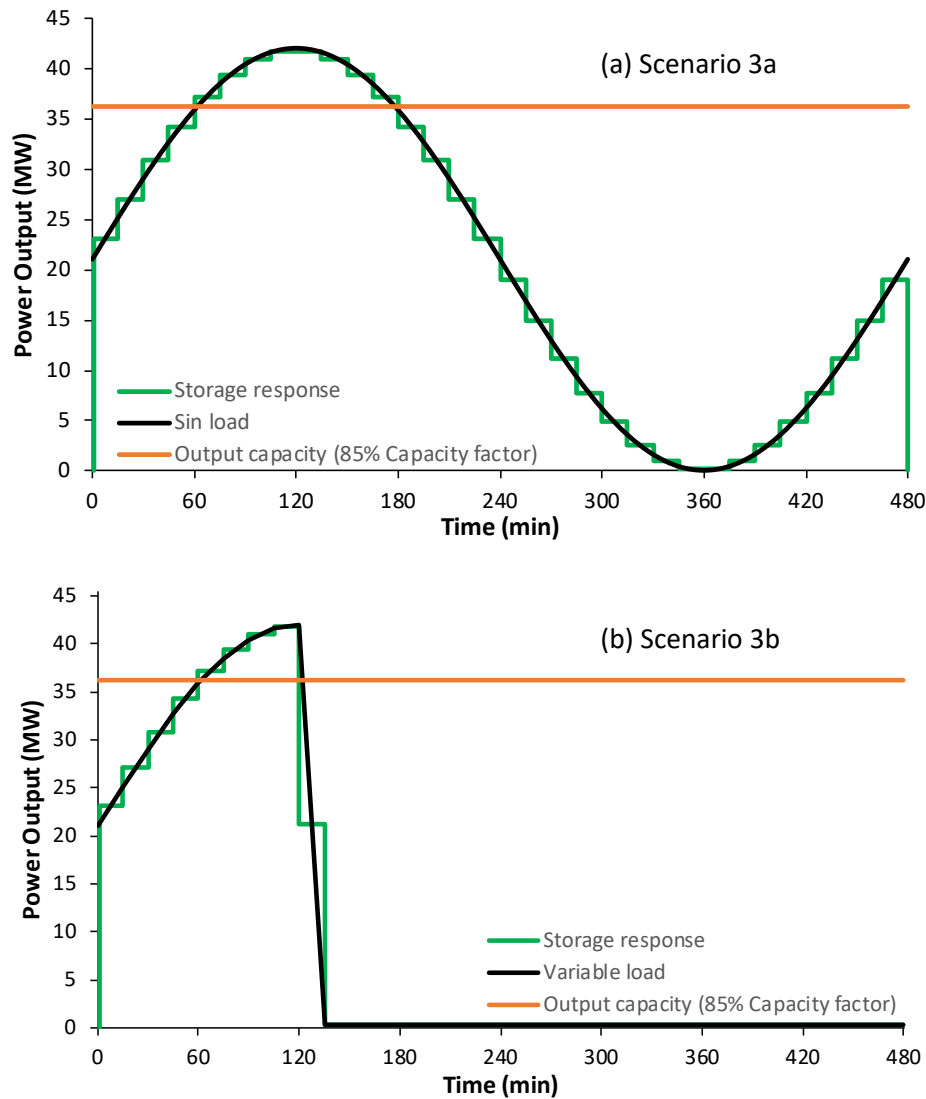
Figure 5.14: Responses of the CaL+SSC system to load variations during peak periods: (a) Scenario 3a, and (b) Scenario 3b.
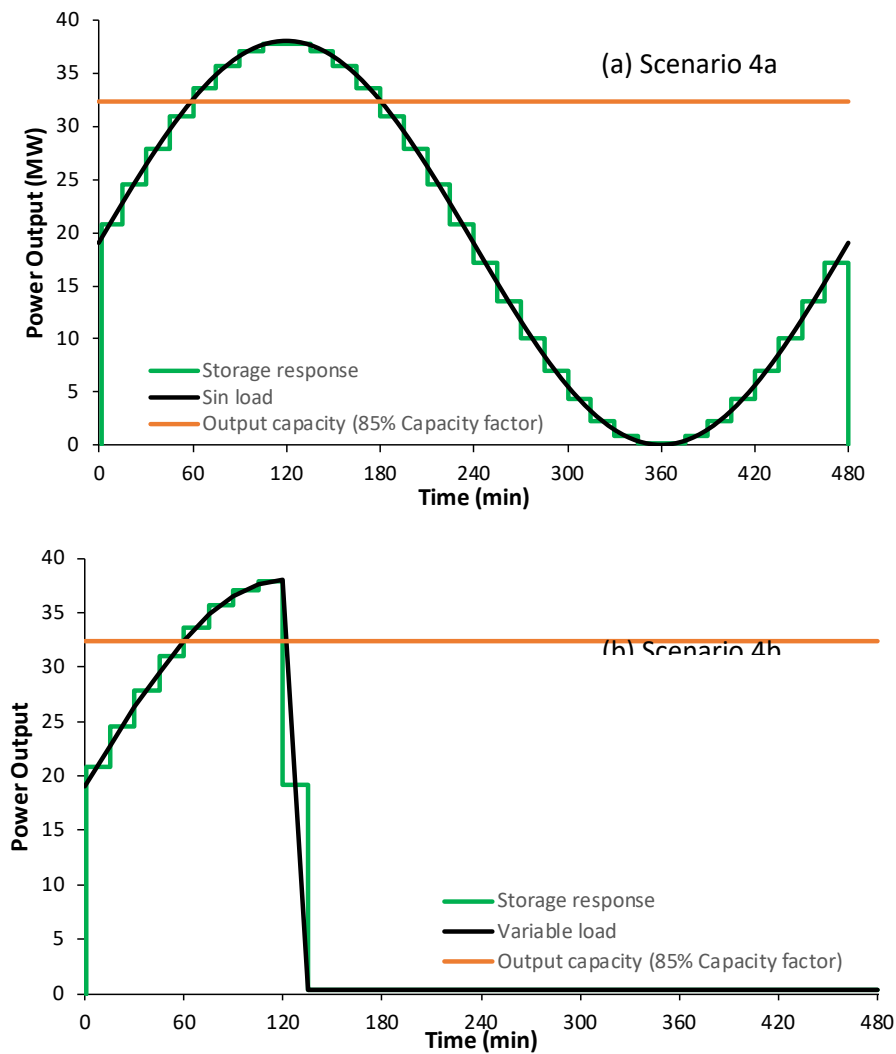
Figure 5.15: Responses of the RES+SSC system to load variations during peak periods: (a) Scenario 4a, and (b) Scenario 4b.

5.3 OXYGEN PRODUCTION

5.3.1 Overview

As discussed in the next chapter, the efficiency and cost of oxygen production is one of the key parameters influencing the economic viability of the redox based thermochemical energy systems under examination here. For this reason, it is vitally important to compare the oxygen production characteristics of these systems with those of conventional technology options (e.g., cryogenic, electrolysis, pressure swing adsorption or PSA, vacuum swing adsorption VSA) and emerging technology options (i.e., thermochemical water splitting or TCWS and ionic transport membrane or ITM) for tonnage production of oxygen. This can be achieved by benchmarking the "Specific Power (SP)" of each technology which takes into account all of the energy inputs and outputs during the production of oxygen.

5.3.2 Specific Power

The specific power (SP) is a measure of energy needed to produce a unit volume or weight of oxygen. Therefore, the specific power can be expressed on a volumetric (kWh/m^3) or gravimetric (GJ/tonne) basis, although the latter is used in this study.

The specific powers for the RES and cryogenic air separation (CAS) systems were calculated in this study using Eqs 5.7 and 5.8 below, respectively. The specific powers for the other technologies were extracted from the data reported in the open literature.

$$SP_{RES} = \frac{(Q_i\eta_i - Q_o\eta_o) + \sum W_{mech.}}{X_{O_2} \times F} \tag{5.7}$$

$$SP_{CAS} = \frac{\sum W_{mech.}}{X_{O_2} \times F} \tag{5.8}$$

where,

Q_i is the input heat duty for reduction (100,000 kWh)

η_i is the thermal efficiency of the primary cycle (~0.34)

Q_o is the output heat duty during oxidation (~76,000 kWh))

η_o is the thermal efficiency of the secondary cycle (0.42)

F is the flow rate of the oxygen stream before storage (~22 tonne/h)

X_{O_2} is the mass fraction of oxygen in the final stream or F (high purity 0.999992)

$W_{mech.}$ is the required mechanical work (~0.0 for RES)
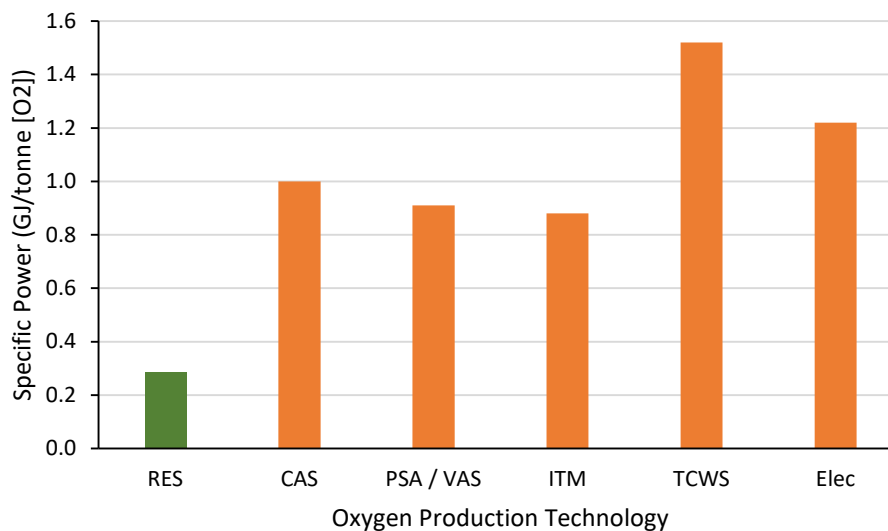
Figure 5.16: Specific power comparison. With the exception of the RES data, the other data points presented have been calculated based on the information in [73].

Figure 5.16 illustrates a comparison of the specific powers of several oxygen production technologies, including the RES system under investigation in this study. It is evident from this figure that the specific power, and thereby the energy footprint, of the RES technology for oxygen production is much lower than its counterparts. In particular, the specific power of RES, at 0.29 GJ/tonne, is 71% lower than that of CAS (at 1 GJ/tonne), which at present constitutes the bulk of air separation assets deployed around the world for the tonnage production of oxygen.

Chapter 6

Results and Discussion:
Techno-economic Assessments and LCA Analysis (Milestone 3)

6.1 LEVELISED COST OF ELECTRICITY

6.1.1 Total Fixed Capital Cost and Total Cost of Production

The total fixed capital cost (TFCC) and total cost of production (TCOP), apart from being important economic indicators, are also needed in other analyses, such as those associated with the levelised cost of electricity (LCOE) and the net present value (NPV). For this reason, the TFCC and TCOP are summarised here in a separate section. Both of these values were calculated for the proposed thermochemical energy storage options based on the methods explained in Chapter 4. In particular, the equipment cost (C_e) and the TFCC were estimated and used to calculate the cost ratio for each plant component for all of the thermochemical technology options under investigation here, as well as for the Standalone-OCGT system. The results are reported in Table 6.1 below. The values of the TFCC and TCOP have also been summarised in Table 6.2 below.

Table 6.1: List of the plant's components and their cost ratio [58-71]

Technology	List of Plant's Components / Equipment	Cost Ratio
Standalone-OCGT	Open Cycle Gas Turbine	62.35%
	Secondary fuel storage (only for the case where LNG is used)	37.65%
RES+OCGT	Open Cycle Gas Turbine	6.80%
	Secondary fuel storage (only for the case where LNG is used)	2.80%
	OCGT heat exchangers	2.02%
	Fluidised bed reactor + Cyclones +Blowers	18.50%
	Oxygen production and storage equipment	63.68%
	Solid silo for make-up stream	0.04%
	Initial solids purchased	6.16%
CaL+OCGT	Open Cycle Gas Turbine	21.18%
	Secondary fuel storage (only for the case where LNG is used)	8.13%
	OCGT heat exchangers	11.10%
	Fluidised bed reactor + Cyclones +Blowers	58.80%
	Solid silo for make-up stream	0.48%
	Initial solids purchased	0.31%

	Supercritical Steam Turbine	4.60%
	Fluidised bed reactor + Cyclones +Blowers	20.00%
RES+SSC	Oxygen production and storage equipment	68.70%
	Solid silo for make-up stream	0.05%
	Initial solids purchased	6.65%
	Supercritical Steam Turbine	18.40%
	Fluidised bed reactor + Cyclones +Blowers	80.50%
CaL+SSC	Solid silo for make-up stream	0.66%
	Initial solids purchased	0.44%

Table 6.2: TFCC and TCOP energy storage options under investigation

Technology	Key Technical Specification		Economic Indicator[*]	
Standalone-OCGT	Power output (MW)	35.00	TFCC (Million A$)	CNG: 28
				LNG: 45
	Secondary fuel (kg/s)	2.22		
	Oxygen production (kg/s)	0.00	TCOP (Million A$/yr)	CNG: 24 LNG: 267
RES+OCGT	Power output (MW)	35.10	TFCC (Million A$)	CNG:398
				LNG: 410
	Secondary fuel (kg/s)	1.07		
	Oxygen production (kg/s)	6.12	TCOP (Million A$/yr)	CNG: 157
				LNG: 159
CaL+OCGT	Power output (MW)	35.00	TFCC (Million A$)	CNG:120
				LNG:131
	Secondary fuel (kg/s)	1.23		
	Oxygen production (kg/s)	0.00	TCOP (Million A$/yr)	CNG:36
				LNG: 38
RES+SSC	Power output (MW)	32.4	TFCC (Million A$)	380
	Secondary fuel (kg/s)	0.00	TCOP (Million A$/yr)	146
	Oxygen production (kg/s)	6.12		
CaL+SSC	Power output (MW)	36.3	TFCC (Million A$)	95
	Secondary fuel (kg/s)	0.00	TCOP (Million A$/yr)	24
	Oxygen production (kg/s)	0.00		

[*]*TFCC and TCOP were different based on the type of secondary fuel used (i.e., CNG or LNG).*

6.1.2 LCOE Calculations and Comparisons

Table 6.3 below shows the results of the LCOE analysis for the selected thermochemical energy storage options, as well as that of the Standalone-OCGT system, with and without a price on carbon. Please note that in cases such as the RES+SSC and CaL+SSC, where no secondary fuel (e.g., CNG or LNG) is consumed, there is no CO_2 emissions, and hence the LCOE with or without a price on carbon would be the same. A broader comparison with other energy storage technologies is presented in Figures 6.1 to 6.4.

The LCOEs of the energy storage options are reported in Table 6.3 below. Please note that, based on the type of secondary fuel consumed by the OCGT, a range for the LCOE is reported. The lower and higher bounds in each row in Table 6.3 correspond to the CNG and LNG fuel, repetively. The results presented in Table 6.3 indicate that the LCOE for the Standalone-OCGT (as the refrerence case) was $275-305/MWh. The LCOE for the CaL+SSC configuration was lower than the reference case by 25-32% (about $207/MWh). However, the LCOE in the CaL+OCGT configuration was higher than the reference by 26-28% ($363-380/MWh or $369-385/MWh based on the type of secondary fuel and including the carbon tax or not). Compared to the reference peaker plant (Standalone-OCGT), the two RES based configurations (RES+OCGT and RES+SSC) resulted in much higher LCOEs if oxygen is vented as a byproduct. However, if the high purity oxygen product is stored and sold, even at a modest wholesale price of $15/m^3 (note the wholesale price of high purity oxygen can be as high as $67/m^3), the corresponding LCOEs were significantly lower than that of the reference peaker plant. In the case of the RES+OCGT configuration, the LCOE could be as low as $75/MWh, which is a reduction of approximately 70%, while for the RES+SSC configuration, the LCOE dropped by a staggering 97%, to a figure of about $8/MWh.

The overall conclusion is that both the redox based (specifically RES+SSC) and the calcination/carbonation based (specifically CaL+SSC) thermochemical energy storage concepts have a competitive edge over conventional technologies for variable load management. Both concepts can be employed for bulk energy storage and are quite suited to utility-scale applications. This would make both concepts ideal candidates for load levelling and time-shifting functions in the context of coal-fired power generation. The same features can be also of significant value for storing energy from intermittent sources such as wind and solar.

Table 6.3: LCOE energy storage options under investigation

Technology	Economic Indicator	A$/MWh
Standalone- OCGT	LCOE (A$/MWh) - no price on carbon	263-293
	LCOE (A$/MWh) - with a price on carbon	275-305
RES+OCGT	LCOE (A$/MWh) - no price on carbon	795-813
	LCOE (A$/MWh) - with a price on carbon	803-821
	LCOE (A$/MWh) - no price on carbon & O_2 revenue	75-93
	LCOE (A$/MWh) - with a price on carbon & O_2 revenue	83-101
CaL+OCGT	LCOE (A$/MWh) - no price on carbon	363-380
	LCOE (A$/MWh) - with a price on carbon	369-385
RES+SSC	LCOE (A$/MWh) - no price on carbon	728
	LCOE (A$/MWh) - with a price on carbon	728

	LCOE (A$/MWh) - no price on carbon & O_2 revenue	8
	LCOE (A$/MWh) - with a price on carbon & O_2 revenue	8
CaL+SSC	LCOE (A$/MWh) - no price on carbon	207
	LCOE (A$/MWh) - with a price on carbon	207

Figure 6.1 below compares the LCOEs of the different energy storage technologies, including the selected thermochemical concepts promoted in this study. It can be seen that the LCOE of the RES option with an oxygen revenue can easily compete with PHS, which at present is the dominant technology option for utility-scale energy storage. In addition, the LCOEs for the CaL and PHS showed similar minimum costs. However, the choice of OCGT as a power unit can make CaL technology more expensive than PHS. The information demonstrated in Figures 6.1 to 6.4 below are chosen amongst the technologies which are capable of storing at least 1 MWh [74-94].
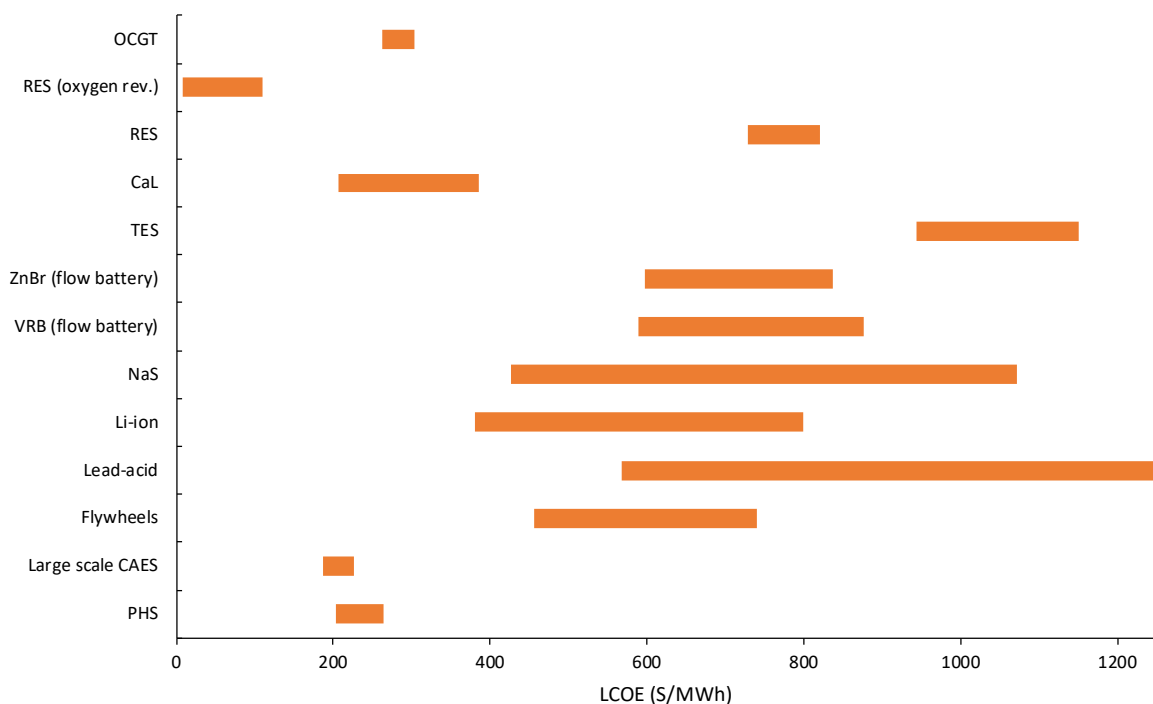
Figure 6.1: A comparison of the LCOEs of various energy storage technologies [64-65, 74-94].

Figure 6.2 below depicts the energy capital costs of the various energy storage technologies, which is essentially the capital cost over the total energy produced in a given year (the ratio of TFCC to the total plant's annual kWh). It can be seen that all of the thermochemical energy storage technologies under investigation here, as well as thermal storage systems, have very low capital energy costs compared to their counterparts. The mechanical energy storage based systems are the second cheapest option, while the most expensive options are the electrical and electrochemical energy storage technologies.
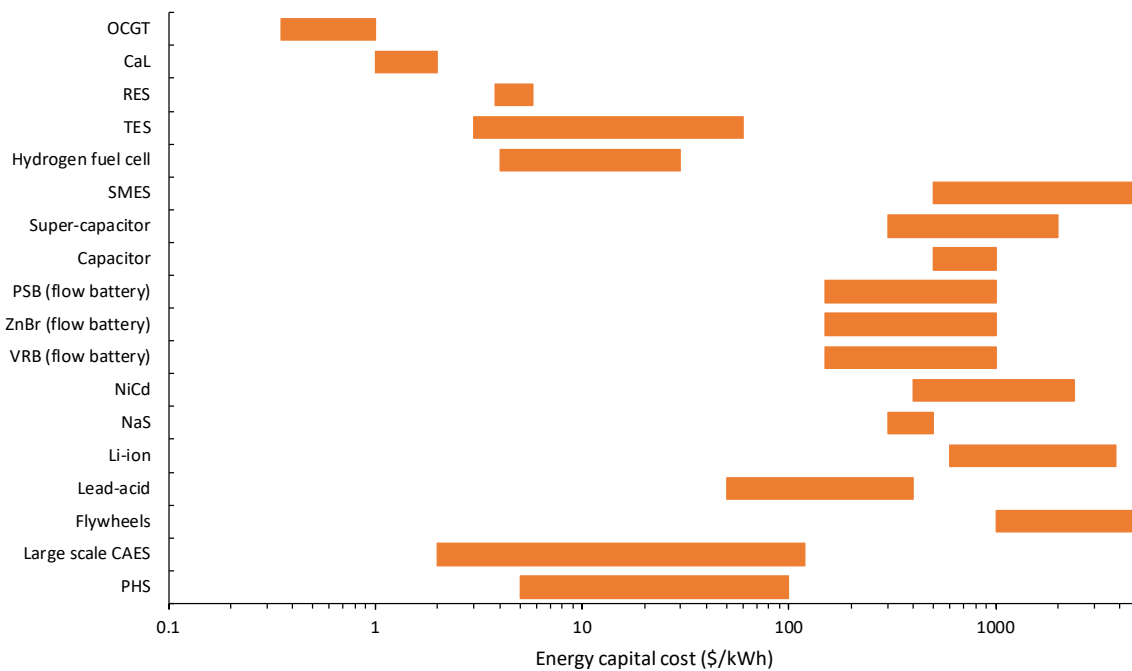
Figure 6.2: Energy capital costs of the various energy storage technologies. Log-scale is used for a better representation [64-65, 74-87].

Figure 6.3 below presents the power capital costs of the different technologies (the ratio of the TFCC to the plant's capacity in kW). Given that the revenue stream from the oxygen sale in the RES option cannot be included in the power capital cost calculations, the RES showed the highest power capital cost.
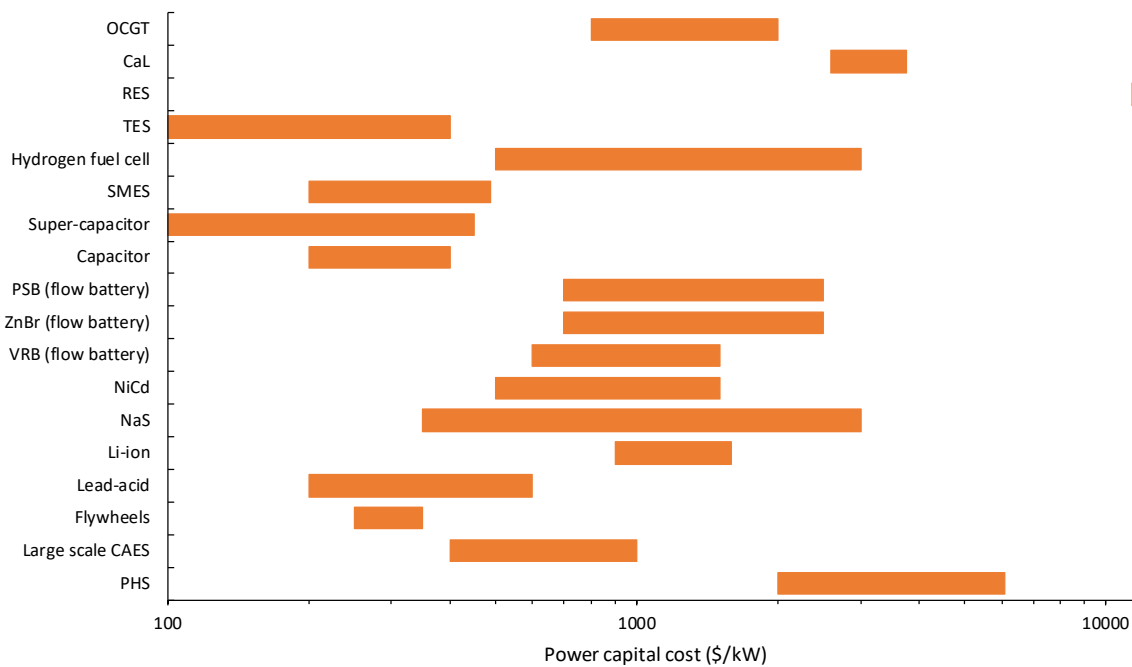
Figure 6.3: Power capital costs of the various energy storage technologies. Log-scale is used for a better representation [64-65, 74-87].
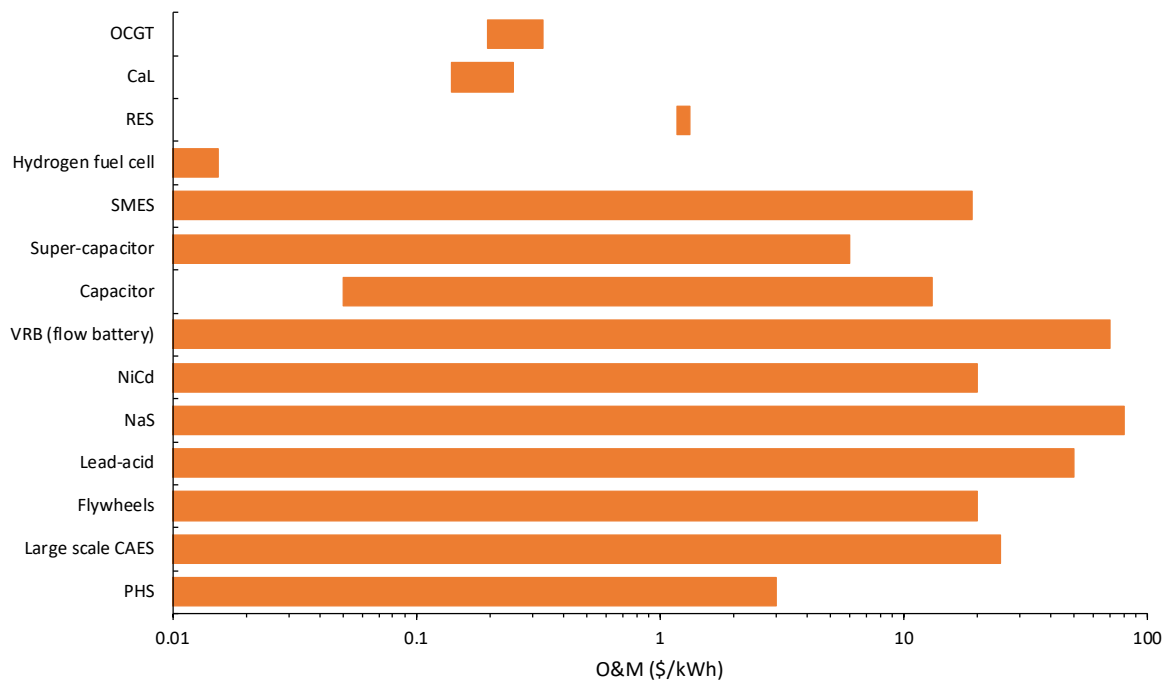
Figure 6.4: O & M costs of the various energy storage technologies. Log-scale is used for a better representation [64-65, 74-87].

Figure 6.4 compares the operation and maintenance costs of the various energy storage technologies (the ratio of O & M to the total of the plant's annual kWh). It is evident that the operation and maintenance costs of the thermochemical methods are very low. The highest operation and maintenance costs were related to the electrochemical technologies. The second most expensive group was the electrical energy storage systems, followed by the mechanical storage technologies, primarily due to undesired losses due to friction and heat transport.

6.2 NET PRESENT VALUE (NPV) AND RELATED ANALYSES

6.2.1 NPV Calculations and Comparisons

Figures 6.5 and 6.6 below present the NPVs of the CaL and RES based technologies, respectively. As shown in Figure 6.5, the NPVs of the CaL+OCGT(CNG) and CaL+OCGT(LNG) configurations were always lower than those of the Standalone-OCGT and CaL+SSC configurations. Therefore, the CaL+OCGT configurations do not represent the best investment opportunities.

In the case of the CaL+SSC configuration, its NPV showed values below those of the Standalone-OCGT in the first 15 years of the plant life, primarily due to higher capital costs. However, from year 15, the CaL+SSC configuration rapidly overtakes the Standalone-OCGT configuration and reaches higher positive values. By the end of the plant's life (25 years) the CaL+SSC technology reached its maximum NPV figure of about $78M.
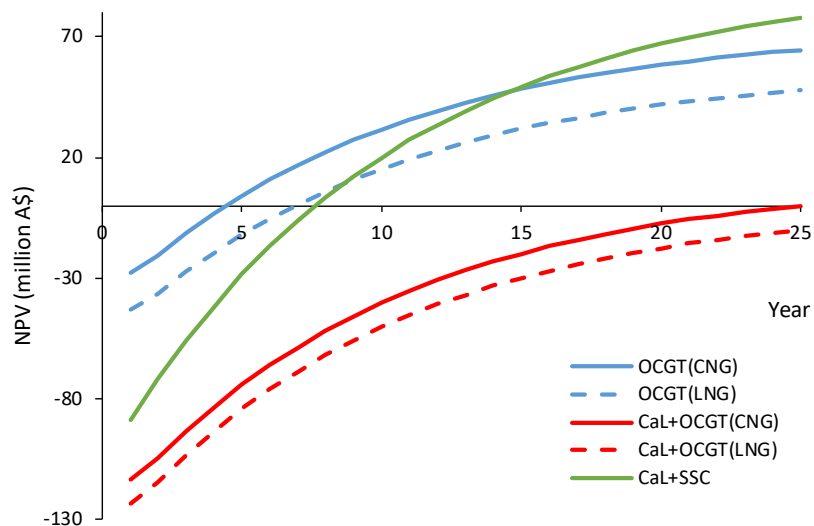
Figure 6.5: NPV plots of the CaL based energy storage technologies and the Standalone-OCGT.
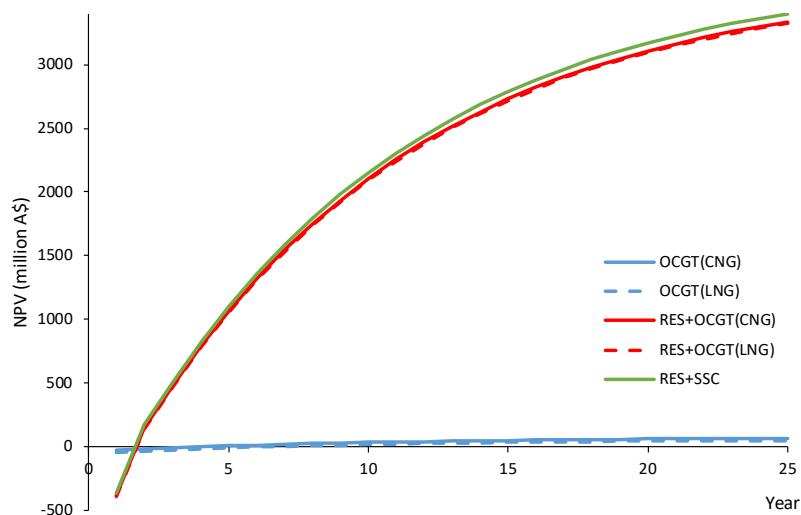
Figure 6.6: NPV plots of the RES based energy storage technologies and the Standalone-OCGT.

According to Figure 6.6, the RES based energy storage technologies are the most profitable projects as their NPV grows very rapidly and becomes positive within the second year of the plant's life. The NPV for the RES+SSC case was slightly higher than those of the RES+OCGT(CNG) or RES+OCGT(LNG) options. This was mainly due to cost of the fuel (CNG or LNG) required in the OCGT power block configuration, while the SSC version does not rely on any secondary fuel.

6.2.2 CF, IRR and SPP Results

A number of NPV related economic indicators, such as the average cash flow (CF), internal rate of return (IRR) and simple payback period (SPP), were also calculated for both the CaL and RES based thermochemical energy storage technologies. Table 6.4 below summarises the results and reports on the CF, IRR and SPP for each technology option.

It is evident from this table that the maximum value of the average CF corresponded to the RES+SSC configuration, while the minimum value was associated with the Standalone-OCGT technology.

As far as the SPP is concerned, the RES based technologies posted the minimum figures, primarily due to their oxygen sale revenue streams.

The IRR results confirmed the above findings and indicated again that the RES based technologies are the most profitable options among those considered in this study. However, given the high capital costs of the RES options (for example, see Figure 6.3) their economic feasibility might be somewhat doubtful. The next best option, from both an economic and technical perspective, appears to be the CaL+SSC system, with IRR figures similar to the reference Standalone-OCGT option and a capital cost which is a fraction of the RES capital cost (only 23% of the RES capital cost).

Table 6.4: Average CF, SPP and IRR for the various thermochemical energy storage options

Economic Indicator	Technology							
	Standalone- OCGT (CNG)	Standalone- OCGT (LNG)	RES+OCGT (CNG)	RES+OCGT (LNG)	RES+SSC	CaL+OCGT (CNG)	CaL+OCGT (LNG)	CaL+SSC
Average cash flow (Million $/yr)	12.1	11.9	622.3	622.3	630.1	19.8	19.8	28.7
Simple pay-back period (yrs)	2.5	4.0	0.7	0.7	0.6	6.3	6.9	3.4
IRR (10 yrs)	34.1%	19%	133.7%	129.7%	142.8%	0.9%	-	16.1%
IRR (15 yrs)	36.3%	22%	133.7%	129.8%	142.9%	7.3%	5.9%	20.1%
IRR (20 yrs)	36.7%	23%	133.7%	129.8%	142.9%	9.6%	8.4%	21.2%

6.3 LCA ANALYSIS

6.3.1 A-LCA Analysis Results

Figures 6.7 and 6.8 summarise the results of A-LCA analyses for CaL+SSC system and the Li-ion battery, respectively. The pie charts presented in these figures for each environmental impact indicator pictorially illustrate the contribution of components and or services essential to energy storage system to the overall impact. As shown in Figure 6.7, the components considered / services considered for the CaL+SSC system were the CaL+SSC unit itself, services, thermal management, civil works, generator, turbine and steel structure. Similarly, the components considered for the Li-ion battery were the battery package itself, services, thermal management, civil works, transformer, inverter and steel structure.

As can be seen, for both CaL+SSC and Li-ion battery the largest contributor to the impact indicators is the storage unit itself primarily due to the impact of raw materials and production phases. The second and third largest contributors to the impact indicators for CaL+SSC are the thermal management and the turbine components while the transformer and inverter are the second and third largest contributors in the case of Li-ion battery.

Interestingly, the trends and percentage contributions of the above components appear to be very similar for both CaL+SSC and the Li-ion battery, but their gross total figures are different. Most noticeably is the amount of CO_2 emissions per MWh which is almost one third of that for the Li-ion battery. As noted earlier, this is largely the artefact of the higher energy density of the CaL+SSC system compared with a Li-ion battery. With the exception of particulate matter and freshwater eutrophication categories, the impact indicators for CaL+SSC are generally lower than corresponding values for the Li-ion battery, indicating that CaL based systems have much more limited environmental impacts compared with Li-ion type battery systems.
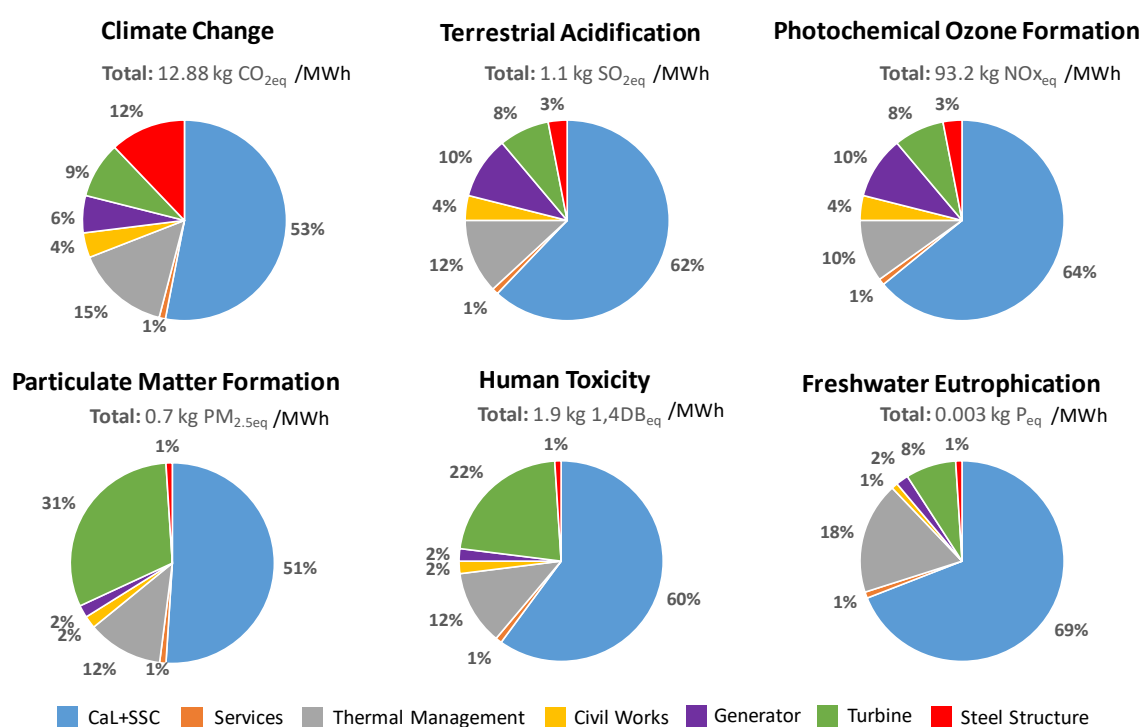
Figure 6.7: Results of the A-LCA analyses for CaL+SSC system.
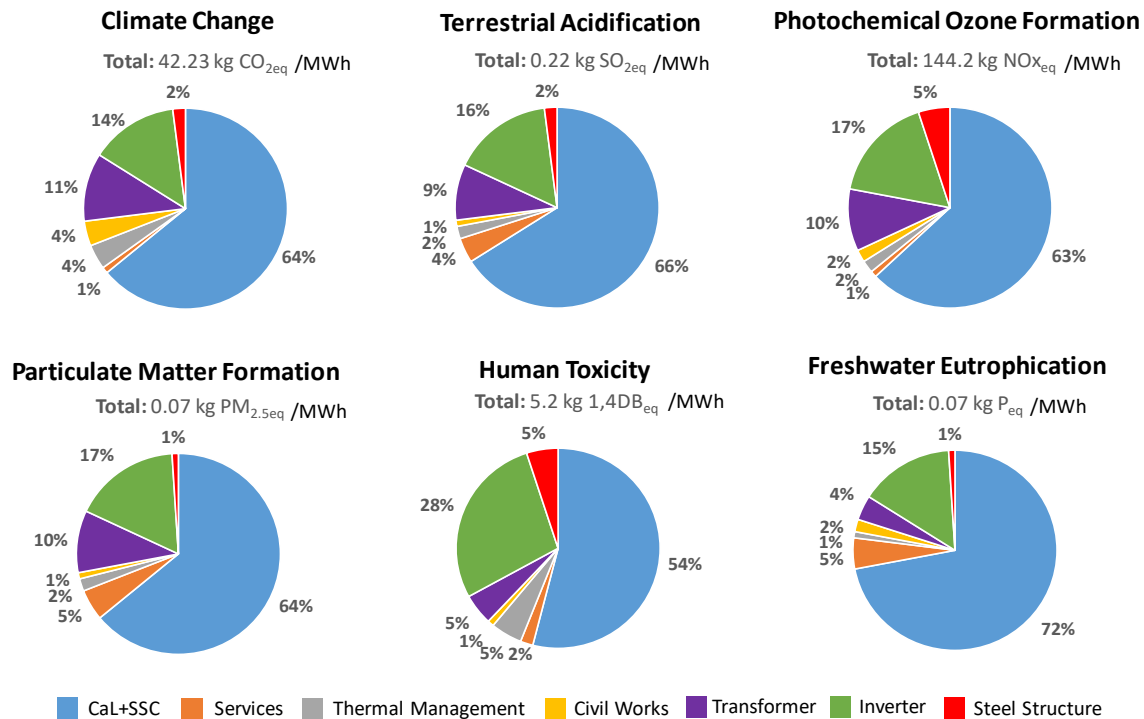
Figure 6.8: Results of the A-LCA analyses for Li-ion battery.

The environmental impacts of the two energy storage systems and a CNG based power unit obtained from the A-LCA analyses were also compared and bench-marked against a reference coal. The results have been summarised below in Table 6.5.

Table 6.5: Environmental impacts of power generation and energy storage options

Impact Indicator	Coal (Ref)	Natural Gas or CNG	CaL+SSC	Li-ion Battery	%Change with Respect to Coal		
					Natral Gas or CNG	CaL+SSC	Li-ion Battery
Climate Change (kg CO_{2eq} / MWh)	1150	721	12.88	42.23	-37%	-99%	-96%
Terrestrial Acidification (kg SO_{2eq} / MWh)	5.2	5.93	1.1	0.22	14%	-79%	-96%
Photochemical Ozone Formation (kg NO_{xeq} / MWh)	2580	2350	93.2	144.2	-9%	-96%	-94%
Particulate Matter Formation (kg $PM2.5_{eq}$ / MWh)	1.8	1.69	0.7	0.07	-6%	-61%	-96%
Human Toxicity (kg $1,4\text{-}Db_{eq}$ / MWh)	4.4	4.63	1.9	5.2	5%	-57%	18%
Freshwater Eutrophication (kg P_{eq} / MWh)	0.0067	0.00554	0.003	0.07	-17%	-55%	945%

Evidently, there is a substantial decrease in the environmental impact of using CaL based energy storage in all impact categories. Li-ion shows a substantial decrease only in 4 out of the 6 impact categories examined here. In particular, compared with the reference coal the Li-ion battery appears to have a much larger impact in the freshwater eutrophication impact category (phosphorous emissions). In contrast, the CaL+SSc system shows 55% reduction in this category, yet again highlighting the environmental benefits of employing a CaL based energy storage system.

6.3.2 C-LCA Analysis Results

As noted in Chapter 4, the basis of C-LCA analyses presented in this study is a projection of the energy mix of NSW in 2030. Figure 6.9 presents a comparison of the NSW's energy mix in 2018 and the projected mix in 2030. The data employed to plot Figure 6.9 were obtained from an independent modelling of the NSW electricity sector by the Climate Change Institute assuming a "Strong Carbon Price" scenario. As this figure indicates, NSW will observe strong growth in large solar and wind energy sources. But perhaps, the strongest growth will be in natural gas which in conjunction with renewables displace significant coal-fired generation capacity. This lowers the NSW reliance on coal from the current figure of 85% to about 46% (almost 50% reduction).
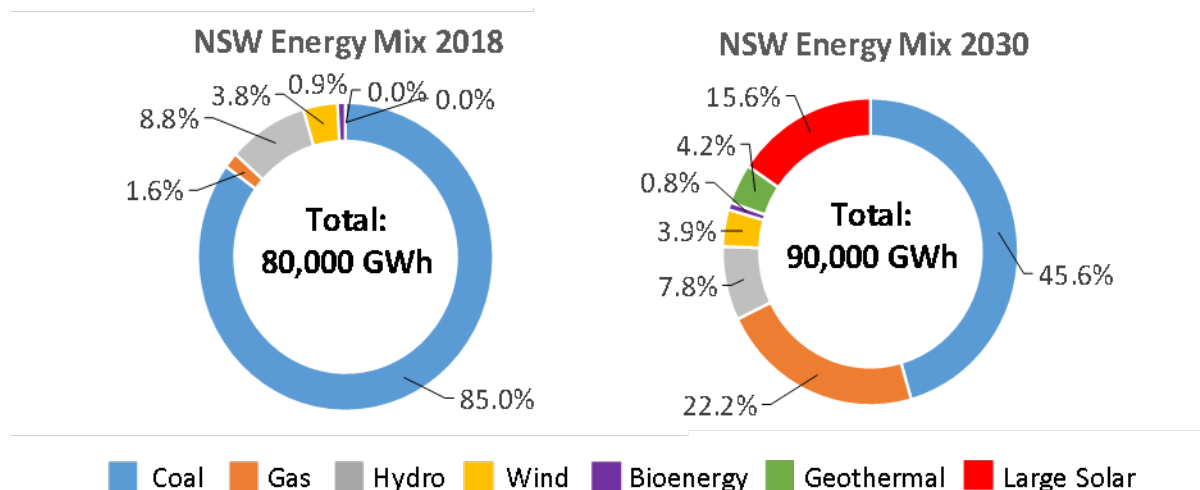
Figure 6.9: The energy mix of NSW (installed capacity in GWh) in 2018 and 2030.

The above projection, however, does not consider any utility-scale energy storage in the NSW energy mix of the future. For this reason, the project team collected data from various sources in order to determine the scale of opportunity for large-scale energy storage in NSW. As part of this exercise the team particularly investigated the projected spare capacity and over-generation of the electricity sector in NSW.

Based on this investigation, the team has determined that in 2030 between 7% and 15% of the State's electricity demand can be met by the utility-scale energy storage. Given the above range, the team selected a figure of 11% (~10,000 GWh) as a reasonable base / opportunity for energy storage in 2030.

Figure 6.10 shows the adjusted NSW energy mix of 2030 which now also incorporates the energy storage. In adjusting the projected energy mix of NSW, the underlying assumption by the project team was that the utility-scale energy storage will only displace coal-fired generation capacity. This is achieved by minimising / eliminating the over-generation of existing coal-fired assets during the off-peak period, in turn, allowing the relevant plants to continuously operate at base-load. This not only will resolve many of the maintenance issues associated with ramping the coal-fired plants up and down, but also represents a much more efficient use of coal which is a valuable energy resource.

As a result of the above assumption, the share of coal-fired generation in 2030 decreases from the projected figure of 46% to about 34% (Figure 6.10), which is good news for the environment.
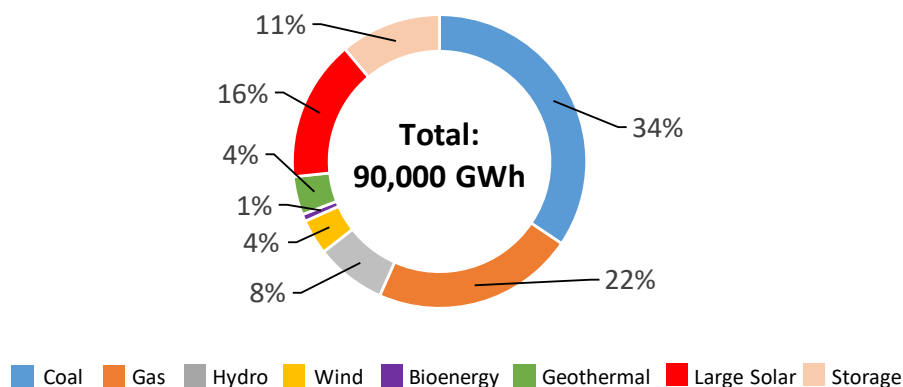
Figure 6.10: The energy mix of NSW in 2030 adjusted for utility-scale energy storage.

The cumulative environmental impacts of the energy storage were determined using the BUA and USES scenarios and the relevant C-LCA analyses were carried out for all 6 environmental impact categories. The cumulative environmental impact results for both scenarios are given in Figure 6.11. The results show similar trends to those observed earlier in the A-LCA analysis. More specifically, the CaL+SSC lower the environmental impact in all six impact categories whereas Li-ion exacerbates the impact in human toxicity and freshwater eutrophication.
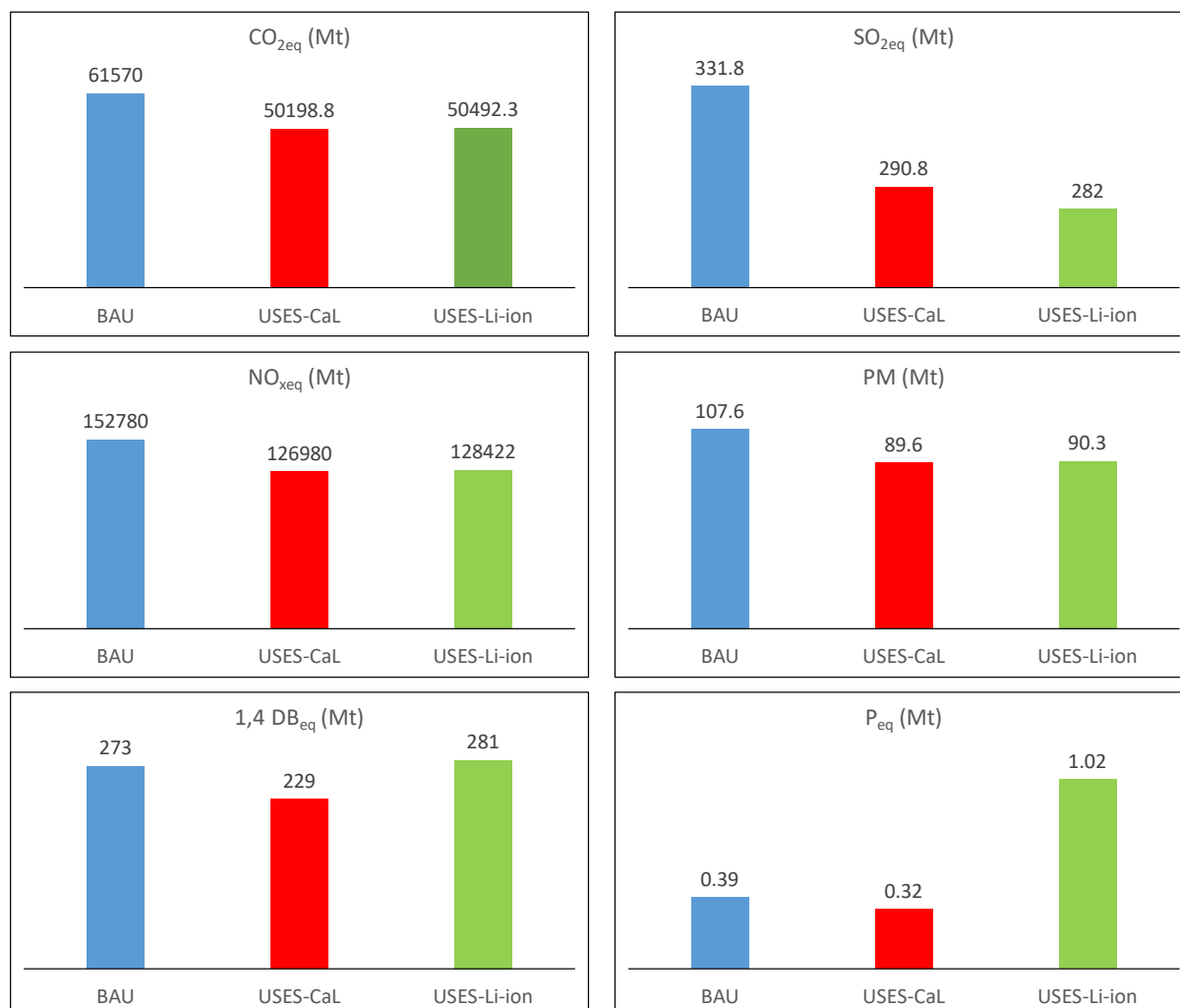
Figure 6.11: Cumulative impact of energy storage in NSW by 2030.

Chapter 7

Results and Discussion: Experimental Studies (Milestones 4-6)

7.1 REACTIVITY AND MATERIAL STUDY (Milestone 4)

The viability of using the reversible conversion of CaO to $CaCO_3$ in calcium looping (CaL) or Cu_2O to CuO in redox energy storage (RES) was investigated in Chapters 3 and 5 through a comprehensive series of thermodynamic analyses using the process simulation package ASPEN$^+$. However, this thermodynamic analysis assumes equilibrium conditions, whereas in practical systems the reactions are usually underpinned by reactivity because the time-scales involved do not allow the reactions to proceed to full equilibrium conditions. The most important consequence of this is that the reactors must be sized and designed based on the reactivity and material study data. Another important piece of information that should be considered is the potential decline in the reactivity of the particles after multiple cyclings. The reactivity study essentially provided insights into how the reaction starts, propagates and ends, and also quantified the impacts of key parameters such as the temperature, size of inventory and gas flow rate.

The experimental methods and techniques which were used to study the reactivity properties have been summarised in Table 7.1 below. Over 300 samples were analysed by thermal gravimetric analysis/differential scanning calorimetry (TGA/DSC), scanning electron microscopy (SEM), X-ray diffraction (XRD) and energy dispersive X-ray spectroscopy (EDS) techniques (see Table 7.1). These samples were taken from more than 100 reactions/ reaction pathways experiments which were carried out using bench-scale fixed and fluidised bed setups connected to a gas analyser (see Table 7.1).

Table 7.1: Analytical techniques and methods that were used to study the reaction kinetics of the particles

Material	TGA/DSC	SEM	XRD	EDS
CuO/Cu_2O	✓	✓	✓	✗
$CaO/CaCO_3$	✓	✓	✓	✓

7.1.1 TGA, SEM, XRD and EDS Results

The theoretical equilibrium temperatures for the CuO/Cu_2O and $CaO/CaCO_3$ systems is shown in Figures 7.1(a) and (b), respectively. To demonstrate the effects of temperature on the equilibrium curves for copper-rich and calcium-rich particles, the X-axes in both Figures 7.1(a) and (b) extend to 350 °C. It is evident from Figure 7.1(a) that the equilibrium partial pressure of the gas remained close to zero for more than half of the temperature span. However, for the calcium-rich particles, the temperature span for which the equilibrium partial pressure is small, was shorter (about one-third of the copper-rich particles). Hence, the dependency of the copper-rich-particles reactivity (the partial pressure of oxygen) on the reaction temperature was smaller compared to the dependency of the calcium-rich particles.

According to Figure 7.1(a), to reduce the copper-rich particles in the normal atmosphere (21% O_2), the temperature should be above 1024 °C. However, if another gas (e.g., pure steam or nitrogen) is being used as the fluidising gas to drop the partial pressure of the O_2 to about 4%, the temperature of the reduction reaction should be about 950 °C.

Based on Figure 7.1(b) below, the decomposition of $CaCO_3$ (e.g., the calcination reaction) is a function of the CO_2 concentration and the fluidised bed temperature. Hence, if the concentration of CO_2 in the fluidising gas is 5.9%, the calcination temperature should be above 740 °C. Another example in Figure 7.1(b) demonstrates that calcination would occur at temperatures beyond 850 °C given the incoming gas to the reactor contains 44.9% CO_2.
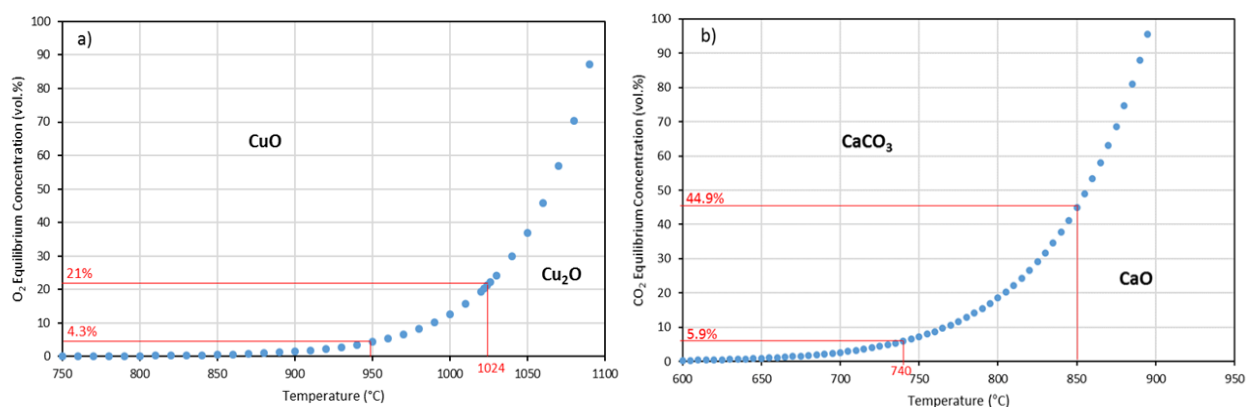
Figure 7.1: Equilibrium curves for: (a) O_2 partial pressure for CuO/Cu_2O, and (b) CO_2 partial pressure for $CaO/CaCO_3$ systems.

In the CaL and RES technologies, the particles are expected to undergo recurring reactions. Therefore, the possible decline in their reactivity should be investigated. The reactivity decline directly increases the operational and maintenance costs, and therefore should be considered in the reactor design.

7.1.2 Copper-rich particles (CuO/Cu2O)

To investigate the decline in the reactivity of the copper-rich particles, preliminary tests were conducted using the TGA technique. Since the equilibrium partial pressure of oxygen is a weak function of the temperature (see Figure 7.1(a)), the reactivity of the copper-rich particles was investigated by utilising different gas compositions during reduction (mostly pure N_2) and oxidation (air). Figure 7.2 below presents the TGA results for copper-rich particles which underwent five cycles. SEM and XRD analyses were also carried out on fresh and final TGA samples.

Each TGA test represented in Figure 7.2 started with a reduction half cycle in which the incoming gas was mainly pure N_2. The drop in the weight fraction was due to the oxygen released during the reduction. At the end of the reduction half-cycle, fresh air was introduced to the TGA and an oxidation half-cycle was initiated. As in all of the reaction pathways shown in Figure 7.2 the minimums and maximums of each cycle remained unchanged, it can be deduced that the reactivity of the copper-rich particles remained constant, regardless of the temperature at which the reduction and oxidation reactions were carried out.

It is evident from Figures 7.2(a) to (d) that the temperature directly affected the reaction rate. A high reaction temperature resulted in a shorter reaction time (from ~500 minutes in Figure 7.2(a) down to ~300 minutes in Figure 7.2(d)).
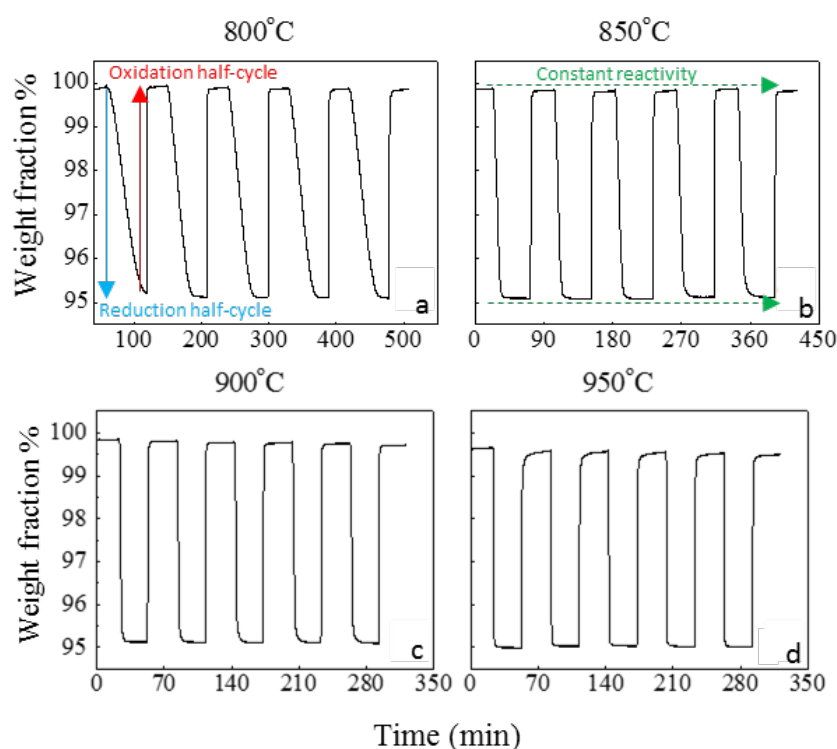
Figure 7.2: TGA results for the reactivity investigation of copper-rich particles at different temperatures which have undergone five cycles. The standard devaiation is less than 0.5% and not shown in the figure.

Figure 7.3 below shows the SEM images of the copper-rich particles at 900 °C. The two images at the top represent fresh particles ((a) and (b)), while the two bottom images ((c) and (d)) show the surfaces of the particles after 5 cycles. As is evident from Figure 7.3, after 5 cycles there was not any change in the grain sizes and the structure of the particles remained unchanged.
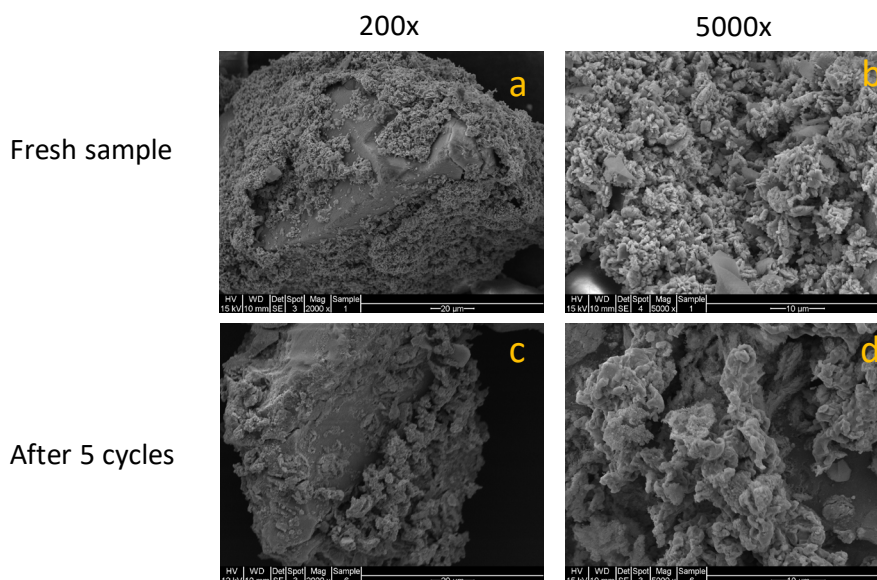
Figure 7.3: SEM results for copper-rich particles: (a) fresh 200x, (b) fresh 5000x, (c) after 5 cycles 200x, and (d) after 5 cycles 5000x.

The SEM results for the copper-rich particles at other temperatures also revealed no changes in the structures. These results supported the findings shown in Figure 7.2 and suggested that the reactivity of the copper-rich particles remained constant.

The crystalline structures of the fresh and cycled copper-rich particles were also investigated using the powder X-ray diffraction technique. The device was capable of loading 45 samples for analysis. Figure 7.4 below demonstrates the average of the multiple XRD results for the copper-rich particles. Amorphous SiO_2 structures were found in the range of $18° \leq 2\theta \leq 30°$ (see Figure 7.4) which indicated that the substrate (silica) did not react with the CuO/Cu_2O particles, and therefore the reactivity of the particles remained unchanged. The observed sharp peaks in Figure 7.4 are related to the crystalline structures of the CuO in the samples.
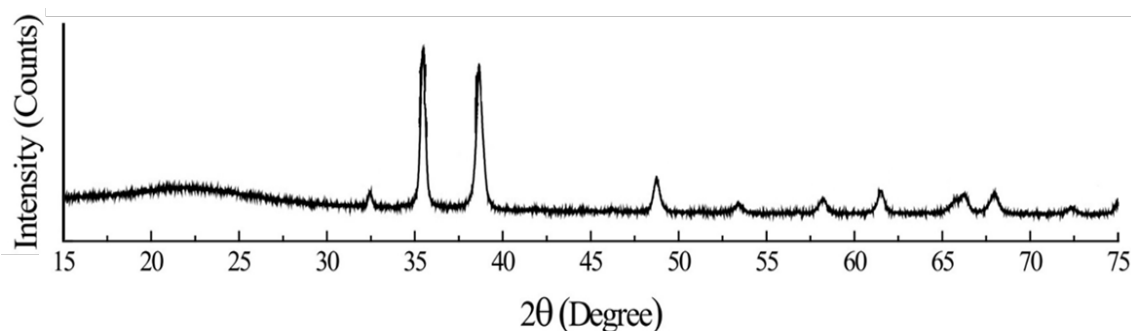
Figure 7.4: XRD results for copper-rich particles.

The observed results (see Figures 7.1 to 7.4) suggested that the reactivity of the copper-rich particles remained unchanged. Therefore, the kinetics of the reduction and oxidation reactions can be expressed using the following equation [88-93]:

$$\frac{d\alpha}{dt} = k \cdot f(\alpha) \cdot (C - C_{eq.})^{n_*} \tag{7.1}$$

where the function $f(\alpha)$ is the conversion function and is determined by the reaction mechanism, t is the time, k is the Arrhenius reaction rate constant and is calculated using the following equation:

$$k = A \cdot \exp\left(-\frac{E}{RT}\right) \tag{7.2}$$

where A is the pre-exponential factor, E is the activation energy, R is the gas constant and T is the reaction temperature.

Exponent n_* in Eq 7.1 is the reaction order. Since the reduction of the CuO is categorised as a thermal decomposition reaction, the value of n_* is zero and the rate would be independent of the oxygen concentration. In contrast, during oxidation, since oxygen is present in the incoming air, n_* will have a non-zero value, which should be determined experimentally. C and $C_{eq.}$ are the oxygen concentration in the inlet gas and the equilibrium oxygen concentration, respectively. Here, $C_{eq.}$ can be calculated from the equilibrium partial pressure of oxygen ($P_{O_2,e}$). The oxygen equilibrium partial pressure can be calculated using the Gibbs free energy using Eq 7.3 below. The Gibbs free energy itself is a function of temperature and is expressed as [91]:

$$P_{O_2,e} = \exp\left(\frac{\Delta G}{RT}\right) \tag{7.3}$$

$$\Delta G = 292 + 0.051T.\log T - 0.37T \qquad (298 \leq T \leq 1323\ K) \tag{7.4}$$

Integrating Eq 7.1 and introducing new conversion functions for different reaction mechanisms:

$$G(\alpha) = \int_0^\alpha \frac{1}{f(\alpha)}\,d\alpha = \int_0^t k\left(C - C_{eq}\right)^{n_*} dt = k\left(C - C_{eq.}\right)^{n_*} t \tag{7.5}$$

Table 7.2 below summarises the analytical formula of the different reaction mechanisms [88-90, 92-93].

Table 7.2: Summarisation of $G(\alpha)$ equations for different reaction mechanisms

Reaction mechanism	Abbreviation	$G(\alpha)$
Diffusion (one dimension)	D1	α^2
Diffusion (two dimensions)	D2	$(1-\alpha)\ln(1-\alpha) + \alpha$
Jander function (three dimensions)	D3	$\left[1-(1-\alpha)^{1/3}\right]^2$
G-B function (three dimensions)	D4	$1 - \frac{2\alpha}{3} - (1-\alpha)^{2/3}$

First order chemical reaction	C1	$-\ln(1-\alpha)$
Second order chemical reaction	C2	$(1-\alpha)^{-1}-1$
Random nucleation and growth (Avrami-Erofe'ev, n=2)	A2	$[-\ln(1-\alpha)]^{1/2}$
Random nucleation and growth (Avrami-Erofe'ev, n=3)	A3	$[-\ln(1-\alpha)]^{1/3}$
Phase boundary reaction (n=2)	R2	$1-(1-\alpha)^{1/2}$
Phase boundary reaction (n=3)	R3	$1-(1-\alpha)^{1/3}$
Mampel power law (n=1)	P1	α
Mampel power law (n=2)	P2	$\alpha^{1/2}$
Mampel power law (n=3)	P3	$\alpha^{1/3}$
Mampel power law (n=4)	P4	$\alpha^{1/4}$

The right-hand side of Eq 7.5 is a function of temperature. Hence, the most appropriate form of $G(\alpha)$ would have the minimum deviation from the observed experimental results. Tables 7.3 and 7.4 below report on the obtained deviations of the experimental results from the fitted mechanisms for the reduction and oxidation reactions, respectively.

According to Table 7.3, the most suitable mechanism for copper-rich particles during reduction was the A2 Avrami-Erofe'ev random nucleation and subsequence growth model (*n=2*). The value of *k* was evaluated by measuring the slope of the linear fit of $[-\ln(1-\alpha)]^{1/2}$ versus time. The evaluated value was then used to estimate the values of the pre-exponential factor (*A*) and the apparent activation energy (*E*) in Eq 7.2. To increase the accuracy of the model, these values were calculated in two separate temperature ranges. The values were *E* = 315 kJ/mol with a pre-exponential factor A = 1.595×10^{14} min^{-1} for temperatures between 800-900 °C and *E* = 176 kJ/mol with A = 1.189×10^8 min^{-1} for temperatures above 900 °C.

An increase in the temperature resulted in an increase in the diffusion coefficient of the released oxygen in the pores as well as in the equilibrium partial pressure (e.g., driving force). Therefore, the observed decrease in the activation energy with the temperature could be attributed to the increase of the mass transfer phenomenon.

Table 7.3: R^2 values for fitting different reaction mechanisms using Eq 7.5 during the reduction reaction in the temperature range of 800 - 975 °C for copper-rich particles

T °C	D1	D2	D3	D4	C1	C2	A2
800	0.8244	0.7630	0.6758	0.7344	0.8582	0.6094	0.9917
825	0.8034	0.7451	0.6616	0.7177	0.8342	0.5909	0.9969
850	0.7678	0.7041	0.5961	0.6698	0.7344	0.3912	0.9604
875	0.7583	0.7008	0.6031	0.6698	0.7311	0.4195	0.9468
900	0.8644	0.8088	0.6938	0.7745	0.8058	0.4188	0.9874

T °C	A3	R2	R3	P1	P2	P3	P4
925	0.8413	0.7835	0.6732	0.7497	0.7990	0.4395	0.9901
950	0.8086	0.7504	0.6426	0.7169	0.7615	0.4209	0.9695
975	0.7661	0.6990	0.5618	0.6571	0.6644	0.2916	0.9182
T °C	**A3**	**R2**	**R3**	**P1**	**P2**	**P3**	**P4**
800	0.8077	0.9423	0.9189	0.9837	0.8625	0.3825	-0.4050
825	0.8926	0.9199	0.8951	0.9648	0.9250	0.5842	-0.0170
850	0.9890	0.8604	0.8260	0.9221	0.9732	0.8454	0.5804
875	0.9916	0.8453	0.8140	0.9024	0.9710	0.8756	0.6372
900	0.9644	0.9316	0.9012	0.9696	0.9325	0.7461	0.4898
925	0.9556	0.9194	0.8890	0.9588	0.8980	0.6065	0.1818
950	0.9905	0.8857	0.8534	0.9339	0.9450	0.7884	0.5321
975	0.9944	0.8370	0.7928	0.9054	0.9723	0.9134	0.7755

The R^2 values in Table 7.4 below show the deviations obtained from the experimental results versus the describing models of the oxidation reactions. The oxidation reactions, which were modelled using the A2, R2 and P1 mechanisms demonstrated the least deviations from the experimental data. However, a careful review of the reported values in Table 7.4 revealed that the R2 model described the oxidation reaction better than other models.

To find k, a linear least-squares regression plot of $k.(C - C_{eq})^{n_*}$ versus $\ln(C - C_{eq})$ was used. The values of k and n_* were obtained as the intercept and slope, respectively. Different values of $(C - C_{eq})$ were achieved by diluting the incoming air with nitrogen. The value of n_* was found to be 0.5. The values of k were found to be 1.959 and 1.651 for 850 and 950 °C, respectively. Moreover, the pre-exponential factor and apparent activation energy were evaluated in two distinct temperature ranges of 800-900 °C and 900-975 °C, which corresponded to the activation energy and pre-exponential factor equal to 3 kJ/mol and 2.67 $m^{3/2}mol^{-1/2}min^{-1}$ and -43 kJ/mol and 0.024 $m^{3/2}mol^{-1/2}min^{-1}$, respectively. The negative activation energy could be due the fact that at high temperatures both the reduction and oxidation reactions were happening simultaneously, especially in the pores, where the diffusion of oxygen from the internal pores was the main reaction barrier.

Table 7.4: R^2 values for fitting different reaction mechanisms using Eq 7.5 during oxidation in the temperature range of 800-975 °C for copper-rich particles

T °C	D1	D2	D3	D4	C1	C2	A2
800	0.7253	0.7057	0.6851	0.6988	0.8866	0.8354	0.9993
825	0.8378	0.8161	0.7912	0.8078	0.9338	0.9009	0.9817
850	0.8496	0.8218	0.7878	0.8106	0.9359	0.8649	0.9901
875	0.8627	0.8335	0.7963	0.8213	0.9229	0.856	0.9786

T °C	A3	R2	R3	P1	P2	P3	P4
900	0.8786	0.8516	0.8166	0.8402	0.9531	0.8825	0.9789
925	0.8294	0.7975	0.7591	0.7848	0.9313	0.8486	0.9853
950	0.8035	0.7761	0.745	0.7657	0.937	0.873	0.9631
975	0.9081	0.8743	0.8288	0.8595	0.9722	0.877	0.9192
T °C	A3	R2	R3	P1	P2	P3	P4
800	0.9374	0.9092	0.9019	0.9291	0.9892	0.9014	0.8052
825	0.8541	0.9627	0.9579	0.9742	0.9493	0.7843	0.5979
850	0.9081	0.9585	0.952	0.9719	0.9548	0.8330	0.6696
875	0.8657	0.9605	0.9544	0.9701	0.9129	0.7414	0.5486
900	0.8529	0.9725	0.9673	0.9812	0.9235	0.7443	0.5212
925	0.8274	0.9594	0.9511	0.9777	0.9357	0.7045	0.4122
950	0.7323	0.9608	0.9536	0.9784	0.9096	0.6070	0.2548
975	0.5938	0.9935	0.9886	0.9955	0.7649	0.2869	-0.2800

7.1.3 Calcium-rich particles (CaO/CaCO3)

nitial experiments were conducted to investigate the effect of the CO_2 concentrations on the carbonation and calcination reactions. For low CO_2 concentrations in the inlet stream (less than 1%), an approach similar to the previous section can be considered. However, with a CO_2 concentration of more than 1%, the carbonation and calcination reactions should be modelled using different sets of equations other than those discussed in the previous section. The scope of this project involves studying reactions with CO_2 concentrations much higher than 1%. Therefore the results for low CO_2 concentration is not reported here.

The flows and concentrations of CO_2 remained constant for both the carbonation and calcination reactions occurring in TGA. This ensured that the conditions under which the reactivity was studied were closer to the simulation conditions, where a fraction of the exhaust gas from the boiler was flowing through the reactor during both the off-peak (calcination reaction) and peak (carbonation reaction) periods without any changes in its composition. The calcination and carbonation temperatures were considered to be 650-750 °C and 850-950 °C, respectively. The CO_2 concentrations were 5, 13 and 20% in the reactivity tests. Figure 7.5 below shows the results for the TGA analysis under 5% CO_2 concentration during both calcination and carbonation.
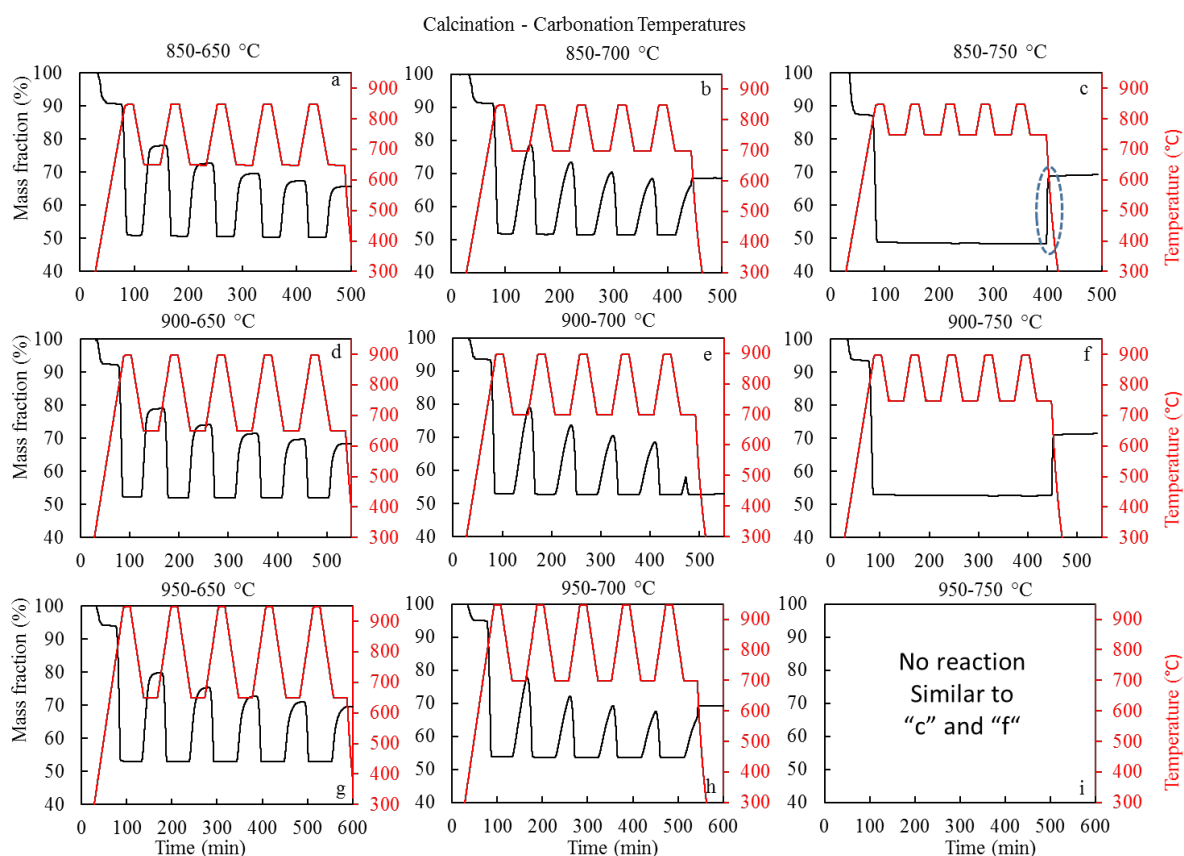
Figure 7.5: TGA results for calcium-rich particles for 5 cycles under 5% CO_2 concentration. The CO_2 concentrations and flows remained constant throughout each test. The two numbers on the top of each experiment correspond to the calcination and carbonation temperatures, respectively. The standard deviation is less than 0.5%.

In Figure 7.5, the red series specifies the temperature and the black series indicates the changes in the sample mass. The horizontal axis reports the time. According to Figures 7.5(a)-(b), (d)-(e) and (g)-(h), after the calcination the mass fraction dropped to about 52% of the original sample. This showed that CO_2 was released during calcination. When all of the CO_2 was released from the sample, the mass fraction remained constant for a few minutes, and a minimum flat line was formed. However, at the start of the carbonation the mass fraction started to rise which demonstrated that CO_2 was being captured from the incoming gas and that heat was being generated.

The presence of sharp peaks in Figure 7.5 represented that although the carbonation reached its maximum the carbonation process was slow, and hence a maximum plateau did not form. It is also evident from the mass fraction series in Figures 7.5(a)-(b), (d)-(e) and (g)-(h), that the maximums of the mass fractions were declining with the number of cycles. This decrease in reactivity was not seen in the results related to the copper-rich particles. Moreover, no carbonation reaction was observed (e.g., increase in the mass after the first calcination) in Figures 7.5(c), (f) and (i). The reason for this was that the equilibrium partial pressure of CO_2 at 750 °C was higher than the incoming CO_2, which caused the driving force for the carbonation reaction to become zero and inhibited the carbonation reaction. This finding confirmed the equilibrium data shown in Figure 7.1.

The region with dashed boundaries in Figure 7.5(c) shows an increase in the mass fraction at the end of the fifth cycle. Since the CO_2 concentration of the flowing gas remained constant, at the end of the tests, when the temperature started to drop from 750 °C, the carbonation reaction started to be undertaken and stopped when the temperature dropped to 650 °C. A similar phenomenon was responsible for the sudden increase in the mass fraction in Figure 7.5(f). Finally, the results for the 5% CO_2 concentration showed that generally low carbonation and calcination temperatures could increase the activity of the particles.
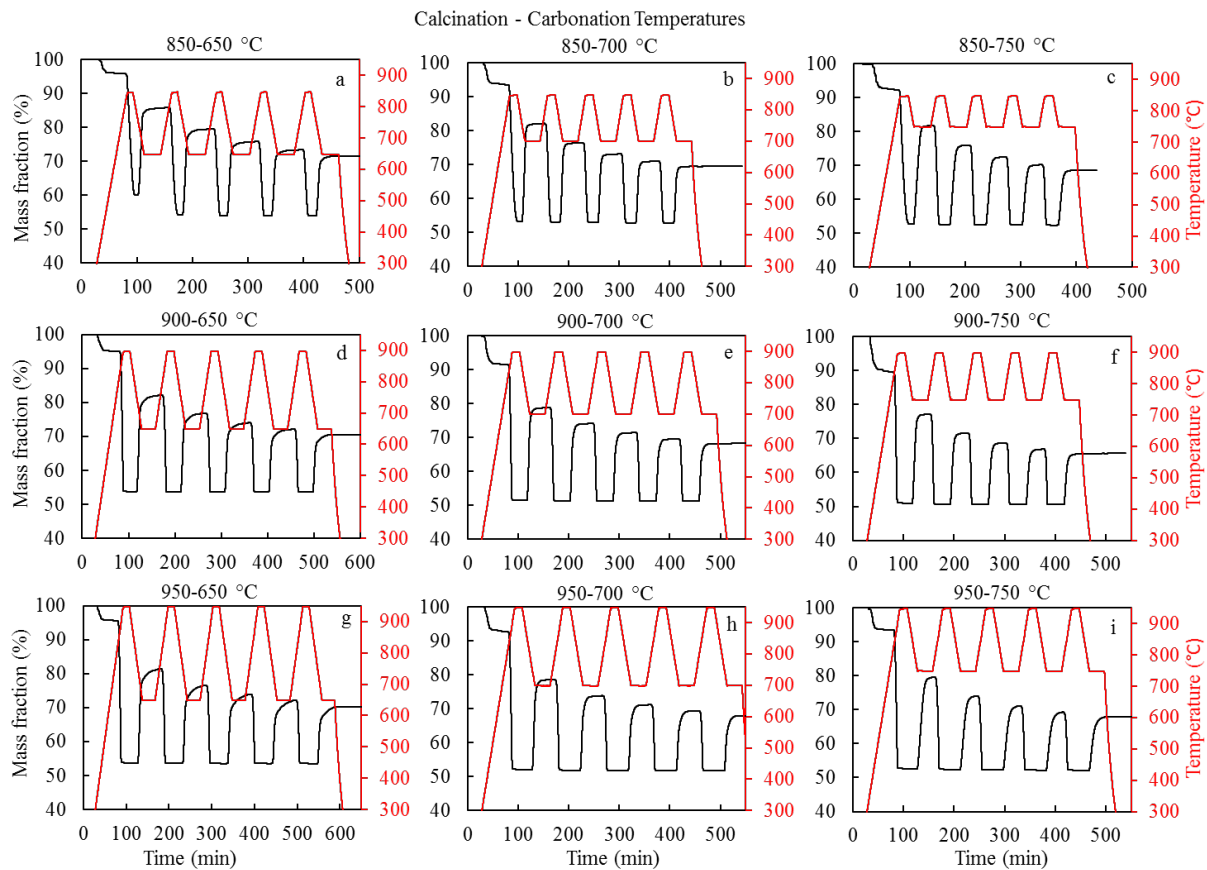
Figure 7.6: TGA results for calcium-rich particles for 5 cycles under a 13% CO_2 concentration. The CO_2 concentrations and flows remained constant throughout each test. The standard deviation is less than 0.5%.

Figure 7.6(a)-(i) show the results of the calcination and carbonation reactions under a 13% CO_2 concentration for 5 cycles. It is evident that the reactivity of the particles dropped as the number of cycles increased. An undesirable effect of introducing CO_2 gas during the calcination process was that it decreased the rate of calcination due to its negative impact on the calcination kinetics. This effect can be seen in Figure 7.5(a). In addition, the observed minimum in each cycle tended to become smaller with the number of cycles, which implied that the calcination time was insufficient under a 13% CO_2 concentration. However, the residual uncalcined fraction of solids in each cycle had a chance to be calcined during the calcination in the next cycles. Hence, the samples were fully calcined after the third cycle. This effect was not seen in higher calcination temperatures (900 and 950 °C), under which the

higher calcination temperatures dominated the effect of the smaller driving force due to the presence of CO_2.

The carbonation reaction in Figure 7.6 occurred at all of the carbonation temperatures (unlike in Figures 7.5(c), (f) and (i)) because the equilibrium partial pressure of the CO_2 remained smaller than the incoming gas. Moreover, the particles were fully carbonated and reached a plateau at any carbonation temperature.
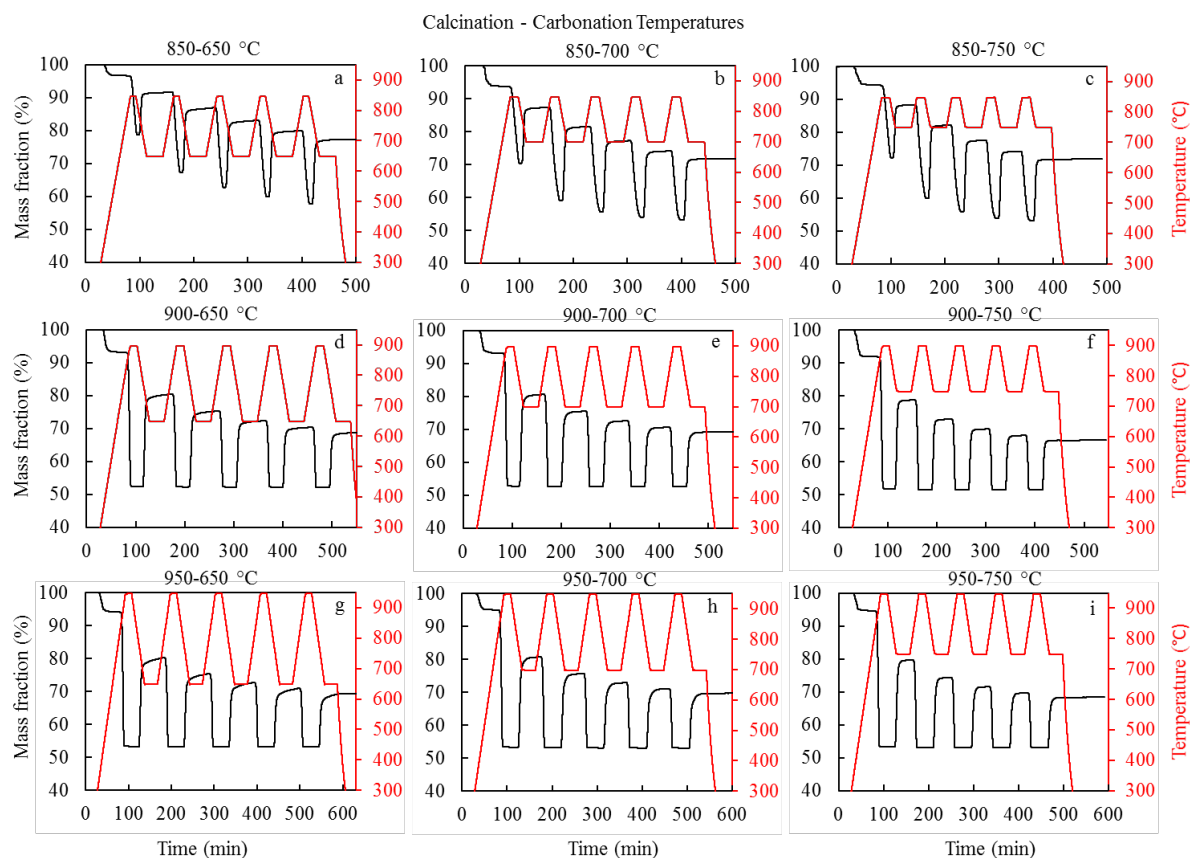
Figure 7.7: TGA results for calcium-rich particles for 5 cycles under a 20% CO_2 concentration. The CO_2 concentrations and flows remained constant throughout each test. The standard deviation is less than 0.5%.

Figures 7.7(a)-(i) show the reactivity of the calcium-rich particles under a 20% CO_2 concentration for 5 cycles. The temperatures for the calcination and carbonation were the same as in Figures 7.5 and 7.6. It is evident from Figures 7.7(a)-(c) that the time required for calcination under a 20% CO_2 concentration was not enough for the calcination reaction to finish. The presence of a high CO_2 concentration was so much that the residual uncalcined solids did not reach the minimum weight fraction, even after the fifth cycle. The high CO_2 concentration during the carbonation process caused the carbonation reaction to reach a plateau at the end of each cycle.

The decline in the reactivity of the calcium-rich particles with the number of cycles could be due to a change in the morphology of the particles. Therefore, a series of EDS, XRD and SEM tests were performed on the cycled particles.

Figures 7.8(a)-(c) report the EDS results for the fresh limestone. The elemental analysis of the specified areas in Figure 7.8(a) are presented in Figures 7.8(b) and (c), respectively. As was expected, the presence of calcium, carbon and oxygen in the sample caused a sharp peak in the signal. The presence of silica and magnesium in the sample was due to the impurities in the sample. As the samples were covered using a Pt sputtering technique, some platinum was found in the signal.
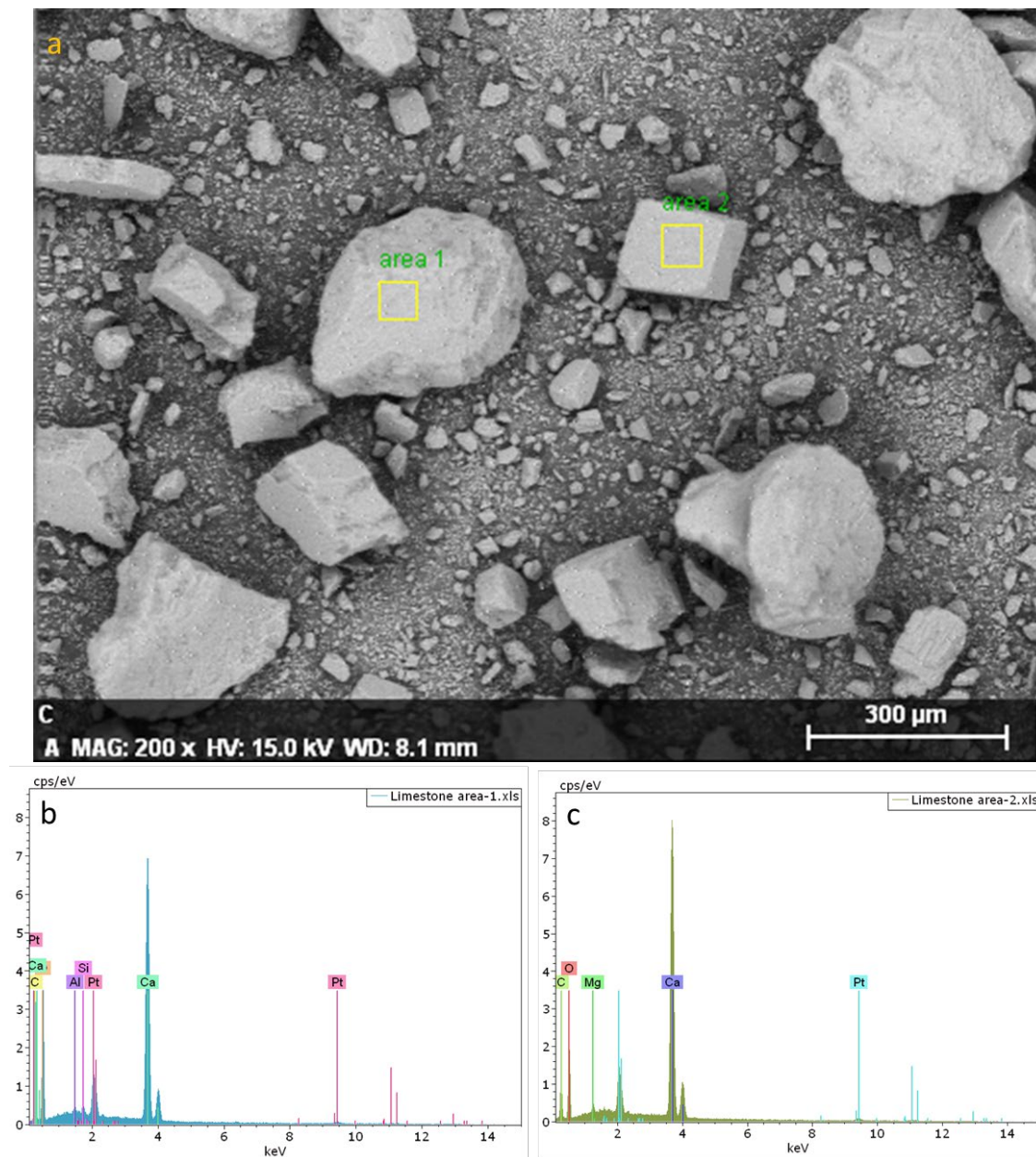
Figure 7.8: EDS results for fresh calcium-rich particles: (a) SEM image containing two specified areas, (b) EDS analysis of area 1, (c) EDS analysis of area 2.

The elemental analysis of the fresh limestone was carried out using the X-ray fluorescence (XRF) technique. Table 7.5 reports the elemental analysis of the fresh limestone. According to Table 7.5, the sample was comprised of more than 97% calcium.

Table 7.5: XRF analysis of Omya limestone

Ca	Fe	Mg	Al	Si	Mn	K
97.56	0.23	0.43	0.15	1.21	0.38	0.04

The structural analysis of the limestone, for fresh and after 30 cycles, was investigated using the XRD technique and is presented in Figure 7.9 below. To study the effects of the cycling on the reactivity of the particles using XRD, the number of cycles was extended to 30 to magnify any possible changes in the crystalline structures of the limestone after cycling. The symbols in Figure 7.9 refer to the crystalline structures of $CaCO_3$ and $Ca(OH)_2$. The main strong peaks in the spectrum coincided with the calcite phase in the limestone. The presence of weak $Ca(OH)_2$ signals was due to the moisture capture of the samples from the ambient environment before their characterisation using XRD. A comparison of fresh limestone and 30 cycles limestone revealed that the main phase in the crystalline structure of the limestone remained unchanged after the cycles. Hence, the effects of the decline in the reactivity of the limestone was not noticable using the XRD results.
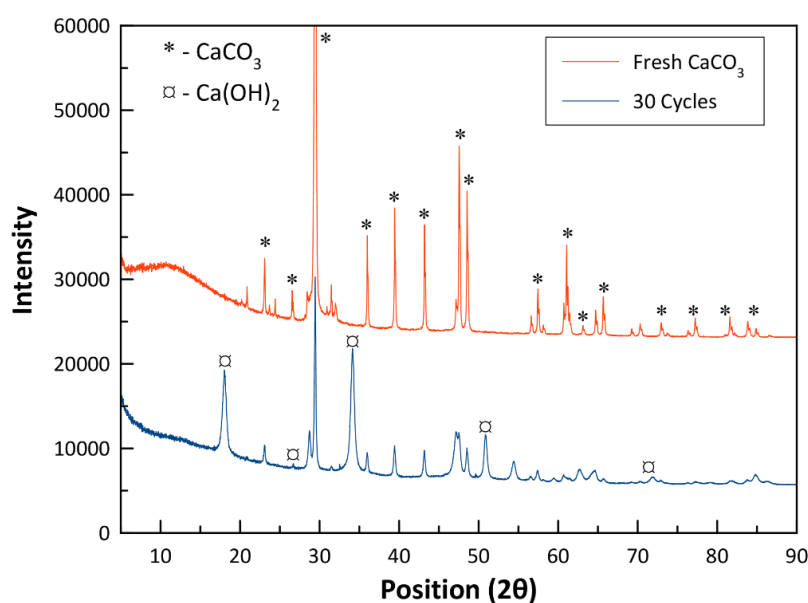
Figure 7.9: XRD analysis of fresh and 30 cycles limestone. The main crystalline structures of the limestones remained unchanged.

The SEM images of the fresh limestone particles and after 5 cycles under different calcination and carbonation temperatures, as well as different CO_2 concentrations, are depicted in Figure 7.10. The scale bars and magnifications for each image are reported. Figures 7.10(a)-(c) below present the surface structures of the fresh limestone under different magnifications. Figures 7.10(d)-(o) show the surface morphologies of the limestone after 5 cycles of calcination and carbonations. The temperatures and CO_2 concentrations under which the reaction was carried out are also reported in each image in Figure 7.10. According to Figure 7.10, the main differences in the particles which had undergone cycling to the fresh limestone was in the pore structures and surface cracks. The surface cracks could appear from the sheet separation (compare Figure 7.10(b) with (e)). The higher degree of cycling could cause more pore

closures and more cracks to appear. The combination of these two effects is believed to lower the cyclic efficiency.
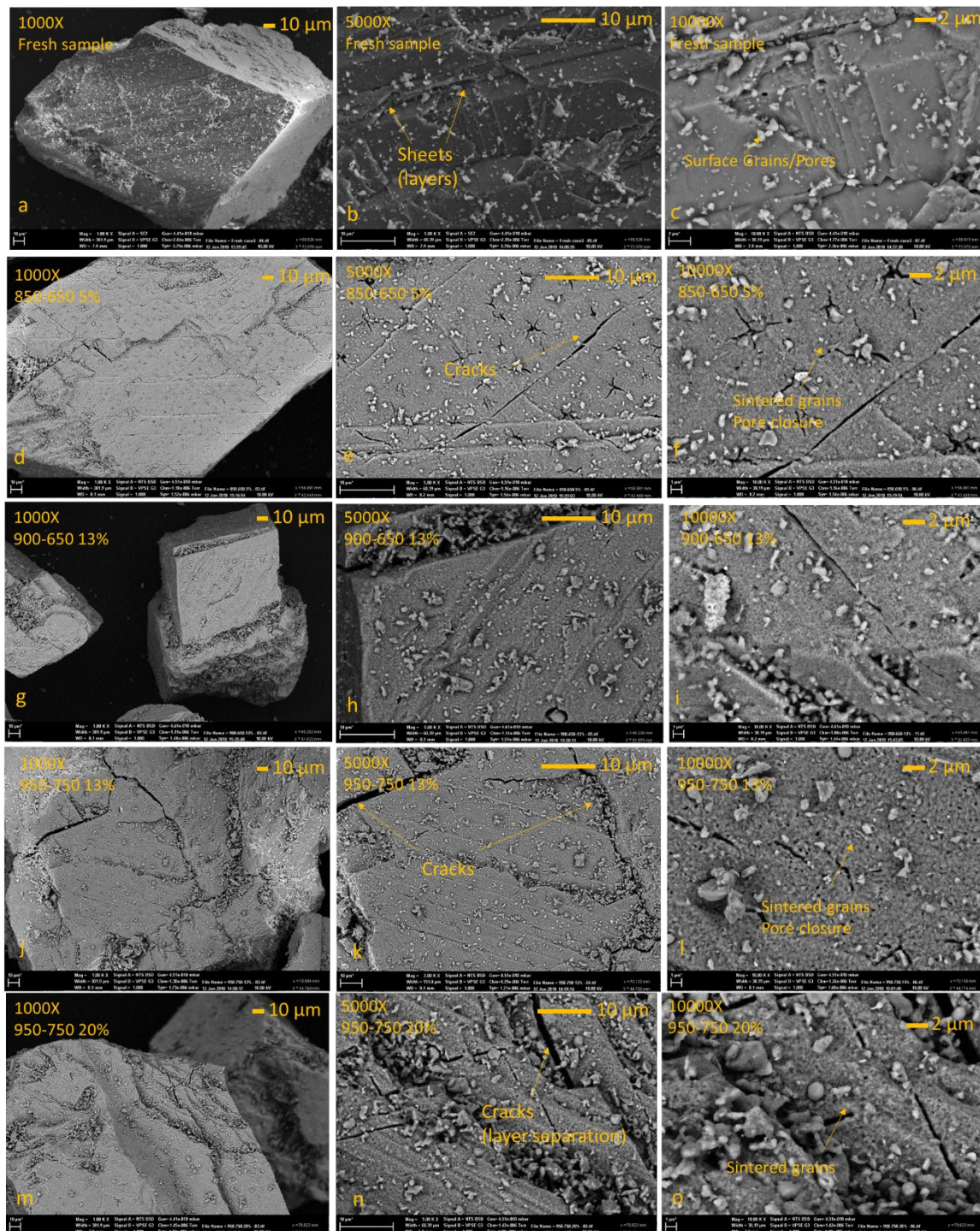
Figure 7.10: SEM images of fresh and cycled calcium-rich particles at different magnifications and reaction conditions.

The pore closure causes some parts of the limestone to not react with CO_2, while the appearance of the cracks leads to a higher degree of particle attrition, which results in finer solids and bed entrainment.

The effects of the CO_2 concentration and the reaction conditions, such as the calcination and carbonation temperatures, on the surface morphology of the particles was not found to be

great. However, it is believed that higher calcination temperatures could increase the rate of the pore closures and sheet separations in highly cycled particles.

The maximum conversion of each cycle is an excellent measure for the reactivity of the particles. As the number of cycles increased, the maximum conversion decreased. This value was calculated for each cycle and is shown in Figures 7.5 - 7.7. To calculate the maximum conversion, the following equation was employed:

$$X_N = \frac{max-min}{min} \times \frac{56}{44} \tag{7.6}$$

where X_N is the conversion of the Nth cycle, and min and max refer to the minimum and maximum weight fractions of each cycle, respectively.

Three semi-empirical equations (Eqs 7.7 - 7.9) were used to match the calculated experimental conversions. These methods are called E1, E2 and E3, respectively [94-96]:

$$E1: \quad X_N = f_m{}^N(1 - f_w) + f_w \tag{7.7}$$

$$E2: \quad X_N = \frac{1}{\frac{1}{1-X_r}+kN} + X_r \tag{7.8}$$

$$E3: \quad X_N = f^{N+1} + b \tag{7.9}$$

where, f_w, X_r and b are called the residual reactivities and represent the conversion when the number of cycles (N) approaches infinity, f_m, k and f are the coefficients of the empirical equations.

Figure 7.11 depicts the experimental conversions obtained from Eq 7.6 and fitted using Eqs 7.7 to 7.9 for 950-650 °C tests under 5, 13 and 20% CO_2 concentrations. The results showed that all of the E1-E3 methods were able to predict the obtained experimental conversion very closely ($R^2 \approx 0.99$). Therefore, E3 might be the most favourable as it is easy to use. The fitted parameters used in E1-E3 (Eqs 7.7 - 7.9) for each set of the calcination-carbonation cycle are reported in Table 7.6.
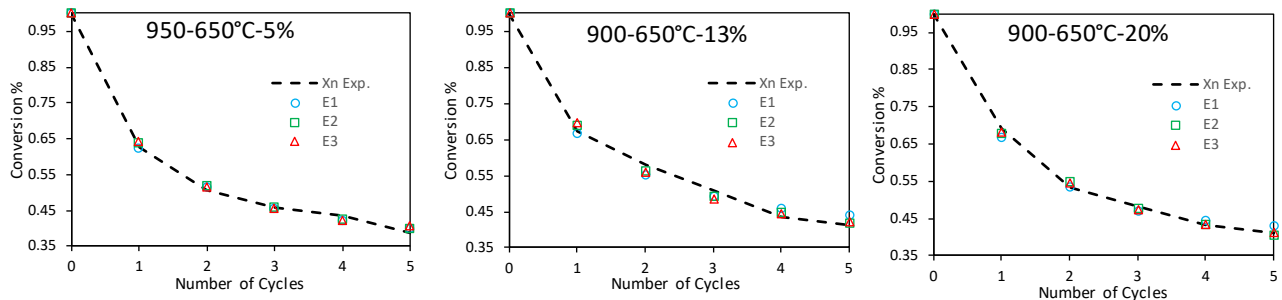
Figure 7.11: The comparison of E1-E3 with the experimental data for 950-650 °C tests under 5, 13 and 20% CO_2 concentrations for 5 cycles.

The results showed that higher calcination and carbonation temperatures led to lower cyclic conversions of the particles. However, an increase in the CO_2 concentration of the fluidising gas improved the conversion. The combination of effects was not found to be more than 5%.

Table 7.6: Fitted parameters to predict the cyclic conversions of calcium-rich particles under 5, 13 and 20% CO_2 concentrations, the error in the presented values is less than 1%

Carb. Temp.	Calcin. Temp	5% CO_2 850 °C	5% CO_2 900 °C	5% CO_2 950 °C	13% CO_2 850 °C	13% CO_2 900 °C	13% CO_2 950 °C	20% CO_2 850 °C	20% CO_2 900 °C	20% CO_2 950 °C
650 °C	f_m	0.47	0.558	0.48	0.515	0.542	0.518	0.555	0.461	0.519
	f_w	0.428	0.378	0.39	0.401	0.419	0.403	0.232	0.419	0.371
	k	0.739	1.423	1.408	0.701	0.947	1.051	1.785	0.978	1.168
	X_r	0.2	0.284	0.279	0.165	0.254	0.25	0.153	0.244	0.232
	f	0.58	0.5	0.505	0.605	0.549	0.54	0.506	0.545	0.537
	b	0.37	0.392	0.386	0.33	0.396	0.382	0.237	0.385	0.352
700 °C	f_m	0.472	0.714	0.467	0.619	0.548	0.579	0.528	0.53	0.553
	f_w	0.383	0.306	0.3	0.421	0.445	0.383	0.357	0.404	0.362
	k	0.901	3.888	1.179	1.158	0.75	1.584	1.274	1.074	1.379
	X_r	0.188	0.332	0.145	0.302	0.24	0.303	0.233	0.249	0.255
	f	0.571	0.375	0.557	0.519	0.568	0.486	0.528	0.535	0.514
	b	0.332	0.383	0.259	0.425	0.409	0.402	0.345	0.388	0.362
750 °C	f_m				0.495	0.469	0.466	0.553	0.448	0.49
	f_w				0.413	0.41	0.4	0.376	0.397	0.377
	k		No carbonation reaction		0.619	0.921	0.91	1.286	0.667	0.934
	X_r				0.148	0.195	0.182	0.26	0.134	0.192
	f				0.611	0.57	0.577	0.521	0.609	0.569
	b				0.335	0.335	0.321	0.372	0.311	0.331

The next step after the determination of the X_N for each reaction was to model the calcination and carbonation reactions. Due to the decrease in the reactivity of the calcium-rich particles with cycling, a different formulation (other than that used for copper-rich particles) was implemented. In this approach, the effect of the particles' structures was considered in the formulation. The newly proposed set of equations were used on each test to model one calcination [97-99] and two carbonation reactions [100-103] using the following equations:

$$\frac{dX_{\text{calc.}}}{dt} = k_{\text{calc.}}\left(C_{CO_2,\text{eq.}} - C_{CO_2}\right)(1 - X_{\text{calc.}})^{0.2} \tag{7.10}$$

where $X_{\text{calc.}}$, $k_{\text{calc.}}$, C_{CO_2} and $C_{CO_2,\text{eq.}}$ were the conversion during calcination, calcination reaction constant, CO_2 concentration in the fluidising gas and the equilibrium concentration of CO_2, respectively.

$$\frac{dX}{dt} = k_s S\left(C_{CO_2} - C_{CO_2,eq.}\right)\left(1 - \frac{X}{X_N}\right)\sqrt{1 - \psi \ln(1-X)} \tag{7.11}$$

where X, k_s, S and ψ were the conversion in the carbonation reaction, the reaction rate constant, the active surface area of the particles and the pore structural parameter, respectively.

ψ was related to the internal pore structure of the particles by using the following equation:

$$\psi = \frac{4\pi L(1-\varepsilon)}{S^2} \tag{7.12}$$

where, L and ε were the the pore length per unit volume and the porosity of particles, respectively. The values of S, L and ε were based on a literature review and were assumed to be equal to 2.9×10^6 m^2/m^3, 1.4×10^{14} m/m^3 and 0.46, respectively [100-103].

Two parameters were fitted ($k_{calc.}$ and k_s) to express the experimental results using Eqs 7.10 and 7.11. Table 7.7 below reports the fitted parameters. The deviations of the model and the experimental results, on average, were below 1% ($R^2 > 0.99$). The results showed that when the concentration of the CO_2 was equal to 13% and 20%, the $k_{calc.}$ increased with the calcination temperature, meaning that the calcination reaction occurred faster. This result was expected as the higher calcination temperature led to a lower carbonation conversion, and hence the particles were calcined faster. It was also found that the k_s decreased with higher CO_2 concentrations, which means that the carbonation conversion increased with higher CO_2 concentrations. Moreover, the k_s decreased with the carbonation temperature, implying that high temperatures increased the $C_{CO_2,eq.}$ and lowered the concentration difference (driving force) in Eq 7.11.

Table 7.7: Fitted $k_{calc.}$ and k_s related to calcination and carbonation reactions under different CO_2 concentrations

Calcination	5% CO$_2$			13% CO$_2$			20% CO$_2$		
	850 °C	900 °C	950 °C	850 °C	900 °C	950 °C	850 °C	900 °C	950 °C
$k_{calc.}$	0.086	0.074	0.022	0.059	0.060	0.063	0.048	0.063	0.056

Carbonation	5% CO$_2$			13% CO$_2$			20% CO$_2$		
	650 °C	700 °C	750 °C	650 °C	700 °C	750 °C	650 °C	700 °C	750 °C
k_s 1st Carb.	8.18E-09	5.66E-09	-	5.17E-09	4.81E-09	3.63E-09	5.35E-09	4.70E-09	4.23E-09
k_s 2nd Carb.	6.68E-09	4.87E-09	-	5.60E-09	5.89E-09	3.77E-09	5.39E-09	4.85E-09	4.01E-09

7.2 LABORATORY-SCALE EXPERIMENTS (Milestone 5)

More than 20 laboratory-scale experiments were undertaken on both copper-rich and calcium-rich particles. The copper-rich particles were experimented on using a quartz fixed bed reactor. In contrast, the calcium-rich particles were investigated using a fluid bed.

7.2.1 Fixed bed reactor

The focus of the laboratory-scale investigation on the copper-rich particles was on the reduction reaction of the particles. Figures 7.12(a) and (b) illustrate the profiles of the oxygen released from the copper-rich particles during reduction. The inlet gas to the reactor contained 5% oxygen and 95% nitrogen. After 5 minutes the oxygen content was reduced to zero. The temperature varied from 800-950 °C.

Figure 7.12(a) demonstrates that the oxygen content started to drop after 10 minutes of the reduction reaction and remained constant for the rest of the oxygen release period. The constant oxygen concentrations during the reductions in Figure 7.12(a) was found to be very close to the equilibrium concentrations (0.12, 0.46 and 1.5%) at 800, 850 and 900 °C. It was also found that the oxidation reactions were faster at lower temperatures (see Figure 7.12(a)). This could be related to the fact that at low temperatures during the reduction, less oxygen was produced. Therefore, a smaller amount of oxygen was required to oxidise the particles completely. A small increase in the oxygen profile followed by a plateau was observed in the oxidation reaction. This could indicate that the period under which the oxidation rate was constant, possibly at its maximum.

Figure 7.12(b) shows the oxygen profiles during reduction and oxidation at 950 °C. The reduction and oxidation periods were 80 and 25 minutes, respectively. The oxygen profile shown in Figure 7.12(b) remained constant for about 50 minutes at 4.5%, and then dropped slowly to zero, indicating full reduction.

For all cases, the ends of the cycles were marked when the outlet oxygen concentration was equal to the inlet oxygen concentration.
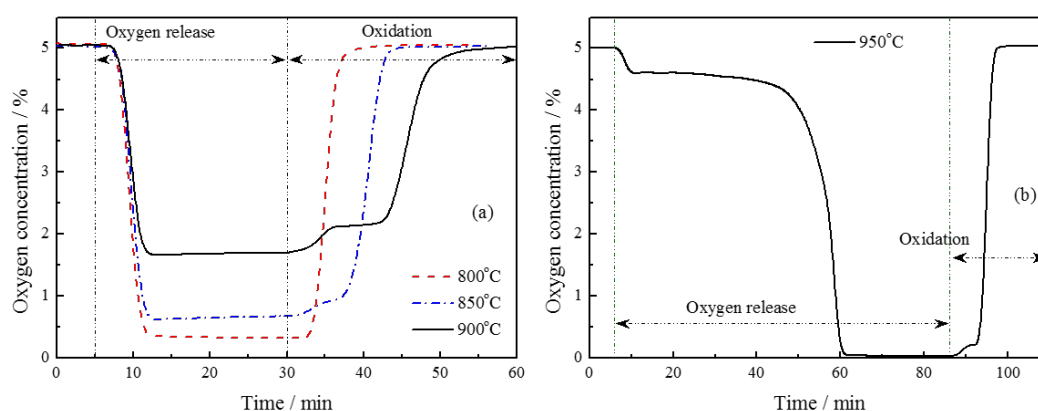
Figure 7.12: Oxygen concentration profiles leaving the fixed bed reactor at (a) 800, 850 and 900 ºC and (b) 950 ºC.

7.2.2 Fluidised bed reactor

In Section 7.1 it was shown that, unlike the copper-rich particles with a constant reactivity, the calcium-rich particles demonstrated a decline with the number of cycles. Hence, some experiments were performed on the particles in the laboratory-scale fluidised bed reactor to investigate the decline in the conversion. In addition, some of the calcium-rich particles were characterised with SEM to find out the effects of the fluidisation on their morphology. In the laboratory-scale fluidised bed tests, the concentrations of the CO_2 during carbonation was 1, 5 and 10%. The fluidising gas during calcination was air. The calcination and carbonation temperatures were 850 and 550 °C, respectively. The carbonation reaction was approximately 3 hours.

Figure 7.13 illustrates the cyclic conversion of the calcium-rich particles with the number of cycles. The decrease in the reactivities of the particles were similar to in the test which was performed in Section 7.1.3. It was found that in the fluid beds the final conversions could be slightly higher than the TGA results. Moreover, high CO_2 concentrations improved the cyclic conversions.
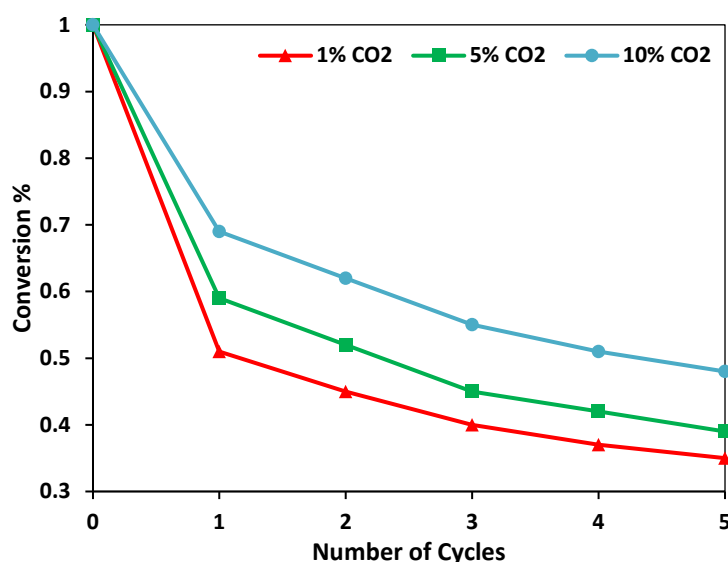
Figure 7.13: Cyclic conversions in the laboratory-scale fluidised bed for 1, 5 and 10% CO_2 concentrations during carbonation. The standard deviation is less than 1% for all the presented data.

The experimental results depicted in Figure 7.13 were fitted using Eqs 7.7 - 7.9 and are reported in Table 7.8 below.

Table 7.8: Fitted parameters using Eqs 7.7 - 7.9 for the laboratory-scale fluidised bed results

Parameters	1% CO_2	10% CO_2	15% CO_2
f_m	0.696	0.631	0.617
f_w	0.300	0.360	0.458
k	3.134	1.983	1.421
x_r	0.302	0.313	0.375

f	0.405	0.461	0.476
b	0.361	0.397	0.486

Figure 7.14 depicts the changes in the structures of the fresh and cycled calcium-rich particles after 5 cycles in the laboratory-scale fluidised bed. It is evident that with the cycling of the particles the surface grains would decrease. Aside from this, due to the nature of the fluidised bed process, the attrition of particles was promoted. Moreover, some cracks and pore closures appeared after the calcination process.
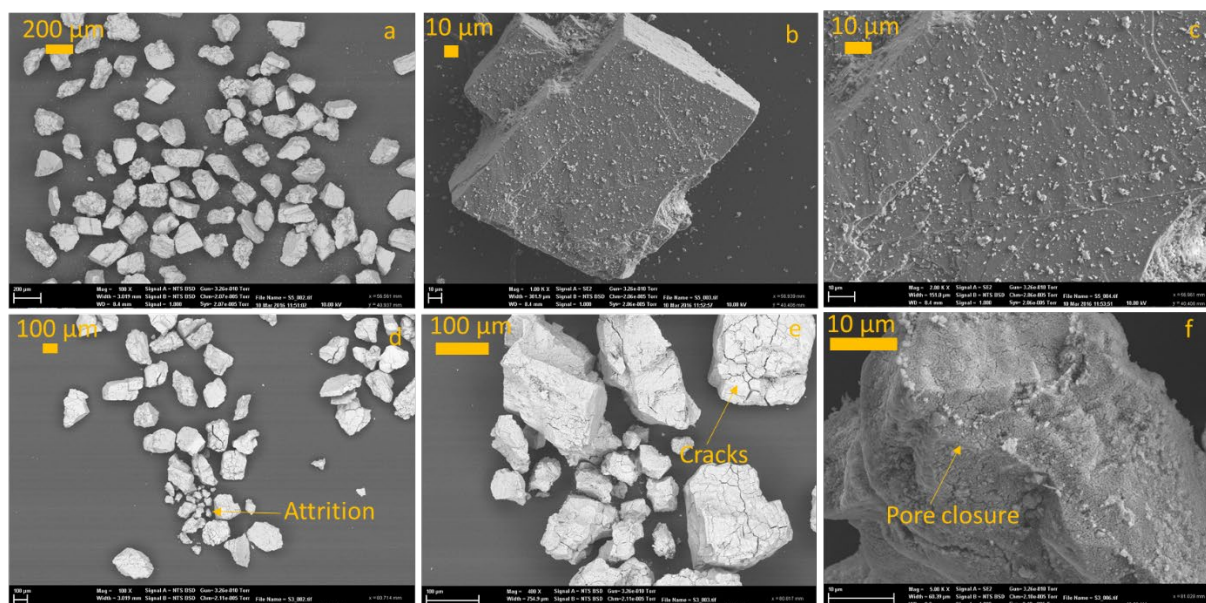
Figure 7.14: Changes in the particles' structures due to cycling. Images (a) - (c) depict fresh particles and images (d) - (f) show cycled particles.

Figure 7.15 illustrates the effects of a number of cycles on the particles' structures. According to Figure 7.15(a), the number density of the surface grains after the first calcination was more than that of the 3rd and 5th calcination shown in Figures 7.15(b) and (c), respectively. In addition, sintering and pore closures were more frequent after the 5th calcination (see Figure 7.15). Hence, it may be concluded that an increase in the number of cycles could decrease the reactivity through attrition and the carrying over by the fluidising gas, the loss of surface grains and sintering [103].
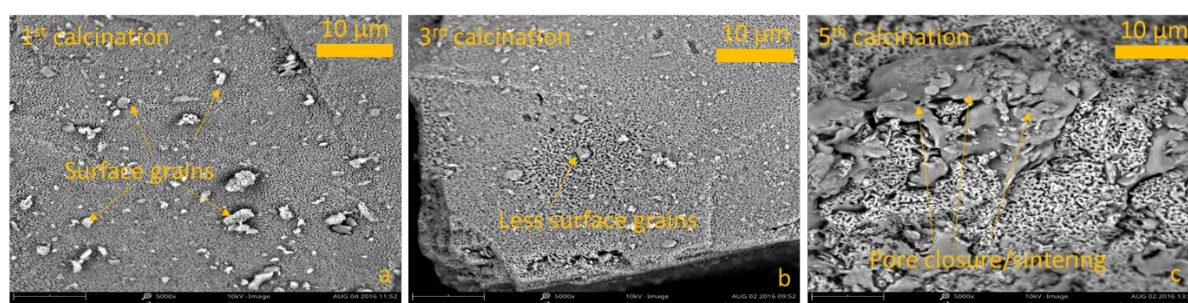
Figure 7.15: The changes in the particles' structures versus the number of cycles. Sintering and pore closures are evident in (c).

The results suggested that a low calcination and carbonation temperature could slow the rate of the particle deactivation, which means that the calcination reaction at 850 °C is more favourable.

7.3 PILOT-SCALE EXPERIMENTS (Milestone 6)

The experiments in this section were carried out only for CaL technology based on economic assessments (please refer to results in Chapter 6). The test in this section preliminary and primary modes. In the preliminary mode, the inventory and inlet gas flow rate were small. In the primary mode, the inventory and inlet gas flow rate were in the range of 50-150 kg and 100-200 m^3/h, respectively. Manifold switching was also investigated.

7.3.1 Preliminary Tests

Six experiments were carried out for the preliminary tests. The temperatures for the carbonation and calcination were 650-700 °C and 850-900 °C, respectively. The CO_2 concentration of the inlet gas was varied between 5% and 20%. The number of cycles was equal to 2. Hence, each experiment included two consecutive calcination and two carbonation cycles. The condition of the experiments was reported in Table 4.8. Figures 7.16(a) and (b) show the CO_2 concentrations of the exhaust gas during the first calcination at 850 and 900 °C, respectively. Since the variations in the CO_2 concentration profiles during calcination were large, two experiments were conducted: high resolution with time intervals equal to one minute and normal resolution with time intervals equal to 5 minutes. According to Figures 7.16(a) and (b), the shape of the peak depends mainly on the temperature at which the calcination process was carried out. Higher temperatures during the calcination (see Figure 7.16(b)) resulted in the generation of a sharper peak and shortened the calcination time. Hence, for the calcination reaction that occurred at 850 °C, the time required to convert ~3 kg calcium carbonate to calcium oxide was about 90 minutes. The required time decreased to ~65 minutes for calcination temperatures as high as 900 °C (approximately 30% quicker).
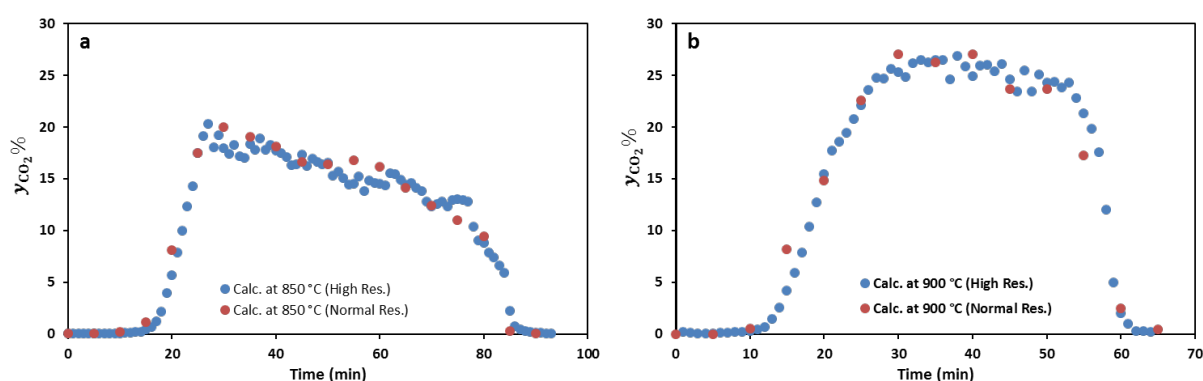
Figure 7.16: CO_2 concentration profiles at the fluid bed outlet versus time for: (a) calcination at 850 °C and (b) 900 °C. Since the inlet gas composition (normal air) in the calcination process for all of the experiments remained constant, it is not shown here.

Figures 7.17(a) and (b) show the CO_2 concentration variations of the gas leaving the fluid bed during the carbonation process. The carbonation temperatures were 650 °C and 700 °C for experiments 1-3 and 4-6, respectively. According to Figures 7.17(a) and (b), the CO_2 concentrations during the second carbonation cycle were higher than the concentrations during the first cycle. In addition, it was evident that the outlet concentration increased with an increase in the CO_2 content of the inlet gas. Hence, in Figures 7.17(a) and (b), the CO_2 concentrations in the blue series was the highest, while the CO_2 concentrations in the green series was the lowest. Moreover, a comparison between Figures 7.17(a) and (b) demonstrates that the temperature in which the carbonation is carried out impacts on the CO_2 concentration. Hence all the CO_2 concentrations at the end of the carbonation in Figure 7.17(a) are smaller than those in Figure 7.17(b) (for the same inlet CO_2 concentration). Therefore, it can be suggested that the CO_2 capture during carbonation was higher when the temperature was 650 °C.
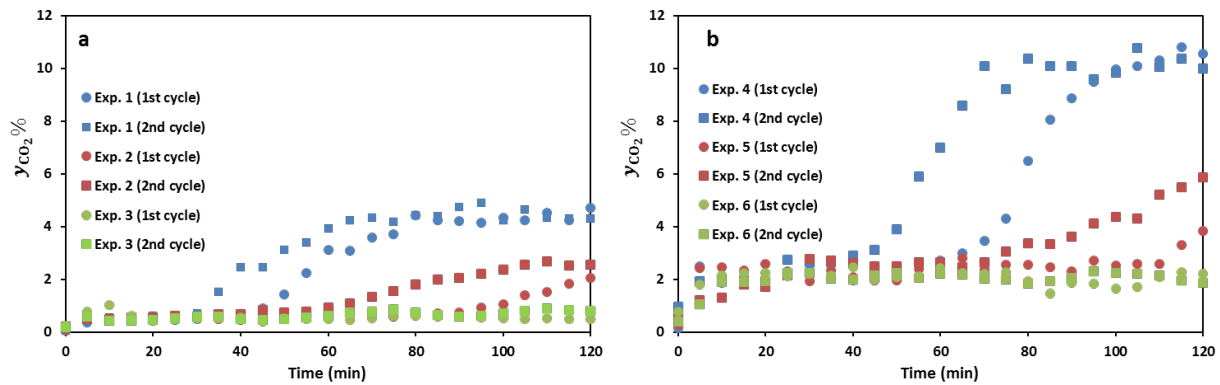
Figure 7.17: CO_2 concentration profile of the gas leaving the fluid bed for: (a) experiments 1-3 and (b) experiments 4-6.

At the end of each carbonation, a sample was taken, and the carbonation reaction conversion was measured using TGA. The results are reported in Table 7.9 below.

Table 7.9: The final conversion of samples taken after each carbonation cycle obtained using TGA

Experiment	1st Carb.	2nd Carb.
1	0.510±0.008	0.402+0.009
2	0.507±0.004	0.361±0.006
3	0.194±0.005	0.208±0.007
4	0.578±0.003	0.446±0.005
5	0.564±0.002	0.464±0.003
6	0.094±0.004	0.075±0.003

The results show that the conversions in experiments 4 and 5 were higher than the others, given the concentration of CO_2 was 13 and 20%, respectively. This implied that the conversion was highest when the carbonation and calcination temperatures were 700 and 850 °C,

respectively. The high conversion rate due to a lower calcination temperature supported the findings of the previous section. However, the carbonation temperature in which the conversion is the highest might be considered contradictory. The increase in the conversion with carbonation temperature can be related to faster kinetics, which means that the conversion would get to a higher degree in a shorter period compared with a lower carbonation temperature. It should be noted that the observed conversion for cases with the carbonation temperature at 650° C was not the final value, and the final conversion could be higher than those reported in experiments 4 and 5, given the carbonation duration was sufficiently long (more than 2 hours).

In order to keep the temperature of the fluid bed constant during calcination or carbonation processes, LPG was used. During the calcination reactions, LPG was used to provide the heat for the endothermic reaction of the calcination. Although the carbonation reaction was exothermic due to the poor insulation of the fluid bed, some LPG was burned to maintain the temperature constant. It should be noted that the duration of the carbonation was about two times more than the duration of the calcination in each experiment. Therefore, the average consumed fuel per hour during the two carbonation cycles (e.g., 0.78 kg/hr) was smaller compared to the average consumed fuel per hour during the two calcination cycles (e.g., 1.72 kg/hr). Based on these results, the smallest LPG usage was related to experiments with a gas mixture containing 5% CO_2. This implied that the carbonation process for experiments 3 and 6 did not complete after 2 hours of the carbonation. Therefore, any CO_2 concentration larger than 5% would be more energetically favourable. The optimum inlet concentrations of CO_2 could vary with the bed inventory, gas flow rate and the fluid bed design.

Moreover, although calcination at 900 °C (experiments 1-3) caused the calcination reactions to be completed quicker, their energy uptake (LPG consumption) was more than the cases (experiments 4-6) in which the calcination was carried out at 850 °C. Hence, it is suggested to carry out the calcination at 850 °C in order to decrease the energy consumption during the calcination.

7.3.2 Primary Tests

The primary experiments using the pilot-scale fluidised bed consisted of 162 experiments. Based on the results gathered in previous sections, the calcination temperature was set at 850 °C. The carbonation temperature varied from 600 to 700 °C. The full experimental conditions were reported in Table 4.9. The calcium-rich particles in the pilot-plant tests did not experience any cycling, and after each calcination and carbonation the bed inventory was renewed. Each experiment was carried out two times. Figure 7.18 illustrates the CO_2 concentrations of the exhaust during the carbonation for three cases. The experimental conditions are reported in the figures. It is evident from Figure 7.18 that the experimental data are scattered around the average black line. To improve the visual quality of the images, the average values of the tests are shown in the rest of the figures in this section.

Figure 7.19 below shows the obtained results for a 5% inlet CO_2 concentration. The flow rates, bed inventories and carbonation temperatures were the variables. Figures 7.19(a)-(i) demonstrate that an increase in the inventory led to a decrease in the outlet CO_2 concentration. Since a higher inventory implies that there was more material, hence the carbonation reaction took longer. It was also shown that the carbonation temperature had an important effect on the recorded outlet concentration.
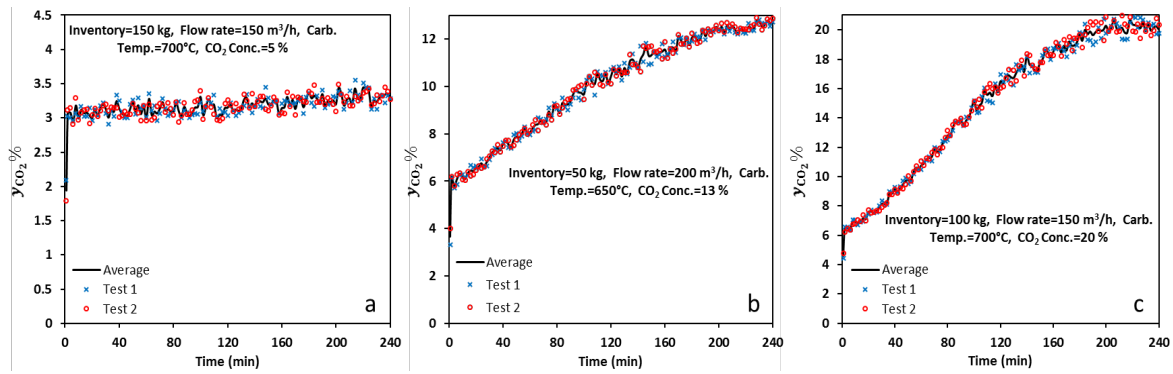
Figure 7.18: Outlet CO_2 concentration versus time during carbonation for two tests and their averages for: (a) 5% inlet CO_2 concentration, (b) 13% inlet CO_2 concentration, (c) 20% inlet CO_2 concentration.
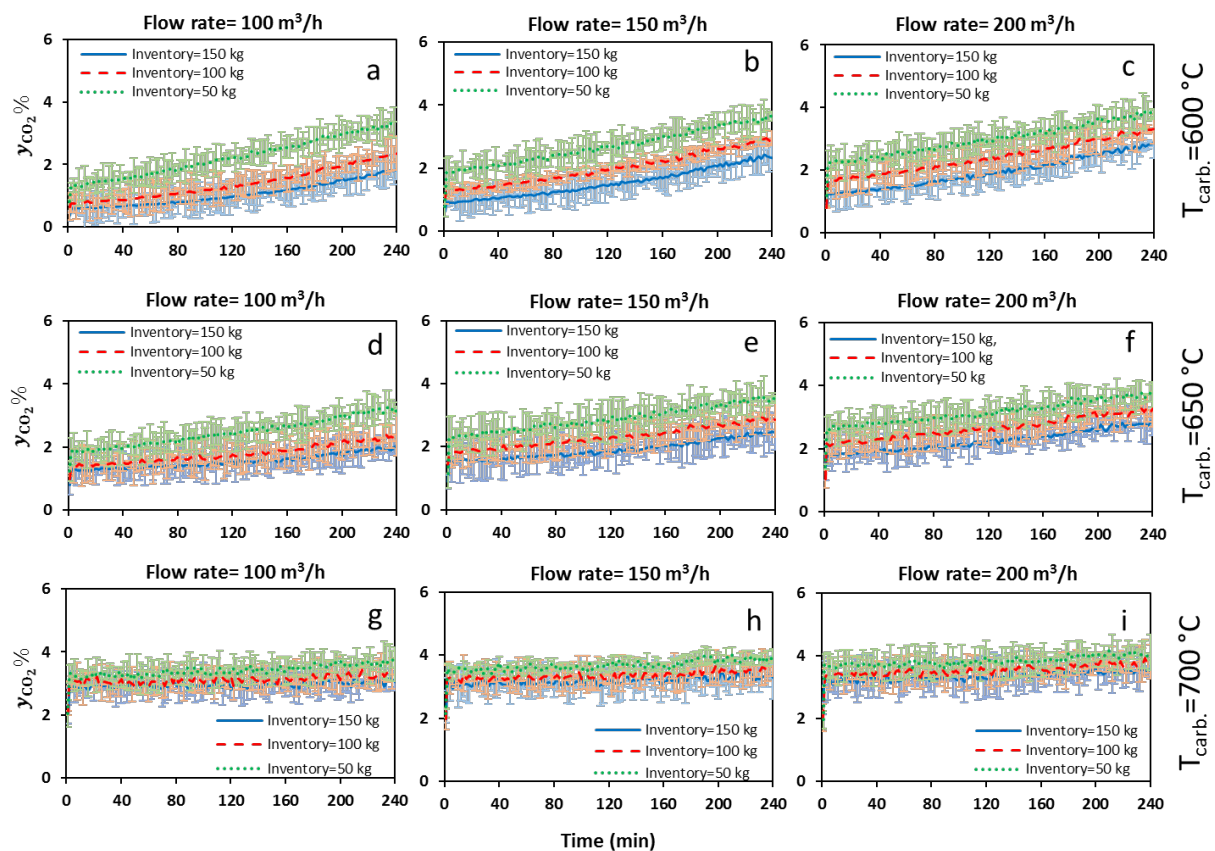
Figure 7.19: Outlet CO_2 concentration versus time during carbonation for 5% inlet CO_2 concentration at three inventories and gas flow rates for: (a)-(c) $T_{carb.}$= 600 °C, (d)-(f) $T_{carb.}$= 650 °C, (g)-(i) $T_{carb.}$= 700 °C.

The tests, which were carried out at 700 °C, were not sensitive to the gas flow rate. This was due to the dominant effect of the high equilibrium CO_2 concentration. It was also evident that for carbonation temperatures lower than 700 °C, there was an increase in the gas flow rate, although it decreased the residence time of fluidising gas, resulting in higher CO_2 concentrations at the end of the carbonation. Comparing the CO_2 outlet concentrations after 10 minutes with those after 240 minutes of the reaction showed that in a constant carbonation temperature, the higher gas flow rate lowered the carbonation conversion. Hence, it is suggested that for a 5% CO_2 concentration the flow rate and carbonation

temperature should be minimal to increase the residence time of the gas in the bed and to increase the carbonation driving force. Finally, the bed inventory should be maximum to produce heat for a longer period.

Figure 7.20 depicts the obtained results for a 13% inlet CO_2 concentration versus time. In each row ((a)-(c), (d)-(f) and (g)-(i)) and column of Figure 7.20, the carbonation temperature and the gas flow rate were constant, respectively. However, the increase in the inventory promoting the carbonation reaction and sudden increase in the outlet CO_2 concentration at the beginning of the carbonation did not occur in all cases. A rise in the flow rate promoted the observed increase. For example, for an inventory equal to 100 kg, cases (a) and (d) did not show any sudden increase, while cases (b), (c), (e) and (f) demonstrated the rise. The increase in the inventory minimised this effect as it aided the contact time (residence time) of the fluidising gas and improved the conversion. An increase in the carbonation temperature decreased the driving force and slowed down the carbonation reaction. However, this effect was not as evident as in the cases with a 5% CO_2 concentration. Finally, higher flow rates decreased the gas residence time. It can be concluded that for a 13% CO_2 concentration, the highest flow rate was the most favourable given the carbonation temperature and bed inventory remained at 600 °C and 150 kg, respectively. It should be noted that a high flow rate in carbonation is more favourable as more reaction heat can be transferred during carbonation.
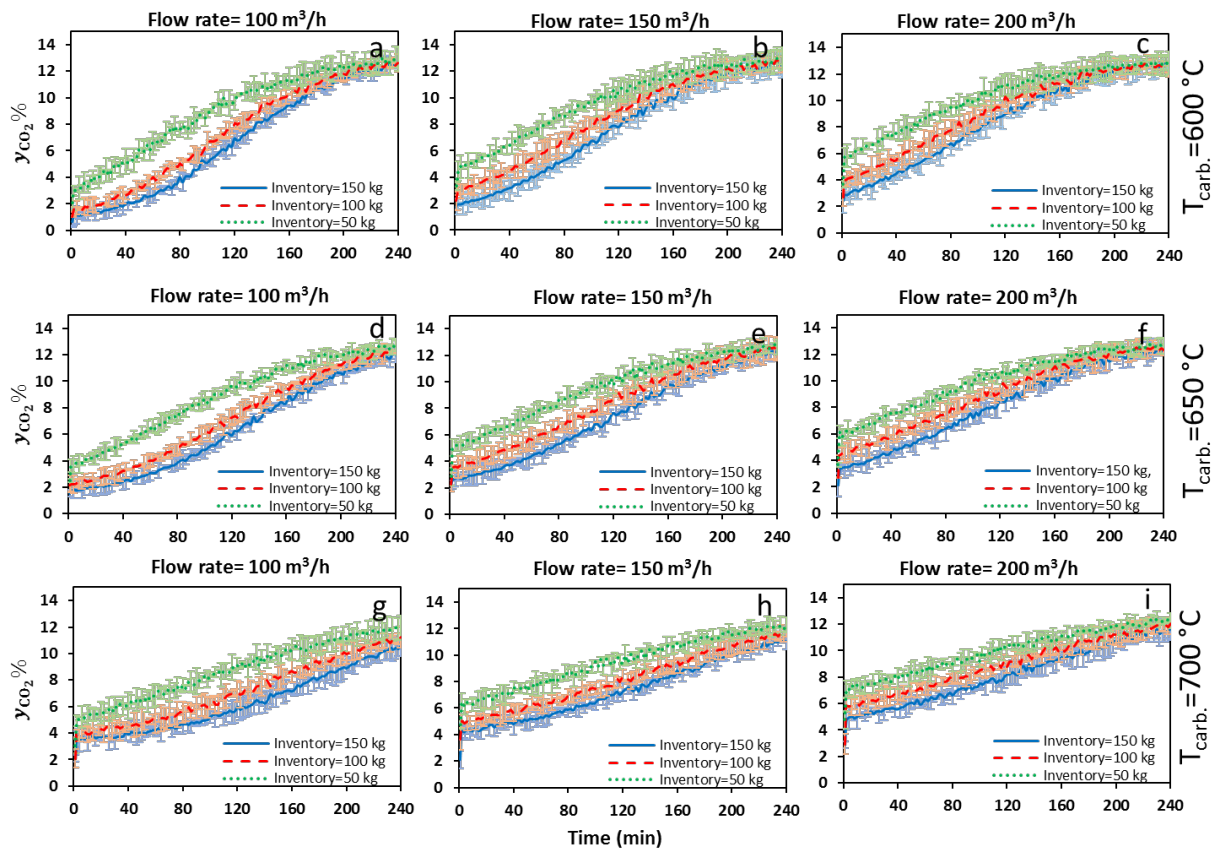
Figure 7.20: Outlet CO_2 concentration versus time during carbonation for a 13% inlet CO_2 concentration at three inventories and gas flow rates for: (a)-(c) $T_{carb.}$= 600 °C, (d)-(f) $T_{carb.}$= 650 °C, (g)-(i) $T_{carb.}$= 700 °C.

Figure 7.21 below shows the obtained results for a 20% CO_2 concentration. The high CO_2 concentration at the inlet caused a sudden increase in the outlet CO_2 concentration in most

of the cases except for (a), (d) and (g), indicating that the bed material should exceed 150 kg if the flow rate were more than 100 m^3/h. Hence, to achieve the best results with a 20% inlet CO_2 concentration, it is suggested that the inventory, gas flow rate and carbonation temperature should be 150 kg, 100 m^3/h and 650 °C, respectively.

Figure 7.22 below presents the CO_2 concentrations of the exhaust during calcination. The calcination condition was always fixed at 850 °C and 200 m^3/h for the calcination temperature and gas flow rate, respectively. Normal air without any CO_2 was used for the calcination. Therefore, the only variable during the calcination was the inventory of the bed. The initial temperature for each calcination was equal to the ambient temperature. Each series in Figure 7.22 shows the averages of the three tests. It is evident that when the bed inventory was 50 kg, the maximum outlet CO_2 concentration was about 35% and the calcination reaction finished earlier. With an increase in the inventory of the bed, the peak increased to above 40% and stayed constant for some time. The period increased when the inventory increased from 100 to 150 kg. All cases showed a sharp increase and decrease in their CO_2 concentrations, marking the initiation and end of the calcination reaction, respectively. The results suggested that the calcination period for the different bed inventories was very similar. This result indicates that the mechanism of supplying the heat to the bed (e.g., by burning LPG in the annulus) was beneficial as an increase in the bed inventory did not drastically affect the required time.
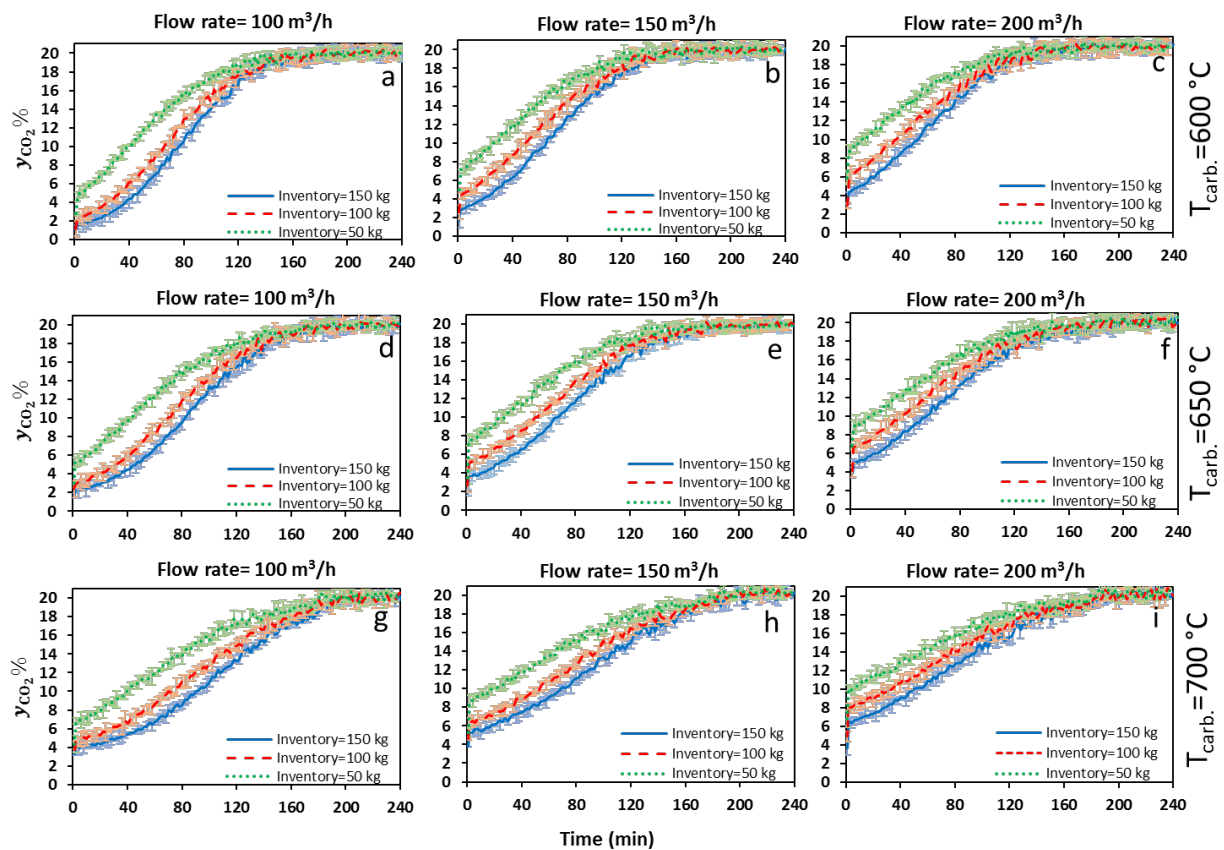
Figure 7.21: Outlet CO_2 concentration versus time during carbonation for a 20% inlet CO_2 concentration at three inventories and gas flow rates for: (a)-(c) $T_{carb.}$= 600 °C, (d)-(f) $T_{carb.}$= 650 °C, (g)-(i) $T_{carb.}$= 700 °C.
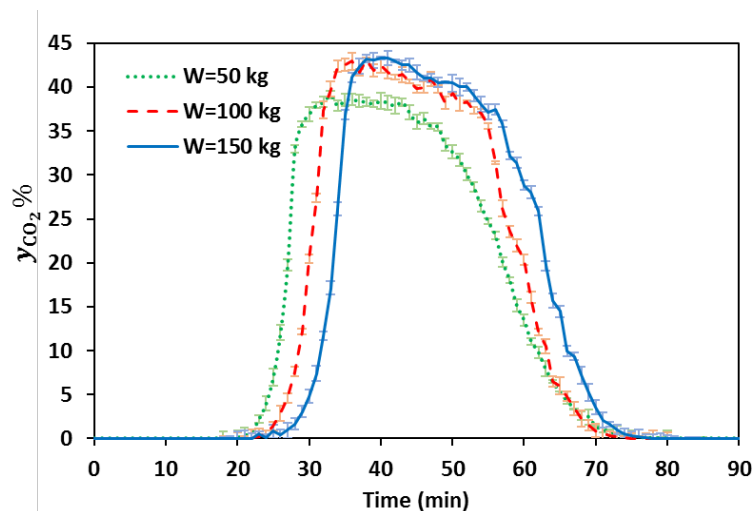
Figure 7.22: Outlet CO_2 concentration versus time during calcination at 850 °C and 200 m^3/h for three inventories.

7.3.3 Manifold Switching

One of the most important investigations undertaken in the project was the examination of the manifold switching (MS) concept where the feed gas streams are systematically switched rather than solids being circulated. The importance of the MS concept is twofold: firstly MS allows us to decouple the solid circulation and particle attrition issues from the reaction kinetics behaviour of particles, and secondly MS enables us to resolve the issues associated with the particle transport in an effective manner.

The experimental results obtained from the MS investigation confirmed the strengths of the concept and its usefulness for CaL process. But the results also highlighted several shortcoming of the MS concept including the formation of undesirable hot spots during both calcination and carbonation phases as well as the complexity of accurately controlling the process especially during the switch over phase.

7.4 LARGE-SCALE EXPERIMENTS (Milestone 6)

The experimental matrix was reported in Table 4.10. The first carbonation cycle was conducted at 600 °C, as shown in Figure 7.23 below. The bed temperature was successfully maintained with only the heat generated from the carbonation reaction. The inlet CO_2 concentration averaged 5 vol.% during the experiment, and a capture efficiency of 90% was achieved (i.e., 90% of the CO_2 was captured by CaO, resulting in a CO_2 outlet concentration of 0.45 vol.%).
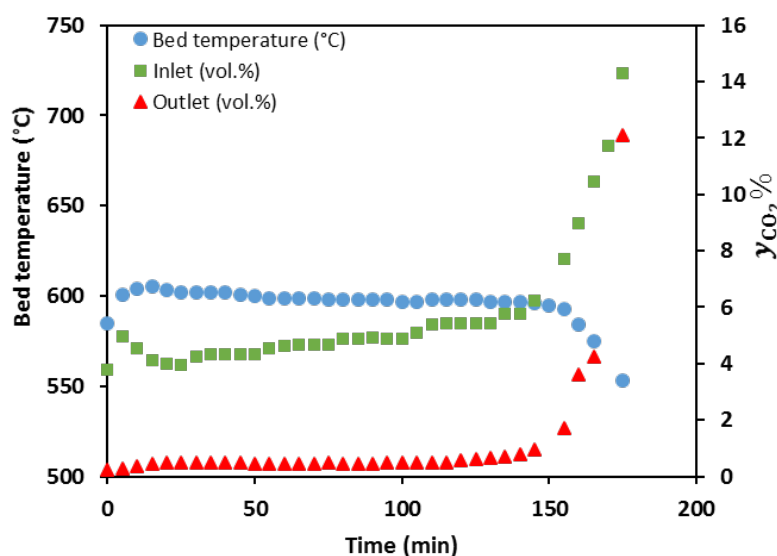
Figure 7.23: Carbonation experiment 1: bed temperature 600 °C, plenum temperature 379°C.

Experiments 2, 3 and 4 were conducted at 700 °C, with Figure 7.24(a) below showing the combined results for experiments 2, 3 and 4. As shown in Figure 7.24(a), the bed temperature was held at 700 °C by maintaining the CO_2 inlet concentration at approximately 11 vol.%. At this temperature, the CO_2 capture efficiency was approximately 65%, which is significantly lower than that observed for 600°C, due to the change in the equilibrium partial pressure. Figure 7.24(a) shows that the results were repeatable, with the three experiments requiring near identical CO_2 concentrations to maintain the bed at 700 °C. There was only a slight difference in the cycle times, with the activity of the stone dust material decreasing slightly with successive cycles. Figure 7.24(b) presents the combined results for experiments 5 and 6, which were performed at 710 °C. The CO_2 concentration required to maintain the bed temperature was between 11.5-12 vol.% and a capture efficiency of 62-65% was achieved. Similar to the experiments performed at 700 °C, the results for experiments undertaken at 710 °C were repeatable.
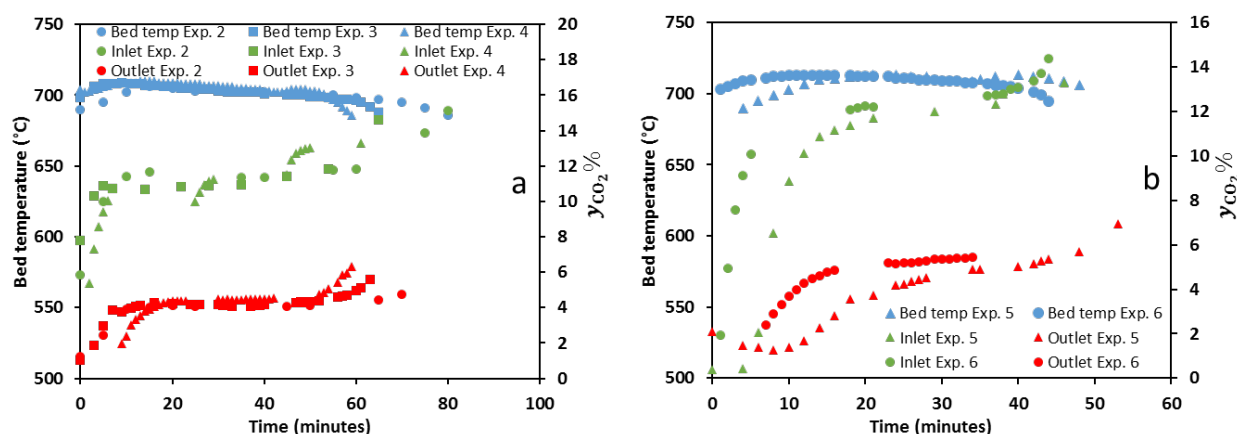
Figure 7.24: Carbonation results for: (a) experiments 2, 3 and 4, and (b) experiments 5 and 6.

After the completion of the first six experiments, it was observed that in the large-scale fluidised bed the heat losses were significant. As such, the temperature differential between the inlet and the fluid bed ranged from 220-300 °C for the first six experiments (see Table 7.10). Hence, for the fluid bed to be maintained at a constant temperature, enough heat must be generated from the carbonation reaction to overcome the temperature differential between the plenum and the fluid bed.

To investigate if higher carbonation temperatures could be reached in the retrofitted large-scale fluidised bed, it was proposed that the natural gas burner be kept switched on during the carbonation experiments. This would overcome some of the heat losses in the system and reduce the temperature differential between the inlet and the fluid bed.

For experiments 7 and 8, as shown in Figure 7.25 below, the burner was operated at 30% opening. In comparison to experiment 5 and 6, a 30% burner opening increased the plenum (inlet) temperature by 150 °C and decreased the temperature differential between the bed and the inlet to 130 °C. It can be seen in Figure 7.25 that the inlet CO_2 concentration of 12.5 vol.% was similar to that in experiments 5 and 6, however with the additional heat provided by the burner, a bed temperature of 730 °C was reached, and the capture efficiency was 43%.
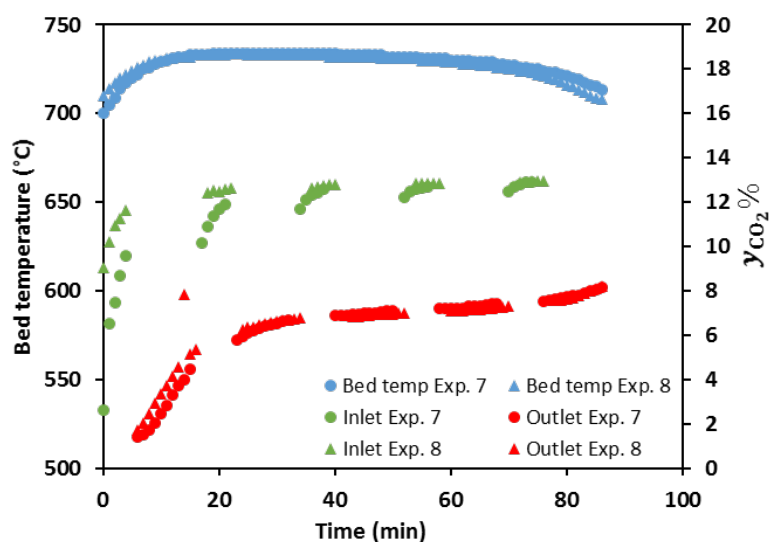
Figure 7.25: Combined results for carbonation experiments 7 and 8; average bed temperature 730 °C, plenum temperature 568 °C, burner opening 30%.

To verify the effects of running the experiments with the addition of the burner, a supplementary experiment was conducted with the burner at 30% opening and no CO_2 injection (see Figure 7.26 below). It can be seen that with only the burner operating, the bed temperature quickly decreased as there was not sufficient CO_2 for the carbonation reaction to proceed (only 1.5 vol% CO_2 from the combustion of natural gas in the burner), with the inlet CO_2 concentration equalling the outlet concentration for close to the duration of the experiment.
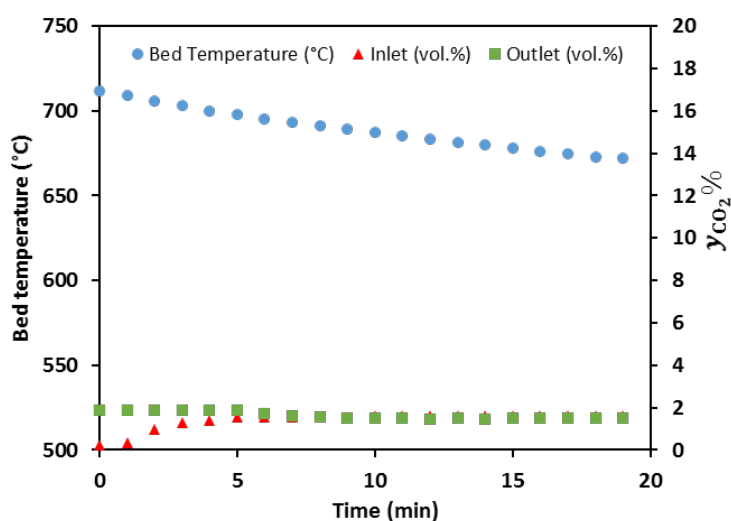
Figure 7.26: Experiment with burner opening of 30% and no CO_2 injection.

Following the experiments conducted with a burner opening of 30%, an experiment (Exp. 9) was performed with a burner opening of 50%, with the results presented in Figure 7.27 below. In comparison to experiments 7 and 8, a burner opening of 50% further increased the plenum (inlet) temperature by 60 °C and decreased the temperature differential between the bed and the inlet to 50 °C (see Table 7.10). The bed temperature was maintained at 740 °C for a CO_2 inlet concentration of 13.5 vol.%, and a capture efficiency of 54% was achieved. The experimental run time before the bed reached saturation was also increased from approximately 90 minutes for experiments 7 and 8 to 140 minutes.
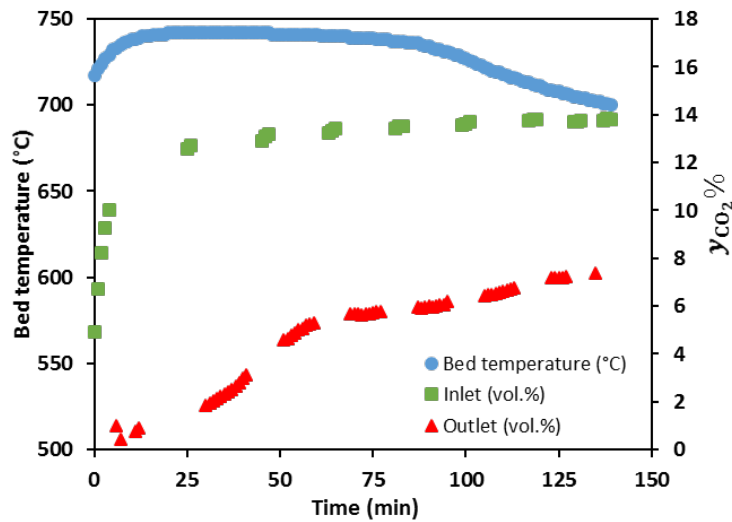
Figure 7.27: Carbonation experiment 9; bed temperature 740 °C, plenum temperature 626 °C, burner opening 50%.

In addition to the steady state carbonation experiments conducted, a ramp experiment (Exp. 10) was also conducted, as presented in Figure 7.28 below. It can be seen that the bed temperature was decreased to 540 °C before the CO_2 was introduced. In order to avoid rapid heating and thermal shock to the reactor refractory lining, the CO_2 concentration was increased in a step wise fashion. Using this method, a heating rate of 3°C/min was easily achieved, demonstrating the fast response ability of the system.
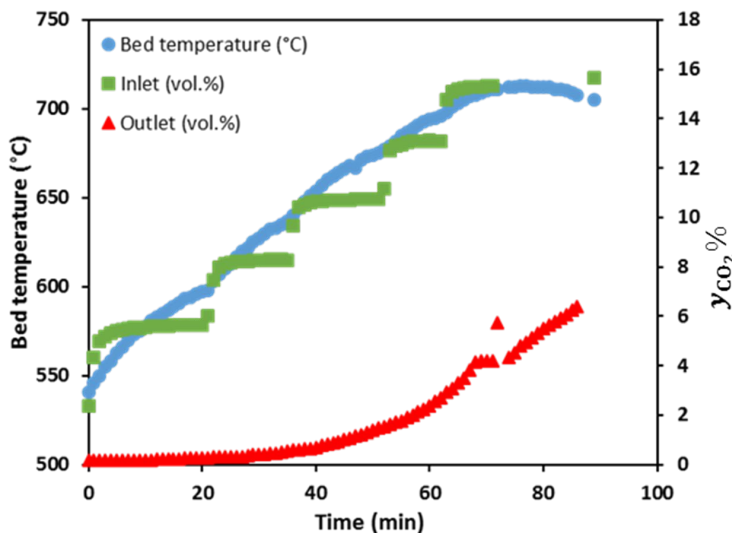
Figure 7.28: Carbonation experiment 10; ramp from bed temperature of 540 to 710 °C.

A summary of the carbonation experimental results are presented in Table 7.10 below. The maximum temperature achieved was 742 °C in experiment 9, which was close to the maximum operating temperature of the large-scale reactor. For the operation to be sustained at 742 °C, sufficient CO_2 above the equilibrium partial pressure must be supplied to the bed in order for carbonation to occur and for heat to be generated. The equilibrium CO_2 partial

pressure for CaO/CaCO$_3$ is presented in Figure 7.28, and it can be seen that at 740 °C, 5.9 vol.% CO$_2$ is required before the carbonation reaction will occur. In the case of experiment 9, 13.4 vol.% CO$_2$ was provided to the bed, of which 7.3 vol.% was captured to generate the required heat to maintain the bed at 740 °C and to overcome the heat losses from the system.

Table 7.10: Summary of the carbonation experimental results

EXP	Bed Temp. (°C)	Burner Opening (%)	Air flowrate (m³/h)	Average Bed Temp. (°C)	Plenum Temp. (°C)	ΔT (°C)	CO$_2$ inlet (vol.%)	CO$_2$ outlet (vol.%)	CO$_2$ captured (vol.%)	Capt. Eff. (%)
1	600	0	1200	599	379	220	4.7	0.5	4.2	89.8
2	700	0	1200	701	395	306	11.6	4.1	7.5	65.0
3	700	0	1200	703	406	297	10.9	4.1	6.8	62.2
4	700	0	1200	706	408	298	10.8	4.1	6.7	62.1
5	710	0	1200	710	426	284	11.5	4.0	7.6	65.5
6	710	0	1200	711	418	293	12.2	4.7	7.6	61.8
7	730	30	1200	731	569	162	12.4	7.1	5.3	42.7
8	730	30	1200	731	567	164	12.8	7.3	5.5	43.3
9	740	50	1200	739	626	113	13.4	6.1	7.3	54.2
10	540-710	0	1200	-	420-630	-	3-16%	0-7%	4-9%	-

The large-scale tests demonstrated that the CaL energy storage technology is capable of producing heat and keeping the bed temperature constant. However, to achieve this the heat loss should be minimised and the fluidised bed reactor should be designed according to the operational conditions.

Chapter 8
Conclusions

In this project the RES and CaL based thermochemical energy storage concepts were theoretically and experimentally examined and their performance characteristics were evaluated through a comprehensive series of process modelling and benchmarking studies.

After developing many flowsheets and simulation scenarios in the feasibility study of Stage 1, it was found that the calcium looping retrofitted to a secondary steam cycle (CaL+SSC) configuration was feasible from both a technical and economic point of view. CaL+SSC successfully met all of the performance targets set out in the funding agreement. The RES+SSC and RES+OCGT configurations were also found to be technically feasible but economically were not viable unless a revenue stream was created by marketing their oxygen by-products. The use of OCGT as the power block for both the RES and CaL configurations required the use of a secondary fuel which, apart from added cost and complexity, would result in additional GHG emissions.

In Stage 2, the energy carrier particles (copper-rich and calcium-rich particles) were characterised in fixed and fluidised beds using different analytical methods. The results showed that the copper-rich particles had very high cyclic stability. These particles did not show any decline in their structures and their reactivities with the number of cycles. However, the particles required high temperatures (900-1100 °C) for these operations. The calcium-rich particles demonstrated a decline in their reactivity with the number of cycles, which was a function of the operating temperatures and the fluidising gas composition. It was also shown that a well-insulated large-scale reactor for the CaL process could maintain the temperature constant for a long period.

The key findings of the project are summarised below:

- From a technical point of view, all four configurations of the energy storage unit were capable of storing electrical energy in a thermochemical form, and were therefore feasible.

- However, from an economic point of view, the RES+SSC and RES+OCGT configurations were found to be viable only when their oxygen by-product streams were assumed to generate revenue. Of the two configurations, the RES+OCGT was found to be the less attractive economically because of the need for a secondary fuel, either compressed natural gas (CNG) or liquefied natural gas (LNG).

- The CaL+OCGT system was found to not be economically viable, primarily because of the need for a secondary fuel (CNG or LNG) which, apart from the added cost and complexity, would result in additional GHG emissions.

- In contrast, the CaL+SSC configuration was found to be feasible from both a technical and economic point of view and it successfully met all of the performance targets set out in the funding agreement.

- The reactivity of the calcium-rich particles dropped after 5 cycles, however due to their lower energy requirements and low cost, they were more suitable than the copper-rich particles if the oxygen production is not important.

- The copper-rich particles demonstrated a stable reactivity after 5 cycles.

- The calcination and carbonation temperatures had an impact on the reactivities of the calcium-rich particles and low temperatures resulted in a high reactivity.

- The reaction mechanisms of the calcium-rich particles for high CO_2 concentrations was more complicated than for the copper-rich particles.

- Calcium-rich particles were used for the field trials. It was noticed that the temperature of the bed during the carbonation process remained constant and that the CO_2 concentration in the exhaust increased gradually over time. This showed that calcium-rich particles could be utilised to prevent the cycling of a power plant and decrease its maintenance and operational costs.

Chapter 9

Recommendations

It is recommended that for the next steps of TES using the CaL, a special fluidised bed reactor should be designed. The fluidised bed should be the type of fast circulation fluidised bed to decrease the footprint and improve the kinetics of the reactions. In addition, the fluidised bed should be designed to be able to operate continuously, meaning constant fresh feed should enter, while the spent particles should leave the reactor and exchange their heat with the incoming feed. This will provide a much better overall efficiency due to the higher constant reactivity of the particles.

References

1. Brouwer, A. S., van den Broek, M., Seebregts, A., Faaij, A. (2015). Applied Energy, 156, 107-128.

2. Van den Bergh, K., Delarue, E. (2015). Energy Conversion and Management, 97, 70-77.

3. Lefton SA., Phil Besuner. (2006) Coal Power Magazine: 16-20.

4. Abadie, L. M. (2015). Journal of Electrical Power & Energy Systems, 64, 41-49.

5. Electrical Energy Storage: Technology Overview and Applications; CSIRO report; 2015.

6. Energy Storage Opportunities and Challenges: A West Coast Perspective White Paper; Ecofys April 4, 2014.

7. Energy Storage Technologies White Paper; Port of Long Beach, Aug 2016.

8. Hugh Bromley; Australia and Global Outlook for Energy Storage Deployment; Bloomberg New Energy Finance, June 2015.

9. Grid Energy Storage; US Department of Energy, Dec 2013.

10. Final Report: Overview of Storage Technologies; Sensible – DELIVERABLE; A Project funded under European Union's Horizon 2020 Innovation program, 2016.

11. Abbas A. Akhil, Georgianne Huff, Aileen B. Currier, Benjamin C. Kaun, Dan M. Rastler, Stella Bingqing Chen, Andrew L. Cotter, Dale T. Bradshaw, and William D. Gauntlett; DOE/EPRI 2013 Electricity Storage Handbook in Collaboration with NRECA; SANDIA REPORT; SAND2013-5131; Unlimited Release; July 2013.

12. Technology Roadmap Energy storage; IEA report 2014.

13. David Connolly; A Review of Energy Storage Technologies for the Integration of Fluctuating Renewable Energy; University of Limerick, Aug 2009.

14. International Electrotechnical Commission. "Electrical energy storage white paper." Geneva, Switzerland: International Electrotechnical Commission (2011).

15. Carnegie, R., Gotham, D., Nderitu, D., and Preckel, P. V. "Utility scale energy storage systems." State Utility Forecasting Group, Purdue University, West Lafayette (2013).

16. Chen, H., Cong, T.N., Yang, W., Tan, C., Li, Y. and Ding, Y., 2009. Progress in electrical energy storage system: A critical review. Progress in Natural Sci., 19(3), pp.291-312.

17. Díaz-González, F., Sumper, A., Gomis-Bellmunt, O. and Villafáfila-Robles, R., 2012. A review of energy storage technologies for wind power applications. Renewable and sustainable energy reviews, 16(4), pp.2154-2171.

18. International Electrotechnical Commission. "Electrical energy storage white paper." Geneva, Switzerland: International Electrotechnical Commission (2011).

19. Ali, M.H., Wu, B. and Dougal, R.A., 2010. An overview of SMES applications in power and energy systems. IEEE Transactions on Sustainable Energy, 1(1), pp.38-47.

20. Hassenzahl, W.V., Hazelton, D.W., Johnson, B.K., Komarek, P., Noe, M. and Reis, C.T., 2004. Electric power applications of superconductivity. Proceedings of the IEEE, 92(10), pp.1655-1674.

21. Giatrakos, G.P., Tsoutsos, T.D., Mouchtaropoulos, P.G., Naxakis, G.D. and Stavrakakis, G., 2009. Sustainable energy planning based on a stand-alone hybrid renewableenergy /

hydrogen power system: application in Karpathos Island, Greece. Renewable Energy, 34(12), pp.2562-2570.

22. Taylor, P., Bolton, R., Stone, D., Zhang, X.P., Martin, C. and Upham, P., 2012. Pathways for energy storage in the UK. Report for the centre for low carbon futures, York.

23. Oberhofer, A. and Meisen, P., 2012. Energy storage technologies & their role in renewable integration. Global Energy Network Institute (GENI).

24. Alkan, C., Günther, E., Hiebler, S., Ensari, Ö.F. and Kahraman, D., 2012. Polyurethanes as solid–solid phase change materials for thermal energy storage. Solar Energy, 86(6), pp.1761-1769.

25. Energy Storage News website, accessed 25.07.2017, https://www.energy-storage.news/news/energyaustralia-ponders-worlds-largest-seawater-pumped-hydro-energy-storage.

26. Ma, T., Yang, H. and Lu, L., 2014. Feasibility study and economic analysis of pumped hydro storage and battery storage for a renewable energy powered island. Energy Conversion and Management, 79, pp.387-397.

27. Luo, X., Wang, J., Dooner, M. and Clarke, J., 2015. Overview of current development in electrical energy storage technologies and the application potential in power system operation. Applied Energy, 137, pp.511-536.

28. Long, Z. and Zhiping, Q., 2008. Review of flywheel energy storage system. In Proceedings of ISES World Congress 2007 (Vol. I–Vol. V). Springer Berlin Heidelberg. pp. 2815-2819

29. Succar S, Williams R. H. Compressed air energy storage: theory, resources, and applications for wind power. Princeton Environmental Inst. Energy Anal Group; 2008.

30. Raju, M. and Khaitan, S.K., 2012. Modeling and simulation of compressed air storage in caverns: a case study of the Huntorf plant. Applied Energy, 89(1), pp.474-481.

31. Ares website, accessed 26.07.2017, http://www.aresnorthamerica.com/.

32. GIGAOM website accessed 26.07.2017, https://gigaom.com/2012/03/27/the-story-of-energy-cache-a-drop-dead-simple-energy-idea/.

33. Solar electricity storage website accessed 26.07.2017, http://www.linkz2u.com/solar/solar-electricity-storage.

34. Chen, H., Cong, T.N., Yang, W., Tan, C., Li, Y. and Ding, Y., 2009. Progress in electrical energy storage system: A critical review. Progress in Natural Sci, 19(3), pp.291-312.

35. Barbour, E., 2013. Investigation into the potential of energy storage to tackle intermittency in renewable energy generation.

36. Smith, S.C., Sen, P.K. and Kroposki, B., 2008, July. Advancement of energy storage devices and applications in electrical power system. In Power and Energy Society General Meeting-Conversion and Delivery of Electrical Energy in the 21st Century, 2008 IEEE (pp. 1-8). IEEE.

37. Kaldellis, J.K. and Zafirakis, D., 2007. Optimum energy storage techniques for the improvement of renewable energy sources-based electricity generation economic efficiency. Energy, 32(12), pp.2295-2305.

38. Divya, K.C. and Østergaard, J., 2009. Battery energy storage technology for power systems: An overview. Electric Power Systems Research, 79(4), pp.511-520.

39. Nguyen, T. and Savinell, R.F., 2010. Flow batteries. The Electrochemical Society Interface, 19(3), pp.54-56.

40. Sum, E. and Skyllas-Kazacos, M., 1985. A study of the V (II)/V (III) redox couple for redox flow cell applications. Journal of Power sources, 15(2-3), pp.179-190.

41. Dietrich, A., Dammel, F. and Stephan, P., 2016. Exergoeconomic Analysis of a Pumped Heat Electricity Storage System with Concrete Thermal Energy Storage. International Journal of Thermodynamics, 19(1), pp.43-51.

42. Decourt, B. and R. Debarre (2013), "Electricity storage", *Factbook.*

43. Schlumberger Business Consulting Energy Institute, Paris, France and Paksoy, H. (2013), "Thermal Energy Storage Today".

44. Moghtaderi B, Maddocks A, Tremain P, Calcium Looping Energy Storage Proof-of-Concept Report, A report Prepared for Jord International Pty Ltd, July 2017.

45. Moghtaderi, B. (2010). Application of chemical looping concept for air separation at high temperatures. *Energy & Fuels*, *24*, 190-198.

46. Moghtaderi, B. (2012). Review of the recent chemical looping process developments for novel energy and fuel applications. *Energy & Fuels*, *26*(1), 15-40.

47. Shah, K., Moghtaderi, B., & Wall, T. (2013). Effect of flue gas impurities on the performance of a chemical looping based air separation process for oxy-fuel combustion. *FUEL*, *103*, 932-942.

48. Shah, K. V., Moghtaderi, B., & Wall, T. F. (2012). Selection of suitable oxygen carriers for chemical looping air separation: A thermodynamic approach. *Energy & Fuels*, *26*(4), 2038-2045.

49. Shah, K., Moghtaderi, B., Zanganeh, J., & Wall, T. (2013). Integration options for novel chemical looping air separation (ICLAS) process for oxygen production in oxy-fuel coal fired power plants. *Fuel*, *107*, 356-370.

50. Alghamdi, Y. A., Doroodchi, E., & Moghtaderi, B. (2013). Mixing and segregation of binary oxygen carrier mixtures in a cold flow model of a chemical looping combustor. *CHEMICAL ENGINEERING JOURNAL*, *223*, 772-784.

51. Song, H., Shah, K., Doroodchi, E., Wall, T., & Moghtaderi, B. (2014). Analysis on Chemical Reaction Kinetics of CuO/SiO_2 Oxygen Carriers for Chemical Looping Air Separation. *ENERGY & FUELS*, *28*(1), 173-182.

52. Song, H., Shah, K., Doroodchi, E., Wall, T., & Moghtaderi, B. (2014). Reactivity of Al_2O_3- or SiO_2-Supported Cu-, Mn-, and Co-based oxygen carriers for chemical looping air separation. *Energy and Fuels*, *28*(2), 1284-1294.

53. Peng, Z., Doroodchi, E., Alghamdi, Y. A., Shah, K., Luo, C., & Moghtaderi, B. (2015). CFD-DEM simulation of solid circulation rate in the cold flow model of chemical looping systems.

54. Shah, K., Zhou, C., Song, H., Doroodchi, E., & Moghtaderi, B. (2015). A novel hybrid chemical-looping oxy combustor process for the combustion of solid and gaseous fuels: Thermodynamic analysis. *Energy and Fuels*, *29*(2), 602-617.

55. Zhou, C., Shah, K., Song, H., Zanganeh, J., Doroodchi, E., & Moghtaderi, B. (2016). Integration Options and Economic Analysis of an Integrated Chemical Looping Air Separation Process for Oxy-fuel Combustion. *Energy and Fuels*, *30*(3), 1741-1755.

56. The Future Role and Challenges of Energy Storage; EU Commission for Energy; 2015.

57. Hanak, D.P., Biliyok, C. and Manovic, V., 2015. Evaluation and modeling of part-load performance of coal-fired power plant with postcombustion CO_2 capture. Energy & Fuels, 29(6), pp.3833-3844.

58. Towler, G. and Sinnott, R.K., 2012. Chemical engineering design: principles, practice and economics of plant and process design. Elsevier.

59. Zhou, Cheng, Kalpit Shah, and Behdad Moghtaderi. "Techno-economic assessment of integrated chemical looping air separation for oxy-fuel combustion: An Australian case study." Energy & Fuels 29, no. 4 (2015): 2074-2088.

60. Fout, T., Zoelle, A., Keairns, D., Turner, M., Woods, M., Kuehn, N., Shah, V., Chou, V. and Pinkerton, L., 2015. Cost and Performance Baseline for Fossil Energy Plants Volume 1a: Bituminous Coal (PC) and Natural Gas to Electricity Revision 3. National Energy Technology Laboratory Report, DOE/NETL-2015/1723.

61. Matche website, accessed 15/09/2015. http://www.matche.com/equipcost/Blower.html

62. Hasler, David, W. Rosenquist, and R. Gaikwad. "New coal-fired power plant performance and cost estimates." Sargent and Lundy project (2009): 1-82.

63. Feedstock, Estimates–Wood. "Equipment Design and Cost Estimation for Small Modular Biomass Systems, Synthesis Gas Cleanup, and Oxygen Separation Equipment." (2006).

64. Allen, A. C. I. L. "Fuel and Technology Cost Review-Data." ACIL Allen (2014).

65. Black, Veatch. "Cost and performance data for power generation technologies." Prepared for the National Renewable Energy Laboratory (2012).

66. Kumar, N., Besuner, P., Lefton, S., Agan, D. and Hilleman, D., 2012. *Power plant cycling costs* (No. NREL/SR-5500-55433). National Renewable Energy Laboratory (NREL), Golden, CO.

67. Operator, Australian Energy Market. "State of energy market" AEMO, Melbourne (May 2017).

68. AEMO website for wholesale electricity price, latest access on 01/10/2017. https://www.aemo.com.au/Electricity/National-Electricity-Market-NEM/Data-dashboard#average-price-table

69. Beaudin, M., Zareipour, H., Schellenberglabe, A. and Rosehart, W., 2010. Energy storage for mitigating the variability of renewable electricity sources: An updated review. Energy for Sustainable Development, 14(4), pp.302-314.

70. Tokuda, N., Kumamoto, T., Shigematsu, T., Deguchi, H., Ito, T., Yoshikawa, N. and Hara, T., "Development of a redox flow battery system". *Sei Tech Rev*, 1998, 45, 88-94.

71. Gevorkian, P., 2012. *Large-scale Solar Power Systems: Construction and Economics*. Cambridge University Press.

72. https://energy.gov/eere/sunshot/concentrating-solar-power-efficiently-leveraging-equilibrium-mechanisms-engineering-new[30/10/2017 3:10:54 PM]

73. Castle, W.F., 2002. Air separation and liquefaction: recent developments and prospects for the beginning of the new millennium. International Journal of Refrigeration, 25(1), pp.158-172.

74. Lazard Ltd. Levelised cost of storage – V2.0, 2016.

75. Lazard Ltd. Levelised cost of storage – V2.0, 2016.

76. Luo, X., Wang, J., Dooner, M. and Clarke, J., 2015. Overview of current development in electrical energy storage technologies and the application potential in power system operation. Applied Energy, 137, pp.511-536.

77. Kazempour, S. Jalal, M. Parsa Moghaddam, M. R. Haghifam, and G. R. Yousefi. "Electric energy storage systems in a market-based economy: Comparison of emerging and traditional technologies." Renewable energy 34, no. 12 (2009): 2630-2639

78. Hadjipaschalis, I., Poullikkas, A. and Efthimiou, V., 2009. Overview of current and future energy storage technologies for electric power applications. Renewable and sustainable energy reviews, 13(6), pp.1513-1522.

79. Wen, Z., Cao, J., Gu, Z., Xu, X., Zhang, F. and Lin, Z., 2008. Research on sodium sulfur battery for energy storage. Solid State Ionics, 179(27), pp.1697-1701.

80. Yang, Z., Zhang, J., Kintner-Meyer, M.C., Lu, X., Choi, D., Lemmon, J.P. and Liu, J., 2011. Electrochemical energy storage for green grid. Chemical reviews, 111(5), pp.3577-3613.

81. De Leon, C. Ponce, A. Frías-Ferrer, José González-García, D. A. Szánto, and Frank C. Walsh. "Redox flow cells for energy conversion." Journal of Power Sources 160, no. 1 (2006): 716-732.

82. Farret, Felix A., and M. Godoy Simoes. Integration of alternative sources of energy. John Wiley & Sons, 2006.

83. Awasthi, A., Karthikeyan, V., Das, V., Rajasekar, S. and Singh, A.K., 2017. Energy Storage Systems in Solar-Wind Hybrid Renewable Systems. In Smart Energy Grid Design for Island Countries (pp. 189-222). Springer International Publishing.

84. McDowall, J. "Integrating energy storage with wind power in weak electricity grids." Journal of Power sources 162, no. 2 (2006): 959-964.

85. Miller, R.J. Capacitors for power grid storage - multi-hour bulk energy storageusing capacitors. JME, Inc. and Case Western Reserve University. In: Trans-Atlantic Workshop on Storage Technologies for Power Grids; 2010.

86. Rydh, C.J. and Sandén, B.A., 2005. Energy analysis of batteries in photovoltaic systems. Part II: Energy return factors and overall battery efficiencies. Energy conversion and management, 46(11), pp.1980-2000.

87. Author, N. "Review of electrical energy storage technologies and systems and of their potential for the UK." EA Technology 1 (2004): 34.

88. Xianchun, L., Hui, S., Qi, W., Meesri, C., Terry, W. A. L. L., & Jianglong, Y. U. (2009). Experimental study on drying and moisture re-adsorption kinetics of an Indonesian low rank coal. Journal of Environmental Sciences, 21, S127-S130.

89. Halikia, I., Neou-Syngouna, P., & Kolitsa, D. (1998). Isothermal kinetic analysis of the thermal decomposition of magnesium hydroxide using thermogravimetric data. Thermochimica Acta, 320(1-2), 75-88.

90. Perkins, C., Lichty, P., & Weimer, A. W. (2007). Determination of aerosol kinetics of thermal ZnO dissociation by thermogravimetry. Chemical Engineering Science, 62(21), 5952-5962.

91. Kubaschewsk, i.O. and Alcock, C.B., Metallurgical thermochemistry. 5th ed. 1979: Oxford Pergamon.

92. Pineau, A., Kanari, N., & Gaballah, I. (2006). Kinetics of reduction of iron oxides by H2: Part I: Low temperature reduction of hematite. Thermochimica acta, 447(1), 89-100.

93. Pineau, A., Kanari, N., & Gaballah, I. (2007). Kinetics of reduction of iron oxides by H2: Part II. Low temperature reduction of magnetite. Thermochimica Acta, 456(2), 75-88.

94. Dean, C. C., Blamey, J., Florin, N. H., Al-Jeboori, M. J., & Fennell, P. S. (2011). The calcium looping cycle for CO2 capture from power generation, cement manufacture and hydrogen production. Chemical Engineering Research and Design, 89(6), 836-855.

95. Shimizu, T., Hirama, T., Hosoda, H., Kitano, K., Inagaki, M., & Tejima, K. (1999). A twin fluid-bed reactor for removal of CO2 from combustion processes. Chemical Engineering Research and Design, 77(1), 62-68.

96. Abanades, J. C. (2002). The maximum capture efficiency of CO2 using a carbonation/calcination cycle of CaO/CaCO3. Chemical Engineering Journal, 90(3), 303-306.

97. Fang, F., Li, Z. S., & Cai, N. S. (2008). Experiment and modeling of CO2 capture from flue gases at high temperature in a fluidized bed reactor with Ca-based sorbents. Energy & Fuels, 23(1), 207-216.

98. Ylätalo, J., Parkkinen, J., Ritvanen, J., Tynjälä, T., & Hyppänen, T. (2013). Modeling of the oxy-combustion calciner in the post-combustion calcium looping process. Fuel, 113, 770-779.

99. Li, Z. S., & Cai, N. S. (2007). Modeling of multiple cycles for sorption-enhanced steam methane reforming and sorbent regeneration in fixed bed reactor. Energy & Fuels, 21(5), 2909-2918.

100. Lee, D. K. (2004). An apparent kinetic model for the carbonation of calcium oxide by carbon dioxide. Chemical Engineering Journal, 100(1-3), 71-77.

101. Abanades, J. C., Anthony, E. J., Lu, D. Y., Salvador, C., & Alvarez, D. (2004). Capture of CO2 from combustion gases in a fluidized bed of CaO. AIChE Journal, 50(7), 1614-1622.

102. Gupta, H., & Fan, L. S. (2002). Carbonation– calcination cycle using high reactivity calcium oxide for carbon dioxide separation from flue gas. Industrial & engineering chemistry research, 41(16), 4035-4042.

103. Hanak, D. P., Anthony, E. J., & Manovic, V. (2015). A review of developments in pilot-plant testing and modelling of calcium looping process for CO_2 capture from power generation systems. Energy & Environmental Science, 8(8), 2199-2249.

Appendices

Figure A1: Standalone OCGT

Figure A2: RES+OCGT

Figure A3: RES+SSC
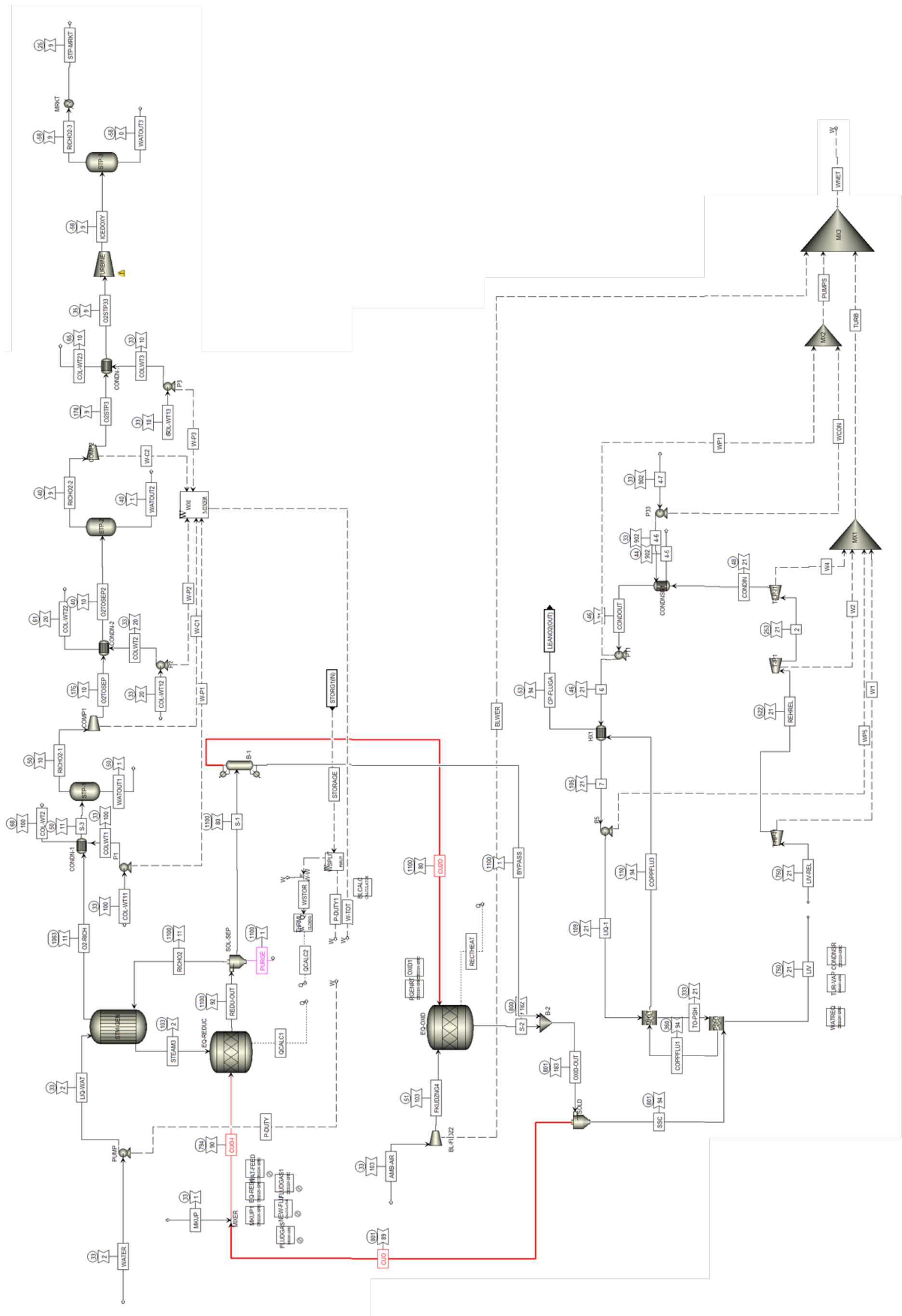
Figure A4: CaL+OCGT
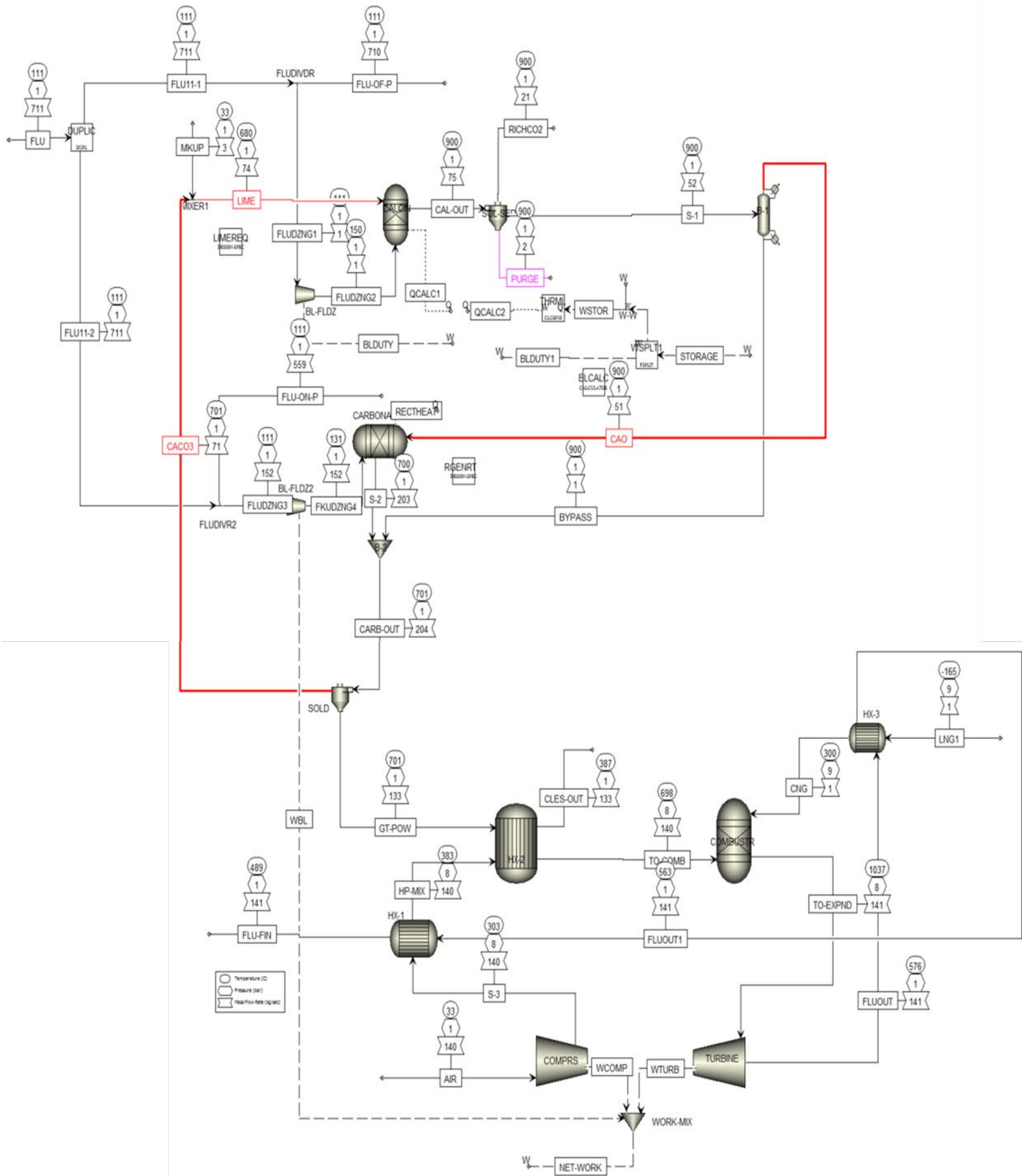
Figure A5: CaL+SSC
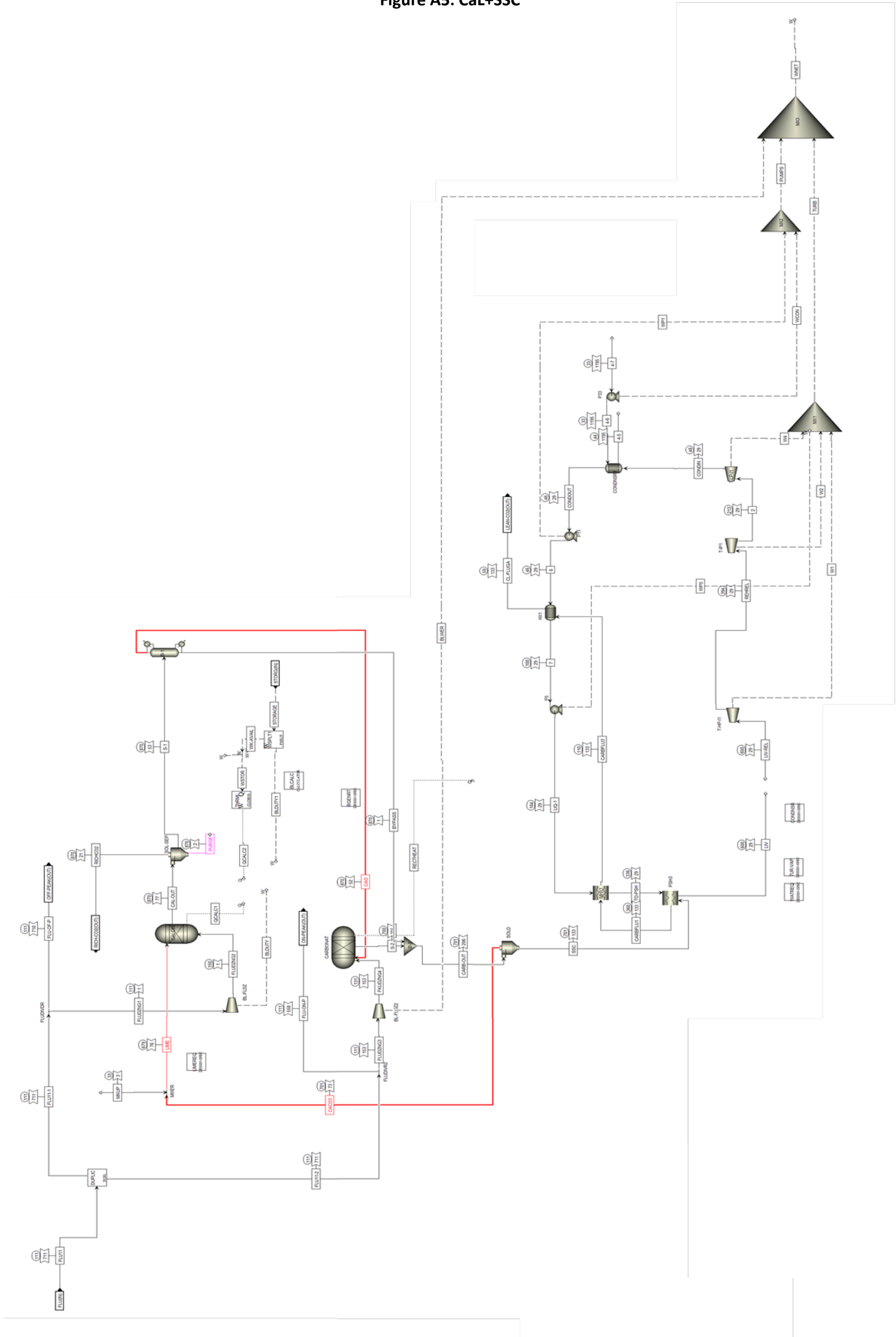
APPENDIX B: A SAMPLE OF OPTIMISATION RESULTS (CaL+SSC)

Table B.1 presents the simulation results for the optimisation of the CaL+SSC case. The solid makeup and the power output have been listed as key simulation results. Fourty one different simulations were prefomred for this case by varying the temperatures of calcination and carbonation reactions as well as the live steam. As is evident, the highlighted case (33) generated the maximum power output and hence was selected as the optimised case.

Table B.1: Simulation results used to optimise the CaL+SSC case

Case	Calciner Temperature (°C)	Carbonator Temperature (°C)	SSC live steam Temperature (°C)	Lime Makeup (kg/sec)	Power Output (MWe)
1	1000	800	750	2.7	35.4
2	950	800	750	2.8	35.5
3	900	800	750	2.9	35.7
4	850	800	750	3.0	35.9
5	1000	800	700	2.7	34.7
6	950	800	700	2.8	34.8
7	900	800	700	2.9	35.0
8	850	800	700	3.0	35.2
9	1000	800	650	2.7	33.9
10	950	800	650	2.8	34.1
11	900	800	650	2.9	34.3
12	850	800	650	3.0	34.5
13	1000	800	600	2.7	33.0
14	950	800	600	2.8	33.2
15	900	800	600	2.9	33.3
16	850	800	600	3.0	33.5
17	1000	750	700	2.6	35.5
18	950	750	700	2.7	35.7
19	900	750	700	2.8	35.8
20	850	750	700	2.9	36.0
21	1000	750	650	2.6	34.8

22	950	750	650	2.7	34.9
23	900	750	650	2.8	35.1
24	850	750	650	2.9	35.3
25	1000	750	600	2.6	34.0
26	950	750	600	2.7	34.2
27	900	750	600	2.8	34.3
28	850	750	600	2.9	34.5
29	1000	700	650	2.6	35.8
30	950	700	650	2.7	35.9
31	900	700	650	2.8	36.1
32	850	700	650	2.9	36.2
33	870	700	650	2.8	36.3
34	1000	700	600	2.6	35.1
35	950	700	600	2.7	35.3
36	900	700	600	2.8	35.4
37	850	700	600	2.9	35.5
38	1000	650	600	2.6	35.2
39	950	650	600	2.7	35.2
40	900	650	600	2.8	35.2
41	850	650	600	2.9	35.2

In this section, the effect of economic parameters on the calculated NPV values is investigated. The graphical representation of the some of selected results is provided in Figures C1-C6. More comprehensive results are provided in Table C1. In all of the considered scenarios, the depreciation method is a straight line, and its duration is 25 years. As a general trend based on the results reported in this section, RES technologies are by far the most beneficial technologies. However, in CaL technologies in cases that cost of capital (i_C, Eq. 4-25) was lower than 14%, CaL+SSC was more beneficial than OCGT (CNG), OCGT (LNG) and CaL+OCGT technologies. For i_C ~15, the NPV values of CaL+SSC were very close to the values calculated for OCGT (CNG), however, were higher than those of OCGT (LNG).
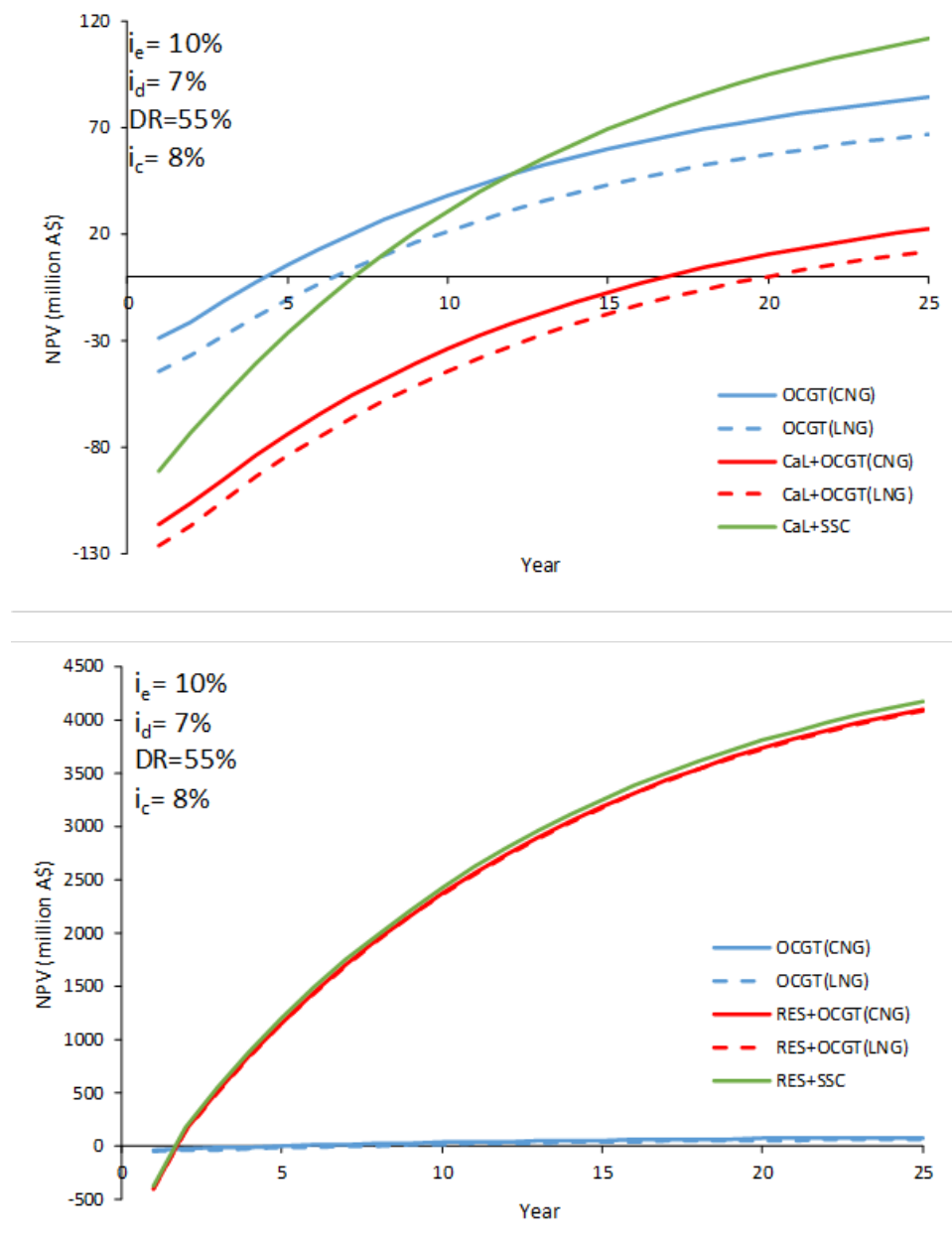
Figure C1: Calculated NPV values for the considered technology. The considered values for the economic parameters are: i_e=10%, i_d=7%, DR=55%, then i_C=8 %
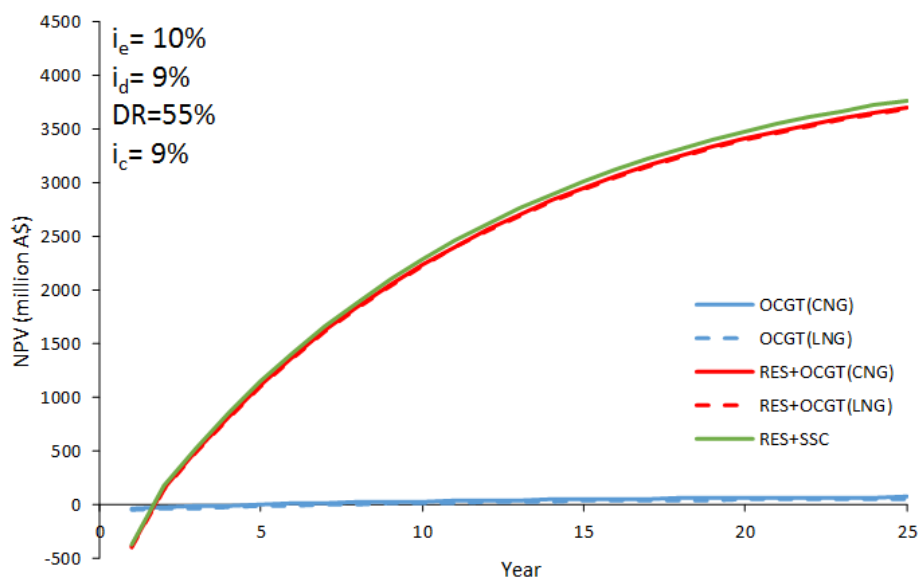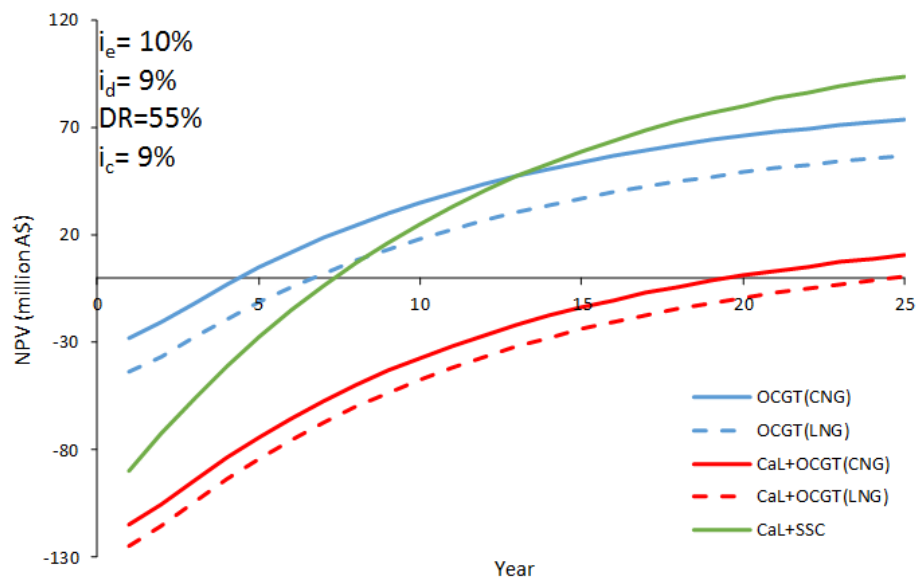
Figure C2: Calculated NPV values for the considered technology. The considered values for the economic parameters are: i_e=10%, i_d=9%, DR=55%, then i_C=9 %
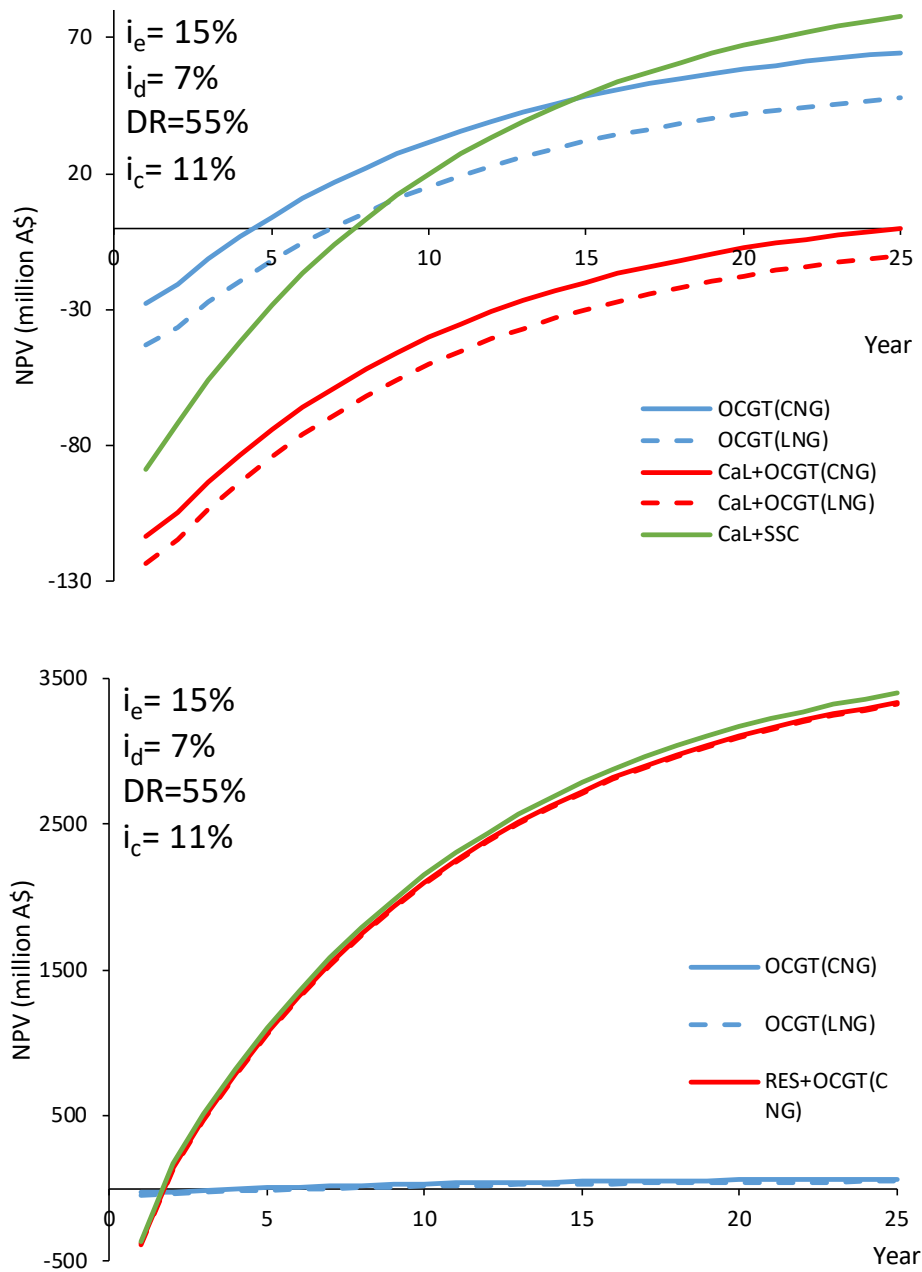
Figure C3: Calculated NPV values for the considered technology. The considered values for the economic parameters are: i_e=15%, i_d=7%, DR=55%, then i_C=11 %
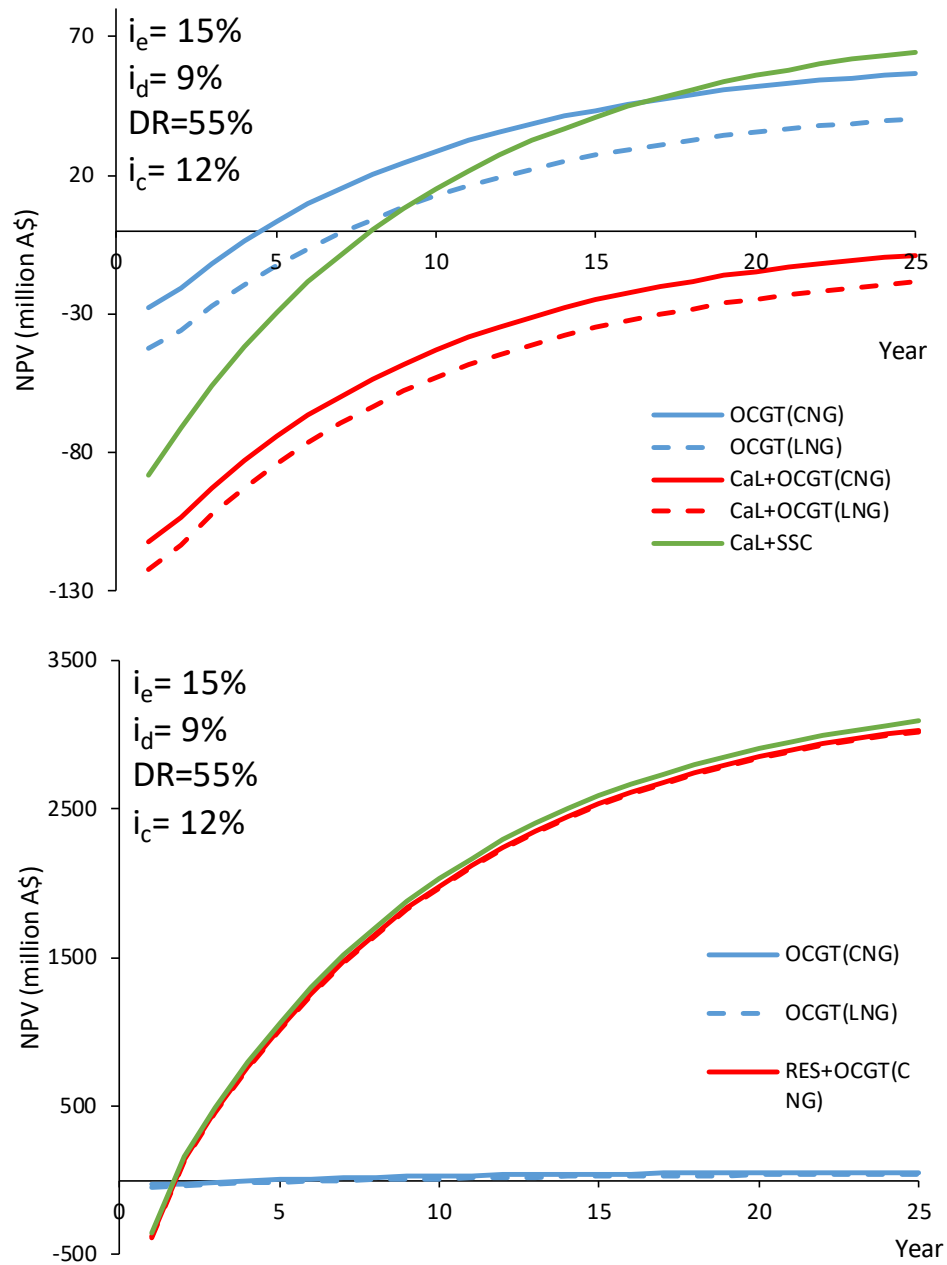
Figure C4: Calculated NPV values for the considered technology. The considered values for the economic parameters are: i_e=15%, i_d=9%, DR=55%, then i_C=12 %
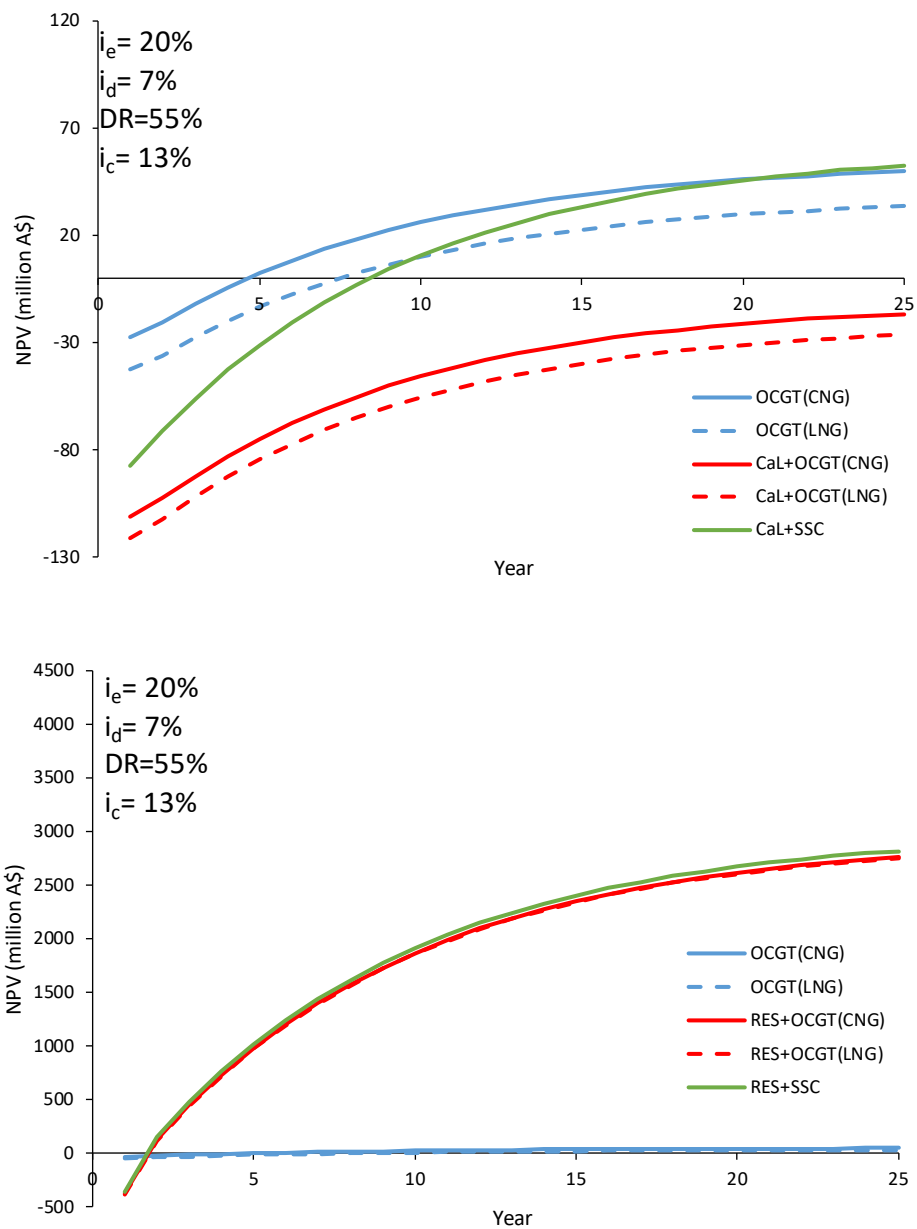
Figure C5: Calculated NPV values for the considered technology. The considered values for the economic parameters are: i_e=20%, i_d=7%, DR=55%, then i_C=13 %
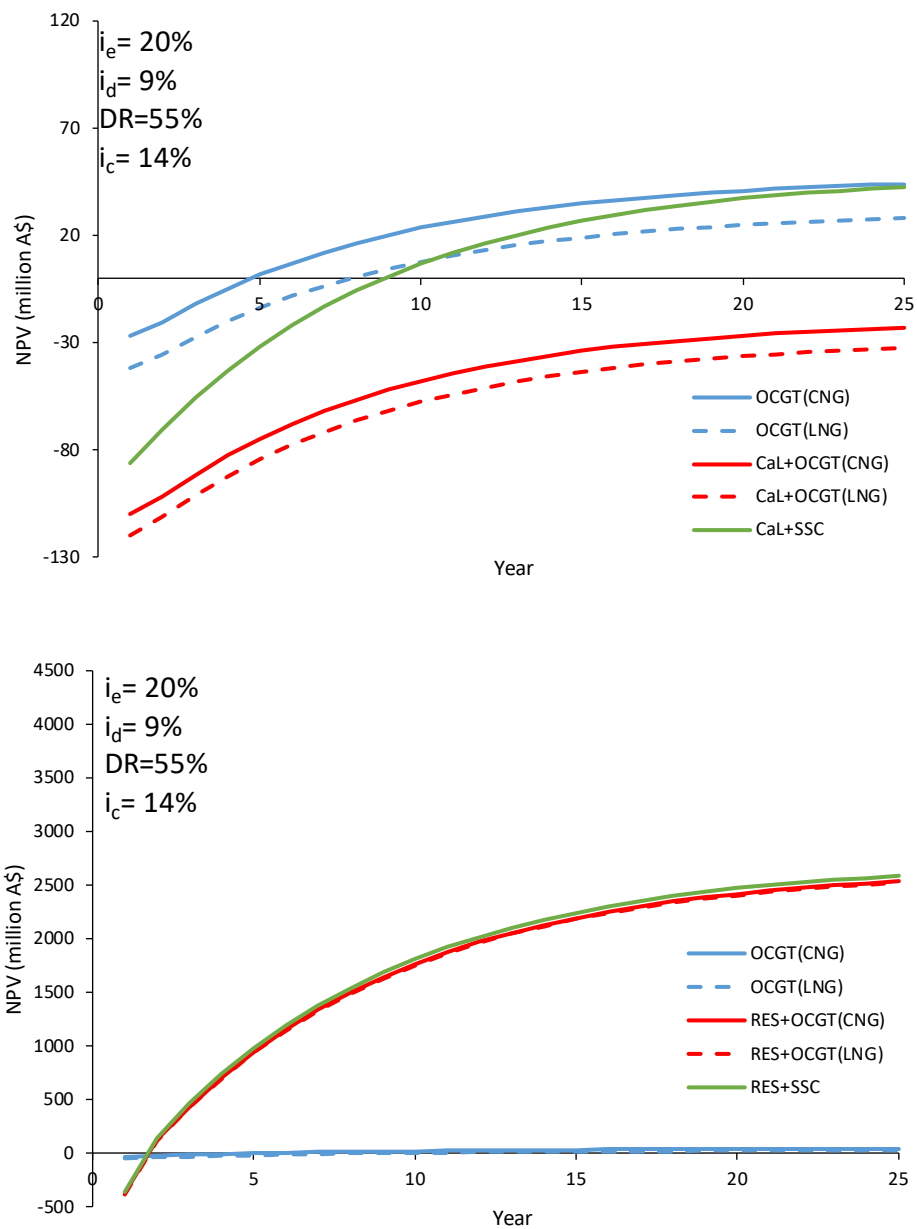
Figure C6: Calculated NPV values for the considered technology. The considered values for the economic parameters are: i_e=20%, i_d=9%, DR=55%, then i_C=14 %

Table C1: Calculated NPV values for the considered technologies

| | Parameters: | i_d | i_e | DR | i_c | | | |
| | | 7% | 10% | 45% | 9% | | | |
Year	OCGT(CNG)	OCGT(LNG)	RES+OCGT(CNG)	RES+OCGT(LNG)	CaL+OCGT(CNG)	CaL+OCGT(LNG)	RES+SSC	CaL+SSC
1	-28.3	-43.9	-387.6	-398.4	-115.4	-125.4	-369.3	-90.5
2	-20.9	-36.9	155.2	144.3	-106.0	-116.2	180.7	-72.9
3	-11.4	-27.5	513.3	502.3	-94.3	-104.5	543.2	-56.1
4	-2.6	-18.8	842.8	831.8	-83.6	-93.7	876.8	-40.7
5	5.5	-10.8	1146.0	1135.0	-73.7	-83.8	1183.9	-26.5
6	13.0	-3.5	1425.2	1414.2	-64.6	-74.7	1466.5	-13.4
7	19.8	3.3	1682.1	1671.1	-56.2	-66.3	1726.6	-1.3
8	26.1	9.5	1918.5	1907.5	-48.4	-58.6	1966.0	9.8
9	31.9	15.3	2136.1	2125.1	-41.3	-51.5	2186.3	20.0
10	37.3	20.6	2336.5	2325.4	-34.8	-45.0	2389.1	29.4
11	42.2	25.4	2520.8	2509.8	-28.8	-39.0	2575.8	38.0
12	46.7	29.9	2690.5	2679.5	-23.2	-33.4	2747.6	46.0
13	50.9	34.0	2846.7	2835.6	-18.1	-28.3	2905.7	53.3
14	54.7	37.8	2990.4	2979.4	-13.4	-23.6	3051.2	60.0
15	58.2	41.3	3122.7	3111.7	-9.1	-19.3	3185.1	66.2
16	61.5	44.5	3244.4	3233.4	-5.1	-15.3	3308.4	71.9
17	64.5	47.4	3356.5	3345.5	-1.5	-11.7	3421.9	77.2
18	67.2	50.2	3459.7	3448.6	1.9	-8.3	3526.3	82.0
19	69.8	52.7	3554.6	3543.6	5.0	-5.2	3622.4	86.5
20	72.1	55.0	3642.0	3630.9	7.8	-2.4	3710.9	90.6
21	74.2	57.1	3722.4	3711.3	10.5	0.3	3792.3	94.4
22	76.2	59.0	3796.4	3785.4	12.9	2.7	3867.2	97.8
23	78.0	60.8	3864.5	3853.5	15.1	4.9	3936.2	101.0
24	79.7	62.5	3927.2	3916.2	17.2	6.9	3999.7	104.0
25	81.2	64.0	3984.9	3973.9	19.0	8.8	4058.1	106.7

| | Parameters: | i_d | i_e | DR | i_c | | | |
| | | 7% | 10% | 55% | 8% | | | |
Year	OCGT(CNG)	OCGT(LNG)	RES+OCGT(CNG)	RES+OCGT(LNG)	CaL+OCGT(CNG)	CaL+OCGT(LNG)	RES+SSC	CaL+SSC
1	-28.4	-44.0	-388.7	-399.5	-115.7	-125.7	-370.4	-90.8
2	-20.9	-37.0	157.2	146.2	-106.3	-116.5	182.7	-73.1
3	-11.3	-27.5	518.2	507.2	-94.5	-104.7	548.2	-56.1
4	-2.4	-18.7	851.3	840.3	-83.6	-93.8	885.6	-40.5
5	5.8	-10.6	1158.8	1147.8	-73.6	-83.8	1196.9	-26.1
6	13.3	-3.1	1442.6	1431.6	-64.3	-74.5	1484.2	-12.8
7	20.3	3.8	1704.6	1693.5	-55.8	-66.0	1749.4	-0.5
8	26.8	10.1	1946.3	1935.3	-47.9	-58.1	1994.2	10.8
9	32.7	16.0	2169.4	2158.4	-40.6	-50.8	2220.1	21.3
10	38.2	21.4	2375.3	2364.3	-33.9	-44.1	2428.5	30.9
11	43.3	26.5	2565.4	2554.3	-27.6	-37.9	2621.0	39.9
12	48.0	31.1	2740.8	2729.7	-21.9	-32.1	2798.5	48.1
13	52.3	35.3	2902.7	2891.6	-16.6	-26.9	2962.4	55.7
14	56.3	39.3	3052.1	3041.0	-11.8	-22.0	3113.7	62.7
15	60.0	42.9	3190.0	3178.9	-7.2	-17.5	3253.3	69.1
16	63.3	46.3	3317.2	3306.2	-3.1	-13.3	3382.2	75.1
17	66.5	49.4	3434.7	3423.6	0.7	-9.5	3501.1	80.6
18	69.4	52.2	3543.1	3532.0	4.3	-6.0	3610.9	85.7
19	72.0	54.9	3643.2	3632.1	7.6	-2.7	3712.2	90.4
20	74.5	57.3	3735.5	3724.4	10.6	0.3	3805.7	94.7
21	76.8	59.5	3820.7	3809.7	13.4	3.1	3892.0	98.7
22	78.9	61.6	3899.4	3888.3	15.9	5.7	3971.6	102.4
23	80.8	63.5	3972.0	3960.9	18.3	8.0	4045.1	105.8
24	82.6	65.3	4039.0	4027.9	20.5	10.2	4112.9	109.0
25	84.3	66.9	4100.8	4089.8	22.5	12.2	4175.5	111.9

Parameters:		i_d	i_e	DR	i_c		
		7%	10%	65%	8%		
Year	OCGT(CNG)	OCGT(LNG)	RES+OCGT(CNG)	RES+OCGT(LNG)	CaL+OCGT(CNG)	CaL+OCGT(LNG)	RES+SSC	CaL+SSC
1	-28.4	-44.1	-389.8	-400.6	-116.0	-126.1	-371.4	-91.1
2	-21.0	-37.1	159.1	148.1	-106.6	-116.8	184.8	-73.2
3	-11.3	-27.5	523.1	512.1	-94.7	-104.9	553.3	-56.2
4	-2.3	-18.6	860.0	849.0	-83.7	-93.9	894.4	-40.4
5	6.0	-10.4	1171.8	1160.8	-73.5	-83.7	1210.1	-25.7
6	13.7	-2.8	1460.4	1449.3	-64.1	-74.3	1502.2	-12.2
7	20.9	4.2	1727.4	1716.4	-55.3	-65.6	1772.6	0.3
8	27.4	10.8	1974.6	1963.5	-47.3	-57.5	2022.9	11.9
9	33.5	16.8	2203.3	2192.3	-39.8	-50.0	2254.5	22.6
10	39.2	22.4	2415.1	2404.0	-32.9	-43.1	2468.8	32.6
11	44.4	27.5	2611.0	2599.9	-26.5	-36.7	2667.2	41.7
12	49.3	32.3	2792.3	2781.2	-20.6	-30.8	2850.8	50.3
13	53.7	36.7	2960.2	2949.1	-15.1	-25.3	3020.7	58.1
14	57.9	40.8	3115.5	3104.4	-10.0	-20.3	3178.0	65.4
15	61.7	44.6	3259.2	3248.1	-5.3	-15.6	3323.5	72.1
16	65.3	48.1	3392.3	3381.2	-1.0	-11.2	3458.2	78.4
17	68.5	51.4	3515.4	3504.3	3.0	-7.2	3582.9	84.2
18	71.6	54.4	3629.4	3618.3	6.8	-3.5	3698.3	89.5
19	74.4	57.1	3734.8	3723.7	10.2	-0.1	3805.0	94.4
20	77.0	59.7	3832.4	3821.3	13.4	3.1	3903.9	99.0
21	79.4	62.1	3922.8	3911.7	16.4	6.1	3995.3	103.3
22	81.6	64.3	4006.4	3995.3	19.1	8.8	4080.0	107.2
23	83.7	66.3	4083.7	4072.6	21.6	11.3	4158.3	110.8
24	85.6	68.2	4155.4	4144.3	23.9	13.7	4230.8	114.2
25	87.4	70.0	4221.6	4210.5	26.1	15.8	4297.9	117.3

Parameters:		i_d	i_e	DR	i_c		
		9%	10%	45%	10%		
Year	OCGT(CNG)	OCGT(LNG)	RES+OCGT(CNG)	RES+OCGT(LNG)	CaL+OCGT(CNG)	CaL+OCGT(LNG)	RES+SSC	CaL+SSC
1	-28.0	-43.5	-384.4	-395.1	-114.4	-124.3	-366.3	-89.8
2	-20.8	-36.7	149.5	138.7	-105.2	-115.3	174.7	-72.5
3	-11.5	-27.5	498.8	487.9	-93.8	-103.9	528.4	-56.1
4	-3.0	-19.1	817.6	806.7	-83.4	-93.5	851.1	-41.1
5	4.8	-11.4	1108.6	1097.7	-73.9	-84.0	1145.8	-27.5
6	11.9	-4.4	1374.3	1363.4	-65.2	-75.3	1414.7	-15.0
7	18.3	2.0	1616.8	1605.9	-57.3	-67.4	1660.3	-3.7
8	24.2	7.8	1838.1	1827.2	-50.1	-60.2	1884.4	6.7
9	29.6	13.1	2040.2	2029.3	-43.5	-53.6	2088.9	16.2
10	34.6	18.0	2224.6	2213.7	-37.5	-47.6	2275.7	24.8
11	39.0	22.4	2393.0	2382.1	-32.0	-42.1	2446.1	32.7
12	43.1	26.5	2546.7	2535.7	-26.9	-37.1	2601.7	39.9
13	46.9	30.2	2687.0	2676.0	-22.4	-32.5	2743.8	46.5
14	50.3	33.6	2815.0	2804.1	-18.2	-28.3	2873.4	52.5
15	53.4	36.6	2931.9	2921.0	-14.4	-24.5	2991.8	58.0
16	56.3	39.5	3038.6	3027.7	-10.9	-21.0	3099.8	63.0
17	58.9	42.0	3136.0	3125.1	-7.7	-17.8	3198.4	67.6
18	61.2	44.4	3224.9	3214.0	-4.8	-14.9	3288.5	71.7
19	63.4	46.5	3306.1	3295.2	-2.1	-12.3	3370.6	75.6
20	65.4	48.5	3380.2	3369.2	0.3	-9.8	3445.6	79.0
21	67.2	50.2	3447.8	3436.9	2.5	-7.6	3514.1	82.2
22	68.8	51.9	3509.3	3498.6	4.5	-5.6	3576.6	85.1
23	70.3	53.4	3565.9	3554.9	6.3	-3.8	3633.7	87.7
24	71.7	54.7	3617.3	3606.4	8.0	-2.1	3685.7	90.1
25	73.0	55.9	3664.3	3653.3	9.6	-0.6	3733.3	92.3

Table C1 Continued:

Parameters:		i_d	i_e	DR	i_c		
		9%	10%	55%	9%		
Year	OCGT(CNG)	OCGT(LNG)	RES+OCGT(CNG)	RES+OCGT(LNG)	CaL+OCGT(CNG)	CaL+OCGT(LNG)	RES+SSC	CaL+SSC
1	-28.1	-43.6	-384.8	-395.5	-114.5	-124.5	-366.6	-89.9
2	-20.8	-36.7	150.2	139.3	-105.3	-115.4	175.4	-72.5
3	-11.5	-27.5	500.4	489.5	-93.9	-104.0	530.0	-56.1
4	-2.9	-19.0	820.4	809.5	-83.4	-93.5	853.9	-41.1
5	4.9	-11.3	1112.7	1101.8	-73.9	-84.0	1149.9	-27.4
6	12.0	-4.3	1379.8	1368.9	-65.2	-75.3	1420.4	-14.9
7	18.5	2.1	1623.9	1613.0	-57.2	-67.3	1667.5	-3.4
8	24.5	8.0	1846.8	1835.9	-49.9	-60.0	1893.2	7.0
9	29.9	13.4	2050.6	2039.6	-43.3	-53.4	2099.5	16.6
10	34.9	18.3	2236.7	2225.8	-37.2	-47.3	2287.9	25.3
11	39.4	22.8	2406.8	2395.8	-31.6	-41.7	2460.1	33.3
12	43.5	26.9	2562.1	2551.2	-26.5	-36.7	2617.4	40.6
13	47.3	30.6	2704.1	2693.2	-21.9	-32.0	2761.2	47.2
14	50.8	34.0	2833.8	2822.9	-17.7	-27.8	2892.5	53.3
15	53.9	37.1	2952.3	2941.4	-13.8	-23.9	3012.5	58.9
16	56.8	40.0	3060.6	3049.7	-10.3	-20.4	3122.1	64.0
17	59.5	42.6	3159.5	3148.6	-7.0	-17.2	3222.3	68.6
18	61.9	45.0	3249.9	3239.0	-4.1	-14.2	3313.8	72.8
19	64.1	47.2	3332.5	3321.5	-1.4	-11.5	3397.4	76.7
20	66.1	49.1	3407.9	3397.0	1.1	-9.1	3473.8	80.2
21	67.9	51.0	3476.9	3465.9	3.3	-6.8	3543.6	83.5
22	69.6	52.6	3539.9	3528.9	5.4	-4.8	3607.3	86.4
23	71.1	54.1	3597.4	3586.5	7.3	-2.9	3665.6	89.1
24	72.5	55.5	3650.0	3639.0	9.0	-1.2	3718.8	91.6
25	73.8	56.8	3698.0	3687.1	10.5	0.4	3767.5	93.9

Parameters:		i_d	i_e	DR	i_c		
		9%	10%	65%	9%		
Year	OCGT(CNG)	OCGT(LNG)	RES+OCGT(CNG)	RES+OCGT(LNG)	CaL+OCGT(CNG)	CaL+OCGT(LNG)	RES+SSC	CaL+SSC
1	-28.1	-43.6	-385.1	-395.8	-114.6	-124.6	-367.0	-90.0
2	-20.8	-36.7	150.8	139.9	-105.4	-115.5	176.1	-72.6
3	-11.4	-27.5	502.0	491.1	-93.9	-104.0	531.6	-56.1
4	-2.9	-19.0	823.1	812.2	-83.4	-93.5	856.8	-41.0
5	5.0	-11.3	1116.8	1105.9	-73.9	-84.0	1154.1	-27.3
6	12.1	-4.2	1385.4	1374.5	-65.1	-75.2	1426.0	-14.7
7	18.7	2.3	1631.0	1620.1	-57.1	-67.2	1674.7	-3.2
8	24.7	8.2	1855.6	1844.7	-49.7	-59.8	1902.1	7.4
9	30.1	13.6	2061.0	2050.1	-43.0	-53.1	2110.1	17.0
10	35.1	18.6	2248.9	2237.9	-36.9	-47.0	2300.3	25.8
11	39.7	23.1	2420.6	2409.7	-31.3	-41.4	2474.2	33.9
12	43.9	27.2	2577.7	2566.8	-26.1	-36.3	2633.2	41.2
13	47.8	31.0	2721.4	2710.5	-21.5	-31.6	2778.7	48.0
14	51.3	34.5	2852.8	2841.8	-17.2	-27.3	2911.7	54.1
15	54.5	37.6	2972.9	2962.0	-13.2	-23.4	3033.4	59.8
16	57.4	40.5	3082.8	3071.8	-9.7	-19.8	3144.6	64.9
17	60.1	43.2	3183.3	3172.3	-6.4	-16.5	3246.3	69.6
18	62.5	45.6	3275.2	3264.2	-3.4	-13.5	3339.4	73.9
19	64.8	47.8	3359.2	3348.2	-0.6	-10.8	3424.4	77.9
20	66.8	49.8	3436.0	3425.1	1.9	-8.3	3502.2	81.5
21	68.7	51.7	3506.3	3495.3	4.2	-6.0	3573.4	84.8
22	70.4	53.4	3570.6	3559.6	6.3	-3.9	3638.4	87.8
23	72.0	54.9	3629.3	3618.4	8.2	-2.0	3697.9	90.6
24	73.4	56.4	3683.1	3672.1	10.0	-0.2	3752.4	93.1
25	74.7	57.6	3732.2	3721.3	11.6	1.4	3802.1	95.4

| | Parameters: | i_d | i_e | DR | i_c | | |
| | | 11% | 10% | 45% | 10% | | |
Year	OCGT(CNG)	OCGT(LNG)	RES+OCGT(CNG)	RES+OCGT(LNG)	CaL+OCGT(CNG)	CaL+OCGT(LNG)	RES+SSC	CaL+SSC
1	-27.8	-43.2	-381.3	-391.9	-113.5	-123.3	-363.3	-89.1
2	-20.7	-36.4	144.0	133.2	-104.4	-114.4	169.0	-72.0
3	-11.6	-27.5	484.8	474.0	-93.3	-103.3	514.0	-56.0
4	-3.4	-19.3	793.3	782.5	-83.2	-93.2	826.4	-41.6
5	4.1	-12.0	1072.7	1061.9	-74.1	-84.1	1109.2	-28.5
6	10.8	-5.3	1325.6	1314.8	-65.9	-75.9	1365.3	-16.6
7	16.9	0.7	1554.6	1543.8	-58.4	-68.4	1597.1	-5.9
8	22.5	6.2	1761.9	1751.1	-51.6	-61.6	1807.0	3.9
9	27.5	11.1	1949.7	1938.8	-45.5	-55.5	1997.1	12.7
10	32.0	15.6	2119.6	2108.8	-39.9	-49.9	2169.2	20.6
11	36.1	19.7	2273.5	2262.7	-34.9	-44.9	2325.0	27.8
12	39.8	23.4	2412.8	2402.0	-30.4	-40.4	2466.0	34.4
13	43.2	26.7	2538.9	2528.1	-26.2	-36.3	2593.7	40.3
14	46.2	29.7	2653.1	2642.3	-22.5	-32.5	2709.3	45.6
15	49.0	32.4	2756.5	2745.7	-19.1	-29.2	2814.0	50.5
16	51.5	34.9	2850.1	2839.3	-16.1	-26.1	2908.8	54.9
17	53.8	37.1	2934.9	2924.0	-13.3	-23.3	2994.6	58.9
18	55.8	39.1	3011.6	3000.8	-10.8	-20.8	3072.3	62.5
19	57.7	41.0	3081.1	3070.3	-8.5	-18.6	3142.6	65.7
20	59.3	42.6	3144.0	3133.2	-6.5	-16.5	3206.3	68.7
21	60.9	44.1	3201.0	3190.1	-4.6	-14.7	3264.0	71.3
22	62.2	45.5	3252.5	3241.7	-2.9	-13.0	3316.2	73.8
23	63.5	46.7	3299.2	3288.4	-1.4	-11.4	3363.5	75.9
24	64.6	47.8	3341.5	3330.6	0.0	-10.1	3406.3	77.9
25	65.6	48.8	3379.7	3368.9	1.2	-8.8	3445.0	79.7

| | Parameters: | i_d | i_e | DR | i_c | | |
| | | 11% | 10% | 55% | 11% | | |
Year	OCGT(CNG)	OCGT(LNG)	RES+OCGT(CNG)	RES+OCGT(LNG)	CaL+OCGT(CNG)	CaL+OCGT(LNG)	RES+SSC	CaL+SSC
1	-27.8	-43.1	-380.9	-391.5	-113.4	-123.2	-363.0	-89.0
2	-20.7	-36.4	143.4	132.6	-104.4	-114.3	168.3	-72.0
3	-11.6	-27.5	483.3	472.5	-93.3	-103.2	512.4	-56.0
4	-3.4	-19.3	790.7	779.9	-83.2	-93.2	823.7	-41.6
5	4.0	-12.0	1068.8	1058.0	-74.1	-84.1	1105.2	-28.6
6	10.7	-5.4	1320.3	1309.6	-65.9	-75.9	1359.9	-16.8
7	16.8	0.6	1547.9	1537.1	-58.5	-68.5	1590.3	-6.1
8	22.3	6.0	1753.7	1742.9	-51.8	-61.8	1798.7	3.5
9	27.3	10.9	1939.9	1929.1	-45.7	-55.7	1987.2	12.3
10	31.7	15.4	2108.3	2097.5	-40.2	-50.2	2157.7	20.2
11	35.8	19.4	2260.7	2249.9	-35.2	-45.2	2312.0	27.3
12	39.5	23.0	2398.5	2387.7	-30.7	-40.7	2451.5	33.8
13	42.8	26.3	2523.2	2512.3	-26.6	-36.7	2577.7	39.6
14	45.8	29.3	2635.9	2625.1	-23.0	-33.0	2691.9	44.9
15	48.5	32.0	2737.9	2727.1	-19.6	-29.7	2795.2	49.7
16	51.0	34.4	2830.2	2819.4	-16.6	-26.6	2888.6	54.0
17	53.2	36.6	2913.6	2902.8	-13.9	-23.9	2973.1	57.9
18	55.2	38.6	2989.1	2978.3	-11.4	-21.5	3049.5	61.5
19	57.1	40.4	3057.4	3046.6	-9.2	-19.2	3118.7	64.7
20	58.7	42.0	3119.2	3108.4	-7.2	-17.2	3181.2	67.6
21	60.2	43.5	3175.1	3164.2	-5.4	-15.4	3237.8	70.2
22	61.5	44.8	3225.6	3214.8	-3.7	-13.7	3289.0	72.6
23	62.8	46.0	3271.4	3260.5	-2.2	-12.2	3335.2	74.7
24	63.9	47.1	3312.7	3301.9	-0.9	-10.9	3377.1	76.7
25	64.9	48.1	3350.1	3339.3	0.4	-9.7	3415.0	78.4

| Parameters: | | i_d | i_e | DR | i_c | | |
| | | 11% | 10% | 65% | 11% | | |
Year	OCGT(CNG)	OCGT(LNG)	RES+OCGT(CNG)	RES+OCGT(LNG)	CaL+OCGT(CNG)	CaL+OCGT(LNG)	RES+SSC	CaL+SSC
1	-27.8	-43.1	-380.6	-391.2	-113.3	-123.1	-362.7	-88.9
2	-20.7	-36.4	142.8	132.0	-104.3	-114.2	167.7	-71.9
3	-11.6	-27.4	481.8	471.0	-93.2	-103.2	510.9	-56.0
4	-3.4	-19.4	788.1	777.3	-83.2	-93.2	821.0	-41.7
5	3.9	-12.1	1064.9	1054.1	-74.2	-84.1	1101.3	-28.7
6	10.6	-5.5	1315.1	1304.3	-66.0	-76.0	1354.6	-16.9
7	16.6	0.5	1541.2	1530.4	-58.6	-68.6	1583.5	-6.3
8	22.1	5.9	1745.6	1734.8	-51.9	-61.9	1790.4	3.2
9	27.0	10.7	1930.2	1919.4	-45.9	-55.9	1977.4	11.9
10	31.5	15.1	2097.1	2086.3	-40.4	-50.5	2146.4	19.7
11	35.5	19.1	2248.0	2237.2	-35.5	-45.5	2299.1	26.8
12	39.1	22.7	2384.3	2373.5	-31.1	-41.1	2437.1	33.2
13	42.4	25.9	2507.5	2496.7	-27.0	-37.1	2561.9	39.0
14	45.4	28.9	2618.9	2608.0	-23.4	-33.4	2674.6	44.2
15	48.1	31.5	2719.5	2708.7	-20.1	-30.1	2776.5	48.9
16	50.5	33.9	2810.4	2799.6	-17.2	-27.2	2868.5	53.2
17	52.7	36.1	2892.6	2881.8	-14.5	-24.5	2951.8	57.0
18	54.7	38.0	2966.9	2956.1	-12.0	-22.1	3027.0	60.5
19	56.5	39.8	3034.0	3023.2	-9.9	-19.9	3094.9	63.7
20	58.1	41.4	3094.7	3083.9	-7.9	-17.9	3156.4	66.5
21	59.5	42.9	3149.5	3138.7	-6.1	-16.1	3211.9	69.1
22	60.9	44.2	3199.1	3188.2	-4.5	-14.5	3262.0	71.4
23	62.1	45.3	3243.8	3233.0	-3.0	-13.0	3307.4	73.5
24	63.1	46.4	3284.3	3273.5	-1.7	-11.7	3348.3	75.4
25	64.1	47.4	3320.9	3310.1	-0.5	-10.5	3385.4	77.1

| Parameters: | | i_d | i_e | DR | i_c | | |
| | | 7% | 15% | 45% | 11% | | |
Year	OCGT(CNG)	OCGT(LNG)	RES+OCGT(CNG)	RES+OCGT(LNG)	CaL+OCGT(CNG)	CaL+OCGT(LNG)	RES+SSC	CaL+SSC
1	-27.6	-42.8	-378.0	-388.6	-112.5	-122.3	-360.2	-88.3
2	-20.6	-36.2	138.3	127.7	-103.6	-113.5	163.0	-71.5
3	-11.7	-27.4	470.5	459.8	-92.8	-102.7	499.3	-56.0
4	-3.8	-19.6	768.6	757.9	-83.0	-93.0	801.2	-42.0
5	3.4	-12.5	1036.3	1025.6	-74.3	-84.2	1072.1	-29.4
6	9.8	-6.2	1276.5	1265.8	-66.5	-76.4	1315.4	-18.2
7	15.5	-0.5	1492.2	1481.5	-59.4	-69.3	1533.8	-8.1
8	20.7	4.6	1685.8	1675.1	-53.1	-63.0	1729.8	1.0
9	25.3	9.2	1859.6	1848.9	-47.4	-57.3	1905.7	9.2
10	29.5	13.3	2015.6	2004.9	-42.3	-52.3	2063.7	16.5
11	33.2	17.0	2155.6	2144.9	-37.8	-47.7	2205.4	23.1
12	36.6	20.3	2281.3	2270.6	-33.6	-43.6	2332.7	28.9
13	39.6	23.3	2394.2	2383.4	-30.0	-39.9	2447.0	34.2
14	42.3	25.9	2495.5	2484.7	-26.7	-36.6	2549.5	39.0
15	44.7	28.3	2586.4	2575.7	-23.7	-33.6	2641.6	43.3
16	46.9	30.5	2668.0	2657.3	-21.0	-31.0	2724.2	47.1
17	48.9	32.4	2741.3	2730.6	-18.6	-28.6	2798.4	50.5
18	50.6	34.1	2807.1	2796.3	-16.5	-26.4	2865.0	53.6
19	52.2	35.7	2866.1	2855.4	-14.5	-24.5	2924.8	56.4
20	53.6	37.1	2919.1	2908.4	-12.8	-22.8	2978.4	58.9
21	54.9	38.4	2966.7	2955.9	-11.3	-21.2	3026.6	61.1
22	56.0	39.5	3009.4	2998.7	-9.9	-19.8	3069.9	63.1
23	57.0	40.5	3047.7	3037.0	-8.6	-18.6	3108.7	64.9
24	58.0	41.4	3082.2	3071.4	-7.5	-17.4	3143.5	66.5
25	58.8	42.2	3113.0	3102.3	-6.5	-16.4	3174.8	67.9

Parameters:		i_d	i_e	DR	i_c		
		7%	15%	55%	11%		
Year	OCGT(CNG)	OCGT(LNG)	RES+OCGT(CNG)	RES+OCGT(LNG)	CaL+OCGT(CNG)	CaL+OCGT(LNG)	RES+SSC	CaL+SSC
1	-27.8	-43.1	-380.8	-391.4	-113.3	-123.2	-362.8	-89.0
2	-20.7	-36.4	143.1	132.3	-104.3	-114.3	168.0	-71.9
3	-11.6	-27.4	482.5	471.7	-93.2	-103.2	511.6	-56.0
4	-3.4	-19.4	789.4	778.6	-83.2	-93.2	822.3	-41.6
5	4.0	-12.1	1066.9	1056.1	-74.1	-84.1	1103.3	-28.6
6	10.7	-5.4	1317.7	1306.9	-66.0	-75.9	1357.3	-16.9
7	16.7	0.5	1544.6	1533.8	-58.5	-68.5	1586.9	-6.2
8	22.2	5.9	1749.6	1738.8	-51.9	-61.9	1794.6	3.4
9	27.1	10.8	1935.1	1924.3	-45.8	-55.8	1982.3	12.1
10	31.6	15.2	2102.7	2091.9	-40.3	-50.3	2152.1	20.0
11	35.7	19.2	2254.3	2243.5	-35.4	-45.4	2305.5	27.1
12	39.3	22.9	2391.4	2380.6	-30.9	-40.9	2444.3	33.5
13	42.6	26.1	2515.3	2504.5	-26.8	-36.9	2569.8	39.3
14	45.6	29.1	2627.4	2616.5	-23.2	-33.2	2683.2	44.6
15	48.3	31.7	2728.7	2717.9	-19.9	-29.9	2785.8	49.3
16	50.7	34.2	2820.3	2809.5	-16.9	-26.9	2878.5	53.6
17	53.0	36.3	2903.1	2892.3	-14.2	-24.2	2962.4	57.5
18	55.0	38.3	2978.0	2967.2	-11.7	-21.8	3038.2	61.0
19	56.8	40.1	3045.7	3034.9	-9.5	-19.5	3106.8	64.2
20	58.4	41.7	3106.9	3096.1	-7.5	-17.5	3168.7	67.0
21	59.9	43.2	3162.3	3151.4	-5.7	-15.7	3224.8	69.6
22	61.2	44.5	3212.3	3201.5	-4.1	-14.1	3275.5	72.0
23	62.4	45.7	3257.6	3246.7	-2.6	-12.6	3321.3	74.1
24	63.5	46.8	3298.5	3287.6	-1.3	-11.3	3362.7	76.0
25	64.5	47.7	3335.5	3324.6	-0.1	-10.1	3400.1	77.8

Parameters:		i_d	i_e	DR	i_c		
		7%	15%	65%	10%		
Year	OCGT(CNG)	OCGT(LNG)	RES+OCGT(CNG)	RES+OCGT(LNG)	CaL+OCGT(CNG)	CaL+OCGT(LNG)	RES+SSC	CaL+SSC
1	-28.0	-43.4	-383.5	-394.2	-114.2	-124.1	-365.5	-89.6
2	-20.8	-36.6	148.0	137.1	-105.0	-115.1	173.1	-72.3
3	-11.5	-27.5	494.9	484.0	-93.7	-103.7	524.3	-56.1
4	-3.1	-19.1	810.8	799.9	-83.4	-93.4	844.2	-41.3
5	4.6	-11.6	1098.5	1087.6	-74.0	-84.0	1135.5	-27.8
6	11.6	-4.7	1360.7	1349.7	-65.4	-75.5	1400.8	-15.5
7	17.9	1.6	1599.2	1588.3	-57.6	-67.7	1642.4	-4.3
8	23.7	7.4	1816.6	1805.7	-50.5	-60.6	1862.5	5.9
9	29.0	12.6	2014.5	2003.6	-44.1	-54.1	2062.9	15.2
10	33.8	17.3	2194.8	2183.9	-38.2	-48.2	2245.4	23.6
11	38.2	21.7	2359.0	2348.1	-32.8	-42.9	2411.7	31.3
12	42.2	25.6	2508.5	2497.6	-27.9	-38.0	2563.1	38.4
13	45.8	29.2	2644.7	2633.8	-23.5	-33.6	2701.0	44.7
14	49.1	32.5	2768.8	2757.9	-19.4	-29.5	2826.5	50.6
15	52.2	35.4	2881.7	2870.8	-15.7	-25.8	2940.9	55.9
16	54.9	38.1	2984.6	2973.7	-12.4	-22.5	3045.1	60.7
17	57.4	40.6	3078.3	3067.4	-9.3	-19.4	3140.0	65.1
18	59.7	42.9	3163.6	3152.7	-6.5	-16.6	3226.4	69.1
19	61.8	44.9	3241.4	3230.5	-4.0	-14.1	3305.0	72.7
20	63.6	46.8	3312.1	3301.2	-1.7	-11.8	3376.7	76.0
21	65.4	48.5	3376.6	3365.7	0.4	-9.7	3442.0	79.1
22	66.9	50.0	3435.3	3424.4	2.3	-7.8	3501.4	81.8
23	68.4	51.4	3488.8	3477.9	4.1	-6.0	3555.6	84.3
24	69.6	52.7	3537.5	3526.6	5.7	-4.4	3604.9	86.6
25	70.8	53.9	3581.8	3570.9	7.1	-3.0	3649.8	88.7

Table C1 Continued:

		Parameters:	i_d	i_e	DR	i_c		
			9%	15%	45%	12%		
Year	OCGT(CNG)	OCGT(LNG)	RES+OCGT(CNG)	RES+OCGT(LNG)	CaL+OCGT(CNG)	CaL+OCGT(LNG)	RES+SSC	CaL+SSC
1	-27.4	-42.5	-375.0	-385.4	-111.6	-121.3	-357.3	-87.6
2	-20.5	-35.9	133.1	122.5	-102.9	-112.7	157.5	-71.1
3	-11.8	-27.4	457.4	446.7	-92.3	-102.1	485.8	-55.9
4	-4.1	-19.8	746.1	735.4	-82.9	-92.7	778.1	-42.4
5	2.8	-13.0	1003.2	992.5	-74.5	-84.3	1038.4	-30.3
6	8.9	-7.0	1232.1	1221.5	-67.0	-76.8	1270.2	-19.6
7	14.3	-1.6	1435.9	1425.3	-60.3	-70.2	1476.6	-10.0
8	19.1	3.2	1617.5	1606.8	-54.4	-64.2	1660.4	-1.5
9	23.4	7.4	1779.1	1768.5	-49.1	-59.0	1824.0	6.1
10	27.3	11.2	1923.1	1912.4	-44.4	-54.3	1969.8	12.8
11	30.7	14.6	2051.2	2040.6	-40.2	-50.1	2099.6	18.8
12	33.8	17.6	2165.4	2154.7	-36.5	-46.4	2215.1	24.2
13	36.5	20.3	2267.0	2256.4	-33.2	-43.0	2318.0	29.0
14	38.9	22.7	2357.5	2346.9	-30.2	-40.1	2409.6	33.2
15	41.0	24.8	2438.1	2427.4	-27.6	-37.5	2491.2	37.0
16	42.9	26.7	2509.9	2499.2	-25.3	-35.1	2563.9	40.3
17	44.6	28.4	2573.8	2563.1	-23.2	-33.0	2628.6	43.3
18	46.2	29.9	2630.7	2620.0	-21.3	-31.2	2686.2	46.0
19	47.5	31.2	2681.3	2670.7	-19.7	-29.5	2737.5	48.4
20	48.7	32.4	2726.5	2715.8	-18.2	-28.0	2783.2	50.5
21	49.8	33.5	2766.6	2756.0	-16.9	-26.7	2823.9	52.4
22	50.7	34.4	2802.4	2791.8	-15.7	-25.6	2860.1	54.1
23	51.6	35.2	2834.3	2823.6	-14.7	-24.5	2892.4	55.6
24	52.4	36.0	2862.7	2852.0	-13.7	-23.6	2921.1	56.9
25	53.0	36.7	2887.9	2877.3	-12.9	-22.8	2946.7	58.1

		Parameters:	i_d	i_e	DR	i_c		
			9%	15%	55%	12%		
Year	OCGT(CNG)	OCGT(LNG)	RES+OCGT(CNG)	RES+OCGT(LNG)	CaL+OCGT(CNG)	CaL+OCGT(LNG)	RES+SSC	CaL+SSC
1	-27.5	-42.7	-377.0	-387.5	-112.2	-121.9	-359.2	-88.1
2	-20.5	-36.1	136.6	125.9	-103.4	-113.3	161.2	-71.4
3	-11.7	-27.4	466.1	455.4	-92.6	-102.5	494.8	-55.9
4	-3.9	-19.6	761.0	750.4	-83.0	-92.9	793.4	-42.1
5	3.2	-12.7	1025.1	1014.4	-74.4	-84.2	1060.8	-29.7
6	9.5	-6.5	1261.5	1250.8	-66.6	-76.5	1300.1	-18.6
7	15.1	-0.9	1473.2	1462.5	-59.7	-69.6	1514.4	-8.7
8	20.2	4.1	1662.6	1651.9	-53.5	-63.4	1706.2	0.2
9	24.7	8.6	1832.3	1821.6	-48.0	-57.9	1878.0	8.1
10	28.8	12.6	1984.1	1973.4	-43.0	-52.9	2031.7	15.2
11	32.4	16.2	2120.1	2109.4	-38.6	-48.5	2169.4	21.6
12	35.6	19.4	2241.8	2231.1	-34.6	-44.5	2292.6	27.3
13	38.5	22.2	2350.8	2340.1	-31.1	-41.0	2402.9	32.4
14	41.1	24.8	2448.3	2437.6	-27.9	-37.8	2501.7	37.0
15	43.5	27.1	2535.6	2524.9	-25.0	-34.9	2590.1	41.1
16	45.5	29.2	2613.8	2603.1	-22.5	-32.4	2669.3	44.8
17	47.4	31.0	2683.8	2673.1	-20.2	-30.1	2740.2	48.0
18	49.1	32.7	2746.5	2735.8	-18.1	-28.1	2803.6	51.0
19	50.6	34.2	2802.6	2791.9	-16.3	-26.2	2860.4	53.6
20	51.9	35.5	2852.8	2842.1	-14.7	-24.6	2911.3	56.0
21	53.1	36.7	2897.8	2887.1	-13.2	-23.1	2956.8	58.1
22	54.2	37.7	2938.0	2927.3	-11.9	-21.8	2997.5	60.0
23	55.2	38.7	2974.1	2963.4	-10.7	-20.6	3034.0	61.7
24	56.0	39.5	3006.3	2995.6	-9.7	-19.6	3066.7	63.2
25	56.8	40.3	3035.2	3024.5	-8.7	-18.6	3095.9	64.5

Parameters:		i_d	i_e	DR	i_c		
		9%	15%	65%	11%		
Year	OCGT(CNG)	OCGT(LNG)	RES+OCGT(CNG)	RES+OCGT(LNG)	CaL+OCGT(CNG)	CaL+OCGT(LNG)	RES+SSC	CaL+SSC
1	-27.7	-42.9	-379.1	-389.6	-112.8	-122.6	-361.2	-88.6
2	-20.6	-36.3	140.1	129.4	-103.9	-113.8	164.9	-71.7
3	-11.7	-27.4	475.0	464.2	-93.0	-102.9	503.9	-56.0
4	-3.6	-19.5	776.3	765.6	-83.1	-93.0	809.0	-41.9
5	3.6	-12.3	1047.6	1036.9	-74.3	-84.2	1083.7	-29.1
6	10.1	-5.9	1291.8	1281.1	-66.3	-76.2	1330.9	-17.7
7	16.0	-0.1	1511.6	1500.8	-59.1	-69.1	1553.4	-7.4
8	21.3	5.1	1709.4	1698.6	-52.6	-62.6	1753.7	1.9
9	26.0	9.8	1887.4	1876.7	-46.8	-56.8	1934.0	10.2
10	30.3	14.0	2047.7	2037.0	-41.6	-51.5	2096.2	17.8
11	34.1	17.8	2192.0	2181.2	-36.9	-46.8	2242.3	24.5
12	37.6	21.2	2321.8	2311.0	-32.6	-42.6	2373.8	30.6
13	40.7	24.3	2438.7	2427.9	-28.8	-38.8	2492.1	36.1
14	43.5	27.1	2543.9	2533.1	-25.4	-35.4	2598.6	41.0
15	46.0	29.6	2638.6	2627.8	-22.3	-32.3	2694.4	45.5
16	48.3	31.8	2723.8	2713.0	-19.5	-29.5	2780.7	49.5
17	50.4	33.8	2800.5	2789.7	-17.0	-27.0	2858.4	53.1
18	52.2	35.7	2869.5	2858.8	-14.8	-24.7	2928.3	56.3
19	53.9	37.3	2931.7	2920.9	-12.7	-22.7	2991.2	59.2
20	55.4	38.8	2987.6	2976.8	-10.9	-20.9	3047.9	61.8
21	56.7	40.1	3038.0	3027.2	-9.2	-19.2	3098.8	64.2
22	57.9	41.3	3083.3	3072.5	-7.8	-17.7	3144.7	66.3
23	59.0	42.4	3124.1	3113.3	-6.4	-16.4	3186.0	68.2
24	60.0	43.3	3160.8	3150.0	-5.2	-15.2	3223.2	70.0
25	60.9	44.2	3193.8	3183.1	-4.2	-14.1	3256.6	71.5

Parameters:		i_d	i_e	DR	i_c		
		11%	15%	45%	13%		
Year	OCGT(CNG)	OCGT(LNG)	RES+OCGT(CNG)	RES+OCGT(LNG)	CaL+OCGT(CNG)	CaL+OCGT(LNG)	RES+SSC	CaL+SSC
1	-27.1	-42.1	-372.0	-382.4	-110.7	-120.3	-354.5	-86.9
2	-20.3	-35.7	128.1	117.5	-102.1	-111.9	152.2	-70.7
3	-11.9	-27.4	444.6	434.1	-91.8	-101.5	472.7	-55.8
4	-4.4	-20.0	724.3	713.7	-82.7	-92.4	755.9	-42.7
5	2.1	-13.5	971.3	960.7	-74.6	-84.3	1006.0	-31.1
6	8.0	-7.7	1189.5	1179.0	-67.5	-77.2	1226.9	-20.9
7	13.1	-2.7	1382.3	1371.7	-61.2	-70.9	1422.1	-11.9
8	17.6	1.8	1552.0	1542.0	-55.6	-65.4	1594.5	-3.9
9	21.7	5.8	1703.0	1692.5	-50.7	-60.5	1746.8	3.2
10	25.2	9.3	1835.9	1825.4	-46.3	-56.1	1881.4	9.4
11	28.3	12.4	1953.3	1942.8	-42.5	-52.3	2000.2	14.9
12	31.1	15.1	2057.0	2046.5	-39.1	-48.9	2105.2	19.8
13	33.5	17.5	2148.7	2138.1	-36.1	-45.9	2198.0	24.1
14	35.7	19.7	2229.6	2219.0	-33.5	-43.3	2279.9	27.9
15	37.6	21.6	2301.1	2290.5	-31.2	-40.9	2352.3	31.2
16	39.3	23.2	2364.2	2353.7	-29.1	-38.9	2416.3	34.2
17	40.8	24.7	2420.0	2409.5	-27.3	-37.1	2472.8	36.8
18	42.1	26.0	2469.3	2458.8	-25.7	-35.4	2522.7	39.1
19	43.3	27.1	2512.9	2502.3	-24.2	-34.0	2566.8	41.2
20	44.3	28.2	2551.3	2540.8	-23.0	-32.8	2605.7	43.0
21	45.2	29.0	2585.3	2574.7	-21.9	-31.7	2640.1	44.6
22	46.0	29.8	2615.3	2604.8	-20.9	-30.7	2670.5	46.0
23	46.7	30.5	2641.8	2631.3	-20.0	-29.8	2697.3	47.2
24	47.3	31.2	2665.3	2654.7	-19.3	-29.0	2721.1	48.3
25	47.9	31.7	2686.0	2675.4	-18.6	-28.4	2742.0	49.3

| Parameters: | | i_d | i_e | DR | i_c | | |
| | | 11% | 15% | 55% | 13% | | |
Year	OCGT(CNG)	OCGT(LNG)	RES+OCGT(CNG)	RES+OCGT(LNG)	CaL+OCGT(CNG)	CaL+OCGT(LNG)	RES+SSC	CaL+SSC
1	-27.2	-42.3	-373.3	-383.7	-111.1	-120.8	-355.7	-87.2
2	-20.4	-35.8	130.3	119.7	-102.5	-112.2	154.6	-70.9
3	-11.9	-27.4	450.2	439.7	-92.0	-101.8	478.5	-55.9
4	-4.3	-19.9	733.9	723.3	-82.7	-92.5	765.7	-42.6
5	2.4	-13.3	985.3	974.7	-74.5	-84.3	1020.2	-30.8
6	8.4	-7.4	1208.2	1197.6	-67.3	-77.0	1245.9	-20.3
7	13.6	-2.2	1405.8	1395.2	-60.8	-70.6	1446.0	-11.0
8	18.3	2.4	1581.0	1570.4	-55.1	-64.9	1623.4	-2.8
9	22.4	6.5	1736.3	1725.7	-50.0	-59.8	1780.6	4.5
10	26.1	10.1	1874.0	1863.4	-45.5	-55.3	1920.0	10.9
11	29.4	13.4	1996.1	1985.5	-41.5	-51.3	2043.6	16.6
12	32.3	16.2	2104.3	2093.7	-38.0	-47.8	2153.2	21.7
13	34.8	18.7	2200.2	2189.6	-34.9	-44.7	2250.3	26.2
14	37.1	21.0	2285.3	2274.7	-32.1	-41.9	2336.4	30.2
15	39.1	23.0	2360.7	2350.1	-29.6	-39.4	2412.7	33.7
16	40.9	24.7	2427.5	2416.9	-27.4	-37.2	2480.4	36.9
17	42.5	26.3	2486.7	2476.1	-25.5	-35.3	2540.4	39.6
18	43.9	27.7	2539.3	2528.7	-23.8	-33.6	2593.6	42.1
19	45.1	28.9	2585.9	2575.3	-22.3	-32.1	2640.7	44.3
20	46.2	30.0	2627.1	2616.5	-20.9	-30.7	2682.5	46.2
21	47.2	31.0	2663.7	2653.1	-19.7	-29.5	2719.6	47.9
22	48.0	31.8	2696.2	2685.6	-18.7	-28.5	2752.4	49.5
23	48.8	32.6	2725.0	2714.3	-17.7	-27.5	2781.6	50.8
24	49.5	33.2	2750.5	2739.8	-16.9	-26.7	2807.4	52.0
25	50.1	33.8	2773.1	2762.5	-16.1	-26.0	2830.3	53.1

| Parameters: | | i_d | i_e | DR | i_c | | |
| | | 11% | 15% | 65% | 12% | | |
Year	OCGT(CNG)	OCGT(LNG)	RES+OCGT(CNG)	RES+OCGT(LNG)	CaL+OCGT(CNG)	CaL+OCGT(LNG)	RES+SSC	CaL+SSC
1	-27.3	-42.4	-374.7	-385.1	-111.5	-121.2	-357.0	-87.5
2	-20.4	-35.9	132.6	122.0	-102.8	-112.6	156.9	-71.1
3	-11.8	-27.4	455.9	445.3	-92.2	-102.0	484.3	-55.9
4	-4.1	-19.8	743.6	733.0	-82.8	-92.7	775.6	-42.4
5	2.7	-13.1	999.6	988.9	-74.5	-84.3	1034.7	-30.4
6	8.8	-7.1	1227.3	1216.6	-67.0	-76.9	1265.3	-19.7
7	14.2	-1.7	1429.9	1419.2	-60.4	-70.3	1470.4	-10.2
8	19.0	3.0	1610.1	1599.5	-54.5	-64.4	1652.9	-1.8
9	23.2	7.2	1770.4	1759.8	-49.3	-59.1	1815.2	5.8
10	27.1	11.0	1913.1	1902.5	-44.6	-54.5	1959.7	12.4
11	30.4	14.4	2040.0	2029.4	-40.5	-50.3	2088.2	18.4
12	33.4	17.3	2153.0	2142.3	-36.8	-46.7	2202.5	23.7
13	36.1	20.0	2253.0	2242.3	-33.5	-43.4	2304.3	28.4
14	38.5	22.3	2342.8	2332.2	-30.6	-40.5	2394.7	32.6
15	40.6	24.4	2422.3	2411.7	-28.0	-37.9	2475.3	36.3
16	42.5	26.3	2493.1	2482.4	-25.7	-35.6	2546.9	39.6
17	44.2	27.9	2556.0	2545.4	-23.6	-33.5	2610.6	42.6
18	45.7	29.4	2612.0	2601.4	-21.8	-31.7	2667.3	45.2
19	47.0	30.7	2661.9	2651.2	-20.2	-30.0	2717.8	47.5
20	48.2	31.9	2706.2	2695.5	-18.7	-28.6	2762.6	49.6
21	49.3	32.9	2745.6	2735.0	-17.5	-27.3	2802.6	51.5
22	50.2	33.9	2780.7	2770.1	-16.3	-26.2	2838.1	53.1
23	51.0	34.7	2811.9	2801.3	-15.3	-25.1	2869.7	54.6
24	51.8	35.4	2839.7	2829.0	-14.4	-24.2	2897.8	55.9
25	52.4	36.1	2864.4	2853.7	-13.6	-23.4	2922.8	57.0

Table C1 Continued:

	Parameters:	i_d	i_e	DR	i_c		
		7%	20%	45%	14%		
Year	OCGT(CNG)	OCGT(LNG)	RES+OCGT(CNG)	RES+OCGT(LNG)	CaL+OCGT(CNG)	CaL+OCGT(LNG)	RES+SSC	CaL+SSC
1	-26.9	-41.8	-368.9	-379.2	-109.8	-119.3	-351.5	-86.2
2	-20.2	-35.5	122.9	112.4	-101.3	-111.0	146.8	-70.2
3	-12.0	-27.3	431.6	421.1	-91.3	-100.9	459.3	-55.7
4	-4.8	-20.2	702.0	691.6	-82.4	-92.1	733.2	-43.1
5	1.5	-14.0	938.9	928.5	-74.7	-84.4	973.0	-31.9
6	7.1	-8.5	1146.5	1136.1	-67.9	-77.6	1183.2	-22.2
7	11.9	-3.7	1328.3	1317.9	-62.0	-71.7	1367.3	-13.7
8	16.2	0.5	1487.6	1477.2	-56.8	-66.5	1528.5	-6.2
9	19.9	4.2	1627.2	1616.7	-52.2	-61.9	1669.8	0.3
10	23.2	7.4	1749.4	1738.9	-48.2	-57.9	1793.6	6.1
11	26.0	10.2	1856.5	1846.0	-44.7	-54.4	1902.0	11.1
12	28.5	12.7	1950.3	1939.8	-41.7	-51.4	1997.0	15.5
13	30.7	14.9	2032.5	2022.0	-39.0	-48.7	2080.7	19.3
14	32.6	16.8	2104.5	2094.0	-36.6	-46.3	2153.1	22.7
15	34.3	18.4	2167.6	2157.1	-34.6	-44.3	2216.9	25.7
16	35.8	19.9	2222.8	2212.3	-32.8	-42.5	2272.9	28.3
17	37.1	21.2	2271.2	2260.7	-31.2	-40.9	2321.9	30.5
18	38.2	22.3	2313.6	2303.1	-29.8	-39.5	2364.8	32.5
19	39.2	23.2	2350.8	2340.3	-28.6	-38.3	2402.4	34.3
20	40.1	24.1	2383.3	2372.8	-27.5	-37.2	2435.4	35.8
21	40.8	24.9	2411.8	2401.3	-26.6	-36.3	2464.3	37.1
22	41.5	25.5	2436.6	2426.3	-25.8	-35.5	2489.5	38.3
23	42.1	26.1	2458.7	2448.2	-25.1	-34.8	2511.7	39.3
24	42.6	26.6	2477.8	2467.4	-24.4	-34.1	2531.1	40.2
25	43.0	27.0	2494.6	2484.2	-23.9	-33.6	2548.1	41.0

	Parameters:	i_d	i_e	DR	i_c		
		7%	20%	55%	13%		
Year	OCGT(CNG)	OCGT(LNG)	RES+OCGT(CNG)	RES+OCGT(LNG)	CaL+OCGT(CNG)	CaL+OCGT(LNG)	RES+SSC	CaL+SSC
1	-27.2	-42.2	-373.2	-383.6	-111.1	-120.7	-355.6	-87.2
2	-20.4	-35.8	130.0	119.5	-102.4	-112.2	154.3	-70.8
3	-11.9	-27.4	449.5	439.0	-92.0	-101.8	477.8	-55.9
4	-4.3	-19.9	732.6	722.1	-82.7	-92.5	764.4	-42.6
5	2.4	-13.3	983.5	973.0	-74.5	-84.3	1018.4	-30.8
6	8.3	-7.4	1205.8	1195.3	-67.3	-77.1	1243.5	-20.4
7	13.6	-2.3	1402.9	1392.3	-60.8	-70.6	1443.0	-11.1
8	18.2	2.3	1577.4	1566.8	-55.1	-64.9	1619.7	-3.0
9	22.3	6.4	1732.1	1721.5	-50.1	-59.9	1776.3	4.3
10	26.0	10.0	1869.2	1858.6	-45.6	-55.4	1915.1	10.7
11	29.2	13.2	1990.6	1980.1	-41.6	-51.5	2038.1	16.4
12	32.1	16.1	2098.3	2087.7	-38.1	-47.9	2147.1	21.5
13	34.7	18.6	2193.7	2183.1	-35.0	-44.8	2243.7	25.9
14	36.9	20.8	2278.2	2267.6	-32.3	-42.1	2329.2	29.9
15	38.9	22.8	2353.1	2342.5	-29.8	-39.6	2405.1	33.4
16	40.7	24.5	2419.5	2408.9	-27.6	-37.5	2472.3	36.5
17	42.2	26.1	2478.3	2467.7	-25.7	-35.5	2531.8	39.3
18	43.6	27.5	2530.4	2519.8	-24.0	-33.8	2584.6	41.7
19	44.9	28.7	2576.6	2566.0	-22.5	-32.3	2631.3	43.9
20	46.0	29.8	2617.5	2606.9	-21.2	-31.0	2672.8	45.8
21	46.9	30.7	2653.7	2643.1	-20.0	-29.8	2709.5	47.5
22	47.8	31.6	2685.9	2675.3	-18.9	-28.8	2742.0	49.0
23	48.5	32.3	2714.4	2703.8	-18.0	-27.8	2770.8	50.3
24	49.2	33.0	2739.6	2729.0	-17.2	-27.0	2796.4	51.5
25	49.8	33.6	2761.9	2751.3	-16.5	-26.3	2819.0	52.6

Table C1 Continued:

	Parameters:	i_d	i_e	DR	i_c		
		7%	20%	65%	12%		
Year	OCGT(CNG)	OCGT(LNG)	RES+OCGT(CNG)	RES+OCGT(LNG)	CaL+OCGT(CNG)	CaL+OCGT(LNG)	RES+SSC	CaL+SSC
1	-27.5	-42.7	-377.5	-388.0	-112.4	-122.1	-359.7	-88.2
2	-20.5	-36.1	137.5	126.8	-103.5	-113.4	162.1	-71.5
3	-11.7	-27.4	468.3	457.6	-92.7	-102.6	497.0	-56.0
4	-3.8	-19.6	764.8	754.1	-83.0	-92.9	797.3	-42.0
5	3.3	-12.6	1030.7	1020.0	-74.3	-84.2	1066.4	-29.6
6	9.6	-6.3	1269.0	1258.3	-66.6	-76.5	1307.7	-18.4
7	15.3	-0.7	1482.6	1471.9	-59.6	-69.5	1524.0	-8.4
8	20.4	4.4	1674.2	1663.5	-53.3	-63.2	1717.9	0.6
9	25.0	8.9	1845.9	1835.2	-47.7	-57.6	1891.8	8.6
10	29.1	12.9	1999.8	1989.1	-42.7	-52.6	2047.6	15.9
11	32.8	16.6	2137.8	2127.0	-38.2	-48.1	2187.3	22.3
12	36.1	19.8	2261.5	2250.7	-34.1	-44.1	2312.6	28.1
13	39.1	22.8	2372.3	2361.6	-30.5	-40.4	2424.8	33.3
14	41.7	25.4	2471.7	2461.0	-27.3	-37.2	2525.5	38.0
15	44.1	27.7	2560.9	2550.1	-24.4	-34.3	2615.7	42.2
16	46.2	29.8	2640.7	2630.0	-21.8	-31.7	2696.6	45.9
17	48.1	31.7	2712.4	2701.6	-19.4	-29.3	2769.1	49.3
18	49.8	33.4	2776.6	2765.8	-17.3	-27.2	2834.1	52.3
19	51.4	34.9	2834.1	2823.3	-15.4	-25.4	2892.3	55.0
20	52.8	36.3	2885.7	2875.0	-13.8	-23.7	2944.6	57.4
21	54.0	37.5	2932.0	2921.2	-12.2	-22.2	2991.4	59.6
22	55.1	38.6	2973.4	2962.7	-10.9	-20.8	3033.4	61.5
23	56.1	39.6	3010.6	2999.9	-9.7	-19.6	3071.0	63.3
24	57.0	40.5	3043.9	3033.2	-8.6	-18.5	3104.8	64.8
25	57.8	41.2	3073.8	3063.0	-7.6	-17.5	3135.0	66.2

	Parameters:	i_d	i_e	DR	i_c		
		9%	20%	45%	15%		
Year	OCGT(CNG)	OCGT(LNG)	RES+OCGT(CNG)	RES+OCGT(LNG)	CaL+OCGT(CNG)	CaL+OCGT(LNG)	RES+SSC	CaL+SSC
1	-26.7	-41.4	-366.0	-376.2	-109.0	-118.4	-348.8	-85.5
2	-20.1	-35.2	118.1	107.7	-100.6	-110.2	141.8	-69.8
3	-12.1	-27.3	419.6	409.3	-90.8	-100.4	447.0	-55.6
4	-5.1	-20.4	681.7	671.4	-82.2	-91.8	712.4	-43.4
5	1.0	-14.4	909.5	899.1	-74.8	-84.4	943.0	-32.7
6	6.3	-9.2	1107.5	1097.1	-68.3	-77.9	1143.5	-23.4
7	10.9	-4.6	1279.6	1269.2	-62.7	-72.3	1317.7	-15.3
8	14.8	-0.7	1429.2	1418.8	-57.8	-67.4	1469.2	-8.3
9	18.3	2.7	1559.2	1548.8	-53.6	-63.2	1600.8	-2.2
10	21.3	5.7	1672.2	1661.8	-49.9	-59.5	1715.2	3.1
11	23.9	8.3	1770.4	1760.1	-46.7	-56.3	1814.7	7.7
12	26.2	10.6	1855.8	1845.4	-43.9	-53.5	1901.1	11.7
13	28.2	12.5	1930.0	1919.6	-41.4	-51.1	1976.3	15.2
14	29.9	14.2	1994.5	1984.1	-39.3	-49.0	2041.6	18.2
15	31.4	15.7	2050.6	2040.2	-37.5	-47.1	2098.3	20.8
16	32.7	17.0	2099.3	2088.9	-35.9	-45.5	2147.7	23.1
17	33.8	18.1	2141.7	2131.3	-34.5	-44.1	2190.6	25.1
18	34.8	19.1	2178.5	2168.1	-33.3	-42.9	2227.8	26.8
19	35.7	19.9	2210.5	2200.1	-32.3	-41.9	2260.2	28.3
20	36.4	20.6	2238.3	2227.9	-31.4	-41.0	2288.4	29.6
21	37.1	21.3	2262.5	2252.1	-30.6	-40.2	2312.9	30.8
22	37.6	21.8	2283.5	2273.1	-29.9	-39.5	2334.1	31.8
23	38.1	22.3	2301.7	2291.4	-29.3	-38.9	2352.6	32.6
24	38.5	22.7	2317.6	2307.2	-28.8	-38.4	2368.7	33.4
25	38.9	23.1	2331.4	2321.0	-28.3	-38.0	2382.7	34.0

Table C1 Continued:

Year	OCGT(CNG)	OCGT(LNG)	RES+OCGT(CNG)	RES+OCGT(LNG)	CaL+OCGT(CNG)	CaL+OCGT(LNG)	RES+SSC	CaL+SSC
Parameters:			i_d	i_e	DR	i_c		
			9%	20%	55%	14%		
1	-27.0	-41.8	-369.6	-379.9	-110.0	-119.5	-352.2	-86.3
2	-20.3	-35.5	124.0	113.5	-101.5	-111.2	147.9	-70.3
3	-12.0	-27.3	434.3	423.8	-91.4	-101.1	462.1	-55.8
4	-4.7	-20.2	706.6	696.2	-82.5	-92.2	737.9	-43.0
5	1.7	-13.9	945.6	935.2	-74.7	-84.4	979.9	-31.8
6	7.3	-8.3	1155.4	1144.9	-67.8	-77.5	1192.2	-21.9
7	12.2	-3.5	1339.5	1329.0	-61.8	-71.5	1378.6	-13.3
8	16.5	0.8	1501.0	1490.5	-56.5	-66.2	1542.1	-5.7
9	20.3	4.5	1642.8	1632.3	-51.9	-61.6	1685.7	0.9
10	23.6	7.8	1767.2	1756.7	-47.8	-57.5	1811.6	6.7
11	26.5	10.7	1876.3	1865.9	-44.3	-54.0	1922.1	11.9
12	29.0	13.2	1972.2	1961.7	-41.1	-50.9	2019.2	16.4
13	31.3	15.4	2056.2	2045.7	-38.4	-48.1	2104.3	20.3
14	33.3	17.4	2130.0	2119.5	-36.0	-45.7	2179.0	23.8
15	35.0	19.1	2194.8	2184.3	-33.9	-43.6	2244.5	26.8
16	36.5	20.6	2251.6	2241.1	-32.0	-41.7	2302.1	29.5
17	37.8	21.9	2301.5	2291.0	-30.4	-40.1	2352.6	31.8
18	39.0	23.0	2345.2	2334.7	-29.0	-38.7	2396.9	33.9
19	40.0	24.0	2383.6	2373.1	-27.7	-37.4	2435.8	35.7
20	40.9	24.9	2417.3	2406.9	-26.6	-36.3	2469.9	37.2
21	41.7	25.7	2446.9	2436.4	-25.6	-35.4	2499.8	38.6
22	42.4	26.4	2472.9	2462.4	-24.8	-34.5	2526.1	39.8
23	43.0	27.0	2495.7	2485.2	-24.1	-33.8	2549.2	40.9
24	43.5	27.5	2515.7	2505.2	-23.4	-33.1	2569.4	41.8
25	44.0	28.0	2533.2	2522.7	-22.8	-32.5	2587.2	42.7

Year	OCGT(CNG)	OCGT(LNG)	RES+OCGT(CNG)	RES+OCGT(LNG)	CaL+OCGT(CNG)	CaL+OCGT(LNG)	RES+SSC	CaL+SSC
Parameters:			i_d	i_e	DR	i_c		
			9%	20%	65%	13%		
1	-27.2	-42.2	-373.2	-383.6	-111.1	-120.7	-355.6	-87.2
2	-20.4	-35.8	130.0	119.5	-102.4	-112.2	154.3	-70.8
3	-11.9	-27.4	449.5	439.0	-92.0	-101.8	477.8	-55.9
4	-4.3	-19.9	732.6	722.1	-82.7	-92.5	764.4	-42.6
5	2.4	-13.3	983.5	973.0	-74.5	-84.3	1018.4	-30.8
6	8.3	-7.4	1205.8	1195.3	-67.3	-77.1	1243.5	-20.4
7	13.6	-2.3	1402.9	1392.3	-60.8	-70.6	1443.0	-11.1
8	18.2	2.3	1577.4	1566.8	-55.1	-64.9	1619.7	-3.0
9	22.3	6.4	1732.1	1721.5	-50.1	-59.9	1776.3	4.3
10	26.0	10.0	1869.2	1858.6	-45.6	-55.4	1915.1	10.7
11	29.2	13.2	1990.7	1980.1	-41.6	-51.5	2038.1	16.4
12	32.1	16.1	2098.3	2087.7	-38.1	-47.9	2147.1	21.5
13	34.7	18.6	2193.7	2183.1	-35.0	-44.8	2243.7	25.9
14	36.9	20.8	2278.2	2267.6	-32.3	-42.1	2329.2	29.9
15	38.9	22.8	2353.1	2342.5	-29.8	-39.6	2405.1	33.4
16	40.7	24.5	2419.5	2408.9	-27.6	-37.5	2472.3	36.5
17	42.2	26.1	2478.3	2467.7	-25.7	-35.5	2531.8	39.3
18	43.6	27.5	2530.4	2519.8	-24.0	-33.8	2584.6	41.7
19	44.9	28.7	2576.6	2566.0	-22.5	-32.3	2631.3	43.9
20	46.0	29.8	2617.5	2606.9	-21.2	-31.0	2672.8	45.8
21	46.9	30.7	2653.7	2643.1	-20.0	-29.8	2709.5	47.5
22	47.8	31.6	2685.9	2675.3	-18.9	-28.8	2742.0	49.0
23	48.5	32.3	2714.4	2703.8	-18.0	-27.8	2770.8	50.3
24	49.2	33.0	2739.6	2729.0	-17.2	-27.0	2796.4	51.5
25	49.8	33.6	2761.9	2751.3	-16.5	-26.3	2819.0	52.6

Table C1 Continued:

	Parameters:	i_d	i_e	DR	i_c		
		11%	20%	45%	16%		
Year	OCGT(CNG)	RES+OCGT(CNG)	RES+OCGT(LNG)	CaL+OCGT(CNG)	CaL+OCGT(LNG)	RES+SSC	CaL+SSC
1	-26.5	-41.1	-363.2	-373.3	-108.1	-117.5	-346.1	-84.8
2	-20.0	-35.0	113.4	103.2	-99.9	-109.4	136.9	-69.4
3	-12.2	-27.2	408.0	397.7	-90.3	-99.8	435.1	-55.6
4	-5.4	-20.6	662.0	651.8	-82.0	-91.5	692.3	-43.6
5	0.5	-14.8	881.1	870.9	-74.8	-84.3	914.1	-33.4
6	5.5	-9.8	1070.1	1059.8	-68.7	-78.2	1105.5	-24.5
7	9.8	-5.5	1233.1	1222.8	-63.3	-72.9	1270.4	-16.9
8	13.6	-1.8	1373.6	1363.3	-58.7	-68.3	1412.7	-10.3
9	16.8	1.4	1494.8	1484.5	-54.8	-64.3	1535.5	-4.6
10	19.6	4.1	1599.3	1589.1	-51.4	-60.9	1641.3	0.3
11	22.0	6.5	1689.5	1679.2	-48.4	-58.0	1732.6	4.5
12	24.1	8.6	1767.3	1757.0	-45.9	-55.4	1811.3	8.2
13	25.9	10.3	1834.3	1824.0	-43.7	-53.2	1879.2	11.3
14	27.4	11.9	1892.2	1881.9	-41.8	-51.3	1937.8	14.0
15	28.8	13.2	1942.0	1931.7	-40.2	-49.7	1988.3	16.4
16	29.9	14.3	1985.1	1974.8	-38.8	-48.3	2031.8	18.4
17	30.9	15.3	2022.2	2011.9	-37.6	-47.1	2069.4	20.1
18	31.7	16.1	2054.2	2043.8	-36.5	-46.1	2101.8	21.6
19	32.5	16.9	2081.7	2071.4	-35.6	-45.2	2129.7	22.9
20	33.1	17.5	2105.5	2095.2	-34.8	-44.4	2153.8	24.0
21	33.7	18.0	2126.1	2115.8	-34.2	-43.7	2174.6	25.0
22	34.1	18.5	2143.8	2133.5	-33.6	-43.1	2192.5	25.8
23	34.5	18.9	2159.0	2148.7	-33.1	-42.6	2208.0	26.6
24	34.9	19.2	2172.2	2161.9	-32.7	-42.2	2221.3	27.2
25	35.2	19.5	2183.6	2173.3	-32.3	-41.8	2232.8	27.7

	Parameters:	i_d	i_e	DR	i_c		
		11%	20%	55%	15%		
Year	OCGT(CNG)	RES+OCGT(CNG)	RES+OCGT(LNG)	CaL+OCGT(CNG)	CaL+OCGT(LNG)	RES+SSC	CaL+SSC
1	-26.7	-41.4	-366.0	-376.2	-109.0	-118.4	-348.8	-85.5
2	-20.1	-35.2	118.1	107.7	-100.6	-110.2	141.8	-69.8
3	-12.1	-27.3	419.6	409.3	-90.8	-100.4	447.0	-55.6
4	-5.1	-20.4	681.7	671.4	-82.2	-91.8	712.4	-43.4
5	1.0	-14.4	909.5	899.1	-74.8	-84.4	943.0	-32.7
6	6.3	-9.2	1107.5	1097.1	-68.3	-77.9	1143.5	-23.4
7	10.9	-4.6	1279.6	1269.2	-62.7	-72.3	1317.7	-15.3
8	14.8	-0.7	1429.2	1418.8	-57.8	-67.4	1469.2	-8.3
9	18.3	2.7	1559.2	1548.8	-53.6	-63.2	1600.8	-2.2
10	21.3	5.7	1672.2	1661.8	-49.9	-59.5	1715.2	3.1
11	23.9	8.3	1770.4	1760.1	-46.7	-56.3	1814.7	7.7
12	26.2	10.6	1855.8	1845.4	-43.9	-53.5	1901.5	11.7
13	28.2	12.5	1930.0	1919.6	-41.4	-51.1	1976.3	15.2
14	29.9	14.2	1994.5	1984.1	-39.3	-49.0	2041.6	18.2
15	31.4	15.7	2050.6	2040.2	-37.5	-47.1	2098.3	20.8
16	32.7	17.0	2099.3	2088.9	-35.9	-45.5	2147.7	23.1
17	33.8	18.1	2141.7	2131.3	-34.5	-44.1	2190.6	25.1
18	34.8	19.1	2178.5	2168.1	-33.3	-42.9	2227.8	26.8
19	35.7	19.9	2210.5	2200.1	-32.3	-41.9	2260.2	28.3
20	36.4	20.6	2238.3	2227.9	-31.4	-41.0	2288.4	29.6
21	37.1	21.3	2262.5	2252.1	-30.6	-40.2	2312.9	30.8
22	37.6	21.8	2283.5	2273.1	-29.9	-39.5	2334.1	31.8
23	38.1	22.3	2301.7	2291.4	-29.3	-38.9	2352.6	32.6
24	38.5	22.7	2317.6	2307.2	-28.8	-38.4	2368.7	33.4
25	38.9	23.1	2331.4	2321.0	-28.3	-38.0	2382.7	34.0

Table C1 Continued:

| | Parameters: | i_d | i_e | DR | i_c | | |
| | | 11% | 20% | 65% | 14% | | |
Year	OCGT(CNG)	OCGT(LNG)	RES+OCGT(CNG)	RES+OCGT(LNG)	CaL+OCGT(CNG)	CaL+OCGT(LNG)	RES+SSC	CaL+SSC
1	-26.9	-41.8	-368.9	-379.2	-109.8	-119.3	-351.5	-86.2
2	-20.2	-35.5	122.9	112.4	-101.3	-111.0	146.8	-70.2
3	-12.0	-27.3	431.6	421.1	-91.3	-100.9	459.3	-55.7
4	-4.8	-20.2	702.0	691.6	-82.4	-92.1	733.2	-43.1
5	1.5	-14.0	938.9	928.5	-74.7	-84.4	973.0	-31.9
6	7.1	-8.5	1146.5	1136.1	-67.9	-77.6	1183.2	-22.2
7	11.9	-3.7	1328.3	1317.9	-62.0	-71.7	1367.3	-13.7
8	16.2	0.5	1487.6	1477.2	-56.8	-66.5	1528.5	-6.2
9	19.9	4.2	1627.2	1616.7	-52.2	-61.9	1669.8	0.3
10	23.2	7.4	1749.4	1738.9	-48.2	-57.9	1793.6	6.1
11	26.0	10.2	1856.5	1846.0	-44.7	-54.4	1902.0	11.1
12	28.5	12.7	1950.3	1939.8	-41.7	-51.4	1997.0	15.5
13	30.7	14.9	2032.5	2022.0	-39.0	-48.7	2080.2	19.3
14	32.6	16.8	2104.5	2094.0	-36.6	-46.3	2153.1	22.7
15	34.3	18.4	2167.6	2157.1	-34.6	-44.3	2216.9	25.7
16	35.8	19.9	2222.8	2212.3	-32.8	-42.5	2272.9	28.3
17	37.1	21.2	2271.2	2260.7	-31.2	-40.9	2321.9	30.5
18	38.2	22.3	2313.6	2303.1	-29.8	-39.5	2364.8	32.5
19	39.2	23.2	2350.8	2340.3	-28.6	-38.3	2402.4	34.3
20	40.1	24.1	2383.3	2372.8	-27.5	-37.2	2435.4	35.8
21	40.8	24.9	2411.8	2401.3	-26.6	-36.3	2464.3	37.1
22	41.5	25.5	2436.8	2426.3	-25.8	-35.5	2489.5	38.3
23	42.1	26.1	2458.7	2448.2	-25.1	-34.8	2511.7	39.3
24	42.6	26.6	2477.8	2467.4	-24.4	-34.1	2531.1	40.2
25	43.0	27.0	2494.6	2484.2	-23.9	-33.6	2548.1	41.0

APPENDIX D: PUBLICATIONS, STAFF AND STUDENTS

Publications: None at this stage although the team is planning to publish four journal articles from this final report including a review paper on the topic of utility-scale energy storgae.

Staff Involved with the Project:

Title	First Name	Surname	Role in the Project
Prof	Behdad	Moghtaderi	Project Leader & Chief Investigator (0.3 FTE in-kind contribution)
Dr	Ahmad	Seyfaee	Chief Investigator (1.0 FTE; employed on the project)
Dr	Cheng	Zhou	Chief Investigator (0.1 FTE in-kind contribution)
Prof	Jianglong	Yu	Chief Investigator (0.1 FTE in-kind contribution)
A/Prof	Elham	Doroodchi	Technical Advisor (0.05 FTE in-kind contribution)
Dr	Andrew	Maddocks	Technical Advisor (0.05 FTE in-kind contribution)
Dr	Priscilla	Tremain	Technical Advisor (0.05 FTE in-kind contribution)
Dr	Jafar	Zanganeh	Technical Advisor (0.05 FTE in-kind contribution)
Dr	Jessica	Alan	Technical Advisor (0.05 FTE in-kind contribution)
Dr	Khadijeh	Paymooni	Technical Advisor (0.05 FTE in-kind contribution)
Dr	Zengbiao	Peng	Technical Advisor (0.05 FTE in-kind contribution)
Dr	Omid	Mowla	Technical Advisor (0.05 FTE in-kind contribution)
Mr	John	Winter	Technician (0.1 FTE in-kind contribution)
Mr	Daniel	Eschebach	Technician (0.1 FTE in-kind contribution)

Students Involved with the Project*:

Title	First Name	Surname	Role in the Project
Mr	Sike	Wu	Research Assistant
Mr	Francis	Nadaraju	Research Assistant
Mr	Mohammed	Ajrash	Research Assistant
Mr	Fengkui	Yin	Research Assistant
Mr	David	Shirzaei	Research Assistant

*No direct graduates from the project. These are postgraduate students who contributed to the project as Research Assistants working outside their own PhD projects.

SIGN OFF:

I, the undersigned, being a person duly authorised by the Grantee, certify that:

(a) the above information is true and complete;
(b) the expenditure of the Funding received to date has been solely on the Project; and
(c) there is no matter or circumstances of which I am aware, that would constitute a breach by the NSW Department of Industry, Skills and Regional Development or, if applicable the End Recipient, of any term of the Funding Agreement between the NSW Department of Industry, Skills and Regional Development and Grantee dated 11/01/2017 that has not been notified by the Grantee.

Signature: *B Moghtaderi*

Position: Director, Priority Research Centre for Frontier Energy Technologies & Utilisation

Name: Behdad Moghtaderi

Date: 28 February 2019 (Draft Final Report)

             24 July 2019 (Revised Final Report)